# Development of Fluorescent Quantum Dots Emitting in Second Near-Infrared Region for Bio-Imaging Applications

A Thesis Submitted

to

**Sikkim University**

In Partial Fulfilment of the Requirement for the

**Degree of Doctor of Philosophy**

By

**Karishma Bhardwaj**

Department of Chemistry

School of Physical Science

February, 2022

6 माइल, सामदुर, तादोंग -737102
गंगटोक, सिक्किम, भारत
फोन-03592-251212, 251415, 251656
टेलीफैक्स -251067
वेबसाइट - www.cus.ac.in

सिक्किम विश्वविद्यालय
SIKKIM UNIVERSITY

6th Mile, Samdur,Tadong -737102
Gangtok, Sikkim, India
Ph. 03592-251212, 251415, 251656
Telefax: 251067
Website: www.cus.ac.in

(भारत के संसद के अधिनियम द्वारा वर्ष 2007 में स्थापित और नैक (एनएएसी) द्वारा वर्ष 2015 में प्रत्यायित केंद्रीय विश्वविद्यालय)
(A central university established by an Act of Parliament of India in 2007 and accredited by NAAC in 2015)

# DECLARATION

I hereby declare that the work embodied in this thesis entitled "**Development of Fluorescent Quantum Dots Emitting in Second Near-Infrared Region for Bio-Imaging Applications.**" to be submitted for the Degree of Doctor of Philosophy in Chemistry of Sikkim University is my original work and the content of this dissertation is based on the experiments which I have performed myself. This dissertation has not been submitted to any other University or Institution for the award of any degree or diploma.

Karishma Bhardwaj

Place: Gangtok, Sikkim
Date: 22/02/2023

**Karishma Bhardwaj**
Roll No: 18PDCH02
Reg. No: 18/Ph.D./CMS/03

6 माइल, सामदुर, तादोंग -737102
गंगटोक, सिक्किम, भारत
फोन-03592-251212, 251415, 251656
टेलीफैक्स -251067
वेबसाइट - www.cus.ac.in

सिक्किम विश्वविद्यालय
SIKKIM UNIVERSITY

6th Mile, Samdur, Tadong -737102
Gangtok, Sikkim, India
Ph. 03592-251212, 251415, 251656
Telefax: 251067
Website: www.cus.ac.in

(भारत के संसद के अधिनियम द्वारा वर्ष 2007 में स्थापित और नैक (एनएएसी) द्वारा वर्ष 2015 में प्रत्यायित केंद्रीय विश्वविद्यालय)
(A central university established by an Act of Parliament of India in 2007 and accredited by NAAC in 2015)

# CERTIFICATE

This is to certify that the thesis titled "**Development of Fluorescent Quantum Dots Emitting in Second Near-Infrared Region for Bio-Imaging Applications.**" submitted to **Sikkim University** in partial fulfilment of the requirement for the degree of **Doctor of Philosophy (Chemistry)** is a result of original research work carried out by **Ms. Karishma Bhardwaj** under my guidance and supervision. The data and results presented in this dissertation are original and have been obtained in this laboratory.

All the assistance and help received during the course of the investigation have been acknowledged by her.

22/2/23
**H.O.D. / In charge**

*Dr. Sanjay Dahal*
Professor
Department of Chemistry
School of Physical Sciences
Sikkim University

Tamang
**Supervisor** 22/02/23

*Dr. Sudarsan Tamang*
Assistant Professor
Department of Chemistry
School of Physical Sciences
Sikkim University

6 माइल, सामदुर, तादोंग -737102
गंगटोक, सिक्किम, भारत
फोन-03592-251212, 251415, 251656
टेलीफैक्स -251067
वेबसाइट - www.cus.ac.in

6th Mile, Samdur,Tadong -737102
Gangtok, Sikkim, India
Ph. 03592-251212, 251415, 251656
Telefax: 251067
Website: www.cus.ac.in

सिक्किम विश्वविद्यालय
SIKKIM UNIVERSITY
(भारत के संसद के अधिनियम द्वारा वर्ष 2007 में स्थापित और नैक (एनएएसी) द्वारा वर्ष 2015 में प्रत्यायित केंद्रीय विश्वविद्यालय)
(A central university established by an Act of Parliament of India in 2007 and accredited by NAAC in 2015)

---

Date : 22/2/2023

## CERTIFICATE FOR PLAGIARISM CHECK

This is to certify that plagiarism check has been carried out for the following Ph.D. thesis with the help of URKUND software and the result is 0% similarity, which is within the permissible limit (below 10 % tolerance rate) as per the norm of Sikkim University.

**"Development of Fluorescent Quantum Dots Emitting in Second Near-Infrared Region for Bio-Imaging Applications."**

Submitted by **Ms. Karishma Bhardwaj** under the supervision of
**Dr. Sudarsan Tamang**, Department of Chemistry,
School of Physical Sciences, Sikkim University.

Karishma Bhardwaj
**Karishma Bhardwaj**
Signature of the candidate

22/02/23
*Dr. Sudarsan Tamang*
Assistant Professor
Department of Chemistry
School of Physical Sciences
Sikkim University

22/2/2023
*Dr. Shri Ram*
Librarian
Sikkim University

*For Kiana*

# Acknowledgment

Completing a Ph.D. is a long and challenging journey, and it is not possible to achieve it without the support and encouragement of many people. I am deeply grateful to God and to the following individuals and institutions for their invaluable contributions to this work.

First and foremost, I would like to express my profound gratitude to my supervisor, Dr. Sudarsan Tamang, for his guidance, mentorship, and unwavering support throughout my Ph.D. journey. His insights and expertise have been instrumental in shaping my research and helping me to overcome numerous obstacles along the way. I am thankful for his patience and continual motivation. His meticulous checking of my thesis and invaluable feedback has significantly improved the quality of my work.

I would like to express my gratitude to Sikkim University for providing me with the opportunity to pursue my Ph.D. degree. I am thankful to Prof. Sanjay Dahal, the Head of the Department of Chemistry, Dr. Anand Parihar, Dr. Somendra Nath Chakraborty, and Dr. Biswajeet Gopal Roy for their continuous guidance and support. My sincere gratitude also extends to the Microbiology and Physics Departments for providing me with the necessary resources and equipment for my research.

I would also like to extend my thanks to Dr. Graeme J. Stasiuk from Kings College London, Dr. Amit Shankar from Kurseong College Darjeeling, and Dr. Lakshi Sakia from NEIST Assam for their valuable collaboration and funding from SERB-DST for the projects.

I am thankful to the Vice Chancellor of Tripura University, Prof. Ganga Prasad Prasain, for his continuous moral support and guidance.

I would also like to thank our lab assistant, Binod Chettri Sir, for his help with the instruments, chemicals, and glassware in the lab.

I am grateful to all my friends, seniors, and juniors namely Susanta Mandal, Surakcha Thapa, Siddhant Basnett, Samuzal Bhuyan, Debesh Sharma, Pankaj Roy, Khanindram Baruah, Karan Chettri, Sagar Rasaily, Bikram Thapa, Sivanand Chettri, Deshaj Bhujel and Dr. Sajan Pradhan, for their support and assistance.

I deeply appreciate my husband, Kishor Prasain, for his love, support, and encouragement, which have constantly motivated and inspired me. Kiana, my newborn daughter during the research journey, has brought joy to my life and reminded me of the importance of balance and perspective. I am grateful to both of them.

Lastly, I would like to extend my heartfelt thanks to my Mom, Dad, Brothers (Pappu & Bikki), my in-laws, and all the family members and relatives for their love and support.

This Ph.D. would not have been possible without the support and encouragement of all these wonderful individuals and institutions, and I am deeply grateful to them all.

Thank you all for being a part of my journey.

**Karishma Bhardwaj**

Ph.D. Scholar

Roll No: 18PDCH02

Sikkim University, Gangtok-737102

# Table of Contents

| *Contents* | *Page No.* |
|---|---|
| Abstract | 1 |
| Aims and objectives | 2 |
| **Chapter I: General Introduction and Literature Review** | **3-54** |
| **1.1.** Introduction to Colloidal Quantum Dots | 4-7 |
| **1.2.** QDs in Biology | 7-8 |
| **1.3.** Near Infrared Emitting (NIR) QDs | 9-10 |
| 1.3.1. Group II-VI NIR QDs: CdX (X = S, Se, Te) | 10-12 |
| 1.3.2. Group IV-VI NIR QDs: PbX (X = S, Se, Te) | 12-13 |
| 1.3.3. Group III-V NIR QDs | 13-15 |
| 1.3.4. Non-toxic alternatives (Group IV QDs) | 15-16 |
| 1.3.5. Silver chalcogenides | 16-31 |
| **1.4.** Biofunctionalization of QDs | 31-32 |
| 1.4.1. Noncovalent conjugation approach | 32-33 |
| 1.4.2. Covalent conjugation approach | 33-34 |
| **1.5.** Research outline | 35 |
| **1.6.** References | 36-54 |
| **Chapter II: Synthesis of NIR-II Quantum Dots.** | **55-102** |
| **2.1.** Introduction | 56-57 |
| **2.2.** Precursors for NIR-II CQDs. | 58-59 |
| **2.3.** Synthesis of $Ag_2X$ (X=S, Se) NCs using substituted thio/selenourea precursors. | 59 |
| 2.3.1. Reactions and synthetic scheme | 59-62 |
| 2.3.2. Role of DDT | 62-63 |
| 2.3.3. Effect of reaction temperature and time on the size of the NCs. | 63-64 |
| 2.3.4. Structure-reactivity relation | 65-68 |
| **2.4.** Characterization of precursors and $Ag_2X$ (X=S, Se) NCs | 68 |
| 2.4.1. $^1$H and $^{13}$C NMR | 68-73 |

2.4.2. Optical characterization 73-74
2.4.3. Structural characterization 74-77
2.4.4. Surface analyses 77-81
**2.5.** Conclusion 82-83
**2.6.** Experimental section 84
2.6.1. Materials 84
2.6.2. Characterization techniques 85-87
2.6.3. Synthesis of $Ag_2S$ NCs 87-89
**2.7.** References 90-102
**Chapter III: Aqueous-soluble $Ag_2S$ NCs and $Ag_2S$/ZnS NCs 103-142**
**3.1.** Introduction 104
**3.2.** Phase transfer 104
3.2.1. L-cysteine as the phase transfer ligand 104-105
3.2.2. Phase transfer reaction 105
3.2.3. Characterisation of $Ag_2S$ QDs 106-108
**3.3.** Stability of $Ag_2S$ QDs in aqueous medium 109
3.3.1. pH 109
3.3.2. Colloidal stability 109-110
3.3.3. Phase stability 111
3.3.4. Photostability 111-112
3.3.5. Improving photostability: synthesis and characterization of $Ag_2S$/ZnS core/shell NCs 112-121
**3.4.**Conclusion 122-123
**3.5.** Experimental section 124
3.5.1. Materials and general considerations 124-125
3.5.2. Characterization methods 125-126
3.5.3. Synthesis 126-131
**3.6.** References 132-142

**Chapter IV: Design of MRI/NIR-II Multimodal Imaging Agent: Application of $Ag_2S$ QDs** **143-176**

**4.1.** Introduction 144-148

**4.2.** Bio-functionalization of $Ag_2S$ QDs as MRI/NIR-II Multimodal Imaging Agent 148

4.2.1. Gd-complex synthesis 148-150

4.2.2. Functionalization of $Ag_2S$ QDs with Gd-L 150-152

**4.3.** Properties of NIR-II/MRI (Gd-QD) multimodal contrast agent. 152

4.3.1. Molar extinction coefficient 152-153

4.3.2. Enhancement of water relaxivity by MRI/NIR-II contrast agent 153-154

**4.4.** Conclusion 155

**4.5.** Experimental Details 156

4.5.1. General Information 156-157

4.5.2. Characterization Methods 157-158

4.5.3. Synthesis 158

4.5.3.1. General Procedures for synthesis of sulphur precursors and $Ag_2S$ NCs 158-159

4.5.3.2. Synthesis of gadolinium complex (Gd-L) and conjugation with colloidal $Ag_2S$ QDs for MRI contrast agents. 160-161

4.5.3.3. Relaxivity measurements 161-162

4.5.3.4. Determination of Optical constants of $Ag_2S$ using DFT 162-167

4.5.3.5. Calculation of quantum yield (QY) 167

4.5.3.6. Spectral Data 168-169

**4.6.** References 170-176

***Annexure A. Supplementary Information*** **177-205**

*Annexure A2*: Supplementary information from Chapter II 178-197

*Annexure A3*: Supplementary information from Chapter III 198-200

*Annexure A4*: Supplementary information from Chapter IV 201-205

***Annexure B: Instrumentation and technique*** **206-268**

B1. Absorption spectroscopy. 207

B1.1. Basic principle 207-208

B1.2. Absorption peak and its origin. 208-211
  B1.3. Effective Mass Approximation Model (EMA) 211-213
  B1.4. Determination of band gap using UV-vis spectroscopy 213-216
  B1.5. Specification and sample preparation 216-217
B2. Photoluminescence (PL) Spectroscopy 217
  B2.1. Basic Principle 217-219
  B2.2. Determination of Band-gap 220
  B2.3. Crystal defects 220-221
  B2.4. Quantum Yield measurements 221-222
  B2.5. Instrumentation and sample preparation 222-223
B3. X-Ray Diffraction 224
  B3.1. Basic principle 224-227
  B3.2. Sample preparation and instrumentation 227-228
B4. Fourier-transform Infrared Spectroscopy (FTIR) 228
  B4.1. Basic Principle 228-231
  B4.2. Sample preparation and Instrumentation 231-232
B5. Thermogravimetric Analyser (TGA) 232
  B5.1. Basic Principle 232-234
B6. Turbidimeter 234
  B6.1. Basic principle 234-235
  B6.2. Sample Preparation and Instrumentation 235-236
B7. Transmission electron microscopy (TEM) 236
  B7. 1. Basic principle 236-240
  B7. 2. Sample preparation and instrumentation: 240-241
B8. X-ray Photoelectron (XPS) Spectroscopy 241
  B8.1 Basic principle 241-243
  B8.2 Chemical environment 243
  B8.3 Back ground correction 243-244
  B8.4 Elemental Analysis 244

B8.5 Sample preparation and Instrumentation 245

B9. Nuclear Magnetic Resonance Spectroscopy (NMR) 246

B9.1 Basic Principle 246-248

B9.2 Chemical Shift 248-249

B9.3. $T_1$ Relaxation (Spin-lattice relaxation) 250

B9.4 $T_2$ Relaxation (Spin-Spin relaxation) 250-251

B9.5 Relaxivity Measurements 251-254

B9.6 Sample preparation and Instrumentation 254-255

B10. References 256-268

***Annexure C: List of figures, tables and schemes*** **269-275**

C1. List of Figures 270-274

C2. List of Tables 274

C3. List of Schemes 275

***Annexure D: List of Abbreviations*** 276-281

***Annexure E: List of publications and conferences*** **282-295**

E1. Details of publications 283-293

E2. Conferences 294-295

.

# Abstract

Bio-compatible, nontoxic colloidal quantum dots with absorption/emission properties in the second near-infrared region (NIR-II, 1000-1400) are highly desirable for optical imaging and biosensing due to superior signal-to-noise ratio in the wavelength window. Highly aqueous stable silver chalcogenide quantum dots offer a non-toxic and stable alternative to existing Pd, As, Hg and Cd-based NIR-II colloidal quantum dots (CQDs). The thesis focuses on QDs emitting in NIR-II emission windows with $Ag_2X$ (X=S, Se) CQDs using thio/selenourea precursors and their analogues. Structure-reactivity study with substituted precursor (H, *p*–Me, *p*–OMe, *p*–I, and *p*–$NO_2$ revealed a linear Hammett relationship. In particular, larger $Ag_2S$ NCs were formed in the presence of an electron-withdrawing group (EWG), such as *p*-OMe, whereas smaller-sized NCs were obtained with an electron-donating group (EDG), like *p*-$NO_2$. These colloidal quantum dots (size < 5 nm) are then aqueous phase transferred with high retention of fluorescence quantum yield (~up to 93 %) and colloidal stability (~ 1 month). In addition, $Ag_2S$/ZnS core-shell NCs were also synthesized through the use of substituted thiourea as a sulfur source. The PL QY from 6.2% to 9.3% upon coating with a ZnS shell (thickness ~0.3 nm). The resulting aqueous core/shell NCs displayed enhanced photostability under blue-LED for up to 2 hours, and remained colloidal stable for approximately 48 days. Finally, these $Ag_2S$ QDs in an aqueous medium were functionalized using Gd-complex containing a thiol terminal group. A multimodal NIR-II/MRI contrast agent was prepared which showed tunable fluorescence (QY~5-6%) in NIR-II region and exhibited increase in MRI $T_1$ relaxivity of water (407-990 $mM^{-1}$ $s^{-1}$ per QD).

# Aims and objectives

1. To develop colloidal synthetic methods for NIR-II emitting QDs containing less toxic constituent elements.
2. To study reactivity of the precursor to QDs, nucleation and growth of NCs formation and their effect on size distribution and size tunability.
3. To study optical and colloidal stability of the QDs in aqueous medium.
4. Bio-functionalisation and its application.

# Chapter I

## *General Introduction and Literature Review*

## 1.1. Introduction to Colloidal Quantum Dots

The small, quasi-spherical inorganic semiconductor nanocrystals (NCs), also known as quantum dots (QDs) or Colloidal Quantum Dots (CQDs), measure approximately 1-10 nm in size and are typically synthesized and stabilized in colloidal form.[1] These QDs exhibit unique size-dependent optical and electrical properties due to the confinement of electron-hole wave functions in three dimensions. They are commonly composed of single-element substances, such as Si or Ge, or binary compounds formed from elements in groups II-VI (CdSe, CdTe, CdS, ZnO, ZnS, etc.), III-V (InP, GaAs), I-VI ($Ag_2S$, $Ag_2Se$, $Ag_2Te$), or IV-VI (PbS, PbSe). QDs have a multitude of technological applications, and their success in synthesis is directly linked to the precise control of synthetic schemes. This formation process typically results from a chemical reaction in which precursor molecules or ions undergo conversion, followed by nucleation and growth phases. QDs, which are larger than atoms but smaller than bulk solids, possess unique properties due to their size, falling within a range that is too big to display behavior characteristic of atoms or molecules, but too small to exhibit characteristics of bulk solids. It is worth mentioning that these materials are too large to behave like atoms or molecules and too small to act as bulk solids. A defining characteristic of these materials is that they have a high concentration of atoms on the surface or at the interface. The unique optoelectronic properties of QDs are attributed to the quantum confinement effect, where the size of the dots is smaller than the Bohr exciton radius, resulting in different properties than those of bulk materials.[2–6]

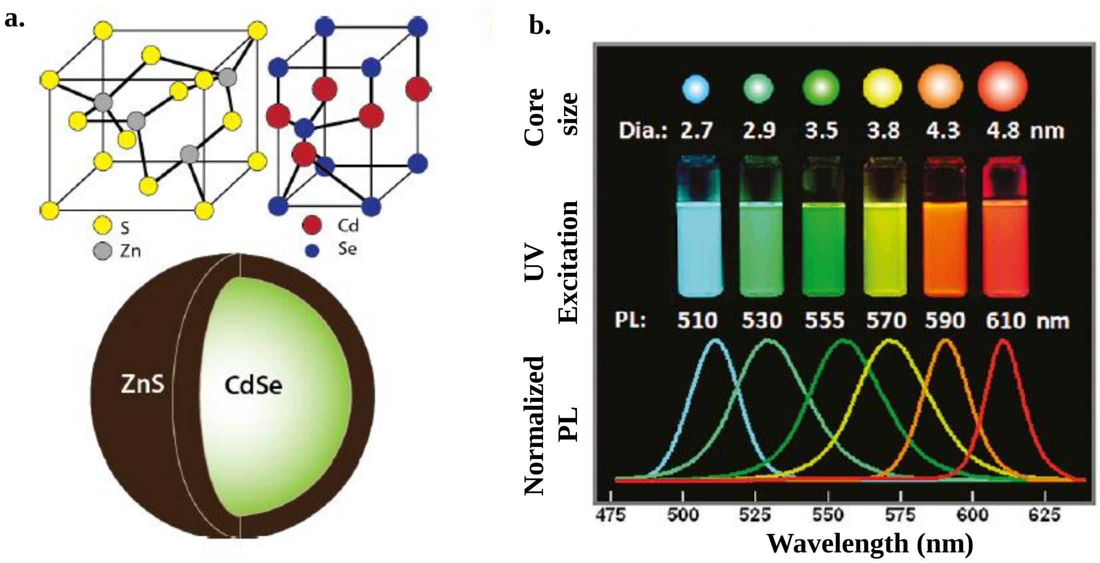

**Figure 1.1:** The Structure and Properties of QDs (a) A Core-Shell QD Cartoon Illustration and the Lattice Structure of CdSe and ZnS and (b) Photograph and Photoluminescence of QDs Samples with Different Diameters under Ultraviolet Illumination Demonstrating Size-Tunable Emission. Adapted with permission from Algar *et al*. Copyright 2011, American Chemical Society.[7]

Various techniques have been developed for producing high-quality NCs, including hot injection,[8] heat-up,[9] cation exchange,[10] and seeded growth method.[11] The hot injection method is primarily utilized for synthesizing QDs as it is a dynamic and straightforward process. The procedure involves introducing a cold solution of one ionic precursor into a hot mixture of the coordinating solvent and the other ionic precursors, causing a burst of nucleation due to the sudden availability of monomers at high temperatures. The formation of additional nuclei is prevented as the monomer concentration quickly drops below the nucleation threshold. This time-based separation between nucleation and growth allows for the synthesis of NCs. The heat-up method has also been widely used as it allows for large-scale production with low batch-to-batch variations.[9] In this technique, all the reactants are added to a single vessel and heated to the desired temperature for nucleation and growth. However, the distinction between nucleation and growth can be challenging in heat-up reactions, leading to Ostwald ripening.[12]

Therefore, careful selection of precursors, stabilizers, and heating rates is essential to achieve monodisperse NCs.

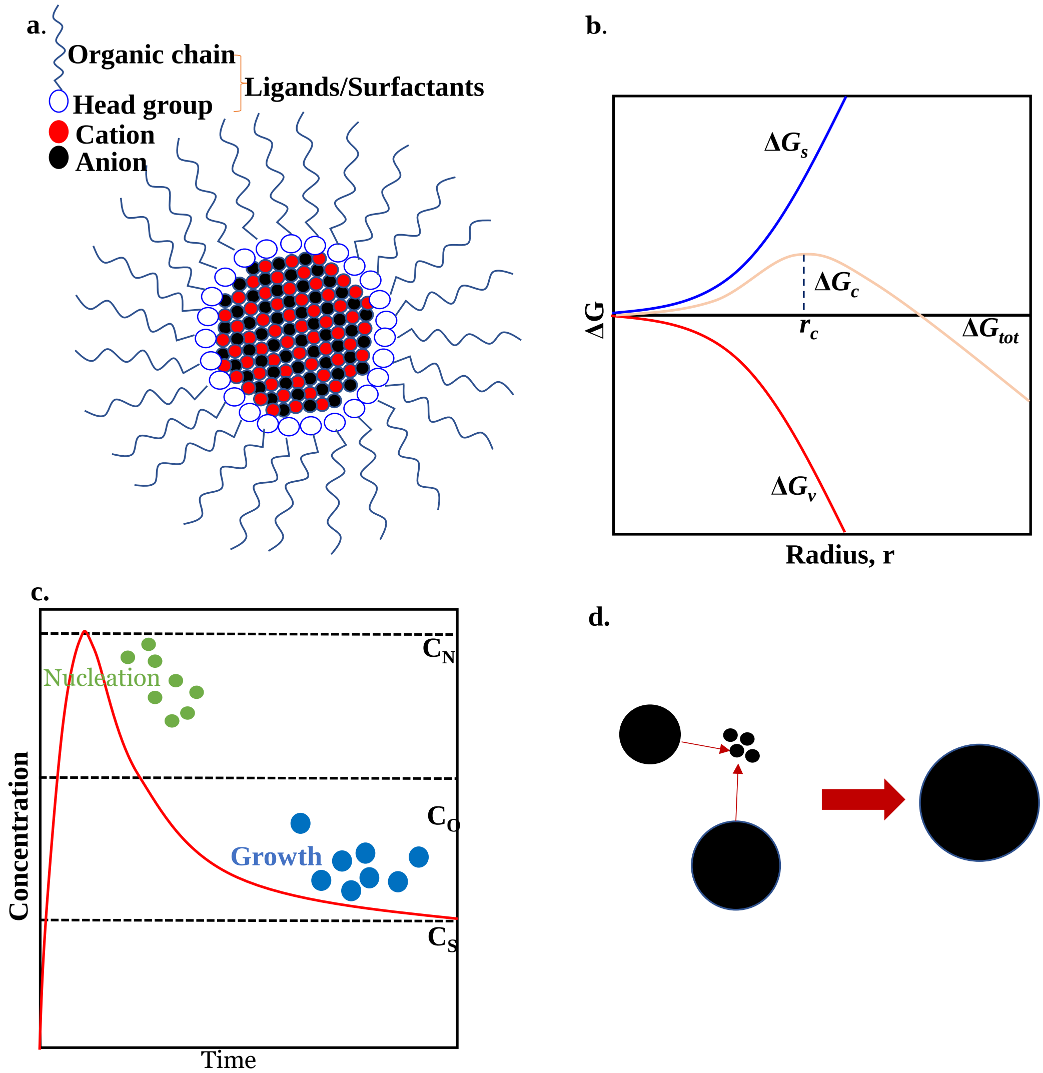
a.
Organic chain
Head group
Ligands/Surfactants
Cation
Anion
b.
ΔG_s
ΔG_c
r_c
ΔG_tot
ΔG
ΔG_v
Radius, r
c.
C_N
Nucleation
Concentration
C_O
Growth
C_S
Time
d.

**Figure 1.2:** Nucleation and growth of semiconductor nanocrystals; (a) Schematic diagram of a colloidal semiconductor nanocrystal; (b) Classical nucleation theory has shown using a plot of Gibbs free energy against the radius of the nucleus; (d) Plot of concentration against time showing the La Mer model for burst nucleation; and (e) Schematic diagram showing the process of Ostwald ripening.[12]

Additionally, the presence of stabilizers such as ligands or surfactants can result in the synthesis of NCs with unique morphologies. This can be understood by examining the synthesis of anisotropic CdSe nanostructures. Due to varying chemical properties among the facets of wurtzite CdSe, different ligands exhibit a preference for binding to specific crystal facets. For example, phosphonic acid ligands bind more readily to non-polar facets, promoting growth in a specific direction. On the other hand, the use of oleic acid as the ligand results in the formation of two-dimensional CdSe sheets.[13]

### 1.2. QDs in Biology

QDs have significant potential in the field of bio-imaging due to their exceptional light absorption and emission properties.[14,15] The wavelength of both emission and absorption is determined by the size and shape of the quantum-confined colloidal NCs. Additionally, the surface ligands can be altered to possess specific functionalities. Despite the benefits of QDs, their initial synthesis often involves non-biocompatible surface-bound organic non-polar ligands, requiring surface modification to make them suitable for biological applications. Surface modification through ligand exchange was first reported by Rosenthal *et al.* in 2002, but this method resulted in decreased fluorescence.[15] However, the exchange of ligands led to a significant decrease in fluorescent emission, reducing it from 38% to nearly 8%. To mitigate this issue, an amphiphilic polymer was utilized instead of encapsulating the non-polar ligands. This allowed the polar reactive groups to remain exposed on the surface while avoiding displacement. Tamang *et al.* demonstrated that this approach prevented fluorescent quenching by blocking the hole-trapping mechanism in the presence of the ligand.[14] Some potential biological applications of such functionalized QDs include:

***a) QDs in drug delivery applications***: Due to higher surface area and the possibility to attach bio-functional molecules on their surface, QDs can be used as drug delivery agent.[16–18]

***b) Target specific QDs for in vivo imaging:*** The utilization of QDs as targeting agents for *in vivo* imaging is a widely accepted practice in the scientific community. One of the key benefits of these specifically binding QDs is the capability to image tumors in a targeted manner. *In vivo* targeting has an advantage over *in vitro* targeting as it provides more intricate information regarding the protein of interest and its natural surroundings. Zhang *et al.* synthesized CdTe:$Zn^{2+}$ QDs that were functionalized with phosphonothioate DNA aptamers containing a targeting sequence. These QDs target lung cancer tumors in vivo, enabling easy and accurate identification of the tumor.[19]

***c) QDs as dynamic trackers for a biological event:***

In biological cells and tissue cultures, QDs can be employed for monitoring and directing various cellular processes. The high fluorescence output of QDs permits precise quantification of the probes with pixel-level resolution and simplifies the localization of individual labeling sites, which can then be charted. Unlike traditional organic dyes, QDs exhibit superior photostability, facilitating extended and in-depth experimentation.[20] The NIR light emitted by QDs (700-2,500 nm) is able to penetrate biological tissues such as skin and blood with greater ease compared to visible light as these tissues exhibit reduced absorption and scattering of light at longer wavelengths. However, at wavelengths exceeding 950 nm, this advantage is diminished due to the heightened absorption of water and lipids. In 2003, simulations and modeling studies showed that the use of quantum dot fluorophores that emit light at 1,320 nm instead of 850 nm can significantly improve signal-to-noise ratios by over 100 times in optical imaging in turbid media like tissue or blood.[21] Most of the NIR QDs are made of highly toxic semiconductor compounds like PbS,[22] PbSe,[21,23–29] InAs,[14,30] or HgTe, limiting their use for in vivo applications. However, the NIR-II window offers a new possibility for sensitive in vivo fluorescence imaging in small animals with the shift to longer wavelengths (1000-1700 nm) providing deeper tissue imaging, high spatial resolution, and high contrast due to reduced auto-fluorescence and tissue scattering.[31]

### 1.3. Near Infrared Emitting (NIR) QDs

The near-infrared (NIR-I and NIR-II) portion of the electromagnetic spectrum is well-suited for fluorescence imaging. The reduction in absorption, scattering, and self-fluorescence from tissues in this region leads to improved image quality and greater tissue penetration, thereby facilitating the diagnosis of diseases and monitoring of treatment outcomes. The NIR region can be further subdivided into NIR-I (650 to 950 nm) and NIR-II (1000 to 1400 nm), which are considered to be biological windows, characterized by the least interference from biological media. In addition, NIR-I photons offer a promising avenue for biomedical imaging, with the ability to incorporate exogenous contrast agents that provide a unique combination of quantum yield, hydrodynamic diameter, absorption, and stability, which cannot be achieved with conventional organic fluorophores.[32,33] In the last two decades, there has been a significant advancement in the field of fluorescent materials. The use of NIR QDs as a novel fluorescent label has become widespread due to their dual benefits.[16,33–36.] NIR QDs have been used in a variety of applications, including biosensing and bioimaging. NIR light, which has a wavelength greater than 650 nm, offers the advantage of low absorption and low autofluorescence in biomedical applications. The following classification of NIR QDs is presented, along with a summary of the synthetic methods used to produce them. The progress of NIR QDs has seen significant growth in recent years. Initially, NIR QDs containing Cadmium (Cd) were produced using visible light-emitting QDs such as CdTe/CdS, CdTe/CdSe, and CdTe/ZnS.[38] However, the toxicity of Cd-based QDs led to the search for alternative, benign elements. For instance, $CuInS_2$/ZnS core/shell QDs, free of elements like Cd, Pb, and Hg, have shown potential as biocompatible probes for biomedical applications. Furthermore, novel NIR QDs such as $Ag_2S$ QDs, carbon dots, and silicon nanoparticles have garnered attention due to their low toxicity.

### 1.3.1. Group II-VI NIR QDs: CdX (X = S, Se, Te)

Kima *et al.* were successful in tuning the fluorescence emission of Group II-VI NIR QDs (CdTe/CdSe) into the NIR light region (840-860 nm) without compromising their absorption cross-section. They coated the QDs with a polydentate phosphine to make them soluble, dispersed, and stable in serum. These type-II NIR QDs were then utilized for sentinel lymph node mapping.[43] Cai *et al.* discovered that the fluorescence emission of rod-like $CdTe_xSe_{1-x}$ NIR QDs was between 650 to 870 nm.[30] They found that the presence of Te significantly impacted the fluorescence emission while the Se component influenced the shape of the QDs. The addition of a ZnS shell over the CdTexSe1-x NIR QDs led to an increase in NIR quantum yield (QY) of up to 80% in chloroform. Inspired by the lattice mismatch strain tuning theory. Han *et al.* synthesized highly luminescent NIR CdTe/CdS QDs. The small CdS cores were compressed by gradual growth of the shell, resulting in a transition from type-I to type-II nanocrystals and significant spectral shifts from the visible to the NIR region (475–810 nm).[44] Similarly, Singh *et al.* reported tunable Ni-doped CdTeSe/CdS NIR QDs, which were converted into an aqueous solution and functionalized with folic acid for NIR fluorescence imaging of cancer cells.[45] In addition to the Cd element, the Hg element also contributes to the emission of QDs in the NIR range. Ma *et al.* discovered $Zn_xHg_{1-x}Se$ QDs with intense red to NIR photoluminescence; they found that as the Hg/Zn precursor ratio increased, the absorption and emission spectra of the QDs shifted to longer wavelengths. The emission maximum shifted from 672 to 907 nm as the Hg/Zn precursor ratio rose from 1 to 40%. The highest quantum yield (25.6%) was achieved at a Hg/Zn precursor ratio of 10% with an emission maximum at 704 nm.[46] Cai *et al.*

reported that NIR emitting $Cd_{1-x}Hg_xTe$ QDs were obtained through in situ mercury cation exchange reaction on CdTe QDs. However, the presence of $Hg^{2+}$ in the QDs is detrimental to human health. The stability and reduced biological toxicity of the QDs were enhanced by using ZnS and DHLA-PEG as protective coating. Paramagnetic $Gd^{3+}$ was conjugated to the surface of water-soluble NIR-emitting QDs through metal interaction ions and high-density ligands. Dualistic Hg-based group II-VI NIR QDs, such as HgS and HgTe QDs, are also available.[47] The most well-researched and utilized material for QDs is Cd(II) based. These QDs can be synthesized with ease through a core precursor such as $CdO/CdCl_2$ being rapidly injected into a hot solution of solvents and stirred for 30 to 60 minutes, resulting in NIR emitting QDs.[45,48] The solvents used in this process have shifted from phosphine-based (tetradecyl phosphonic acid, octadecyl phosphonic acid) to fatty acids (oleic acid, 1-octadecyl) to enhance their biological compatibility. The use of fatty acids also enables a smoother transition between crystal shapes, leading to increased energy conversion in the crystal structure of the QDs and extending the emission wavelength.

The synthesis of Cd(II)-based QDs can be performed in both organic-phase and biocompatible aqueous phase. In 2018, Cui *et al.* outlined a synthesis process using $CdCl_2$ in a bovine serum albumin, BSA solution and adding L-cysteine as the sulfur source. Upon heating the solution at 800 °C for 30 minutes, water-soluble CdS QDs were produced with a first excitonic peak at 450 nm, enabling excitation at 468 nm and emission at 730 nm. These QDs possess suitable optical properties for direct cell imaging and can be optimized through doping, resulting in a blue or red shift in emission maximum with improved photoluminescence quantum yield and fluorescence emission.[49]

The utilization of cells in the production of QDs has been made possible through the implementation of a bio-friendly method. Cd(II) has historically been the primary element used in the synthesis of QDs, however, the synthetic methods have significantly advanced in order to enhance their optical properties. Currently, there are multiple reports of Cd-based QDs that are synthesized with alternative precursors emitting in the NIR range. Improved optical results are achieved through the application of hot injection and heat-up techniques. After surface functionalization, the water solubility of Cd(II) QDs can render them suitable for biological applications. Despite the extensive research on this material for its potential in bio-applications, its toxicity as a heavy metal remains a major concern.[50]

### 1.3.2. Group IV-VI NIR QDs: PbX (X = S, Se, Te)

Lead chalcogenides have demonstrated the most potential among narrow-bandgap semiconductor materials for biomedical applications. Rao *et al.* synthesized PbS QDs through biomineralization processes of biomolecules, resulting in a QD emission at a range of 800-1050 nm and a quantum yield of 3.6%.[49] Nie *et al.* reported a dual-emission nanohybrid based on NIR, consisting of Au nanoparticles and PbS QDs, with two emission peaks at 640 and 813 nm.[51] Hollingsworth *et al.* addressed the instability in size and fluorescence that can result from surface oxidation of PbSe QDs by producing PbSe/CdSe core/shell NIR QDs, combining the narrow bandgap and high efficiency of PbSe with the chemical stability provided by the CdSe shell.[52] They further demonstrated the chemical versatility of the new nanocrystals by performing additional shell growth to create PbSe/CdSe/ZnS core/shell/shell NIR QD.[53] Kraus *et al.* discovered ultra-small PbSe QDs with exciton absorptions reaching as low as 700 nm and a high relative quantum yield (QY) of up to 90%.[23] However, there were fewer reports on the NIR fluorescence of PbTe QDs.[54] Most studies focused on the relationship between the size of the QDs and their exciton absorption. Liu *et al.* synthesized PbTe QDs with sizes ranging from 4 to 14 nm, and observed exciton absorption from 1900 to almost 2400 nm.[55] The QDs PL emission wavelength was tunable by changing the Zn and In precursor concentrations and increasing the Cu precursor concentration, with a range from 465 to 700 nm. Peng *et al.* prepared $AgInS_2$ nanoparticles with a tunable PL peak in the range of 570–720 nm and a PL QY of approximately 8%.[56] Torimoto *et al.* reported the preparation of $AgInS_2$-ZnS QDs with a maximum QY of 24%, and the PL wavelength of these QDs could be tuned from 540 to 720 nm by altering the chemical composition. Additionally, coating the $AgInS_2$-ZnS QDs with a ZnS shell resulted in the highest QY of 80%.[57]

### 1.3.3. Group III-V NIR QDs

The crucial role of Group III-V NIR QDs in the development of bioimaging probes has been well documented in the literature. Most of the focus in the NIR window has been on In- and As-based QDs. These QDs exhibit photoluminescence or electroluminescence in the NIR I to NIR-II range (700–1400 nm). InAs QDs were first produced by Alivisatos *et al.* using the dehalosilylation reaction of $InCl_3$ and $As(SiMe_3)_3$ with trioctylphosphine acting as both a solvent and capping agent at temperatures between 240-265 °C. Xie and co-workers reported the synthesis of high quality, narrow-spectrum InAs/CdSe QDs through a one-pot growth process.[60] Fang *et al.* demonstrated the synthesis of InP and InAs QDs using $PCl_3$ and $AsCl_3$ as the phosphorus source.[38] One of the challenges with III-V NIR QDs is their low quantum yield. To address this issue, many efforts have been made to design core/shell structures to enhance the QY. Banin *et al.* synthesized InAs/CdSe/ZnSe structures, where the intermediate CdSe layer reduces the strain between the InAs core and ZnSe outer shell.[61] This structure exhibited a high QY of over 70% and the emission wavelength could be tuned from 885 to 1425 nm by adjusting the shell thickness and core size. Chen *et al.* reported on the synthesis of ultrasmall (<10 nm) NIR emission QDs capped with mercaptopropionic acid (MPA) for passive tumor-targeting imaging.[40] The Peng and Co-workers group proposed a method to synthesize ZnSe-coated Cu-deposited InP QDs (Cu:InP/ZnSe) with a high QY of 40%. The emission wavelength was tunable from 630 to 1100 nm, making these QDs promising for NIR bioimaging due to the lack of toxic heavy metal elements.[30] In 2001, Murray *et al.* reported on the successful synthesis of colloidal lead-based NIR QDs through the hot-injection method of precursors TOP-Se and Pb(II) oleate in a solvent solution at 150°C.[62] By controlling the reaction temperature, the authors were able to produce QDs of varying sizes ranging from 3.5 to 15 nm, leading to differences in optical properties. The smallest QDs exhibited exciton absorption at 1200 nm, whereas the largest QDs showed absorption at 2200 nm, all within the second NIR window. The NIR-emitting lead sulfide (PbS) QDs have since been used for in vivo fluorescence imaging of cerebral blood vessels in mice. The synthesis of PbS QDs involved reacting $PbCl_2$ and hexadimethyldisilathiane in a mixture of oleyl amine and oleic acid through the hot-injection method. To improve dispersibility in aqueous solutions, mercaptoundecanoic acid was introduced as a surface modifier after synthesis.

The QDs demonstrated an emission peak at 1100 nm with a relatively low photoluminescence quantum yield (PLQY) of 8% in water. Although lead sulfide (PbS) QDs have the ability to exhibit tunable emission in the NIR range, making them a highly promising option, they are vulnerable to surface oxidation and exhibit a significant decrease in PL QY upon phase transfer into the water. As such, the development of a core/shell PbS structure is a direction that could lead to the utilization of these QDs in biomedical applications. Similar to cadmium (II) (Cd(II)), Pb(II)-based QDs can also be synthesized using the hot-injection and heat-up methods to emit in the NIR region. Pb(II) as the core element can emit in the NIR-II region (1000-1400 nm), whereas Cd(II) materials emit in the NIR-I region (700-950 nm), making them useful for imaging experiments where tissue autofluorescence and water absorption are minimized. Despite these favorable optical properties, the toxic nature of the precursors poses a major hindrance to their clinical use and calls for safer, biocompatible alternatives.

### 1.3.4. Non-toxic alternatives (Group IV QDs)

In 2006, Sun *et al.* successfully synthesized Carbon CQDs while purifying Single-Walled Carbon Nanotubes for the first time.[64] These CQDs exhibited superior biological compatibility and low toxicity, making them ideal for use in biomedical imaging. Two major synthesis methods for CQDs exist, top-down and bottom-up.[65,66] The top-down approach involves transforming significant carbon precursors, such as nanodiamonds, carbon nanotubes, or carbon fibers, into smaller particles through physical or chemical processes. On the other hand, the bottom-up approach involves the fusion of small carbon molecules into larger particles through solvothermal or microwave synthesis. However, a limitation of the bottom-up method is that it primarily produces blue- or green-emitting CQDs. Despite being a relatively new field of research, CQDs have already been applied to several systems and therapies, including photothermal therapy, photodynamic therapy, and chemical and biological applications. Microwave methodology was used to synthesize CQDs through the pyrolysis of glycerine in the presence of polydopamine.[67] Li *et al.* produced NIR-emitting CQDs by combining the solvothermal method and microwave methods, with emission peaks at 770 nm and a PLQY of 11%. Further optimization of the different techniques used is necessary, as the emission peaks obtained through hydrothermal and microwave methods only barely occur in the NIR-I range, and PLQYs obtained through these methods are generally lower in comparison to other materials.[68]

### 1.3.5. Silver chalcogenides

QDs containing silver and sulfides, such as ZnS,[69,70] PbS,[25,71] CdS,[38] $Ag_2Te$,[72] $Ag_2Se$,[72–76] and $Ag_2S$,[35,77–80] have gained attention as fluorescent labels in biological and medical diagnostics. However, PbS and CdS are not favorable due to their toxic nature. Hence, it is crucial to synthesize QDs with low toxicity and high emission. The silver chalcogenide ($Ag_2X$, X = S, Se, Te) QDs, with low toxicity and simple synthesis, are ideal for biological labeling due to their NIR emission. $Ag_2S$ QDs emitting in the NIR-II region are considered a promising alternative to other QDs in biology as they offer improved signal-to-noise ratio compared to visible and NIR-I counterparts. $Ag_2S$ exists in three forms: monoclinic $\alpha$-$Ag_2S$, body-centered cubic $\beta$-$Ag_2S$, and face-centered cubic $\gamma$-$Ag_2S$.

The monoclinic $\alpha$-$Ag_2S$ phase is stoichiometrically balanced, while the cubic $\beta$-$Ag_2S$ and $\gamma$-$Ag_2S$ phases exhibit a slight excess of Ag or are non-stoichiometric. $Ag_2S$ QDs have a low solubility product ($K_{sp} = 6.3 \times 10^{-50}$), reducing the likelihood of $Ag^+$ ion release into biological environments.[79–83] Additionally, they possess a low band gap (bulk: 1.1 eV) and the potential for quantum confinement at sizes below 4 nm, allowing for tunable emission in the 700-1400 nm range.[84] The bulk band gap of $Ag_2Se$ is 0.15 eV with a calculated exciton Bohr radius of 2.9 nm, making them suitable for low hydrodynamic diameter and efficient renal clearance. $Ag_2S$ has been shown to have minimal toxicity at lower to moderate doses, making it a promising candidate for in-vivo imaging. Despite its potential applications, the synthesis of $Ag_2X$ colloids is not as well-studied as other semiconductor NCs from the II-IV, III-V, and II-VI groups.

In 2003, Lim *et al.* conducted a study examining simulations and models of optical imaging in turbid media, including tissue and blood. They discovered that using quantum dot fluorophores with an emission wavelength of 1,320 nm, as opposed to 850 nm, could result in a 100-fold improvement in signal-to-noise ratio. However, the absence of biocompatible fluorescent probes in the NIR-II region between 1,000 and 1,350 nm prevented the use of this potentially advantageous spectral range for *in vivo* imaging. In 2004, Liu *et al.* reported a method for synthesizing $Ag_2S$ QDs that exhibited a size distribution of 5.9 ± 1.65 nm with an absorption peak at 330 nm.[18,81]

In 2009, Welsher *et al.* reported on the potential for generating biocompatible single-walled carbon nanotubes with fluorescence emitting between 950 and 1,400 nm. These nanotubes facilitated deep and highly sensitive in vivo imaging of blood vessels through the skin's deep layers. This study demonstrated the benefits of fluorescence imaging in the NIR-II window, leading to new imaging opportunities. However, concerns arose regarding the non-degradable nature of these particles and their needle-like structure, which could cause tissue damage and chronic toxicity if inhaled. These limitations prompted further investigations and advancements in the NIR-II window.[85,86]

In 2010, Wang *et al.* published a report on the NIR emission of $Ag_2S$ QDs synthesized using a single-source precursor (SSP) of Ag(DDTC) $(C_2H_5)_2NCS_2Ag$ in combination with oleic acid and oleyl amine ligands in octadecene at 200°C,[87,88] following the heat-up method reported by Du *et al.* in the same year. The findings showed that the resulting $Ag_2S$ QDs were monodisperse with a diameter of 10.2 ±0.4 nm, exhibiting NIR emission centered at 1058 nm when excited with 785 nm radiation, with a narrow full width at half maxima (FWHM) value of 21 nm.[87]

In 2012, Peng *et al.* synthesized NIR $Ag_2S$ QDs with tunable emission through a two-step process. The first step involved the production of small-sized $Ag_2S$ QDs through the injection of Bis(trimethylsilyl)amine $(TMS)_2$ into a mixture of silver acetate (AgAc), myristic acid (MA), 1-octylamine (OA), and 1-octadecene under argon flow at a specified temperature. The second step involved the seed-mediated growth of large-sized $Ag_2S$ QDs through the addition of Ag(OA) solution and sulfur solution into toluene solutions containing small-sized $Ag_2S$ QDs. The results indicated that the spherical particles produced had a size of 1.5 ± 0.4 nm and the photoluminescence covered a wavelength range of 690 to 1227 nm. It was concluded that the emission-tunable $Ag_2S$ nanocrystals show great potential for in vivo studies in multiple nano diagnostics and multicolor imaging. [80,89]

Additionally, Hong *et al.* utilized a single-source precursor $(C_2H_5)_2NCS_2Ag$ to synthesize PEG-$Ag_2S$ QDs ($d_{hydrodynamic} = 26.8$ nm, $\lambda_{ex} = 808$ nm, $\lambda_{em} = 1100$ nm, PLQY = 15.5%) in a study inspired by the work of Wang *et al.* in 2010.[90–92] Similarly, Zhang *et al.* reported the characteristics and cytotoxic effects of $Ag_2S$ QDs (d = 5-10 nm, $\lambda_{em}$ = 1000–1320 nm, PLQY = 15.5%) coated with PEG-DHLA.[93] These QDs were evaluated for targeting experiments in breast cancer cell line (MDA-MB-468) and human glioblastoma cell line (U87 MG), and for cytotoxicity in the mouse fibroblast cell line (L929). During the targeting investigation, it was observed that the functionalized QDs, conjugated with proteins, are capable of recognizing the epidermal growth factor receptor (EGFR) with higher expression levels in MDA-MB-468 cells as compared to U87MG cells. The results indicated that the QDs displayed exceptional targeting ability towards MDA-MB-468 cells, displaying significant NIR emission intensities, which was not observed in U87MG cells, thereby highlighting the specificity of the QDs and the NIR emission response. The cytotoxicity studies conducted on $Ag_2S$ QDs demonstrated negligible impact on cell proliferation, apoptosis and necrosis, reactive oxygen species production, and DNA damage in L929 cells. This comprehensive study highlights the potential of Ag(I)-based QDs for biomedical imaging and provides a robust biological foundation for further optimization and development.[93]

In 2013, Yang *et al.* reported on the synthesis of ultrasmall NIR-II-emitting $Ag_2S$ QDs in an aqueous phase using a sol-gel method at room temperature. The BSA served as the capping agent for the QDs. The resulting BSA-$Ag_2S$ QDs exhibited ultrasmall sizes of less than 10 nm and a tunable NIR-II emission band from 1050 to 1294 nm. The synthesis process involved the incubation of silver nitrate $AgNO_3$ with BSA, followed by slow injection of sodium sulfide $Na_2S$ solution, and subsequent purification through dialysis. The procedure was conducted at room temperature and in aqueous solutions. The biocompatibility of the $Ag_2S$ QDs was confirmed through cytotoxicity and hemolysis measurements, making them a promising candidate for use as a fluorescent label in *in vivo* imaging.[94]

In 2014, Zhang *et al.* utilized the single-source precursor method to synthesize hydrophobic PEG-$Ag_2S$ NIR QDs emitting at 1058 nm from $(C_2H_5)_2NCS_2Ag$. These $Ag_2S$ NIR QDs, which exhibited emission at 1200 nm, demonstrated improved spatial resolution in the imaging of angiogenesis and facilitated the tracking of mesenchymal stem cells in vivo.[95] Similarly, Chen *et al.* synthesized $Ag_2S$ (NIR-II, 1.0–1.4 μm) QDs for in vivo tracking of human mesenchymal stem cells with high sensitivity and high spatial and temporal resolution. The chemical and photostability of the QDs were found to be stable for 30 days, making them suitable for long-term cell tracking. The use of NIR-II region for *in vivo* imaging showed negligible autofluorescence in living tissues, with the capability to detect over 1000 cells. The in situ translocation and distribution of transplanted hMSCs in the lung and liver were monitored for up to 14 days with a temporal resolution of less than 100 ms. The results concluded that $Ag_2S$ QDs are a suitable NIR-II nanoprobe for non-invasive, long-term stem cell tracking with high sensitivity and elevated spatial and temporal resolution, making them suitable for further clinical applications in imaging-guided cell therapies. Most of the previously reported NIR-emitting $Ag_2S$ QDs were synthesized using high-temperature organometallic routes, requiring further re-dispersion into an aqueous solution for use in biosystems. However, this transfer from organic solvent to water often drastically compromises the PL intensity and stability of Ag-based QDs. Therefore, advancements are necessary to prepare stable and water-dispersible NIR $Ag_2S$.[96]

Reports of aqueous NIR-emitting $Ag_2S$ QDs synthesis have been documented by Jiang *et al.* They synthesized $Ag_2S$ QDs that were terminated with carboxylic acids in ethylene glycol at 145 °C, resulting in tunable PL emission ranging from 510 to 1221 nm.[49] Yang *et al.* designed a one-pot aqueous synthesis of $Ag_2S$ QDs using BSA as a capping reagent at room temperature, resulting in PL emission varying from 1050 to 1294 nm.[97] Despite the successful synthesis of NIR $Ag_2S$ QDs, the utilization of external capping or stabilizing agents such as ethylene glycol and BSA hinder further applications of these QDs as they do not exist in the human body.[94] Pang *et al.* also reported emission-tunable $Ag_2S$ QDs through a two-step procedure.[98,99]

Pang *et al.* reported on the use of aqueous $Ag_2S$ QDs encapsulated with 3-mercaptopropionic acid as an optical probe in *in vivo* studies with mice.[100] Hocaoglu and co-workers were the first to report an aqueous synthesis of highly luminescent and cytocompatible $Ag_2S$ stabilized with 2-mercaptopropionic acid.[100] Cui *et al.* also reported on the aqueous synthesis of $Ag_2S$ NIR QDs using RNase A as a template via a biomimetic process. These NIR QDs exhibit the highest QY (39%) reported in the literature, even after aging. For the first time, effective imaging properties and high cytocompatibility of $Ag_2S$ NIR were demonstrated in mammalian cells at extremely high doses (up to 200 μg/mL).[101]

Jiang *et al.* synthesized $Ag_2S$ QDs with carboxylic acid termination in ethylene glycol at 145 °C, resulting in tunable photoluminescence (PL) emission ranging from 510 to 1221 nm.[80] Similarly, Yang *et al.* successfully conducted a one-pot synthesis of $Ag_2S$ QDs in an aqueous environment using BSA as the capping agent at room temperature.[94] This method yielded PL emissions ranging from 1050 to 1294 nm. Despite the ability to produce NIR $Ag_2S$ QDs, the use of external stabilizing agents such as ethylene glycol and BSA can limit their applications in the human body. Inspired by these findings, Gui *et al.* developed a novel approach to synthesize NIR emitting $Ag_2S$ QDs *via* cation exchange, using visible-emitting CdS QDs and $Ag^+$ ions in an aqueous solution.[102] This is the first study to synthesize NIR-II PL emissive $Ag_2S$ QDs directly from visible-emitting CdS QDs through cation exchange. The study involved the preparation of glutathione-capped CdS QDs in an aqueous solution, followed by the addition of $AgNO_3$, which resulted in a quick and complete exchange between $Cd^{2+}$ and $Ag^+$ ions, forming $Ag_2S$ QDs. The resulting $Ag_2S$ QDs showed typical NIR-II emission, high PL stability, a small diameter (~3.5 nm), and a QY of 2.3%. The $Ag_2S$ QDs also exhibited low cytotoxicity and excellent biocompatibility, making them suitable for effective in vitro and in vivo bioimaging applications as an ideal NIR-II PL emissive nanoprobe.[103]

In 2015, Duman *et al.* successfully showcased the first NIR emitting cationic $Ag_2S$ NIR QDs with a coating comprised of 2-mercaptopropionic acid (2MPA) and polyethyleneimine PEI (branched, 25 kDa). This combination of materials was designed as a dual function for both gene delivery and optical imaging. The QDs demonstrated impressive NIR-I window ($\lambda_{em}$ = 810-840 nm) luminescence, which was stabilized through a combined use of a small molecule and a polymeric material, resulting in a QY of 150% (for LDS 798 at pH 7.4) - the highest recorded in the literature for $Ag_2S$. Additionally, these cationic particles were found to be optimally compatible with cells, even without PEGylation. Confocal laser microscopy easily detected solid optical signals, and effective conjugation and transfection of green fluorescence protein plasmid (pGFP) were observed in HeLa and MCF-7 cell lines with a 40% efficiency. The results indicated that these $Ag_2S$ NIR QDs exhibit great potential as new theragnostic materials.[104]

Chunyan Li *et al.* reported an *in vivo* study to monitor the behavior of protein nanocages (PNCs) using $Ag_2S$ QDs with fluorescence in the NIR-II window. The study used simian virus 40 (SV40) PNCs as a model and found that the NIR-II fluorescence property of the $Ag_2S$ QDs enabled real-time tracking of the PNCs in living mice with high stability, fidelity, and spatiotemporal resolution. The results showed that the surface PEGylation of the PNCs prolonged its blood circulation time, leading to different in vivo behavior. This study highlights the importance of surface properties in determining in vivo behavior and demonstrates the feasibility of $Ag_2S$ QDs in the real-time tracking of PNCs.[33] This approach can be useful in optimizing surface properties for PNC-based in vivo biomedical applications such as vaccines, biosensing, and targeted delivery.[32] Once again, Chunyan Li *et al.* have presented a novel nanoprobe (Gd-DOTA-$Ag_2S$ QDs, referred to as Gd-$Ag_2S$ nanoprobe) that combines two imaging modalities (magnetic resonance, MRI, and NIR-II fluorescence) for preoperative diagnosis and imaging-guided surgery of brain tumors. The Gd-assisted $T_1$ MR imaging was utilized to clearly outline a tumor in the brain (U87MG) of a mouse model. The intraoperative dissection of the tumor was precisely carried out using the NIR-II fluorescence imaging of $Ag_2S$ QDs after intravenous inoculation of the Gd-$Ag_2S$ probe. The synthesis of the nanoprobe involves three steps. Firstly, monodispersed $Ag_2S$ QDs coated with dihydrolipoic acid conjugated polyethylene glycol (DHLA-PEG Amino) were prepared using a previously established method.[74] Secondly, the DOTA-mono-N-hydroxy-succinimide ester (DOTA-mono-NHS) was conjugated with $Ag_2S$ QDs. Thirdly, gadolinium chloride hexahydrate was added to the DOTA-activated $Ag_2S$ QDs to result in the dual-modality nanoprobe of Gd-$Ag_2S$. The as-prepared Gd-$Ag_2S$ nanoprobe exhibited a decent relaxivity parameter of $4.9\times10^{-3}m^{-1}\ s^{-1}$ in water at a field strength of 11.7 T at 25 °C and a high quantum yield of 15%.[33] Furthermore, no significant histological alterations were observed in the major organs of mice following a one-month exposure to Gd-$Ag_2S$ nanoprobe. These findings suggest that the nanoprobe possesses remarkable biocompatibility, thereby establishing a promising "Detection and Operation" approach based on the Gd-$Ag_2S$ nanoprobe for future clinical applications. This innovative dual-modality nanoprobe has thus paved the way for investigating in vivo biological processes, including drug discovery and screening, as well as potential clinical applications.[33]

In 2016, Chenghua Song *et al.* demonstrated a tumor vasculature-targeted nano drug (T&D@RGD-$Ag_2S$) with dual anti-angiogenic and chemotherapeutic activities in a human U87-MG malignant glioma xenograft model. The nano drug, which incorporates a specific recognition peptide (cRGD) for tumor vascular targeting, the broad-spectrum endothelial inhibitor TNP-470, and the chemotherapeutic drug doxorubicin (DOX), effectively inhibited tumor growth. The T&D@RGD-$Ag_2S$ nano-drug rapidly and specifically bound to the tumor vasculature following intravenous injection. Effective angiogenesis inhibition by TNP-470 resulted in a significant reduction in tumor vascular density. These findings provide a promising approach for treating a wide range of tumors and hold great potential for future clinical applications.[105]

Gao *et al.* have reported on the direct synthesis of water-soluble monoclinic $Ag_2S$ NIR fluorescent QDs at ambient temperature for specific cancer imaging and photothermal therapy (PTT) using a designed aptamer (Apt43) as a template. The Apt43 comprises two fragments: an aptamer S2.2 sequence for explicit recognition of cancer cells and an 18-cytosine (18-C) extending spacer for growing $Ag_2S$ QDs. Apt43-$A_{g2}S$ QDs can be used as photothermal agents for in vivo ablation of tumors constructed on the bodies of nude mice and in vitro killing of MCF-7 cells. Almost all MCF-7 cells died quantitatively after being incubated with the QDs (at 100 μg $mL^{-1}$) for two hours and irradiated under an 808 nm laser at a power density of 1.0 W $cm^{-2}$ for 10 minutes. Apt43-$Ag_2S$ QDs exhibit high photothermal conversion capabilities, good biocompatibility, water-solubility, and ease of synthesis at ambient temperature, making them promising candidates for clinical tumor diagnosis and therapy.[106]

Chen *et al.* conducted further experimentation on the synthesis of $Ag_2S$ QDs with a peak emission of approximately 1100 nm, using β-lactoglobulin (β-LG) as a biological template. The use of this protein coating enhances the water solubility, enables swift biodistribution, and reduces the in vivo toxicity of the QDs. β-LG-capped $Ag_2S$ QDs exhibit higher photostability and biocompatibility in comparison to currently utilized NIR emitters, thereby holding great potential for in vivo NIR-II imaging applications.[67]

In 2017, Wu *et al.* reported a novel sensor with high selectivity for $Zn^{2+}$ and $Cd^{2+}$ based on NIR fluorescent QDs. The authors utilized a two-step approach to synthesize water-soluble NIR-II QDs, which involved terminating the QDs with n-dodecyl mercaptan groups followed by a surface ligand exchange using thioglycolic acid. Surface passivation led to enhanced fluorescence, and the interaction of $Zn^{2+}$ and $Cd^{2+}$ with thioglycolic acid on the QD surface resulted in the formation of Zn-thiol and Cd-thiol complex shells, respectively. This process restored defects and suppressed nonradiative recombination pathways. The authors observed a linear relationship between ion concentration and fluorescence intensity, leading to lowered detection limits of 760 nM for $Zn^{2+}$ and 546 nM $Cd^{2+}$ at a pH of 7.4. Furthermore, $Ag_2S$ QDs synthesized in this study were capable of detecting exogenous Zn(II) in cells, demonstrating the potential for the application of NIR-II fluorescent $Ag_2S$ QDs in the detection of $Zn^{2+}$ in biology and $Cd^{2+}$ in the environment.[107]

In 2018, He *et al.* described a technique for producing NIR-II Pb:$Ag_2S$ QDs using cation doping with a transition metal, $Pb^{2+}$ ions, into $Ag_2S$ nanocrystals to modify their optical properties. The low PLQY of $Ag_2S$ QDs can be attributed to the high mobility of $Ag^+$ ions in the crystal, which results in a high number of cation deficiencies and crystal defects. Consequently, cation doping can enhance the crystal structure and significantly improve optical performance. The researchers found that by varying the levels of Pb doping in the nanocrystals, Pb:$Ag_2S$ QDs with bright emission (PLQY up to 30.2%) in the range of 975 to 1242 nm can be prepared while maintaining the ultrasmall particle size (≈2.7–2.8 nm). Therefore, cation doping can facilitate the renovation of the crystal structure of $Ag_2S$ QDs and the modulation of their optical properties.[108] Vardar *et al.* investigated the cytotoxicity of $Ag_2S$ QDs coated with meso-2,3-dimercaptosuccinic acid (DMSA) in Chinese hamster lung fibroblast (V79) cells at various concentrations (5-2000 µg/mL). Their results showed that the cell viability decreased above 400 µg/mL (MTT assay), and DMSA/$Ag_2S$ QDs did not induce cell death at 800 µg/mL (NRU assay) but caused DNA damage at the studied concentrations. Furthermore, the mRNA expression levels of Bax, Bcl-2, p53, caspase-3, caspase-9, and survivin genes were altered in cells exposed to 500 and 1000 µg/mL DMSA/$Ag_2S$ QDs. However, DMSA/$Ag_2S$ QDs were biocompatible at low doses, making them suitable for cell labeling applications.[101]

In 2019, Xing *et al.* introduced a novel method for synthesizing ultrasmall monodispersed $Ag_2S$ QDs with strong fluorescence properties in the NIR-II region.[101] The authors used a hot-injection approach with single precursors in different solvent systems to prepare the $Ag_2S$ QDs. By varying the ratios of OAm, DDT, and glycerine, the particle sizes of the $Ag_2S$ QDs could be easily controlled as detailed in a table provided by the authors. Moreover, they demonstrated that surface modification of the hydrophilic $Ag_2S$ QDs allowed successful application in cancer cell imaging, highlighting their potential in biomedical research.[101] In 2019, Gutiérrez *et al.* presented a new method for the electrochemical quantification of $Ag_2S$ QDs. The technique relied on the electrochemical reduction of $Ag^+$ to Ag 0 at −0.3 V on screen-printed carbon electrodes (SPCEs) followed by anodic stripping voltammetry oxidation that yielded a current peak at +0.06 V, representing the analytical signal. The method achieved quantification of water-stabilized $Ag_2S$ QDs at concentrations between $2 \times 10^9$ and $2 \times 10^{12}$ QD $mL^{-1}$ with good reproducibility (RSD: 5%). In addition, $Ag_2S$ QDs were evaluated as tags for Escherichia coli (*E. coli*) bacteria detection in biosensing applications. The attached bacteria were isolated from the sample solution through centrifugation and then analyzed quantitatively on the SPCE surface. This strategy offers a promising proof-of-concept alternative to conventional laboratory-based testing, with advantages such as high sensitivity, short assay time, and low research costs.[109] Shu *et al.* successfully synthesized Pb-doped $Ag_2S$ QDs, which exhibited optimal fluorescence properties and tunable emission within the range of 950-1200 nm.[110] Meanwhile, Hashemkhani *et al.* reported on the synthesis of $Ag_2S$-GSH QDs with superior colloidal and optical stability, which remained stable for up to one year and emitted within the range of 700-900 nm. The team was able to achieve the smallest QD size (approximately 7 nm) with the highest quantum yield (70%) through varying reaction parameters such as temperature, pH, growth time, and sulfur source. Stability testing indicated that the optimal conditions were at pH 10 and a temperature of 50 ℃ using $Na_2S$ as the sulfur source, with no degradation observed over 2 hours of reaction time. Photothermal Therapy (PTT) was evaluated using 795 nm continuous-wave fiber-coupled diode laser, and both aqueous solutions of QDs and HT29 and MCF7 cells were examined. The results showed that the $Ag_2S$-GSH QDs had the potential to be used in theragnostic applications due to their lack of cytotoxicity at concentrations up to 200 µg/mL.[111]

Awasthi *et al.* in 2020 reported the use of $Ag_2S$ QDs emitting in the NIR-II range to track metastatic tumor cells in the bloodstream. A549 cancer cells were incubated with PEG-PATU-coated $Ag_2S$ QDs and injected into a mouse. The distribution of $Ag_2S$ QDs was monitored over 24 hours using NIR-II emission, which showed fluorescence intensity initially observed in the liver but redistributed throughout the body at later time points. The same dose of PEG-PATU $Ag_2S$ QDs injected into healthy controls remained controlled within the liver throughout the experiment, indicating the imaging potential of this technique for in vivo cancer cell behavior. Additionally, the use of $Ag_2S$ QDs for angiography was explored, revealing high spatial resolution images of the vascular system in real time.[44] Li *et al.* used $Ag_2S$ QDs for imaging traumatic brain injury (TBI) in conjunction with an organic dye to form a Forster resonance energy transfer (FRET) pair resulting in the quenching of the emission.[112] Hunt *et al.* conducted a study that demonstrated the targeted delivery of $Ag_2S$-based QDs coated with various biopolymer shell coatings to liver sinusoidal endothelial cells (LSECs) in vitro and in vivo after oral administration. The QDs were labeled with 3H-oleic acid or a fluorescent tag, and 14C-metformin was placed within a drug-binding site. The researchers found that QDs coated with a biopolymer layer of formaldehyde-treated serum albumin (FSA) or gelatine showed high specificity targeting of LSECs or hepatocytes, which improved the bioavailability and delivery of metformin to LSECs.[113] Bhardwaj *et al.* developed $Ag_2S$-based QDs that emitted NIR-II light and were transferred from the organic phase to the aqueous phase. The ligands on the surface of the QDs were replaced with Gd chelates to create a dual-modal MRI-fluorescence probe. Although in vivo and in vitro applications were not performed, the results indicated that the MRI contrast agent efficacy of the multimodal nanoprobe increased. The longitudinal relaxivity of the QD-Gd conjugate increased from 5.36 mM $^{-1}$s $^{-1}$ (at 400 MHz) for the Gd chelate to 7.75 mM $^{-1}$s $^{-1}$ and 8.27 mM $^{-1}$s $^{-1}$ per Gd (at 400 MHz) when attached to the surface of the Ag2S QDs. The overall relaxivity of the QD-Gd conjugate was recorded to be 7.75 mM $^{-1}$s $^{-1}$ and 8.27 mM $^{-1}$s $^{-1}$ per Gd (at 400 MHz), indicating a potentially extremely high relaxivity of 407.8 mM $^{-1}$s $^{-1}$ and 990.3 mM $^{-1}$s $^{-1}$ per QD (at 400 MHz), which can improve the sensitivity of MRI. The dual-modal contrast agents have the potential to provide excellent anatomic resolution due to the MRI moiety and molecular concentration sensitivity due to the fluorescent moiety.[114]

In 2021, Han *et al.* reported the synthesis of aqueous $Ag_2S$ NPs with a size of 15 nm, which were utilized as photothermal agents. The study demonstrated that both in vitro and in vivo, $Ag_2S$ NPs displayed effective photothermal conversion when irradiated with an 808 nm laser. These results suggest that the synthesized NPs could serve as contrast agents for biocompatibility and photoacoustic imaging. Furthermore, the in vivo results revealed that the frequency of $Ag_2S$ NP-mediated photothermal therapy (PTT) impacted cancer therapeutic outcomes. Increasing the frequency efficiently reduced primary tumor recurrence and alleviated metastasis.[115] Ren *et al.* also synthesized aqueous $Ag_2S$ QDs through a water-phase microwave method at low temperature. The synthesized $Ag_2S$ QDs displayed bright red luminescence, with an average particle size of approximately 2.5 nm, and were uniformly dispersed in an aqueous solution. The QDs displayed excellent fluorescent properties, excellent stability, low cytotoxicity, and biocompatibility, making them ideal for bioimaging HeLa cells.[116]

$Ag_2Se$ QDs possess similar biocompatibility and excellent properties as $Ag_2S$ and $Ag_2Te$ QDs, and in addition, exhibit a narrow direct band-gap of 0.15 eV compared to 0.93 eV and 0.06 eV for $Ag_2S$ and $Ag_2Te$, respectively. $Ag_2Se$ has two stable solid phases, namely metallic $\alpha$-$Ag_2Se$ and semiconductor $\beta$-$Ag_2Se$. The PLQY of $Ag_2Se$ QDs was first reported to be 1.7% by Yarema *et al.*, who used lithium bis(trimethylsilyl)amide, $Li[N(SiMe_3)_2]$ for synthesis.[117] Subsequently, Sahu *et al.* developed a method for synthesizing NIR-emitting $Ag_2Se$ QDs with average diameters between 2.7 and 10.4 nm. Gu *et al.* reported the first-ever aqueous $Ag_2Se$ QDs with fluorescence emission in the range of 700-820 nm.[118] Zhu *et al.* prepared tunable NIR-II emitting $Ag_2Se$ QDs with a PL QY of 9.58% by the hot injection method. Meanwhile, Dong *et al.* produced oil-soluble 1-dodecanethiol capped $Ag_2Se$ QDs, which could emit above 1300 nm and are more suitable for in vivo imaging due to their narrow band-gap of 0.15 eV.[74]

A novel approach was presented by Tan *et al.* for the synthesis of aqueous $Ag_2Se$ QDs at room temperature. In contrast to traditional methods, the strategy involved the use of a multidentate polymer (MDP), specifically poly-(acrylicacid)-graft-mercaptoethylamine (PAA-g-MEA), as a capping agent. The incorporation of MDP resulted in a reduction in the hydrodynamic dimensions of QDs, as well as an improvement in their colloidal stability, photostability, and PLQY. The synthesis of QDs involved the addition of precursors to an aqueous solution of $AgNO_3$, followed by the addition of $Na_2SeO_3$ and $NaBH_4$ with pre-synthesized MDP. The solution was then injected with $N_2H_4·H_2O$ and continuously stirred, resulting in the production of MDP-$Ag_2Se$ capped QDs.[120]

Ma *et al.* have reported the synthesis of dual-modality contrast agents for $T_1$-weighted MR imaging and high spatial resolution NIR-IIb fluorescence imaging by coupling Gd-DTPA with $Ag_2Se$ QDs ($Ag_2Se$-Gd QDs). *In vitro* evaluations indicated that these prepared $Ag_2Se$-Gd QDs exhibit low cytotoxicity and remarkable contrast properties for both $T_1$-weighted MR imaging and fluorescence imaging. *In vivo* studies further confirmed that $Ag_2Se$-Gd QDs are among the best contrast agents for dual-modality imaging with high spatial resolution. The longitudinal relaxivity ($r_1$) of $Ag_2Se$-Gd QDs was measured to be 2.9791 $mM^{-1}$ $s^{-1}$ at 3T.[76] Ge *et al.* have developed a novel strategy to synthesize $Ag_2Se$ QDs by targeting the increased glucose consumption of tumors. They used glucosamine to add glucose molecules to the surface of the QDs through reacting the pendant carboxylic acids of the coating ligands. The results showed that the glucose-coated $Ag_2Se$ QDs exhibited increased uptake in MCF-7 cells compared with non-conjugated QDs, as assessed by flow cytometry. *In vivo* experiments also demonstrated that the glucose-coated QDs showed tumor accumulation 2 hour post-injection and were still detectable after 7 days. In tumor-bearing mice, $Ag_2Se$ QD fluorescence was still observable 7 days post-injection in the kidneys. In nude mice, Ag could be detected in both the heart (5.41 G 4.8 mg $g^{-1}$) and kidneys (113.73 G 19.00 mg $kg^{-1}$) after injecting glucose-coated $Ag_2Se$ QDs (150 mg $kg^{-1}$ is the dose injected). However, no significant difference in blood biochemistry was observed over this period.[73] Limited reports exist on the synthesis of $Ag_2Te$ QDs. Sahu *et al.* proposed a one-pot synthesis approach for producing colloidal $Ag_2Te$ QDs through a single-step process employing $AgNO_3$, tellurium salt, and TOP. The study revealed that the stability of $Ag_2Te$ QDs in air is solvent-dependent and is affected by the concentration of the dissolved $Ag_2Te$ QDs.[121] Dai *et al.* observed similar behavior in the stability of PbSe QDs.[122] Yarema *et al.* reported the fluorescent properties of $Ag_2Te$ QDs with an average diameter of 3.2 nm.[117] Chen *et al.* synthesized $Ag_2Te$ QDs via facile cation exchange between $Ag^+$ and $Cd^{2+}$ ions in an aqueous solution, resulting in a PL emission peak with wavelengths ranging from 900 to 1300 nm and a PLQY of 2.1%. Zhang *et al.* demonstrated the hot-injection synthesis of $Ag_2Te$ QDs by mixing Ag(OAc) and 1-dodecanethiol at 120°C and injecting tributylphosphine-Te. The resulting $Ag_2Te$ QDs were then coated with an $Ag_2S$ shell by adding further Ag(OAc) and oleylamine-S. The shelling process increased the diameter of the QDs from $4.06 \pm 0.16$ nm to $4.89 \pm 0.10$ nm, with a PLQY of 4.3%. Both $Ag_2Te$ and $Ag_2Te/Ag_2S$ QDs had an emission maximum at 1300 nm, but the latter had a 3.2-fold greater photoluminescence intensity.[93]

## 1.4. Biofunctionalization of QDs

Various biomolecules, such as antibodies, proteins, peptides, DNA, and signaling molecules, were utilized to biofunctionalized heavy metal-free $Ag_2S$ QDs through covalent and noncovalent conjugation methods. Noncovalent conjugation is defined by the hydrophobic, electrostatic, and high-affinity interactions between biomolecules and the surface of $Ag_2S$ QD nanoprobe. On the other hand, covalent conjugation involves the combination of chemistry with activated functional groups that already exist on the surface of QDs to attach biomolecules to the $Ag_2S$ QD nanoprobe. Two approaches to bio-functionalizing QDs are depicted below.[88,123,124]

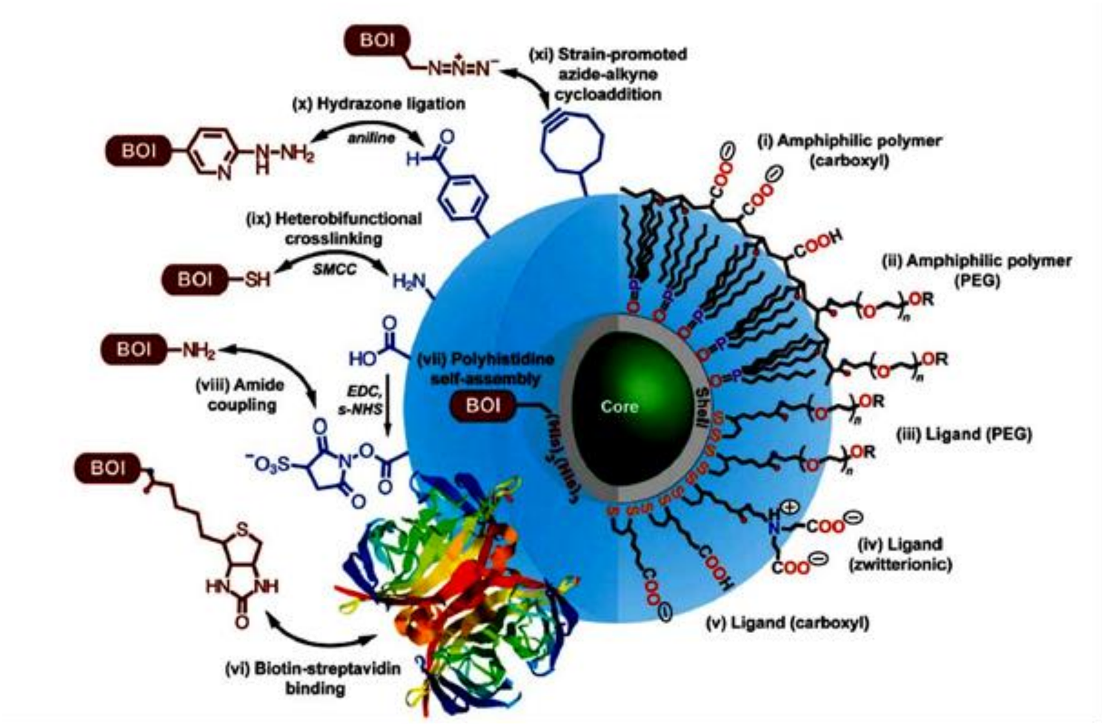
BOI
(xi) Strain-promoted azide-alkyne cycloaddition
(x) Hydrazone ligation
aniline
(ix) Heterobifunctional crosslinking
SMCC
(viii) Amide coupling
EDC, s-NHS
(vii) Polyhistidine self-assembly
Core
Shell
(His)6
(i) Amphiphilic polymer (carboxyl)
(ii) Amphiphilic polymer (PEG)
(iii) Ligand (PEG)
(iv) Ligand (zwitterionic)
(v) Ligand (carboxyl)
(vi) Biotin-streptavidin binding

**Figure 1.3:** Schematic representation of Bio-functionalisation of QDs. Adapted with permission from Salmanogli *et al.* Copyright 2011, Cancer Nanotechnol.[125]

### 1.4.1. Noncovalent conjugation approach

The process of noncovalently conjugating biomolecules to $Ag_2S$ QD surfaces involves electrostatic interaction and high-affinity binding. The charged groups on the surface of the QD nanoprobe are attracted to oppositely charged biomolecules, following the principle of electrostatic interaction. This method is relatively simple and widely used, as it does not require external reagents or chemicals. However, the electrostatic interaction can be affected by factors such as ionic strength, pH, and charge. For high-affinity bioconjugation, the binding affinity between biomolecules and the surface of the dot nanoprobe is crucial. The biotin and streptavidin (SA) contact is a widely used high-affinity interaction, where an SA-functionalized dot nanoprobe is combined with biotinylated biomolecules.[126] Biotinylation of biomolecules typically requires amine-, thiol-, or carboxyl-reactive biotin reagents. The covalent bonding of SA to QD nanoprobes with carboxyl groups on the surface is achieved using EDC. The method of electrostatic interaction was utilized to prepare affibody-functionalized $Ag_2S$ QDs, which are intended for use in photoacoustic imaging (PAI). Affibodies, comprising 58 amino acids and a 3-helix bundle structure, serve as scaffold proteins. Zhang *et al.* have demonstrated that the positively charged ZEGFR:1907 found in the epidermal growth factor receptor electrostatically interacts with the negatively charged -COOH on the surface of the $Ag_2S$ QDs, creating the affibody-functionalized $Ag_2S$ QDs.[92] The study by Jiang *et al.* synthesized aqueous $Ag_2S$ QDs with carboxylic acid group (3-MPA), which were subsequently modified to include the epidermal growth factor receptor 1-targeted small protein affibody ZEGFR:1907. The ZEGFR:1907-$Ag_2S$ QDs were used for targeted PAI of EGFR-overexpressed tumors, which demonstrated the potential for synthesizing nanoprobes for tumor-targeted imaging without complex chemical conjugation.[127]

### 1.4.2. Covalent conjugation approach

The proposed approach entails the formation of covalent bonds, specifically amide bonds, between activated $Ag_2S$ QDs and biomolecules. Carbodiimide coupling chemistry, which involves the use of EDC coupling or N,N-Dicyclohexylcarbodiimide (DCC) coupling, is a widely employed method for achieving covalent chemistry. The reaction involves the coupling of carbodiimide-activated carboxylic acid groups on the surface of QDs with the primary amines of biomolecules. One significant benefit of this approach is the formation of a zero-length amide bond, which avoids the introduction of lengthy linker species and reduces the size of the $Ag_2S$ QDs. In their initial study, Yang *et al.* successfully produced NIR-II-emitting ultrasmall $Ag_2S$ QDs in an aqueous solution at room temperature using a one-pot sol-gel approach. To act as a capping agent, BSA protein was bio-conjugated to the QDs.[94] This was followed by the work of Tang *et al.*, who employed EDC/Sulfo-NHS coupling chemistry to synthesize peptide-functionalized $Ag_2S$ QDs for cellular and deep tissue imaging. In this current research, the surface of $Ag_2S$ QDs was capped with 3-MPA, and the carboxyl group of 3-MPA was activated with EDC/sulfo-NHS before being covalently linked with cyclic arginine-glycine aspartic acid (Arg-Gly-Asp-D-Phe-Lys, cRGDfK) peptide for NIR fluorescence imaging.[128] Finally, Zhang *et al.* reported the fabrication of $Ag_2S$ QDs coated with the triblock copolymer Pluronic F127 (PF127) functionalized with FA, coupling chemistry for photoacoustic imaging.[92] Duman *et al.* synthesized FA-PEG conjugated $Ag_2S$ QDs for drug delivery and in vitro applications. In their study, they used cationic $Ag_2S$ NIR QDs and coated them with 2-mercaptopropionic acid (2MPA) and polyethyleneimine (PEI) as a theragnostic material for gene delivery and optical imaging. The QDs exhibited high luminescence in the NIR-I window ($\lambda_{em}$ = 810-840 nm), and simultaneous use of a small molecule and a polymeric material provided the highest quantum yield of 150% (to LDS 798 at pH 7.4) reported in the literature for $Ag_2S$ stabilization on the surface.[104] Asik *et al.* also demonstrated PEGylated $Ag_2S$ QDs for targeted drug delivery using a one-step hydrothermal method. They prepared PEG conjugated $Ag_2S$ QDs by mixing $AgNO_3$ and $Na_2S$ salts in thiolated polyethylene glycol (MPEG-SH) and carboxylic acid functionalized MPEG-SH (CMPEG-SH), followed by preparation of PEG-$Ag_2S$ conjugated QDs using EDC/NHS coupling chemistry. The overexpressed folate receptor observed in cancerous cells was targeted with folic acid (FA) conjugated PEG-$Ag_2S$ QDs, which demonstrated the potential of FA-PEG-$Ag_2S$ QDs as a targeted drug delivery vehicle using DOX. DOX was loaded with FA-PEG fabricated $Ag_2S$ QDs using electrostatic interaction within DOX and FA-PEG-$Ag_2S$ QDs.[112]

## 1.5. Research Outline

Against this background, the thesis focuses on the synthesis and characterization of $Ag_2X$ (X=S, Se) semiconductor QDs in the Second Near-Infrared (NIR-II) region and their utilization in biology. The first chapter presents a comprehensive overview of colloidal QDs, including their synthesis methods, properties, and applications, as well as a review of NIR-II QDs and their biofunctionalization. The second chapter investigates the synthesis of different precursors, including thiourea, thiocarbamate, dithiocarbamate, and selenourea, by reacting isothiocyanate/isoselenocyanate with commercially available phenols, thiophenols, or aryl amines. The study also assesses the impact of the reactivity of substituted precursors (H, p–Me, *p*–OMe, *p*–I, and *p*–$NO_2$) on the size of the QDs. The third chapter outlines the aqueous solubilization of the QDs using L-cysteine and the synthesis of $Ag_2S$/ZnS core-shell QDs for improved photostability and PL quantum yield. The fourth chapter evaluates the use of $Ag_2S$ QDs as a contrast agent for magnetic resonance imaging (MRI) and compares their longitudinal relaxivity with other MRI contrast agents. The fifth chapter details the instruments and methods used for characterizing the synthesized QDs.

## 1.6. References

(1) Verwey, E. J. W. Theory of the Stability of Lyophobic Colloids. *J Phys Colloid Chem* **1947**, *51*, 780–788.

(2) Steigerwald, M. L.; Brus, L. E. Synthesis, Stabilization, and Electronic Structure of Quantum Semiconductor Nanoclusters. *Annual Review of Materials Science* **1989**, *19*, 170–178.

(3) Brus, L. E. A Simple Model for the Ionization Potential, Electron Affinity, and Aqueous Redox Potentials of Small Semiconductor Crystallites. *J Chem Phys* **1983**, *79*, 480–489.

(4) Henglein, A. Small-Particle Research: Physicochemical Properties of Extremely Small Colloidal Metal and Semiconductor Particles. *Chem Rev* **1989**, *89*, 1122–1130.

(5) Weller, H. Quantized Semiconductor Particles: A Novel State of Matter for Materials Science. *Advanced Materials* **1993**, *5*, 1192–1210.

(6) Mori, N.; Beton, P. H.; Wang, J.; Eaves, L. Theory of Resonant Tunneling through a Quantum Wire. *Phys Rev B* **1995**, *51*, 1130–1140.

(7) Algar, W. R.; Susumu, K.; Delehanty, J. B.; Medintz, I. L. Semiconductor Quantum Dots in Bioanalysis: Crossing the Valley of Death. *Anal Chem* **2011**, *83*, 1231–1230.

(8) Schwabacher, J. C.; Kodaimati, M. S.; Weiss, E. A. Origin of the PH Dependence of Emission of Aqueous Dihydrolipoic Acid-Capped PbS Quantum Dots. . *The Journal of Physical Chemistry C* **2019**, *123*, 17574–17579.

(9) Nag, A.; Kundu, J.; Hazarika, A. Seeded-Growth, Nanocrystal-Fusion, Ion-Exchange and Inorganic-Ligand Mediated Formation of Semiconductor-Based Colloidal Heterostructured Nanocrystals. *CrystEngComm* **2014**, *16*, 9391–9307.

(10) Tamang, S.; Beaune, G.; Texier, I.; Reiss, P. Aqueous Phase Transfer of InP/ZnS Nanocrystals Conserving Fluorescence and High Colloidal Stability. *ACS Nano* **2011**, *5*, 9392–9402.

(11) Carbone, L.; Nobile, C.; de Giorgi, M.; Sala, F. della; Morello, G.; Pompa, P.; Hytch, M.; Snoeck, E.; Fiore, A.; Franchini, I. R.; Nadasan, M.; Silvestre, A. F.; Chiodo, L.; Kudera, S.; Cingolani, R.; Krahne, R.; Manna, L. Synthesis and Micrometer-Scale Assembly of Colloidal CdSe/CdS Nanorods Prepared by a Seeded Growth Approach. *Nano Lett* **2007**, *7*, 2942–2950.

(12) Sear, R. P. Quantitative Studies of Crystal Nucleation at Constant Supersaturation: Experimental Data and Models. *CrystEngComm* **2014**, *16*, 6506–6522.

(13) Pound, G. M.; Mer, V. K. la. Kinetics of Crystalline Nucleus Formation in Supercooled Liquid Tin [1,2]. *J Am Chem Soc* **1952**, *74*, 2322–2332.

(14) Tamang, S.; Lee, S.; Choi, H.; Jeong, S. Tuning Size and Size Distribution of Colloidal InAs Nanocrystals via Continuous Supply of Prenucleation Clusters on Nanocrystal Seeds. *Chemistry of Materials* **2016**, *28*, 8119–8122.

(15) Zrazhevskiy, P.; Sena, M.; Gao, X. Designing Multifunctional Quantum Dots for Bioimaging, Detection, and Drug Delivery *Chem Soc Rev* **2010**, *39*, 4326–4354.

(16) Asik, D.; Yagci, M. B.; Demir Duman, F.; Yagci Acar, H. One Step Emission Tunable Synthesis of PEG Coated $Ag_2S$ NIR Quantum Dots and the

Development of Receptor Targeted Drug Delivery Vehicles Thereof. *J Mater Chem B* **2016**, *4*, 1941–1950.

(17) Chen, G.; Tian, F.; Zhang, Y.; Zhang, Y.; Li, C.; Wang, Q. Tracking of Transplanted Human Mesenchymal Stem Cells in Living Mice Using Near-Infrared $Ag_2S$ Quantum Dots. *Adv Funct Mater* **2014**, *24*, 2481–2488.

(18) Lim, Y. T.; Kim, S.; Nakayama, A.; Stott, N. E.; Bawendi, M. G.; Frangioni, J. v. Selection of Quantum Dot Wavelengths for Biomedical Assays and Imaging. *Mol Imaging* **2003**, *2*, 1141–1148.

(19) C. L. Zhang.; One-Pot Synthesized Aptamer-Functionalized CdTe:$Zn^{2+}$ Quantum Dots for Tumor Targeted Fluorescence Imaging in Vitro and in Vivo. *Anal Chem* **2013**, *85*, 5843–5849.

(20) Hou, B.; Cho, Y.; Kim, B. S.; Hong, J.; Park, J. B.; Ahn, S. J.; Sohn, J. I.; Cha, S.; Kim, J. M. Highly Monodispersed PbS Quantum Dots for Outstanding Cascaded-Junction Solar Cells. *ACS Energy Lett* **2016**, *1*, 834–839.

(21) Ma, W.; Swisher, S. L.; Ewers, T.; Engel, J.; Ferry, V. E.; Atwater, H. A.; Alivisatos, A. P. Photovoltaic Performance of Ultrasmall PbSe Quantum Dots. *ACS Nano* **2011**, *5*, 4334–4339.

(22) Moreels, I.; Lambert, K.; Smeets, D.; de Muynck, D.; Nollet, T.; Martins, J. C.; Vanhaecke, F.; Vantomme, A.; Delerue, C.; Allan, G.; Hens, Z. Size-Dependent Optical Properties of Colloidal PbS Quantum Dots. *ACS Nano* **2009**, *3*, 3023–3030.

(23) Du, H.; Chen, C.; Krishnan, R.; Krauss, T. D.; Harbold, J. M.; Wise, F. W.; Thomas, M. G.; Silcox, J. Optical Properties of Colloidal PbSe Nanocrystals. *Nano Lett* **2002**, *2*, 200312–200319.

(24) Moreels, I.; Lambert, K.; de Muynck, D.; Vanhaecke, F.; Poelman, D.; Martins, J. C.; Allan, G.; Hens, Z. Composition and Size-Dependent Extinction Coefficient of Colloidal PbSe Quantum Dots. *Chemistry of Materials* **2007**, *19*, 6101–6106.

(25) Ellingson, R. J.; Beard, M. C.; Johnson, J. C.; Yu, P.; Micic, O. I.; Nozik, A. J.; Shabaev, A.; Efros, A. L. Highly Efficient Multiple Exciton Generation in Colloidal PbSe and PbS Quantum Dots. *Nano Lett* **2005**, *5*, 2112–2130.

(26) Moreels, I.; Lambert, K.; de Muynck, D.; Vanhaecke, F.; Poelman, D.; Martins, J. C.; Allan, G.; Hens, Z. Composition and Size-Dependent Extinction Coefficient of Colloidal PbSe Quantum Dots. *Chemistry of Materials* **2007**, *19*, 6101–6106.

(27) Campos, M. P.; Hendricks, M. P.; Beecher, A. N.; Walravens, W.; Swain, R. A.; Cleveland, G. T.; Hens, Z.; Sfeir, M. Y.; Owen, J. S. A Library of Selenourea Precursors to PbSe Nanocrystals with Size Distributions near the Homogeneous Limit. *J Am Chem Soc* **2017**, *139*, 2296–2305.

(28) Dai, Q.; Wang, Y.; Li, X.; Zhang, Y.; Pellegrino, D. J.; Zhao, M.; Zou, B.; Seo, J.; Wang, Y.; Yu, W. W. Size-Dependent Composition and Molar Extinction Coefficient of PbSe Semiconductor Nanocrystals. *ACS Nano* **2009**, *3*, 1518–1524.

(29) Yu, W. W.; Falkner, J. C.; Shih, B. S.; Colvin, V. L. Preparation and Characterization of Monodisperse PbSe Semiconductor Nanocrystals in a Noncoordinating Solvent. *Chemistry of Materials* **2004**, *16*, 3002–3010

(30) Battaglia, D.; Peng, X. Formation of High Quality InP and InAs Nanocrystals in a Noncoordinating Solvent. . *Nano Lett* **2002**, *2*, 1027–1030.

(31) Shu, Y.; Yan, J.; Lu, Q.; Ji, Z.; Jin, D.; Xu, Q.; Hu, X. Pb Ions Enhanced Fluorescence of $Ag_2S$ QDs with Tunable Emission in the NIR-II Window: Facile One Pot Synthesis and Their Application in NIR-II Fluorescent Bio-Sensing. *Sens Actuators B Chem* **2020**, *307*, 127952–127999.

(32) Li, C.; Li, F.; Zhang, Y.; Zhang, W.; Zhang, X.-E.; Wang, Q. Real-Time Monitoring Surface Chemistry-Dependent In Vivo Behaviors of Protein Nanocages via Encapsulating an NIR-II $Ag_2S$ Quantum Dot. *ACS Nano* **2015**, *9*, 12255–12263.

(33) Li, C.; Li, W.; Liu, H.; Zhang, Y.; Chen, G.; Li, Z.; Wang, Q. An Activatable NIR-II Nanoprobe for In Vivo Early Real-Time Diagnosis of Traumatic Brain Injury. *Angewandte Chemie* **2020**, *132*, 2354–2363.

(34) Karimipour, M.; Bagheri, M.; Molaei, M. Enhancement of Durability of NIR Emission of $Ag_2S$@ZnS QDs in Water. *Modern Physics Letters B* **2017**, *31*, 301–306.

(35) Karimipour, M.; Moradi, N.; Molaei, M. Strong NIR Luminescent $Ag_2S$@ZnS Core-Shells Synthesized by a Novel One Pot Pulsed Microwave Irradiation. *J Lumin* **2017**, *182*, 91–97.

(36) Bhardwaj, K.; Pradhan, S.; Basel, S.; Clarke, M.; Brito, B.; Thapa, S.; Roy, P.; Borthakur, S.; Saikia, L.; Shankar, A.; Stasiuk, G. J.; Pariyar, A.; Tamang, S. Tunable NIR-II Emitting Silver Chalcogenide Quantum Dots Using Thio/Selenourea Precursors: Preparation of an MRI/NIR-II Multimodal Imaging Agent. *Dalton Transactions* **2020**, *49*, 15425–15432.

(37) Hilderbrand, S. A.; Weissleder, R. Near-Infrared Fluorescence: Application to in Vivo Molecular Imaging. *Curr Opin Chem Biol* **2010**, *14*, 71–79.

(38) Xie, R.; Kolb, U.; Li, J.; Basché, T.; Mews, A. Synthesis and Characterization of Highly Luminescent CdSe-Core CdS/$Zn_{0.5}Cd_{0.5}S$/ZnS Multishell Nanocrystals. *J Am Chem Soc* **2005**, *127*, 7480–7488.

(39) He, D.; Garg, S.; Wang, Z.; Li, L.; Rong, H.; Ma, X.; Li, G.; An, T.; Waite, T. D. Silver Sulfide Nanoparticles in Aqueous Environments: Formation, Transformation and Toxicity. *Environmental Science: Nano*. *RSC* **2019**, 8, 1674–1687.

(40) Lu, C.; Chen, G.; Yu, B.; Cong, H. Recent Advances of Low Biological Toxicity $Ag_2S$ QDs for Biomedical Application. *Advanced Engineering Materials* **2014**, *1* (8),1919–1923.

(41) Sun, H.; Zhang, F.; Wei, H.; Yang, B. The Effects of Composition and Surface Chemistry on the Toxicity of Quantum Dots. *J Mater Chem B* **2013**, *1*, 6485–6494.

(42) Allocca, M.; Mattera, L.; Bauduin, A.; Miedziak, B.; Moros, M.; de Trizio, L.; Tino, A.; Reiss, P.; Ambrosone, A.; Tortiglione, C. An Integrated Multilevel

Analysis Profiling Biosafety and Toxicity Induced by Indium- and Cadmium-Based Quantum Dots in Vivo. *Environ Sci Technol* **2019**, *53*, 1185–1194.

(43) Kima, S. H.; Manb, M. T.; Leea, H. S. Size and Shell Effects on CdSe Quantum Dots in Binary Ligand System. *Applied Science and Convergence Technology* **2020**, *29*, 87–90.

(44) Awasthi, P.; An, X.; Xiang, J.; Kalva, N.; Shen, Y.; Li, C. Facile Synthesis of Noncytotoxic PEGylated Dendrimer Encapsulated Silver Sulfide Quantum Dots for NIR-II Biological Imaging. *Nanoscale* **2020**, *12*, 1128–1132.

(45) Chakraborty, I. N.; Roy, S.; Devatha, G.; Rao, A.; Pillai, P. P. InP/ZnS Quantum Dots as Efficient Visible-Light Photocatalysts for Redox and Carbon-Carbon Coupling Reactions. *Chemistry of Materials* **2019**, *6*, 2258–2262.

(46) Rosson, T. E.; Claiborne, S. M.; McBride, J. R.; Stratton, B. S.; Rosenthal, S. J. Bright White Light Emission from Ultrasmall Cadmium Selenide Nanocrystals. *J Am Chem Soc* **2012**, *134*, 8006–8009.

(47) Smith, A. M.; Mancini, M. C.; Nie, S. Bioimaging: Second Window for in Vivo Imaging. *Nature Nanotechnology* **2009**, *6*, 710–711.

(48) Órdenes-Aenishanslins, N.; Anziani-Ostuni, G.; Monrás, J. P.; Tello, A.; Bravo, D.; Toro-Ascuy, D.; Soto-Rifo, R.; Prasad, P. N.; Pérez-Donoso, J. M. Bacterial Synthesis of Ternary CdSAg Quantum Dots through Cation Exchange: Tuning the Composition and Properties of Biological Nanoparticles for Bioimaging and Photovoltaic Applications. *Microorganisms* **2020**, *8*, 6312–6321.

(49) Cui, L.; Rao, J. Chemical Methodology for Labelling and Bioconjugation. In *The Chemistry of Molecular Imaging*, **2014**, *6*, 25–53.

(50) Gönen, M.; Egbuchunam, T. O.; Balköse, D.; Inal, F.; Ülkü, S. Preparation and Characterization of Magnesium Stearate, Cobalt Stearate, and Copper Stearate and Their Effects on Poly(Vinyl Chloride) Dehydrochlorination. *Journal of Vinyl and Additive Technology* **2015**, *21*, 235–244.

(51) Han, M.; Gao, X.; Su, J. Z.; Nie, S. Quantum-Dot-Tagged Microbeads for Multiplexed Optical Coding of Biomolecules; *J Am Chem Soc* **2001**, *5*, 2521–2529.

(52) Bear, J. C.; Hollingsworth, N.; Roffey, A.; McNaughter, P. D.; Mayes, A. G.; Macdonald, T. J.; Nann, T.; Ng, W. H.; Kenyon, A. J.; Hogarth, G.; Parkin, I. P. Doping Group IIB Metal Ions into Quantum Dot Shells via the One-Pot Decomposition of Metal-Dithiocarbamates. *Adv Opt Mater* **2015**, *3*, 704–712.

(53) Hanson, C. J.; Hartmann, N. F.; Singh, A.; Ma, X.; DeBenedetti, W. J. I.; Casson, J. L.; Grey, J. K.; Chabal, Y. J.; Malko, A. v.; Sykora, M.; Piryatinski, A.; Htoon, H.; Hollingsworth, J. A. Giant PbSe/CdSe/CdSe Quantum Dots: Crystal-Structure-Defined Ultrastable Near-Infrared Photoluminescence from Single Nanocrystals. . *J Am Chem Soc* **2017**, *139*, 7110–7111.

(54) Murphy, J. E.; Beard, M. C.; Norman, A. G.; Ahrenkiel, S. P.; Johnson, J. C.; Yu, P.; Mićić, O. I.; Ellingson, R. J.; Nozik, A. J. PbTe Colloidal Nanocrystals: Synthesis, Characterization, and Multiple Exciton Generation. *J Am Chem Soc* **2006**, *128*, 3241–3247.

(55) Liu, J.; Cao, D.; Zhang, L. Molecular Dynamics Study on Nanoparticle Diffusion in Polymer Melts: A Test of the Stokes-Einstein Law. *Journal of Physical Chemistry C* **2008**, *112*, 6653–6661.

(56) Wei, J.; Li, F.; Chang, C.; Zhang, Q. Synthesis of Emission Tunable $AgInS_2$/ZnS Quantum Dots and Application for Light Emitting Diodes. *J Phys Commun* **2020**, *4*, 2314–2341.

(57) Tan, L.; Liu, S.; Li, X.; Chronakis, I. S.; Shen, Y. A New Strategy for Synthesizing $AgInS_2$ Quantum Dots Emitting Brightly in Near-Infrared Window for in Vivo Imaging. *Colloids Surf B Biointerfaces* **2015**, *125*, 222–229.

(58) Battaglia, D.; Peng, X. Formation of High Quality InP and InAs Nanocrystals in a Noncoordinating Solvent. *Nano Lett* **2002**, *2*, 1027–1030.

(59) Zhao, J.; Zhong, D.; Zhou, S. NIR-I-to-NIR-II Fluorescent Nanomaterials for Biomedical Imaging and Cancer Therapy. *J Mater Chem B* **2018**, *6*, 349–365.

(60) Alivisatos, A. P.; Gu, W.; Larabell, C. Quantum Dots as Cellular Probes. *Annu Rev Biomed Eng* **2005**, *7*, 55–76.

(61) Aharoni, A.; Mokari, T.; Popov, I.; Banin, U. Synthesis of InAs/CdSe/ZnSe Core/Shell1/Shell2 Structures with Bright and Stable Near-Infrared Fluorescence. *J Am Chem Soc* **2006**, *128*, 1112–1130.

(62) Murray, C. B.; Sun, S.; Gaschler, W.; Doyle, H.; Betley, T. A.; Kagan, C. R. Colloidal Synthesis of Nanocrystals and Nanocrystal Superlattices. *IBM J Res Dev* **2001**, *45*, 3122–3129.

(63) Imamura, Y.; Yamada, S.; Tsuboi, S.; Nakane, Y.; Tsukasaki, Y.; Komatsuzaki, A.; Jin, T. Near-Infrared Emitting PbS Quantum Dots for in Vivo Fluorescence Imaging of the Thrombotic State in Septic Mouse Brain. *Molecules* **2016**, *21*, 2154–2159.

(64) Sun, Y.-P.; Zhou, B.; Lin, Y.; Wang, W.; Fernando, K. A. S.; Pathak, P.; Meziani, M. J.; Harruff, B. A.; Wang, X.; Wang, H.; Luo, P. G.; Yang, H.; Kose, M. E.; Chen, B.; Veca, L. M.; Xie, S.-Y. Quantum-Sized Carbon Dots for Bright and Colorful Photoluminescence. *J Am Chem Soc* **2006**, *128*, 7756–7757.

(65) Bai, Y.; Zhang, B.; Chen, L.; Lin, Z.; Zhang, X.; Ge, D.; Shi, W.; Sun, Y. Facile One-Pot Synthesis of Polydopamine Carbon Dots for Photothermal Therapy. *Nanoscale Res Lett* **2018**, *13*, 1123–1129.

(66) Bera, D.; Qian, L.; Tseng, T.-K.; Holloway, P. H. Quantum Dots and Their Multimodal Applications: A Review. *Materials* **2010**, *3*, 6440–6445.

(67) Chen, J.; Kong, Y.; Wo, Y.; Fang, H.; Li, Y.; Zhang, T.; Dong, Y.; Ge, Y.; Wu, Z.; Zhou, D.; Chen, S. Facile Synthesis of β-Lactoglobulin Capped $Ag_2S$ Quantum Dots for in Vivo Imaging in the Second near-Infrared Biological Window. *J Mater Chem B* **2016**, *4*, 6271–6278.

(68) Li, D.; Liang, C.; Ushakova, E. v.; Sun, M.; Huang, X.; Zhang, X.; Jing, P.; Yoo, S. J.; Kim, J.; Liu, E.; Zhang, W.; Jing, L.; Xing, G.; Zheng, W.; Tang, Z.; Qu, S.; Rogach, A. L. Thermally Activated Upconversion Near-Infrared Photoluminescence from Carbon Dots Synthesized via Microwave Assisted Exfoliation. *Small* **2019**, *15*, 5050–5078.

(69) Jiang, P.; Zhu, C.-N.; Zhu, D.-L.; Zhang, Z.-L.; Zhang, G.-J.; Pang, D.-W. A Room-Temperature Method for Coating a ZnS Shell on Semiconductor Quantum Dots. *J Mater Chem C Mater* **2015**, *3*, 1039–1045.

(70) Zhuang, J.; Zhang, X.; Wang, G.; Li, D.; Yang, W.; Li, T. Synthesis of Water-Soluble ZnS : $Mn^{2+}$ Nanocrystals by Using Mercaptopropionic Acid as Stabilizer. *J Mater Chem* **2003**, *13*, 1067–1070.

(71) Ellingson, R. J.; Beard, M. C.; Johnson, J. C.; Yu, P.; Micic, O. I.; Nozik, A. J.; Shabaev, A.; Efros, A. L. Highly Efficient Multiple Exciton Generation in Colloidal PbSe and PbS Quantum Dots. *Nano Lett* **2005**, *5*, 865–871.

(72) Zhu, C.-N.; Jiang, P.; Zhang, Z.-L.; Zhu, D.-L.; Tian, Z.-Q.; Pang, D.-W. $Ag_2Se$ Quantum Dots with Tunable Emission in the Second Near-Infrared Window. *ACS Appl Mater Interfaces* **2013**, *5*, 1186–1189.

(73) Ge, X.-L.; Huang, B.; Zhang, Z.-L.; Liu, X.; He, M.; Yu, Z.; Hu, B.; Cui, R.; Liang, X.-J.; Pang, D.-W. Glucose-Functionalized near-Infrared $Ag_2Se$ Quantum Dots with Renal Excretion Ability for Long-Term in Vivo Tumor Imaging. *J Mater Chem B* **2019**, *7*, 1236–1239.

(74) Dong, B.; Li, C.; Chen, G.; Zhang, Y.; Zhang, Y.; Deng, M.; Wang, Q. Facile Synthesis of Highly Photoluminescent $Ag_2Se$ Quantum Dots as a New Fluorescent Probe in the Second Near-Infrared Window for in Vivo Imaging. *Chemistry of Materials* **2013**, *25*, 2503–2509.

(75) Ge, J.-P.; Xu, S.; Liu, L.-P.; Li, Y.-D. A Positive-Microemulsion Method for Preparing Nearly Uniform $Ag_2Se$ Nanoparticles at Low Temperature. *Chemistry - A European Journal* **2006**, *12*, 3672–3677.

(76) Gu, Y.-P.; Cui, R.; Zhang, Z.-L.; Xie, Z.-X.; Pang, D.-W. Ultrasmall Near-Infrared $Ag_2Se$ Quantum Dots with Tunable Fluorescence for in Vivo Imaging. *J Am Chem Soc* .**2012**, *134* , 79-82.

(77) Mirahmadi, F. S.; Marandi, M.; Karimipour, M.; Molaei, M. Microwave Activated Synthesis of $Ag_2S$ and $Ag_2S$@ZnS Nanocrystals and Their Application in Well-Performing Quantum Dot Sensitized Solar Cells. *Solar Energy* **2020**, *202*, 155–163.

(78) Purushothaman, B.; Song, J. M. $Ag_2S$ Quantum Dot Theragnostics. *Biomater Sci* **2021**, *9*, 151–156.

(79) Tiwari, A.; Dhoble, S. J. Synthesis, Functional Properties, and Applications of $Ag_2S$ Semiconductor Nanocrystals. *Nanoscale Compound Semiconductors and their Optoelectronics Applications*; Elsevier. **2022**, 5, 191–228.

(80) Jiang, P.; Tian, Z.-Q.; Zhu, C.-N.; Zhang, Z.-L.; Pang, D.-W. Emission-Tunable Near-Infrared $Ag_2S$ Quantum Dots. *Chemistry of Materials* **2012**, *24*, 5137–5139.

(81) Lim, W. P.; Zhang, Z.; Low, H. Y.; Chin, W. S. Preparation of $Ag_2S$ Nanocrystals of Predictable Shape and Size. *Angewandte Chemie International Edition* **2004**, *43*, 460566–460577.

(82) Sadovnikov, S. I.; Gusev, A. I.; Chukin, A. v.; Rempel, A. A. High-Temperature X-Ray Diffraction and Thermal Expansion of Nanocrystalline and Coarse-Crystalline Acanthite α-$Ag_2S$ and Argentite β-$Ag_2S$. *Physical Chemistry Chemical Physics* **2016**, *18*, 4617–4626.

(83) Gusev, A. I.; Sadovnikov, S. I.; Chukin, A. v.; Rempel, A. A. Thermal Expansion of Nanocrystalline and Coarse-Crystalline Silver Sulfide $Ag_2S$. *Physics of the Solid State* **2016**, *58*, 251–257.

(84) Du, Y.; Xu, B.; Fu, T.; Cai, M.; Li, F.; Zhang, Y.; Wang, Q. Near-Infrared Photoluminescent $Ag_2S$ Quantum Dots from a Single Source Precursor. *J Am Chem Soc* **2010**, *132*, 1470–1471.

(85) Welsher, K.; Liu, Z.; Sherlock, S. P.; Robinson, J. T.; Chen, Z.; Daranciang, D.; Dai, H. A Route to Brightly Fluorescent Carbon Nanotubes for Near-Infrared Imaging in Mice. *Nat Nanotechnol* **2009**, *4*, 773–782.

(86) Welsher, K.; Liu, Z.; Sherlock, S. P.; Robinson, J. T.; Chen, Z.; Daranciang, D.; Dai, H. A Route to Brightly Fluorescent Carbon Nanotubes for Near-Infrared Imaging in Mice. *Nat Nanotechnol* **2009**, *4*, 773–782.

(87) Du, Y.; Xu, B.; Fu, T.; Cai, M.; Li, F.; Zhang, Y.; Wang, Q. Near-Infrared Photoluminescent $Ag_2S$ Quantum Dots from a Single Source Precursor. *J Am Chem Soc* **2010**, *132*, 1470–1471.

(88) Wang, G.; Li, Z.; Ma, N. Next-Generation DNA-Functionalized Quantum Dots as Biological Sensors. *ACS Chemical Biology*, **2018**, *6*, 1705–1713.

(89) Jiang, P.; Zhu, C.-N.; Zhang, Z.-L.; Tian, Z.-Q.; Pang, D.-W. Water-Soluble $Ag_2S$ Quantum Dots for near-Infrared Fluorescence Imaging in Vivo. *Biomaterials* **2012**, *33*, 5130–5135.

(90) Zhang, Y.; Hong, G.; Zhang, Y.; Chen, G.; Li, F.; Dai, H.; Wang, Q. $Ag_2S$ Quantum Dot: A Bright and Biocompatible Fluorescent Nanoprobe in the Second Near-Infrared Window. *ACS Nano* **2012**, *6*, 3695–3702.

(91) Zhang, Y.; Hong, G.; Zhang, Y.; Chen, G.; Li, F.; Dai, H.; Wang, Q. $Ag_2S$ Quantum Dot: A Bright and Biocompatible Fluorescent Nanoprobe in the Second Near-Infrared Window. *ACS Nano* **2012**, *6*, 3695–3702.

(92) Zhang, Y.; Hong, G.; Zhang, Y.; Chen, G.; Li, F.; Dai, H.; Wang, Q. $Ag_2S$ Quantum Dot: A Bright and Biocompatible Fluorescent Nanoprobe in the Second Near-Infrared Window. *ACS Nano* **2012**, *6*, 3695–3702.

(93) Zhang, Y.; Hong, G.; Zhang, Y.; Chen, G.; Li, F.; Dai, H.; Wang, Q. $Ag_2S$ Quantum Dot: A Bright and Biocompatible Fluorescent Nanoprobe in the Second near-Infrared Window. *ACS Nano* **2012**, *6*, 3695–3702.

(94) Yang, H.-Y.; Zhao, Y.-W.; Zhang, Z.-Y.; Xiong, H.-M.; Yu, S.-N. One-Pot Synthesis of Water-Dispersible $Ag_2S$ Quantum Dots with Bright Fluorescent Emission in the Second near-Infrared Window. *Nanotechnology* **2013**, *24,* 2118–2123.

(95) Zhang, Y.; Liu, Y.; Li, C.; Chen, X.; Wang, Q. Controlled Synthesis of $Ag_2S$ Quantum Dots and Experimental Determination of the Exciton Bohr Radius. *Journal of Physical Chemistry C* **2014**, *118*, 4918–4923.

(96) Zhang, X.; Liu, M.; Liu, H.; Zhang, S. Low-Toxic $Ag_2S$ Quantum Dots for Photoelectrochemical Detection Glucose and Cancer Cells. *Biosens Bioelectron* **2014**, *56*, 307–312.

(97) Yang, H.; Santra, S.; Walter, G. A.; Holloway, P. H. GdIII-Functionalized Fluorescent Quantum Dots as Multimodal Imaging Probes. *Advanced Materials* **2006**, *18*, 2890–2894.

(98) Jiang, P.; Tian, Z. Q.; Zhu, C. N.; Zhang, Z. L.; Pang, D. W. Emission-Tunable near-Infrared $Ag_2S$ Quantum Dots. *Chemistry of Materials* **2012**, *24,* 1123–1125.

(99) Gu, Y.-P.; Cui, R.; Zhang, Z.-L.; Xie, Z.-X.; Pang, D.-W. Ultrasmall Near-Infrared $Ag_2Se$ Quantum Dots with Tunable Fluorescence for *in Vivo* Imaging. *J Am Chem Soc* .**2012**, *134* , 79-82.

(100) Hocaoglu, I.; Demir, F.; Birer, O.; Kiraz, A.; Sevrin, C.; Grandfils, C.; Yagci Acar, H. Emission Tunable, Cyto/Hemocompatible, near-IR-Emitting $Ag_2S$ Quantum Dots by Aqueous Decomposition of DMSA. *Nanoscale* **2014**, *6*, 11921–11931.

(101) Xing, L.; Xu, S.; Cui, J.; Wang, L. Solvent Tailored Strategy for Synthesis of Ultrasmall $Ag_2S$ Quantum Dots with Near-Infrared-II Luminescence. *J Nanosci Nanotechnol* **2019**, *19*, 4549–4555.

(102) Gui, R.; Sun, J.; Liu, D.; Wang, Y.; Jin, H. Retracted Article: A Facile Cation Exchange-Based Aqueous Synthesis of Highly Stable and Biocompatible $Ag_2S$ Quantum Dots Emitting in the Second near-Infrared Biological Window *Dalton Transactions*. **2014**, *43*, 16690-16697.

(103) Zhao, M.-Q.; Zhang, Q.; Tian, G.-L.; Wei, F. Emerging Double Helical Nanostructures. *Nanoscale* **2014**, *6*, 9339–9354.

(104) Duman, F. D.; Hocaoglu, I.; Ozturk, D. G.; Gozuacik, D.; Kiraz, A.; Yagci Acar, H. Highly Luminescent and Cytocompatible Cationic $Ag_2S$ NIR-Emitting Quantum Dots for Optical Imaging and Gene Transfection. *Nanoscale* **2014**, *7*, 11352–11362

(105) Song, C.; Zhang, Y.; Li, C.; Chen, G.; Kang, X.; Wang, Q. Enhanced Nanodrug Delivery to Solid Tumors Based on a Tumor Vasculature-Targeted Strategy. *Adv Funct Mater* **2016**, *26*, 4192–4200.

(106) Gao, J.; Wu, C.; Deng, D.; Wu, P.; Cai, C. Direct Synthesis of Water-Soluble Aptamer-$Ag_2S$ Quantum Dots at Ambient Temperature for Specific Imaging and Photothermal Therapy of Cancer. *Adv Healthc Mater* **2016**, *5*, 2437–2449.

(107) Wu, Q.; Zhou, M.; Shi, J.; Li, Q.; Yang, M.; Zhang, Z. Synthesis of Water-Soluble $Ag_2S$ Quantum Dots with Fluorescence in the Second Near-Infrared Window for Turn-On Detection of Zn(II) and Cd(II). *Anal Chem* **2017**, *89*, 6616–6623.

(108) He, H.; Lin, Y.; Tian, Z.-Q.; Zhu, D.-L.; Zhang, Z.-L.; Pang, D.-W. Ultrasmall Pb:$Ag_2S$ Quantum Dots with Uniform Particle Size and Bright Tunable Fluorescence in the NIR-II Window. *Small* **2018**, *14*, 21315–21350.

(109) Amor-Gutiérrez, O.; Iglesias-Mayor, A.; Llano-Suárez, P.; Costa-Fernández, J. M.; Soldado, A.; Podadera, A.; Parra, F.; Costa-García, A.; de la Escosura-Muñiz, A. Electrochemical Quantification of $Ag_2S$ Quantum Dots: Evaluation of Different Surface Coating Ligands for Bacteria Determination. *Microchimica Acta* **2020**, *187*, 4133–4145.

(110) Yuan, L.-D.; Deng, H.-X.; Li, S.-S.; Wei, S.-H.; Luo, J.-W. Unified Theory of Direct or Indirect Band-Gap Nature of Conventional Semiconductors. *Phys Rev B* **2018**, *98* (24), 245203–245210.

(111) Aydemir, D.; Hashemkhani, M.; Acar, H. Y.; Ulusu, N. N. Evaluation of the Biocompatibility of the GSH-Coated $Ag_2S$ Quantum Dots in Vitro: A Perfect Example for the Non-Toxic Optical Probes. *Mol Biol Rep* **2020**, *47*, 2213–2220.

(112) Li, L.; Reiss, P. One-Pot Synthesis of Highly Luminescent InP/ZnS Nanocrystals without Precursor Injection. *J Am Chem Soc* **2008**, *130*, 11588–11589.

(113) Hunt, N. J.; Lockwood, G. P.; le Couteur, F. H.; McCourt, P. A. G.; Singla, N.; Kang, S. W. S.; Burgess, A.; Kuncic, Z.; le Couteur, D. G.; Cogger, V. C. Rapid Intestinal Uptake and Targeted Delivery to the Liver Endothelium Using Orally Administered Silver Sulfide Quantum Dots. *ACS Nano* **2020**, *14*, 4512–4534.

(114) Bhardwaj, K.; Pradhan, S.; Basel, S.; Clarke, M.; Brito, B.; Thapa, S.; Roy, P.; Borthakur, S.; Saikia, L.; Shankar, A.; Stasiuk, G. J.; Pariyar, A.; Tamang, S. Tunable NIR-II Emitting Silver Chalcogenide Quantum Dots Using Thio/Selenourea Precursors: Preparation of an MRI/NIR-II Multimodal Imaging Agent. *Dalton Transactions* **2020**, *49*, 15425–15432.

(115) Han, R.; Xiao, Y.; Yang, Q.; Pan, M.; Hao, Y.; He, X.; Peng, J.; Qian, Z. $Ag_2S$ Nanoparticle-Mediated Multiple Ablations Reinvigorates the Immune Response for Enhanced Cancer Photo-Immunotherapy. *Biomaterials* **2021**, *264*, 120451–120460.

(116) Ren, Q.; Ma, Y.; Zhang, S.; Ga, L.; Ai, J. One-Step Synthesis of Water-Soluble Silver Sulfide Quantum Dots and Their Application to Bioimaging. *ACS Omega* **2021**, *6*, 6361–6367.

(117) Yarema, M.; Pichler, S.; Sytnyk, M.; Seyrkammer, R.; Lechner, R. T.; Fritz-Popovski, G.; Jarzab, D.; Szendrei, K.; Resel, R.; Korovyanko, O.; Loi, M. A.; Paris, O.; Hesser, G.; Heiss, W. Infrared Emitting and Photoconducting Colloidal Silver Chalcogenide Nanocrystal Quantum Dots from a Silylamide-Promoted Synthesis. *ACS Nano* **2011**, *5*, 3758–3765.

(118) Sahu, A.; Khare, A.; Deng, D. D.; Norris, D. J. Quantum Confinement in Silver Selenide Semiconductor Nanocrystals. *Chemical Communications* **2012**, *48,* 5458–5460.

(119) Zhu, C. N.; Jiang, P.; Zhang, Z. L.; Zhu, D. L.; Tian, Z. Q.; Pang, D. W. $Ag_2Se$ Quantum Dots with Tunable Emission in the Second Near-Infrared Window. *ACS Appl Mater Interfaces* **2013**, *5,* 1186–1189.

(120) Tan, L.; Zhou, Y.; Ren, F.; Benetti, D.; Yang, F.; Zhao, H.; Rosei, F.; Chaker, M.; Ma, D. Ultrasmall PbS Quantum Dots: A Facile and Greener Synthetic Route and Their High Performance in Luminescent Solar Concentrators. *J Mater Chem A Mater* **2017**, *5,* 10250–10260.

(121) Sahu, A.; Qi, L.; Kang, M. S.; Deng, D.; Norris, D. J. Facile Synthesis of Silver Chalcogenide ($Ag_2E$; E = Se, S, Te) Semiconductor Nanocrystals. *J Am Chem Soc* **2011**, *133,* 6509–6512.

(122) Zhang, J.; Zhang, X.; Zhang, J. Y. Size-Dependent Time-Resolved Photoluminescence of Colloidal CdSe Nanocrystals. *The Journal of Physical Chemistry C* **2009**, *113*, 9512–9515.

(123) Zebibula, A.; Alifu, N.; Xia, L.; Sun, C.; Yu, X.; Xue, D.; Liu, L.; Li, G.; Qian, J. Ultrastable and Biocompatible NIR-II Quantum Dots for Functional Bioimaging. *Advanced Functional Materials.* **2018**, *28,* 1703451–1703465.

(124) Susumu, K.; Uyeda, H. T.; Medintz, I. L.; Pons, T.; Delehanty, J. B.; Mattoussi, H. Enhancing the Stability and Biological Functionalities of Quantum Dots via Compact Multifunctional Ligands. *J Am Chem Soc* **2007**, *129,* 13987–13996.

(125) SalmanOgli, A. Nanobio Applications of Quantum Dots in Cancer: Imaging, Sensing, and Targeting. *Cancer Nanotechnol* **2011**, *2*, 2212–2215.

(126) Sung, A.-M.; Piirma, I. Electrosteric Stabilization of Polymer Colloids. *Langmuir* **1994**, *10*, 1393–1398.

(127) Jiang, P.; Chen, Z. Ligand Effect on the Synthesis of Emission-Tunable near-Infrared $Ag_2S$ Quantum Dots. *New Journal of Chemistry* **2017**, *41*, 5707–5712.

(128) Tang, R.; Xue, J.; Xu, B.; Shen, D.; Sudlow, G. P.; Achilefu, S. Tunable Ultrasmall Visible-to-Extended Near-Infrared Emitting Silver Sulfide Quantum Dots for Integrin-Targeted Cancer Imaging. *ACS Nano* **2015**, *9*, 230–250.

# Chapter II

## *Synthesis of NIR-II Quantum Dots*

## 2.1. Introduction

In fluorescence bioimaging, the second near-infrared (NIR-II, 1000-1400 nm) emitting Quantum Dots (QDs) can benefit from improved spatial resolution and deep tissue penetration, due to low light scattering and several other factors such as high signal-to-noise ratio, low absorbance of water, and other biomolecules compared to their visible (400-750 nm) and the NIR-I (750-900 nm region) counterparts.[1–7] QD-based fluorophores have superior quantum yield (QY) compared with organic dye.[8,9] They exhibit size-tunable fluorescence, broad absorption window, and high molar extinction coefficient.[2,5–7,10] However, NIR-II fluorophores simultaneously possessing high QY, photo-stability, and biocompatibility are very difficult to synthesize. Moreover, the majority of currently available QDs-based NIR-II fluorophores contain extremely dangerous $Cd^{2+}$, $As^{3-}$, $Pb^{2+}$, and $Hg^{2+}$ ions, which are not environment-friendly and practical for their use in bio-imaging. In this respect, silver chalcogenides have tremendous potential in the field of *in vivo* bioimaging and sensing.[2,3,11–14] $Ag_2S$ has a low solubility product ($K_{sp} = 6.3 \times 10^{-50}$) with very little probability of releasing $Ag^+$ ions into the biological environment[3,15–17] and is considered relatively non-toxic.[17–19] Studies have revealed that at low to moderate levels, $Ag_2S$ has very low cytotoxic or genotoxic effects, making it suitable for use in *in vivo* imaging.[20] Moreover, due to its narrow band gap (1.1 eV in bulk form) and the possibility of quantum confinement when its size is reduced to less than 4 nm (with an exciton Bohr radius of 2.2 nm), it is an ideal option for adjusting its emission within the 700-1400 nm spectrum (ranging from visible to NIR).[21] Likewise, the calculated exciton Bohr radius using bulk parameters for $Ag_2Se$ is 2.9 nm, and the bulk band-gap is 0.15 eV.[22,23] Size-tunability in the visible and NIR region at sizes far below 4-5 nm results in a low hydrodynamic diameter and potentially easy renal clearance from the body. The colloidal synthesis of $Ag_2X$ (X=S, Se) is still less explored than that of II-IV, III-V, and II-VI semiconductor nanocrystals (NCs), although having enormous potential in biology. Typically, a method for controlling the size of $Ag_2X$ QDs is to alter the temperature[24,25] the reaction time,[22,26] or both of these parameters.[18,27] Altering time and temperature can both influence the average final size, but doing so undermines competitive effects like Ostwald ripening[28–31] and unchecked molecular precursor depletion, both of which have a negative impact on the ability to manage final size distribution.[32,33] Recent research on the synthesis of II-VI and IV-VI semiconductor NCs by Vela *et al.* and Owen *et al.* has suggested a more logical method for controlling the photophysical characteristics of nanocrystals (NCs) via the reactivity of precursor. The effect of phosphine-chalcogenide precursor reactivity on the make-up and morphology of CdS/CdSe NCs was demonstrated by Vela *et al.*[34] Similar to this, Owen et al. later reported the size-dependent optical characteristics of PbS/PbSe by varying the reactivity of thio/selenourea derivatives.[35,36] However, in the case of silver chalcogenides, our research group is the first one to implement the strategies to produce $Ag_2X$ (X=S, Se) NCs. Therefore, we have reported a simple synthesis of $Ag_2X$ (X=S, Se) NCs with favorable environmental and biological properties that are controllable in the critical NIR-II region (900-1400 nm) by modifying the substituent groups on substituted thio/selenourea and their equivalents. In this chapter, a new method for the synthesis (sections 2.2 and 2.3) and characterization (section 2.4) of NIR-II emitting silver chalcogenides QDs are discussed, which are followed by the conclusion (section 2.5) and the experimental details (section 2.6).

## 2.2. Precursors for NIR-II CQDs

Substituted thiourea is a known sulfur precursor for different sulfides such as ZnS,[37,38] CuS,[36,37] PbS,[36] CdS[39], $CuFeS_2$[39], etc. Its growing popularity in semiconductor nanocrystal (NCs) synthesis is attributed to its solubility in non-polar solvent (well suited for hot injection techniques) and the presence of a labile C-S bond due to C-N pi-bonding[40] which can be easily broken under mild reaction conditions. Substituted thiocarbamate is a sulfur analog of carbamates with similar traits and dithiocarbamate is related to thiocarbamates by the replacement of O with S (Figure 2.1).

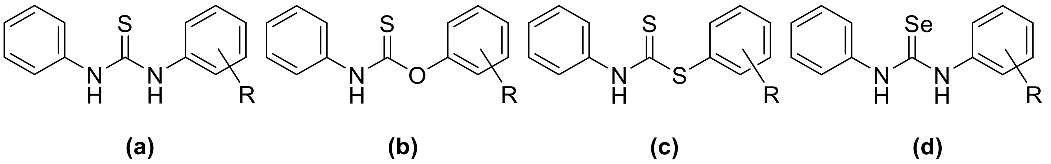

**Figure 2.1:** Representative structures of substituted thiourea (a) thiocarbamate (b) dithiocarbamate (c) selenourea (d). Here R is the substituent group outlined in Figure 2.2.

By reacting isothiocyanate/isoselenocyanate with readily available phenols, thiophenols, or aryl amines, we synthesized a range of substituted thiourea, thiocarbamate, dithiocarbamate, and selenourea precursors (Scheme 2.2a). The reactions are carried out in different solvents such as toluene, dioxane, chloroform, or ethanol depending on the solubility of the reactants. The reaction afforded pure products with a product yield of up to 91 percent at room temperature. The reaction time is 5 to 30 minutes depending on the reactivity of the substituted phenols or thiophenols or aryl amines. In certain circumstances, such as in the reaction of nitroaniline with isothiocyanate in acetonitrile, heating to reflux temperature and a longer reaction time is needed. This is attributed to the lower reactivity of nitroaniline compared to other substituted anilines. The pure product can be easily isolated by the filtration method as evident from NMR data and does not require additional purification using column chromatography. $^1$H and $^{13}$C NMR for all synthesized precursors (**3a-9b**) are provided in Annexure, A2.1.1.

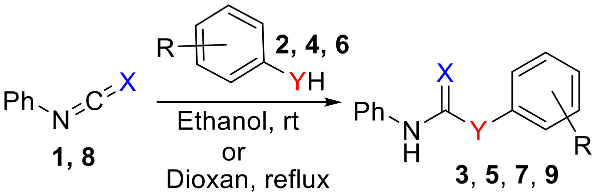

**Thiourea**
(X = S, Y = NH)
R : H, **3a**, 82%;
*p*-Me, **3b**, 80%;
*p*-OMe, **3c**, 91%;
*p*-I, **3d**, 60%;
*p*-NO$_2$, **3e**, 41%;
*p*-Br, **3f**, 65%;
*m*-NO$_2$, **3g**, 67%;
*p*-OH, **3h**, 75%;
*p*-C$_6$H$_4$-NH$_2$, **3i**, 80%;

**Thiocarbamate**
(X = S, Y = O)
R : *p*-Br, **5a**, 60%;
*p*-OMe, **5b**, 55%;
*p*-NO$_2$, **5c**, 65%;

**Dithiocarbamate**
(X = S, Y = S)
R : *p*-Br, **7a**, 70%;
*p*-OMe, **7b**, 50%;
*p*-NO$_2$, **7c**, 60%;

**Selenourea**
(X = Se, Y = NH)
R : H, **9a**, 85%;
*p*-OMe, **9b**, 85%;

**Figure 2.2:** Synthesis of a wide range of thiourea, thiocarbamate, dithiocarbamate and selenourea derivatives.

## 2.3. Synthesis of Ag$_2$X (X=S, Se) NCs using substituted thio/selenourea precursors

### 2.3.1. Reactions and synthetic scheme

The synthesis of Ag$_2$X (X=S, Se) NCs is based on the reaction of Ag(I) with substituted thio/selenourea precursors at elevated temperatures (~120-150 °C) (Figure 2.3a). The reaction takes place *via* a nucleophilic attack on Ag$^+$ by the precursor through the C=S bond (Figure 2.3b). The reaction is driven by the C-N pi-bonding in the case of thiourea and C-O and C-S pi bonding in the case of thiocarbamate and dithiocarbamate respectively.

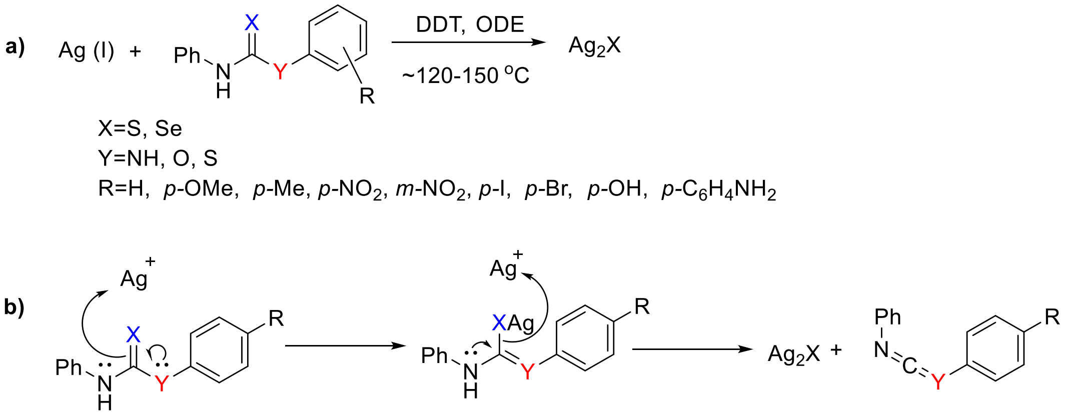

**Figure 2.3:** (a) General reaction for the synthesis of $Ag_2S$/Se NCs. (b) The mechanism for the formation of $Ag_2S$/Se NCs *via* a nucleophilic attack on $Ag^+$ by the precursor through the C=S bond.

To achieve monodispersity, the S or Se precursor is quickly injected into the hot solution of Ag(I) dissolved in 1-octadecene (ODE) in the presence of dodecane thiol (DDT). A distinct color change from red to black indicated the formation of $Ag_2X$ QDs and the reaction was quenched by immediate cooling in an ice bath. This method of synthesis of NCs in non-polar high boiling solvent *via* the "hot injection method" was first introduced by Murray *et. al.*.[41]The rapid injection of one of the precursors to the hot solution of the other precursor followed by cooling of the reaction mixture ensures separation of nucleation and growth stages which is important for achieving monodispersity (Introduction section 1.1). The reaction is performed in strictly air-free conditions using Schlenk-line. The schematic representation of the reaction setup is shown below (Scheme 2.1). The as-synthesized NCs were purified *via* the centrifugation method to remove excess ligands. The centrifugation method of purification involves the use of a polar co-solvent (e.g. ethanol or methanol) to destabilize the NCs dispersed in a polar solvent (e.g. hexane or toluene or TCE).[42,43] The "destabilization" of the colloidal NCs followed by centrifugation results in the precipitation of NCs from the solution.

Multiple (three times) cycle of the process was employed for the excess ligand and other undesired side products of the reaction.

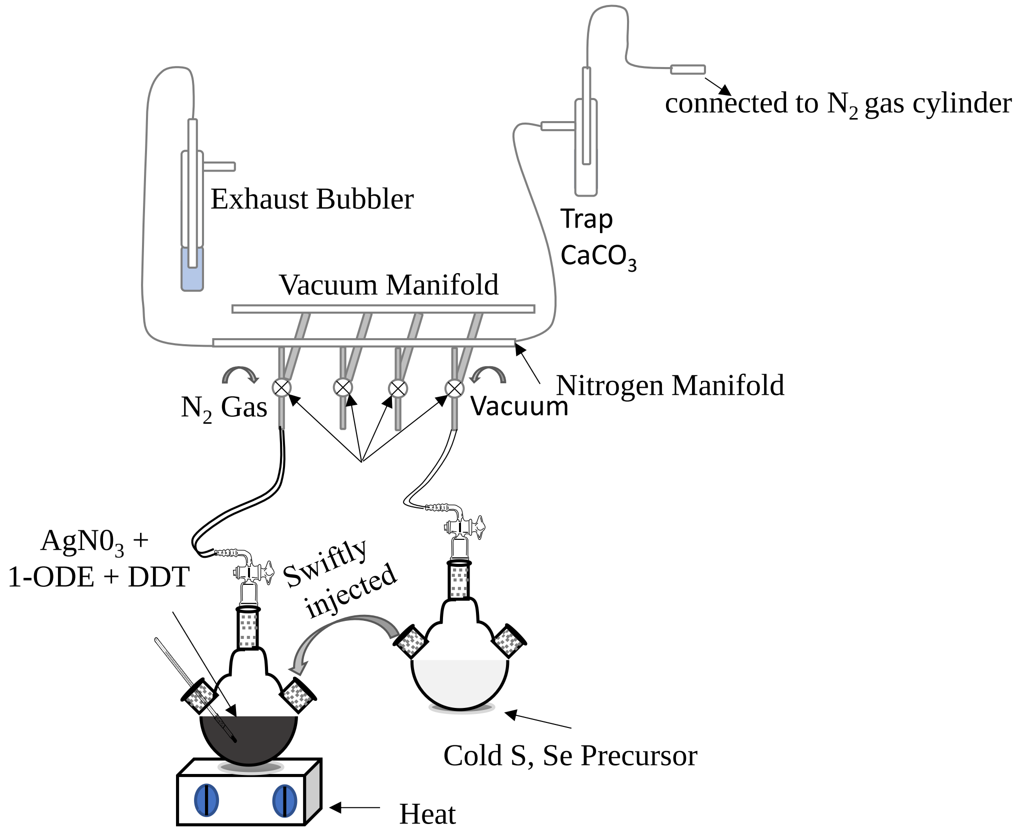
connected to $N_2$ gas cylinder
Exhaust Bubbler
Trap
$CaCO_3$
Vacuum Manifold
Nitrogen Manifold
$N_2$ Gas
Vacuum
$AgN0_3$ +
1-ODE + DDT
Swiftly injected
Cold S, Se Precursor
Heat

**Scheme 2.1.** Experimental set up for synthesis of $Ag_2X$ NCs

The photoluminescence (PL) emission spectra of $Ag_2S$ CQDs prepared using different substituted thiourea precursors (3a-i) are shown in Figure 2.4. The emission is in the NIR range (1020 –1210 nm). Similarly, emission was tunable in the region of 900 nm to 1300 nm by simply changing the substituent groups in thiocarbamates (5a-c), dithiocarbamate (7a-c), and selenourea precursors (9a-b) (Figure 2.4).

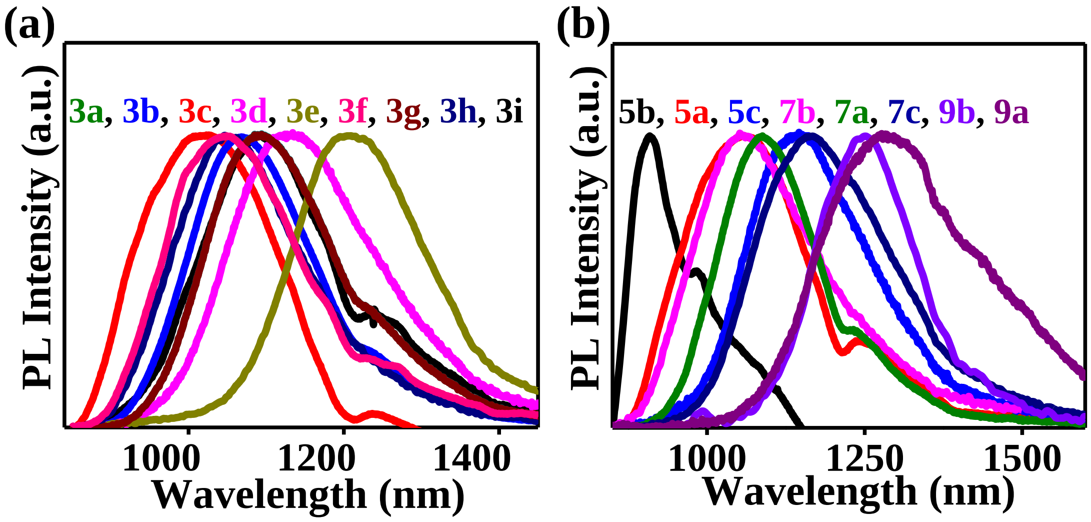

**Figure 2.4:** (a) PL spectra of $Ag_2S$ NCs produced from thiourea precursors (3a-g) and (b) $Ag_2S$/Se NCs synthesized from thiocarbamate (5a-c), dithiocarbamate (7a-c), and selenourea derivatives with tunable emission wavelength (9a-b).

### 2.3.2. Role of DDT

According to the Hard-Soft Acid Base (HSAB) principle,[44] the soft acid Ag (I) ion has a higher affinity for soft bases like thiol (-SH) or thiolates more than the amines or carboxylates. In our case, the presence of DDT is essential for the successful synthesis of stable $Ag_2X$ (X=S, Se) NCs. In fact, our attempts to synthesize the $Ag_2S$ NCs by simply reacting Ag oleate with thiourea (3a) in ODE at the decomposition temperature of the precursor (~150 °C) were not successful. The colloidal dispersion was poor and PL was not detectable (Annexure, A2.33). No improvement in colloidal stability or optical properties was noted even when oleyl amine was added during the reaction as a co-capping ligand (Annexure A2.34). Clearly, DDT is crucial for the reaction. To further understand the role of DDT, we attempted to synthesize $Ag_2S$ NCs using only DDT at the reaction temperatures (120-150 °C). However, $Ag_2S$ NCs were not formed, possibly due to the high decomposition temperature (>340 °C) of DDT. At elevated temperatures (~200 °C) reaction of DDT with Ag(I) led to the formation of $Ag_2S$ NCs as detected by XRD and optical studies (Annexure, A2.38). However, size distribution and PL were poor. The reaction of substituted thiourea with Ag(I) at ~120-150 °C in the presence of DDT in ODE led to the formation of highly stable and size-tunable $Ag_2S$ CQDs. Based on these results and literature reports, we conclude that

(a) DDT is an ideal capping ligand for stabilizing $Ag_2S$ NCs due to the strong affinity of -SH (soft base) to $Ag^+$ (soft acid). Furthermore, thiol-bound Ag (I) is not readily reduced to the undesirable species because of lower standard redox potential compared to that of a free $Ag^+$ ion.[45–47]

(b) DDT is not the source of S for the reaction, since its decomposition temperature (>340 °C) is much higher than the reaction temperature (120-150 °C). The sulfur is solely supplied by substituted thiourea.[48] Figure 2.5 shows the Thermogravimetric analysis (TGA) micrographs of representative precursors (3c and 3e).

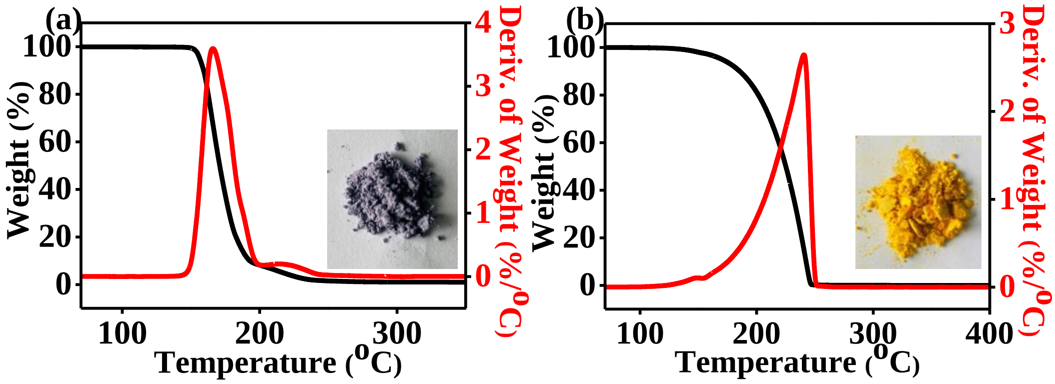

**Figure 2.5:** TGA micrographs of precursors (a) 3c and (a) 3e showing weight % vs temperature profile (black line) and its derivative (red line). Decomposition temperature of 3c is 145 °C, while that of 3e is 150 °C.

### 2.3.3. Effect of reaction temperature and time on the size of the NCs

The final size or size distribution and the optical characteristics of the NCs are strongly influenced by the reaction time[47,49] and temperature.[50,51] Increasing reaction temperature led to the formation of larger-sized NCs which is attributed to Ostwald ripening (for materials with greater solubility) and oriented attachment (for crystals with low solubility) In the first case, the growth of the larger particles is due to the dissolution of the smaller ones, in the second by merging the smaller ones.[50,51] Similarly, the longer the reaction time, the larger the size of the NCs. The absorption and emission wavelength ($\lambda_{max}$) are dependent on size.

A simple Brus equation[52] (Equation 2.1) can be used to correlate the size of the NCs ($R$) and the effective band gap of NCs

$$E_g = E_{g(b)} + \frac{h^2}{8R^2}\left(\frac{1}{m_e}+\frac{1}{m_h}\right) \qquad 2.1$$

where $E_{g(b)}$ is the bulk nanocrystals band gap energy (1.1 eV), $m_e$ ($0.286\, m_o$) and $m_h$ (1.096) are the effective electron and hole masses of the $Ag_2S$, respectively,[53] and ħ is Plank's constant ($4.13 \times 10^{-15} eV$).

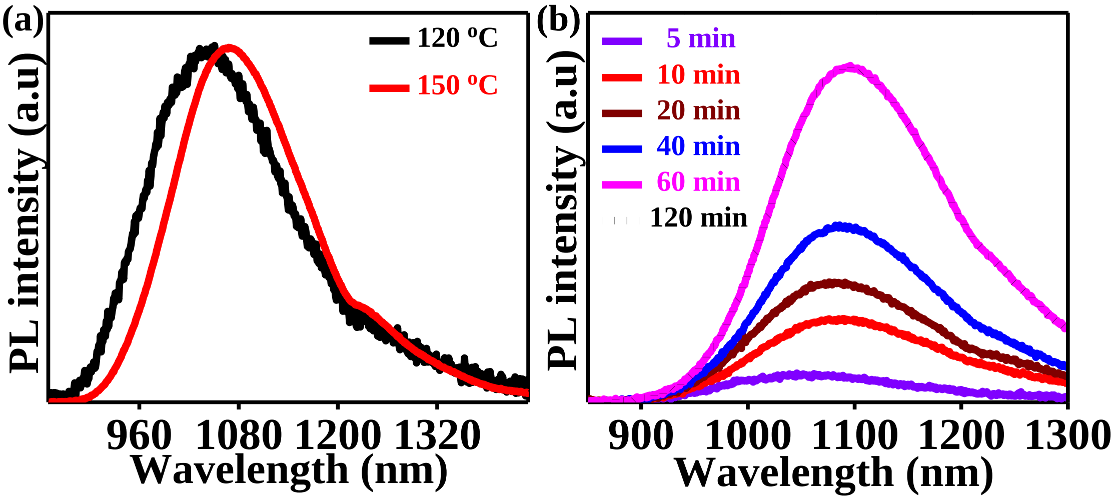

**Figure 2.6:** (a) The reaction of precursor, 3b with Ag(I) at 120 °C (black) and 150 °C (red). (b) $Ag_2S$ NCs synthesized from precursor, 3a at 150 °C exhibiting a temporal evolution of the PL emission peak. The peak saturates after 90 minutes (dotted dark blue).

### 2.3.4. Structure-reactivity relation

Hammett equation-named after Louis Planck Hammett- relates the equilibrium constant $(K)$ or reaction rate constant $(k)$ with the nature of substituent of the benzene ring quantified by so called substituent constant $(\sigma)$ and the reaction constant $(\rho)$:

$$log\frac{k}{k_o} = \sigma\rho \qquad 2.2$$

where, $k_o$ is the reference reaction rate of the unsubstituted reactant and $k$ is the substituent reactant. Hammett substituent parameter $(\sigma)$ considers both the inductive and resonance effects of the substituent and, therefore, it is a useful equation to find the structure-reactivity relationship.[54] In our case, since the formation of $Ag_2S$/Se NCs, takes place *via* a nucleophilic attack on $Ag^+$ by the precursor through the C=S bond the nature of the substituent on the benzene ring is expected to influence the reaction rate or reactivity of the molecule. Table 2.1 lists the values of $\sigma$ for different *para* substituents.

**Table 2.1:** List of reactivity of para substituents with their Hammett substituent parameters.[55]

| ***Para* Substituent** | **Hammett substituent parameter, σ** |
|---|---|
| **OMe** | **-0.268** |
| **Me** | **-0.170** |
| **H** | **0.0** |
| **I** | **+0.276** |
| **$NO_2$** | **+0.770** |

Based on these values, the expected reactivity of the substituted thiourea precursor is as follows:

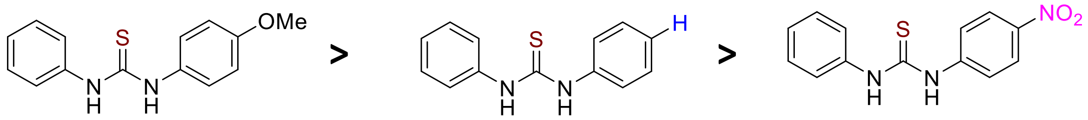

**Figure 2.7:** Reactivity of the substituents (R= O, Me, H, and $NO_2$) at the *para* position of the precursor.

To investigate the influence of thiourea conversion reactivity on final size, $Ag_2S$ NCs were synthesized using thiourea precursors with various substituent groups (Figure 2.8, 3a-e) under the same reaction conditions (15 min, 150 °C). As anticipated the size of the NCs (demonstrated in the PL emission maxima) correlated linearly with the substituent constant ($\sigma$).

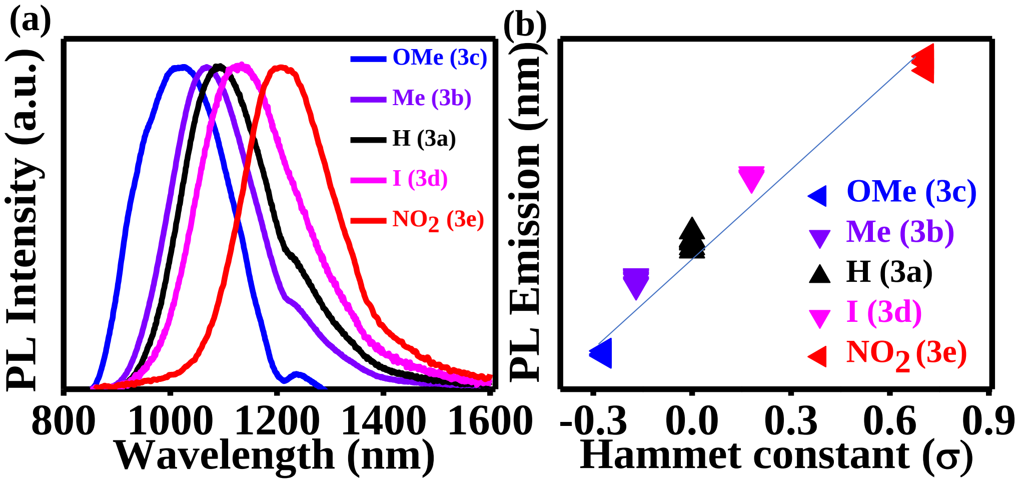

**Figure 2.8: (a)** PL spectra of $Ag_2S$ QDs synthesized from thiourea precursors (3a–e) consisting of different substituents at the para position of the phenyl ring (H, *p*–Me, *p*–OMe, *p*–I, and *p*–$NO_2$) **b)** A linear correlation between the PL emission wavelength ($\lambda_{max}$) and corresponding Hammett constants ($\sigma$) for *para* substituents.

Clearly, the ability of nitrogen to donate its lone pair and subsequent nucleophilic attack on $Ag^+$ by the precursor through the C=S bond (see Scheme 2.2a) is influenced by the strength of electron-donating (+R) or withdrawing groups (-I) at the para position of the phenyl ring (H, *p*–Me, *p*–OMe, *p*–I, and *p*–$NO_2$). Scheme 2.2 shows -R effect of *p*–$NO_2$ (Scheme 2.2a), +I effect of *p*–Me (Scheme 2.2b).

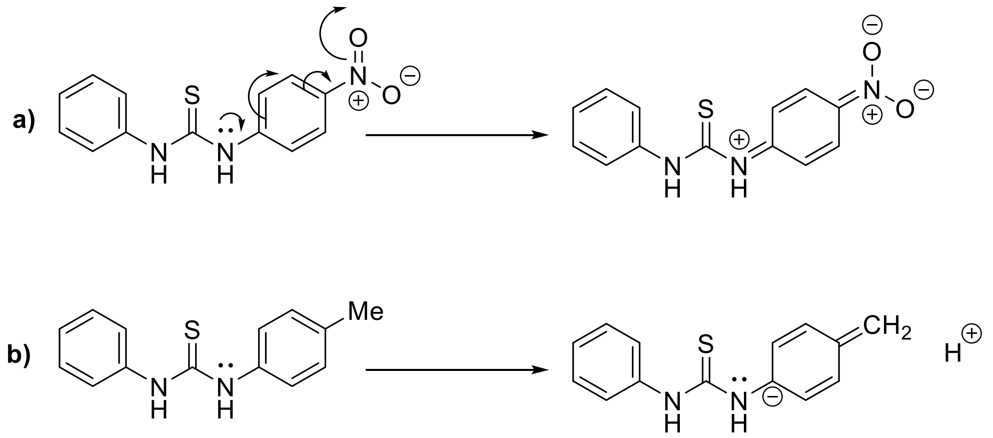

**Scheme 2.2:** (a) Resonance (-R) effect of the nitro group leading to a decrease in the electron density on the nitrogen atom. (b) Hyperconjugation effect of nitro group (+I effect) leading to increase in the electron density on the nitrogen atom.

We used aldehydes (-CHO), nitro group (-$NO_2$), and halogen (X=Cl, Br, I) as electron-withdrawing groups (EWGs) and alcohol groups (-OH), amine groups (-$NH_2$), methoxy (-OMe) and methyl groups (Me) as electron donating groups (EDGs). All the groups are *para* substituents, except for the nitro group where both *para* (3e) and *meta* (3g) substituents were used. EDGs increase the reactivity of the molecule by increasing electron density on nitrogen atom adjacent to the C=S bond and the effect is opposite for the EWGs.[56,57] In our case, the $Ag_2S$ QDs synthesized by the thiourea (3a) with no substituent group in the phenyl ring had a PL emission peak at 1094 nm (Figure 2.8a). The PL emission showed a clear blue shift to 1071 nm when the methyl group was present in the phenyl ring (*p*-Me, precursor 3b). When *p*-OMe is the substituent in the phenyl ring (3c), the smallest sized $Ag_2S$ NCs with PL emission ($\lambda_{max}$) around 1024 nm were formed. On the other hand, the presence of a halogen substituent (3d) led to a redshift of the PL peak ($\lambda_{max}$~1133 nm) indicating decrease in the reactivity of the precursor. In the presence of precursor, 3e carrying *p*-$NO_2$ group, a significant red-shift ($\lambda_{max}$~1209 nm) was observed, suggesting the formation of largest-sized $Ag_2S$ QDs among all the substituent tested. In summary, a substantial and predictable effect of the electronic structure of the precursor on its reactivity (and consequently on the size of the $Ag_2S$ NCs) was observed as the PL emission maxima corresponded linearly with the respective Hammett constants (σ) of the different substituents (3a-e; H, *p*-Me, *p*-OMe, *p*-I, and *p*-$NO_2$) of the thiourea precursor (Figure 2.8 b).[58]

## 2.4. Characterization of precursors and $Ag_2X$ (X=S, Se) NCs

The as-synthesized precursors were characterized by TGA (Figure 2.5) and Nuclear Magnetic Resonance (NMR).

### 2.4.1. $^1H$ and $^{13}C$ NMR

**1,3-Diphenylthiourea (3a).** Aniline (2a, 0.55 g, 5.0 mmol) in toluene (10 mL) was reacted with phenyl isothiocyanate (1, 0.07 g, 5 mmol) in toluene (10 mL) to yield 1,3-diphenyl thiourea (3a) in an 82% yield, following the prevailing method *A*.$^1H$ NMR (400 MHz, DMSO-$d_6$) $\delta$ 9.77 (s, 2H), 7.48 (d, 4H, *J*= 7.6 Hz), 7.32 (t, 4H, *J*=7.6 Hz), 7.11 (t, 2H, *J*=7.4 Hz).$^{13}C$ {$^1H$} NMR (100 MHz, DMSO-$d_6$) 179.6, 139.4, 128.4, 124.3, 123.6.

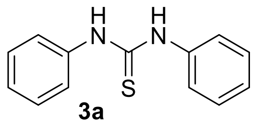

**3a**

**1-Phenyl-3-*p*-tolylthiourea** (**3b).** In accordance with method B, 1-phenyl-3-p-tolylthiourea was synthesized in 80% yield by reacting solutions of p-toluidine (2b, 0.54 g, 5.0 mmol) and phenyl isothiocyanate (1, 0.07 g, 5 mmol) in toluene (10 mL), yielding 3b.$^1H$ NMR (400 MHz, DMSO-$d_6$) δ 9.70 (s, 2H), 7.50 (d, 2H, *J*=7.7 Hz), 7.37–7.30 (m, 4H), 7.15–7.10 (m, 3H), 2.28 (s, 3H). $^{13}C$ {$^1H$} NMR (100 MHz, DMSO-$d_6$) 179.6, 139.5, 136.7, 133.6, 128.3, 124.3, 123.8, 123.6, 20.5.

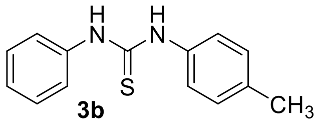

**3b**

**1-(4-Methoxyphenyl)-3-phenylthiourea** (**3c**). According to the general approach (Method *A*), 1-(4-methoxyphenyl)-3-phenylthiourea, was synthesized by reacting 4-methoxyaniline (2c, 0.62 g, 5.0

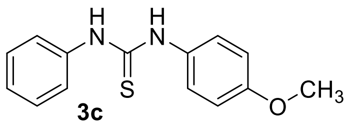

**3c**

mmol) and phenyl isothiocyanate (1, 0.07 g, 5 mmol) in toluene (10 mL) solution. The resulting product, 3c, was obtained in a 91% yield.$^{1}$H NMR (400 MHz, $CDCl_3$) δ 7.75 (s, broad, 2H), 7.39 (d, 4H, *J*=4.2 Hz), 7.29–7.27 (m, 3H), 6.94 (d, 2H, *J*=8.8 Hz), 3.82 (s, 3H). $^{13}$C {$^{1}$H} NMR (100 MHz, $CDCl_3$) 180.7, 159.0, 129.6, 127.7, 127.0, 125.3, 115.0, 55.5.

**1-(4-Iodophenyl)-3-phenylthiourea (3d).** 1-(4-iodophenyl)-3-phenylthiourea was synthesized using the basic approach (Method *A*) which involved the reaction of p-iodoaniline (2d, 1.09 g, 5.0 mmol) in toluene (10 mL) with phenyl isothiocyanate (1, 0.07 g, 5 mmol) in toluene (10 mL). This resulted in the formation of 3d in a yield of 60%.$^{1}$H NMR (400 MHz, DMSO-$d_6$) $\delta$ 9.84 (d, 2H *J*=12.8 Hz), 7.66 (d, 2H, *J*=8.5 Hz), 7.47 (d, 2H, *J*=7.9 Hz), 7.33 (*t*, 4H, *J*= 8.3 Hz), 7.13 (*t*, 1H, *J*=7.3 Hz). $^{13}$C {$^{1}$H} NMR (100 MHz, DMSO-$d_6$) 179.4, 139.3, 139.2, 137.0, 128.4, 125.6, 124.5, 123.6, 88.4.

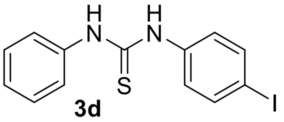

**3d**

**1-(4-Nitrophenyl)-3-phenylthiourea** (**3e**). 1-(4-nitrophenyl)-3-phenylthiourea was synthesized *via* Method *A*, by reacting p-nitroaniline (2e, 0.69 g, 5.0 mmol) in acetonitrile (10 mL) and phenyl isothiocyanate (1, 0.07 g, 5 mmol) in acetonitrile (10 mL) under reflux for 24 hours at 80 °C. The final product, 3e, was obtained in a yield of 41%.$^{1}$H NMR (400 MHz, $CDCl_3$) $\delta$ 8.09 (d, 2H, *J* = 9.0 Hz), 7.39–7.23 (m, 5H), 6.64 (d, 2H, *J*= 9.0 Hz), 4.42 (s, 2H). $^{13}$C {$^{1}$H} NMR (100 MHz, $CDCl_3$) 182.9, 147.6, 130.1, 120.8, 113.4, 109.2, 100.3.

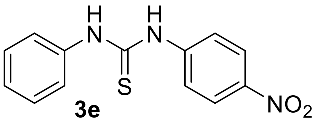

**3e**

**1-(4-Bromophenyl)-3-phenylthiourea** (**3f**). The synthesis of 1-(4-bromophenyl)-3-phenylthiourea was accomplished *via* Method *A*, involving the reaction of p-bromoaniline (2f, 0.86 g, 5.0 mmol) and phenyl isothiocyanate (1, 0.07 g, 5 mmol) in toluene (10 mL) to obtain compound 3f in 65% yield. $^{1}$H NMR (400 MHz, DMSO-$d_6$) $\delta$ 9.79 (d, 2H, *J*=8.3 Hz), 7.47–7.40 (m,

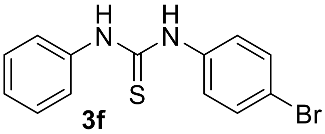

**3f**

4H), 7.33–7.26 (m, 4H), 7.08 (*t*, 1H, *J*=7.3 Hz), $^{13}$C {$^1$H} NMR (100 MHz, DMSO-d$_6$) 182.5, 142.1, 141.3, 131.3, 131.1, 128.1, 127.4, 126.5.

**1-(3-nitrophenyl)-3-phenylthiourea (3g).** 3g of 1-(3-nitrophenyl)-3-phenylthiourea was obtained in 67% yield by reacting solutions of *m*-nitroaniline (2g, 0.67 g, 5.0 mmol) in toluene (10 mL) and phenyl isothiocyanate (1, 0.07 g, 5 mmol) in toluene (10 mL) using Method *A*. $^1$H NMR (400 MHz, DMSO-d$_6$) $\delta$ 10.08 (s, 2H), $\delta$ 8.50 (s, 1H) 7.91–7.85 (m, 2H), 7.55 (*t*, 1H, *J*= 8.2 Hz), 7.42 (*d*, 2H, *J*=7.6Hz), 7.33–7.29 (*m*, 2H), 7.11 (*t*, 1H, *J*=7.3Hz) $^{13}$C{$^1$H} NMR (100 MHz, DMSO-d$_6$) 180.4, 148.1, 141.6, 139.5, 130.1, 129.2, 125.5, 124.5, 119.1, 118.2.

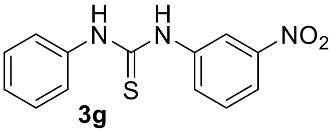

**3g**

**1-(4-Hydroxyphenyl)-3-phenylthiourea**(**3h**)**.**1-(4-hydroxyphenyl)-3-phenylthiourea, 3h was prepared using Method *A* by reacting p-hydroxy aniline (2h, 0.55 g, 5.0 mmol) in acetonitrile (10 mL) with phenyl isothiocyanate (1, 0.07 g, 5 mmol) in acetonitrile (10 mL), yielding 3h in 78% yield.$^1$H NMR (400 MHz, DMSO-d$_6$) $\delta$ 9.49 (d, 2H, *J*= 4.28 Hz), 9.35 (s, 1H), 7.46 (d, 2H, *J*= 8 Hz), 7.30 (*t*, 2H *J*= 7.7 Hz), 7.17 (d, 2H, *J*= 8.6 Hz), 7.10 (t, 1H, *J*= 7.4 Hz), 6.72 (d, 2H, *J*= 8.6 Hz). $^{13}$C {$^1$H} NMR (100 MHz, DMSO-d$_6$) 179.8, 154.8, 139.6, 130.4, 128.2, 126.2, 124.1, 123.6, 114.9.

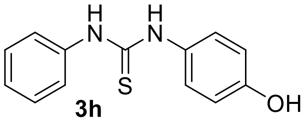

**3h**

**O-Phenylphenylcarbamothioate (5a).** O-phenylcarbamothioate, 5a was obtained in 60% yield by reacting phenol (4a, 0.47 g, 5.0 mmol) and phenyl isothiocyanate (1, 0.07 g, 5 mmol) in acetonitrile (10 mL) using Method *B* of the general procedure. $^1$H NMR (400 MHz, CDCl$_3$) $\delta$ 8.17 (s, broad, 1H), 7.66–7.64 (m, 3H), 7.48–7.46 (m, 3H), 7.38 (t, 2H, *J*=7.16 Hz), 7.28 (t, 1H, *J*=7.92 Hz). $^{13}$C {1H} NMR (100 MHz, CDCl$_3$) $\delta$ 179.6, 138.4, 137.0, 129.9, 128.9, 126.8, 125.4, 123.5, 120.5.

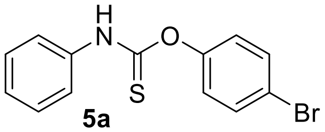

**5a**

***O*-(4-Methoxyphenyl)phenylcarbamothioate (5b).** O-(4-Methoxyphenyl) phenylcarbamodithioate, 5b, was synthesized using Method *B*. A solution of 4-methoxy phenol (4b, 0.70 g, 5.0 mmol) in acetonitrile (10 mL) was reacted with a solution of phenyl isothiocyanate (1, 0.07 g, 5 mmol) in acetonitrile (10 mL), resulting in a 55% yield of the desired product. $^1$H NMR (400 MHz, CDCl$_3$) $\delta$ 8.18 (bs, 1H), 7.58 (d, 2H, *J*=8.2 Hz), 7.46 (d, 2H, *J*=7.9 Hz), 7.34 (t, 2H, *J*=7.4 Hz), 7.26–7.21 (m, 1H), 7.04 (d, 2H, *J* = 8.7 Hz), 3.87 (s, 3H). 13C {1H} NMR (100 MHz, CDCl$_3$) $\delta$ 180.7, 159.0, 129.6, 127.7, 127.0, 125.3, 115.0, 55.7.

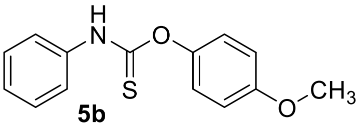

**5b**

***O*-(4-Nitrophenyl) phenylcarbamothioate (5c).** O-(4-Nitrophenyl) phenylcarbamothioate, 5c was synthesized via Method B by reacting p-nitrophenol (4c, 0.69 g, 5.0 mmol) and phenyl isothiocyanate (1, 0.07 g, 5 mmol) in acetonitrile (10 mL) to obtain a 65% yield of the desired compound. $^1$H NMR (400 MHz, CDCl$_3$) $\delta$ 8.22 (bs, 1H), 7.69 (d, 2H, *J*=7.4 Hz), 7.51–7.49 (m, 4H), 7.43 (d, 2H, *J*=6.8 Hz), 7.31(s, 1H). $^{13}$C {$^1$H} NMR (100 MHz, CDCl$_3$) $\delta$ 182.9, 147.6, 130.1, 120.8, 113.4, 109.2, 100.3.

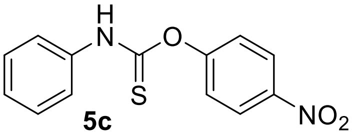

**5c**

**4-Bromophenylphenylcarbamodithioate(7a).**

4-bromophenylphenylcarbamodithioate was synthesized via Method *B*, where a solution of p-bromo benzenethiol (6a, 0.89 g, 5.0 mmol) in acetonitrile (10 mL) was reacted with a solution of phenyl isothiocyanate (1, 0.07 g, 5 mmol) in acetonitrile (10 mL), resulting in a 70% yield of the final product (7a). $^1$H NMR (400 MHz, CDCl$_3$) $\delta$ 8.18 (s, broad, 1H), 7.65 (d, 2H, *J*=7.3 Hz), 7.48–7.40 (m, 4H), 7.38–7.36 (m, 2H), 7.28 (s, 1H). $^{13}$C {1H} NMR (100 MHz, CDCl$_3$) $\delta$ 179.6, 138.4, 137.0, 129.9, 128.9, 126.8, 125.4, 123.5, 120.5.

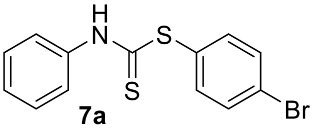

**7a**

**4-Methoxyphenylphenylcarbamodithioate(7b).**

4-methoxyphenylphenylcarbamodithioate was synthesized using Method *B* by reacting

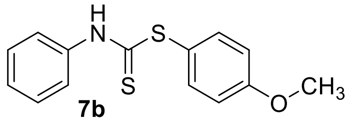
7b

p-methoxy benzenethiol (6b, 0.70 g, 5.0 mmol) and phenyl isothiocyanate (1, 0.07 g, 5 mmol) in acetonitrile (10 mL) to obtain 7b in 50% yield. $^1$H NMR (400 MHz, CDCl$_3$) $\delta$ 8.20 (bs, 1H), 7.61 (d, 2H, *J* = 8.2 Hz), 7.49 (d, 2H, *J*= 8.0 Hz), 7.37 (t, 2H, *J*= 7.9 Hz), 7.28–7.24 (m, 1H), 7.07 (d, 2H, *J* = 8.7 Hz), 3.90 (s, 3H). $^{13}$C {$^1$H} NMR (100 MHz, CDCl$_3$) $\delta$ 180.5, 158.8, 129.4, 127.6, 126.9, 125.1, 115.4, 114.8, 55.5.

**4-Nitrophenylphenylcarbamodithioate (7c).** 4-nitrophenylphenylcarbamodithioate,

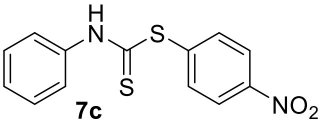
7c

7c was obtained in 65% yield by reacting p-nitro benzenethiol (6c, 0.77 g, 5.0 mmol) and phenyl isothiocyanate (1, 0.07 g, 5 mmol) in acetonitrile (10 mL) according to Method *B*.$^1$H NMR (400 MHz, CDCl$_3$) $\delta$ 8.19 (s, broad, 1H), 7.65 (d, 2H, *J*=7.3 Hz), 7.47–7.45 (m, 4H), 7.39–7.36 (m, 2H), 7.29–7.25 (m, 1H). $^{13}$C {$^1$H} NMR (100 MHz, CDCl$_3$) $\delta$ 179.8, 137.1, 129.5, 127.1, 125.3, 125.1, 99.9.

**1,3-Diphenylselenourea (9a)**. Phenyl isoselenocyanate (8, 3 mmol) and aniline (2a, 3

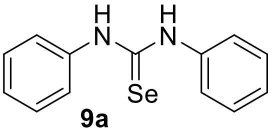
9a

mmol) were reacted using Method *C* to prepare 1,3-diphenylselenourea. The product 9a was obtained in a yield of 91%.$^1$H NMR (400 MHz, DMSO-d$_6$) $\delta$ 10.14 (s, broad, 2H), 7.39–7.31 (m, 4H), 7.29–7.22 (m, 4H), 7.15 (t, 2H, *J*= 6.8 Hz). $^{13}$C {1H} NMR (100 MHz, DMSO-d$_6$) $\delta$ 179.2, 140.3, 129.1, 125.8, 125.2.

**1-(4-Methoxyphenyl)-3-phenylselenourea (9b)**. 1-(4-Methoxyphenyl)-3-

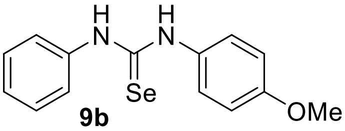
9b

phenylselenourea was synthesized in 93% yield via Method *C* by reacting 4-methoxyaniline (2c, 3 mmol) with phenyl isoselenocyanate (8, 3 mmol) using a general procedure.$^1$H NMR (400

MHz, DMSO-$d_6$) δ 9.96 (d, 2H, *J*=9.2 Hz), 7.37–7.28 (m, 4H), 7.24 (d, 2H, *J*=8.8 Hz ), 7.16–7.14 (m, 1H), 6.88 (d, 2H, *J*= 8.8 Hz ), 3.72 (s, 3H). $^{13}$C {1H} NMR (100 MHz, DMSO-$d_6$) *δ* 179.2, 157.6, 140.3, 129.1, 127.4, 125.7, 125.4, 114.4, 55.8.

### 2.4.2. Optical characterization

Figure 2.4 and 2.8a show the emission spectra of different-sized $Ag_2X$ NCs synthesized using precursors of varying reactivity. The entire NIR-II region (~900-1400 nm) was accessible by reacting Ag(I) with substituted thio/selenourea precursors at 150 $^{o}$C for 15 minutes. Due to the increased reactivity of thiocarbamate compared to thiourea and dithiocarbamate, it produced smaller-sized $Ag_2S$ NCs ($\lambda_{max}$ ~900 nm) (Figure 2.4b). The higher reactivity of thiocarbamate is attributed to the presence of an oxygen atom adjacent to the C=S bond as an electron donating group (EDG) which increases the reactivity of the molecule by increasing electron density on the nitrogen atom adjacent to the C=S bond. The electronegativity order of N, S, and O is O>N>S according to the Mulliken scale, with values of 9.6, 8.4, and 7.2, respectively.[59] As a result, the reactivity order of the precursors is thiocarbamate>thiourea>dithiocarbamate. This order is also evident in the size of the NCs created from these precursors under similar conditions, as seen in Figure 2.4. Additionally, the size of $Ag_2Se$ NCs was affected by the substituents, as demonstrated by the PL spectra in Figure 2.4b. This observation corresponds with the data obtained for $Ag_2S$ NCs. For instance, precursor 9a, which has a para substituent of H, yielded larger-sized NCs compared to precursor 9b, which has a para substituent of -OMe.

**Table 2.2:** PL emission peak and its line-width (FWHM) for the $Ag_2X$ (X=S, Se) NCs synthesized using substituted thiourea, selenourea, thiocarbamate, and dithiocarbamate.

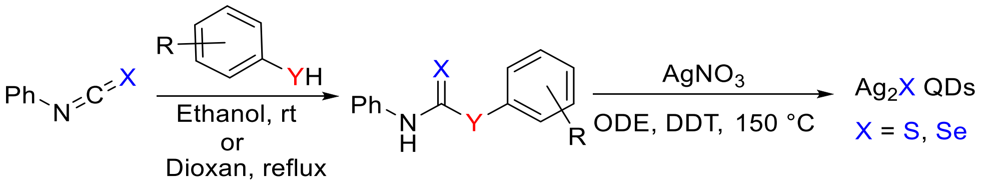

| S. No. | Precursor | Constituents (X Y R) | | | NCs | PL emission (nm) | FWHM |
|---|---|---|---|---|---|---|---|
| 1 | 3a | S | NH | H | $Ag_2S$ | 1094 | 196 |
| 2 | 3b | S | NH | *p*-Me | $Ag_2S$ | 1071 | 221 |
| 3 | 3c | S | NH | *p*-OMe | $Ag_2S$ | 1024 | 229 |
| 4 | 3d | S | NH | *p*-I | $Ag_2S$ | 1133 | 218 |
| 6 | 3e | S | NH | *p*-$NO_2$ | $Ag_2S$ | 1209 | 198 |
| 7 | 3f | S | NH | *p*-Br | $Ag_2S$ | 1049 | 219 |
| 8 | 3g | S | NH | *m*-$NO_2$ | $Ag_2S$ | 1090 | 198 |
| 9 | 3h | S | NH | *p*-OH | $Ag_2S$ | 1053 | 216 |
| 10 | 3i | S | NH | *p*-$C_6H_4$-$NH_2$ | $Ag_2S$ | 1093 | 198 |
| 11 | 5a | S | O | *p*-Br | $Ag_2S$ | 1055 | 215 |
| 12 | 5b | S | O | *p*-OMe | $Ag_2S$ | 909 | 118 |
| 13 | 5c | S | O | *p*-$NO_2$ | $Ag_2S$ | 1144 | 135 |
| 14 | 7a | S | S | *p*-Br | $Ag_2S$ | 1061 | 142 |
| 15 | 7b | S | S | *p*-OMe | $Ag_2S$ | 1088 | 148 |
| 16 | 7c | S | S | *p*-$NO_2$ | $Ag_2S$ | 1163 | 198 |
| 17 | 9a | Se | NH | *p*-H | $Ag_2Se$ | 1251 | 218 |
| 18 | 9b | Se | NH | *p*-OMe | $Ag_2Se$ | 1302 | 256 |

### 2.4.3. Structural Characterization

**Transmission electron microscopy (TEM):** The as-synthesized $Ag_2S$ NCs were purified to remove excess ligands and their size was determined using TEM. For brevity, two different-sized NCs were analyzed viz., one with the lowest ($\lambda_{max}$ ~1024 nm, QD1) and the highest PL emission ($\lambda_{max}$ ~1209 nm, QD2). It is noteworthy that QD1 was prepared using *p*-$NO_2$ substituted thiourea (3e) and QD1 was prepared using *p*-OMe substituted thiourea (3c). From the TEM micrograph, the calculated size of QD1 and QD2 are 2.2 ± 0.52 and 4.2 ± 1.1 nm respectively. Figures 2.9 and 2.10 show the TEM images and corresponding size distribution of QD1 and QD2 $Ag_2S$ NCs. The

HRTEM images further confirmed the monoclinic crystal structure of $Ag_2S$ NCs. The assigned *d*-spacing is for the planes (-121) and (031) of the monoclinic phase[60] SAED patterns for the QD1 and QD2 (Figures 2.9b and 2.10b) are also consistent with monoclinic phase.

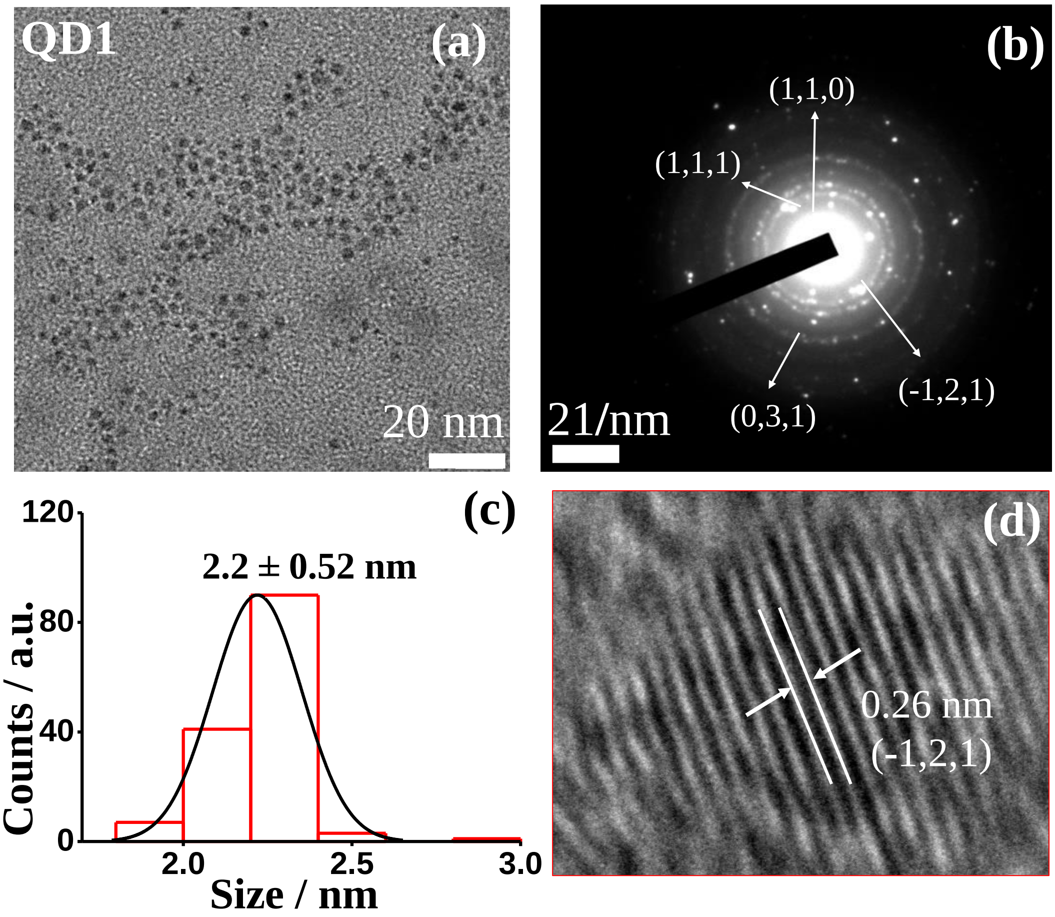

QD1
(a)
20 nm
(b)
(1,1,0)
(1,1,1)
(-1,2,1)
(0,3,1)
21/nm
(c)
2.2 ± 0.52 nm
Counts / a.u.
120
80
40
0
2.0
2.5
3.0
Size / nm
(d)
0.26 nm
(-1,2,1)

**Figure 2.9:** (a) TEM micrograph of 2.2 ± 0.52 nm **QD1** (b) the corresponding SAED pattern (c) the size distribution curve and (d) HRTEM image showing lattice fringes.

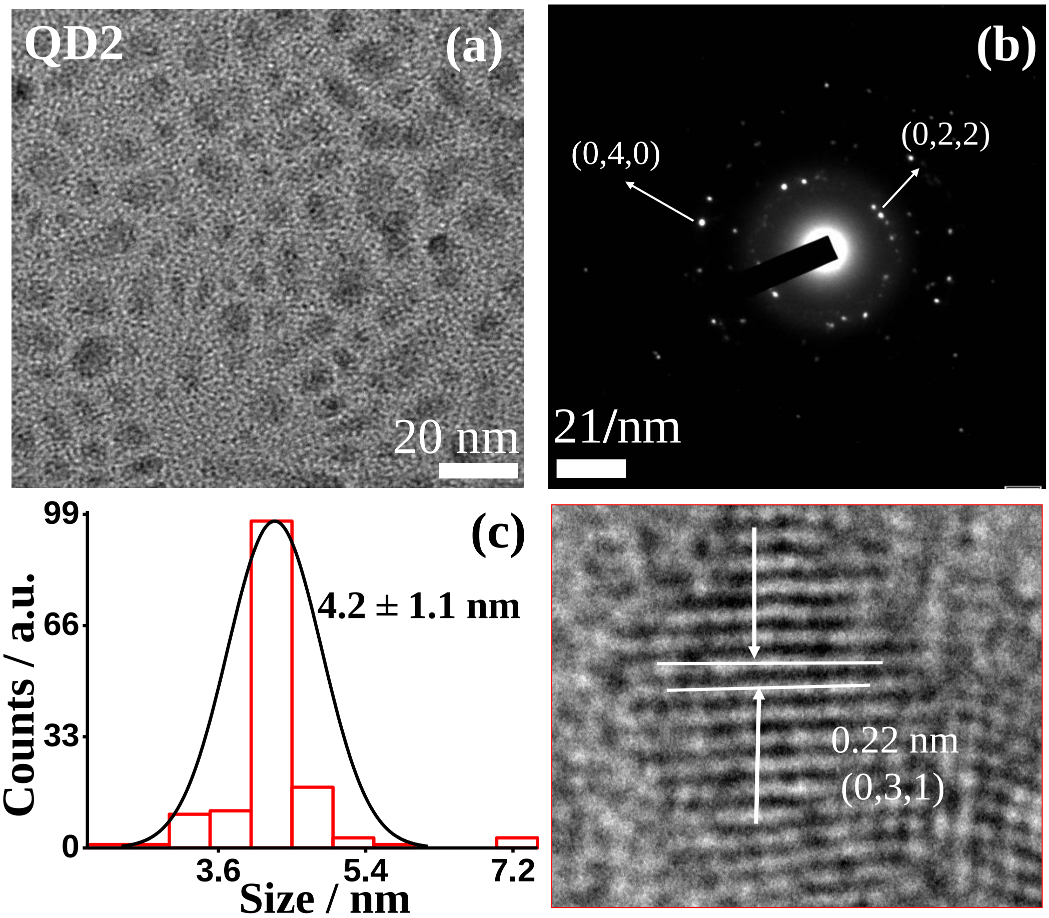

**Figure 2.10:** (a) TEM micrograph of 4.2 ± 1.1 nm **QD2** (b) the corresponding SAED pattern (c) the size distribution curve and (d) HRTEM image showing lattice fringes.

**X-ray diffraction (XRD):** XRD results (Figure 2.11) confirmed the monoclinic $Ag_2S$ (JCPDS 14-0072) [61,62] NCs with space group $P2_1/c$. The measured $2\theta$ values for $Ag_2S$ are 26.3, 28.9, 31.5, 34.3, 36.8, 40.7, 43.4, and 53.2 indexed to the planes (012), (111), (-112), (-121), (121), (200), and (-213) respectively. From the XRD spectra, the broadening of peaks is clearly visible in the smaller-sized NCs (QD2) due to the finite size effect in accordance with the Debye-Scherer equation.

$$D = \frac{K\lambda}{B\cos\theta} \qquad 1.4$$

Where, $D$ is the crystallite size (nm), $K$ is the shape factor and $B$ is the full width at half maximum (fwhm, nm). Typically, its value is taken as 0.9 for spherical NCs,[63] $\lambda$ , is the wavelength of X-ray (Å) and $\theta$ is the Bragg's angle (radian). The calculated crystallite sizes are 2.3 nm and 4.3 nm for QD1 and QD2 respectively. Similarly, the XRD results (Annexure, A2.36) confirmed the orthorhombic ($\beta$-form) $Ag_2Se$ (JCPDS 024-1041)[64] NCs with space group *P2221*. After annealing at 180 °C for 1 hour, the diffraction peaks in the XRD spectra became more prominent (Annexure, 2.36b).

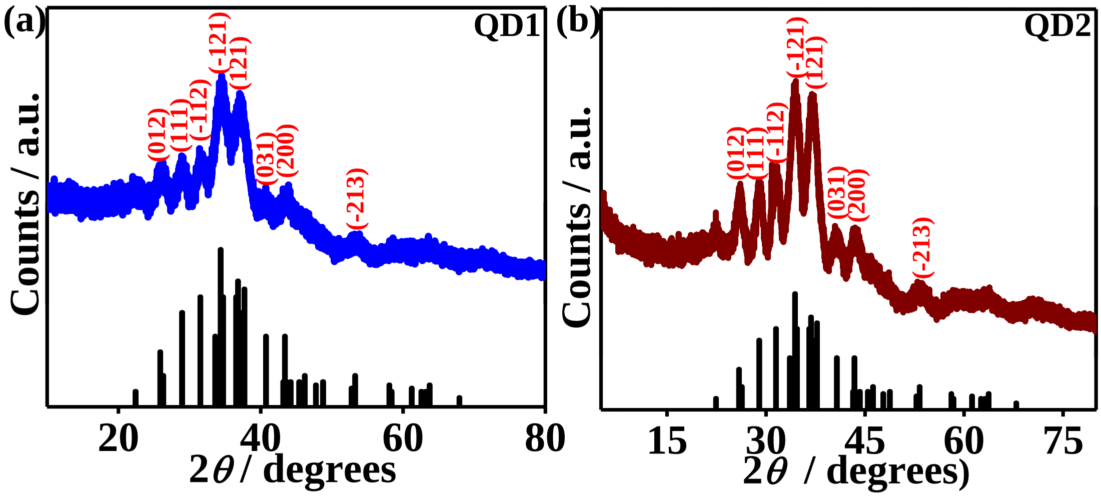

**Fig 2.11:** XRD spectra of monoclinic a) **QD1** and b) **QD2**. The bars indicate the positions of standard monoclinic $Ag_2S$; JCPDS 00-014-0072).[62]

### 2.4.4. Surface Analyses

Due to the high surface-to-volume ratio in these NCs, the nature of surface impacts functionality,[43,65,66] reactivity,[67–69] crystal structure, phase stability,[70–73], and even hydrodynamic diameter.[74–76] It is, therefore, important to study the surface of the NCs. In our case, the surface was investigated using Fourier transform infrared spectroscopy (FTIR) and X-ray photoelectron spectroscopy (XPS).

**FTIR:** The characteristic asymmetric and symmetric C-H stretching peaks of pure DDT are 2922 $cm^{-1}$ and 2851 $cm^{-1}$ respectively (Figure 2.12). FTIR analysis of purified $Ag_2S$ NCs confirmed the presence of surface-bound DDT. The characteristic asymmetric and symmetric C-H stretching peaks are observed at 2916 $cm^{-1}$ and 2847

$cm^{-1}$ respectively. A slight shift of frequencies towards lower values is due to the binding of thiol group on to the $Ag_2S$ NCs surface.[77]

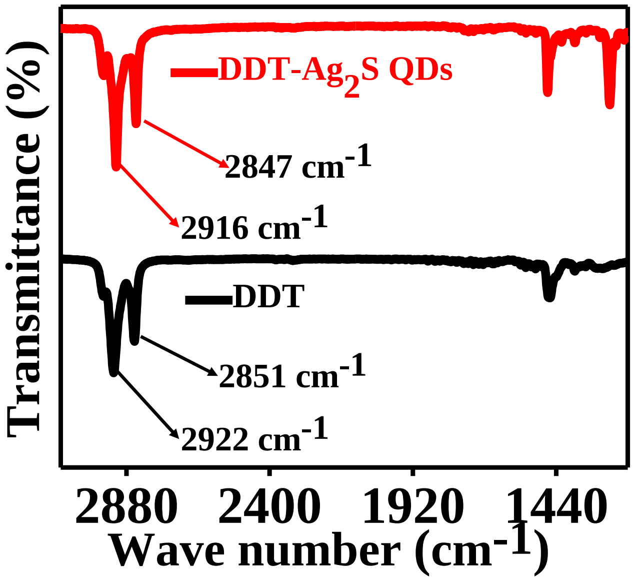

**Figure 2.12:** FTIR Spectra $Ag_2S$ NCs.

**XPS:** The existence of two noticeable peaks at 368.9 eV and 374.9 eV in the Ag 3d core-level spectra of $Ag_2S$ NCs (Figure 2.13c) are attributed to Ag $3d_{5/2}$ and $3d_{3/2}$, respectively, in accordance with the literature report.[78,79] The spectra are calibrated with respect to C 1S (284.8 eV). From the survey graph, the calculated Ag:S ratio is 1:1.6. The observed atomic ratio (S/Ag), which is on the higher side (~1.6) compared to the theoretical value (~0.5) is attributed to the presence of DDT on the surface, which is also consistent with FTIR data. Similar observations are reported in the literature for $Ag_2S$ NCs capped with DDT prepared under different condition.[79]

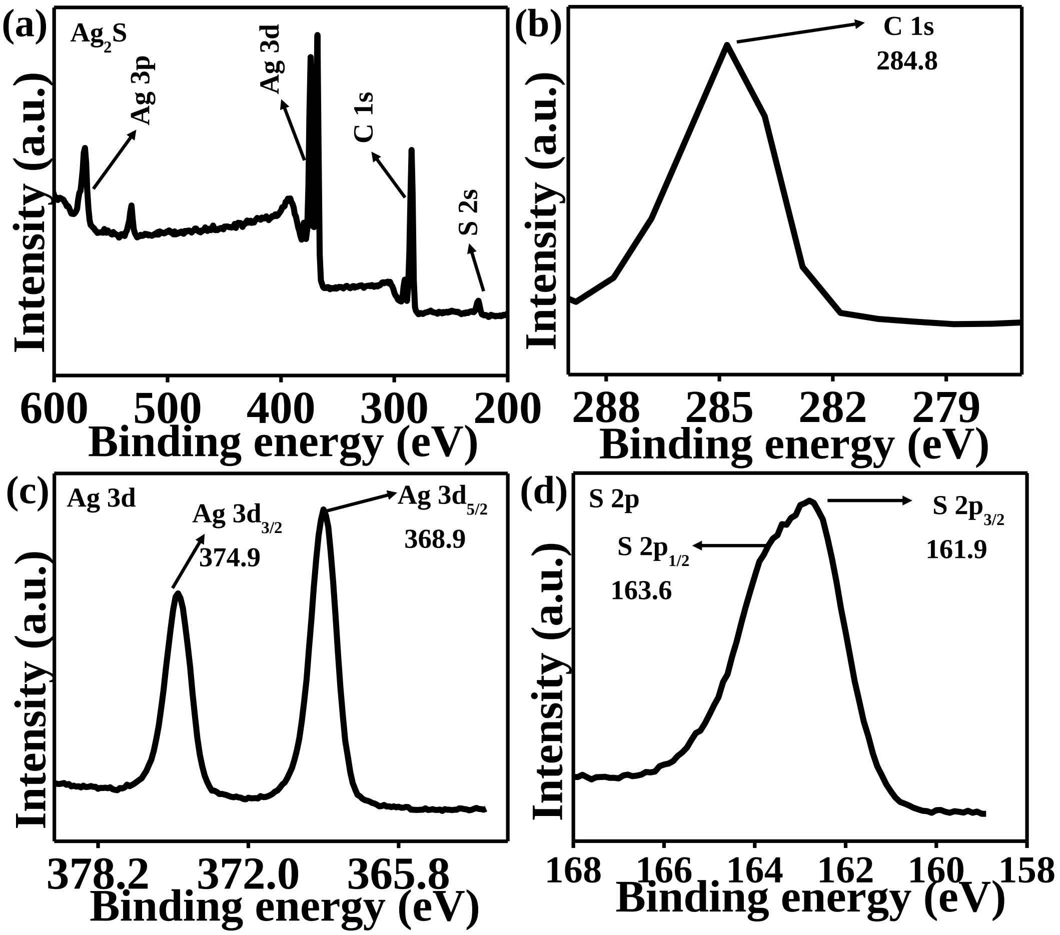

**Figure 2.13:** XPS spectra of $Ag_2S$ NCs are presented in the figure, showing: (a) the survey scan; (b) the C 1s spectrum which was calibrated at 284.8 eV; (c) the Ag 3d core level spectrum; and (d) the S 2p binding energy spectrum.

Upon deconvolution of the S 2p peak, we observed two distinct components assigned to S-H (162.9 and 164.1 eV), and S-Ag (161.3 and 162.5 eV) peaks based on the literature report.[79] In addition to the S-Ag peak, the existence of S-H binding energies also explains the presence of surface bound DDT.

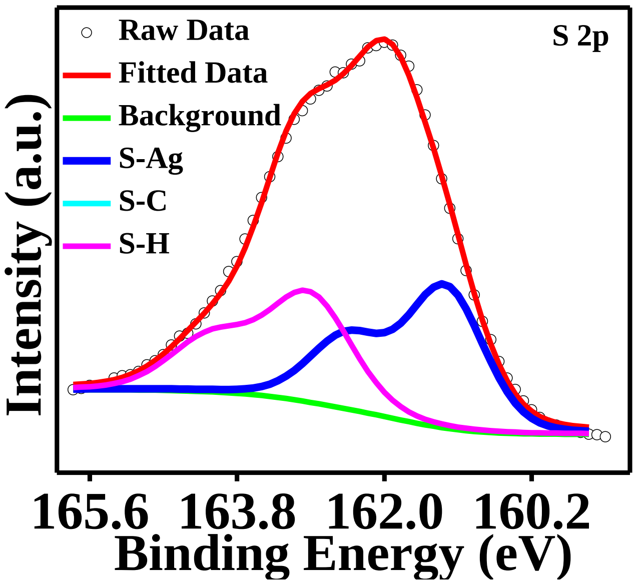

**Figure 2.14:** The S 2p core-level XPS spectrum of deconvoluted $Ag_2S$ NCs shows two distinct chemical environments. The first corresponds to S-Ag, which represents the $Ag_2S$ NCs, and the second corresponds to S-H, which represents the ligand.

The surface of the $Ag_2Se$ NCs was further analyzed using XPS. As shown in the Figure 2.15, two distinct peaks at 368.9 eV and 374.9 eV were assigned to Ag $3d_{5/2}$ and Ag $3d_{3/2}$ respectively. The peak at around 54.8 eV corresponds to Se 3d of $Ag_2Se$ NCs.[80–82] The presence of surface-bound thiol is confirmed by the S 2p peak cantered at 163.7 eV. The Ag: Se ratio on the surface is 1.93:1, which is close to the theoretical value (~2:1).

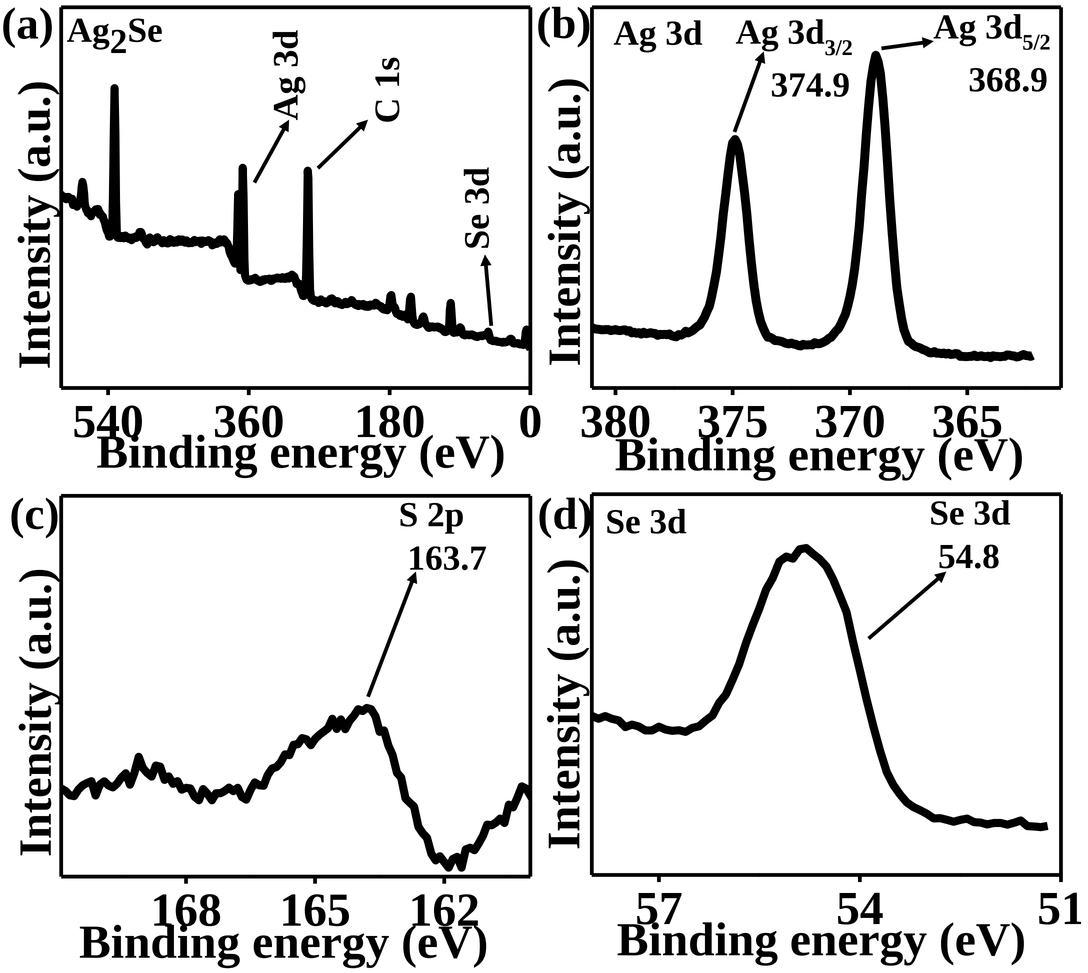

**Figure 2.15:** XPS spectra of $Ag_2Se$ NCs: (a) the survey analysis; (b) 3d Ag; (c) S 2p and (d) Se 3d spectra.

## 2.5. Conclusion

In this chapter, we discussed the preparation of a library of different substituted thiourea, thiocarbamate, dithiocarbamate, and selenourea precursors by reacting isothiocyanate/isoselenocyanate with commercially available phenols, thiophenols or aryl amines. We developed a novel method for the synthesis of silver chalcogenide, $Ag_2X$ (X=S, Se) NCs using these substituted thioureas, thiocarbamate, dithiocarbamate, and selenourea. This method allows for size-tunable synthesis of $Ag_2X$ (X=S, Se) NCs emitting in the entire NIR-II region ~(900-1300 nm). The sole function of 1-DDT in the reaction is the solubilization and stabilization of the NCs as confirmed by FTIR and a few controlled experiments. A detailed investigation was carried out to understand the role of the reactivity of the substituted precursor (H, *p*–Me, *p*–OMe, *p*–I, and *p*–$NO_2$) on the size of the NCs. A linear structure-reactivity relationship was established by plotting the Hammette substituent constant and the PL emission (~size) of the NCs. Larger-sized $Ag_2S$ NCs (QD2) is formed when the substituent R is an EWG such as *p*–OMe. On the other hand, the presence of EDG such as *p*–$NO_2$ led to the formation of smaller-sized NCs (QD1). As a representative case, two different-sized NCs namely, QD1 and QD2 were thoroughly characterized using UV-Vis spectroscopy, PL spectrofluorometer, TEM, XPS, XRD, and FTIR were used to establish the crystal structure, surface chemistry, and optical properties. The overview of the synthetic conditions and properties of QD1 and QD2 are outlined in Table 2.3.

**Table 2.3:** Summary of the synthetic conditions and properties of QD1 and QD2

| **NCs ( $Ag_2S$)** | **QD1** | **QD2** |
|---|---|---|
| Synthetic conditions | Temperature, 150°C<br>Time, 15 minutes<br>R = *p*-OMe | Temperature, 150°C<br>Time, 15 minutes<br>R = *p*-$NO_2$ |
| Absorption ($\lambda_{abs}$) | 4.2 ± 1.1 | 1209 |
| Emission ($\lambda_{em}$) | 1024 nm | 1209 nm |
| FWHM | 229 | 196 |
| Quantum Yield (QY) | 6.9 % | 6.2% |
| Particle size (TEM) | (2.2 ± 0.52) nm | (4.2 ± 1.1) nm |
| Crystallite size (XRD) | 2.3 nm | 4.3 nm |
| Crystal Structure | monoclinic | monoclinic |

## 2.6. Experimental section

### 2.6.1. Materials

For the synthesis of NIR-II $Ag_2X$ (X=S, Se) NCs, the following listed chemicals were used.

| **Chemical** | **Purity** | **Supplier** |
|---|---|---|
| Toluene | 95% | Sigma Aldrich |
| Dimethoxy ethane | ≥99% | Sigma Aldrich |
| Diglyme | ≥99% | Sigma Aldrich |
| Tetramethylammonium hydroxide (TMAH) | ≥99% | Sigma Aldrich |
| Tetrachloroethylene | ≥99% | Sigma Aldrich |
| 1-Octadecene | 90% | Sigma Aldrich |
| Triethylamine | ≥99% | Sigma Aldrich |
| Octylamine | 99% | Sigma Aldrich |
| Oleyl amine | 70% | Sigma Aldrich |
| Phenyl isothiocyanate | 98% | Sigma Aldrich |
| Silver nitrate | 99% | Thomas Baker |
| Aniline | 99% | TCI |
| N,N′-Dicyclohexylcarbodiimide (DCC) | 99% | TCI |
| DOTA-GA (t-Bu)4 | 99% | TCI |
| Amino-thiophenol | ≥99% | TCI |
| Trifluoroacetic acid (TFA) | ≥99% | TCI |
| 4-Dimethylamino pyridine (DMAP) | ≥99% | TCI |
| Selenium powder | ≥98% | TCI |
| 1-Dodecanethiol (DDT) | ≥98% | TCI |
| 1-Octane thiol | ≥98% | TCI |
| Cadmium chloride | ≥98% | Thomas Baker |

The purification process was not performed before using these. Additionally, deuterated solvents were purchased from Sigma Aldrich. The progression of the chemical reactions was monitored in analytical thin layer chromatography (TLC) using plates coated with silica gel 60 F254, with the use of a UV lamp or $I_2$ stain.

### 2.6.2. Characterization techniques

**NMR:** The Bruker ASCENDTM (400 MHz) spectrometer was used to record the $^1H$ NMR, $^{13}C$ NMR, with either $CDCl_3$ or $D_2O$, or DMSO-$d_6$ as the solvent. The multiplicities were indicated as *s* for singlet, *d* for doublet, *t* for triplet, *q* for quartet, and m for multiplet. The solid samples were tested for their solubility in the desired solvents and mixed in a glass vial. Using a glass Pasteur pipette, the sample was transferred to the NMR tube. The NMR tube was then labeled and scanned in the NMR instrument.

**TGA:** The TA Instruments TGA Q50 Analyzer was used to obtain the TGA data. During the analysis, the instrument was subjected to a controlled temperature increase at a rate of 20 degrees per minute until it reached a final temperature of 600 °C. Inside the heating furnace, the flow of $N_2$ gas was kept at 60 mL per min, and inside the balance chamber, it was kept at 40 mL per min. Two platinum pans were utilized, where one was utilized as a reference point while the other was used to place the solid sample. The TGA instruments were immediately operated on the solid samples that were placed on the sample pan.

**UV-Vis spectrophotometer:** To obtain the UV-visible absorption spectra, the PerkinElmer spectrophotometer with a scan rate of 480 nm/s and Agilent Technologies Cary 100 UV-vis were employed. For these measurements, the sample was dissolved in either anhydrous hexane or anhydrous tetrachloroethylene (TCE).

**Vis-NIR spectrofluorometer:** The PL spectra of $Ag_2X$ (X=S, Se) NCs were obtained using the HORIBA Scientific spectrophotometer (Model: PTI-QM 510). The NCs were distributed in either hexane or TCE and the solution.

**TEM:** In order to obtain TEM images, the JEOL-JEM-2100 Plus electron microscope was used. HRTEM images were captured using a 200 kV electron source. To prepare the samples, a nanocrystal solution in hexane was drop-casted onto a carbon-coated surface. The copper grids, which were purchased from EMS, were stored in a vacuum desiccator overnight. The average particle size was determined using 400 particles. The lattice fringes were used to obtain the lattice plane and calculations were performed using the Image J program.

**FTIR:** The FT-IR spectra were obtained using the Bruker ALPHA E, 200396 instrument. Liquid samples are immediately dropped onto the surface of the instruments, and the spectrum was obtained. For solid samples, they were first ground in a mortar along with anhydrous potassium bromide (KBr). Then, a piece of paper was taken and a hole was cut out of it. The grounded sample was then poured into this hole, and a pallet was made using a hydraulic press. The resulting sample was inserted into the IR sample holder, attached with scotch tape, and then analyzed by running the spectrum.

**XRD:** The $Ag_2X$ (X=S, Se) NCs, which had undergone purification, were dissolved in hexane and deposited on a clean and dry glass slide using a drop-casting technique. The resulting film on the glass slide was then analyzed using the PANalytical X-Ray diffractometer, where Cu Kα ($\lambda$=1.54 Å) as the incident radiation (40 kV and 30 mA).

**XPS:** XPS samples were created on carbon-coated silicon wafers within a glovebox to prevent charging. The Thermo-Scientific ESCALAB Xi+ spectrometer, which utilized an Al Kα (1486.7 eV) X-ray source, was used to obtain XPS spectra. Constant analyzer energy (CAE) of 50 eV was used for high-resolution spectra, and a CAE of 100 eV was used for survey spectra. The XPS peaks were analyzed using XPS peak 4.1 software with the Gaussian-Lorentzian (SGL) function and a fixed ratio of 80:20 for peak deconvolution. The background of the spectrum was corrected using the Shirley method. The S 2p peak was separated into S $2p_{3/2}$ and S $2p_{1/2}$ peaks, exhibiting a spin-orbit splitting of approximately 1.2 eV with a full width at half maximum (FWHM) of 1-1.2. The CASA XPS software was employed to determine the elemental composition, and the relative sensitivity factors were corrected to calculate the atomic percentage (%).

### 2.6.3. Synthesis of precursors and $Ag_2S$ NCs

**Substituted thiourea synthesis (*Method A*):** The synthesis method used was based on previously published research, but with some minor adjustments. [35] A typical synthesis involved mixing a solution of phenyl isothiocyanate (5.0 mmol) in toluene with a solution of aniline 5.0 mmol in 10 mL toluene 10 mL. The resulting mixture was stirred for a specified duration, after which the precipitate was thoroughly dried under vacuum to remove toluene. This resulted in extremely good yields of the required precursor.

**Thiocarbamate and dithiocarbamate substitutes (*Method B*)**: The thiocarbamate and dithiocarbamate derivatives were prepared with some slight modifications to a previous study.[83] A solution of 5.0 mmol thiol or phenols in 10 mL acetonitrile was mixed with phenyl isothiocyanate (5.0 mmol) in acetonitrile. Triethylamine (5.0 mmol) was added to the mixture, and the reaction was stirred for 24 hours at 75 °C in an inert atmosphere. The solvents were then removed under vacuum in a rotating evaporator before adding n-hexane. The produced precipitates (thiocarbamate or dithiocarbamate) were filtered using a Buchner funnel and washed twice or thrice with n-hexane. The desired product (precursor) was dried in a desiccator before using it in an experiment.

**Selenourea synthesis (*Method C*):** The preparation of phenyl isoselenocyanate was carried out according to a previously published method. .[84] In summary, an ethanol solution of aromatic amine, 3 mmol was added to a chloroform solution of phenyl isoselenocyanate (3 mL) (EtOH, 2.5 mL). The reaction was exothermic and allowed to cool to room temperature. To complete the reaction, the mixture was further stirred under reflux conditions for 5-10 minutes. After cooling, a crystalline precipitate was formed, which was filtered and dried under vacuum.

**Synthesis of silver sulfide ($Ag_2S$) NCs:** To prepare the sulfur precursor, 0.2 mmol of it was dissolved in 1 mL of dimethoxymethane and left to degas for 30 minutes at room temperature in a double-necked round bottom flask (A) under a nitrogen environment for another 30 minutes. Meanwhile, in another 50 mL three-necked round bottom flask (B), a combination of silver nitrate (0.034 g, 0.2 mmol), 1-octadecene (3.5 mL), and 1-dodecanethiol (DDT) was vacuumed for 30 minutes at ambient temperature and then for 15 minutes at 120 °C to obtain a pale-yellow solution. The temperature of the reaction mixture was then raised to 150 °C while maintaining a nitrogen environment. Depending on the substituents in the *p*-position to the precursors, the reaction mixture was allowed to turn black from red quickly after injecting the cold precursor solution of flask A into the hot solution of flask B. The reaction mixture was then rapidly cooled in an ice bath.

**Synthesis of silver selenide ($Ag_2Se$) NCs:** The substituted selenourea precursor (0.2 mmol) was dissolved in dimethoxymethane (1 mL) and degassed for 30 minutes at room temperature in a double-necked round bottom flask (A). The reaction was maintained in a nitrogen environment for an additional 30 minutes. In a second 50 mL three-necked round bottom flask (B), a light-yellow solution was obtained by degassing a combination of silver nitrate (0.034 g, 0.2 mmol), 1-octadecene (3.5 mL), and 1-dodecanethiol (0.5 mL) under vacuum for 30 minutes at ambient temperature and 15 minutes at 120 °C. The temperature of this reaction mixture was then increased to 150 °C in a nitrogen environment. Depending on the precursor's nature, the cold precursor solution from flask A was rapidly injected into the heated solution in flask B, and the reaction mixture was kept until it turned black from red. The reaction mixture was promptly cooled in an ice bath after the desired reaction was achieved.

**NCs purification:** The QDs were initially mixed with 4 mL of ethanol/methanol and 1 mL of hexane. After being centrifuged twice at 6000 rpm for 15 minutes, the supernatant was discarded, and the precipitate was mixed with 3 mL of ethanol/methanol, 1 mL of hexane, and 1 mL of toluene. This mixture was then centrifuged twice at 6000 rpm for 5 minutes. The resulting QDs were dispersed in 0.5 mL of toluene and centrifuged for 2 minutes at 6000 rpm. Finally, the QDs were dispersed in 1 mL of hexane/TCE and centrifuged once at 3000 rpm for further purification.

**Synthesis of CdS NCs:** Substituted thiourea precursor, specifically 1-(4-methoxyphenyl)-3-phenylthiourea (3c) with a quantity of 0.2 millimoles, was mixed with dimethoxy ethane (1 millilitre) and left to remove any gases for 30 minutes at room temperature in a flask with two necks labeled flask A. It was then kept under a nitrogen gas environment for an additional 30 minutes. In a different flask labeled flask B with three necks and a capacity of 50 millilitres, a mixture of cadmium chloride (0.028 grams or 0.2 millimoles), 1-octadecene (3.5 millilitres), and oleic acid (1 millilitre) was used. These components were degassed by vacuum at room temperature for 30 minutes, then further degassed at 120°C for 15 minutes while being kept in a nitrogen atmosphere. The reaction mixture in flask B was quickly cooled in an ice bath after the cold precursor solution of flask A was added rapidly to the heated solution of flask B. In order to compare the UV-vis absorbance of the cadmium sulfide (CdS) nanocrystals (NCs) made from 3c, another thiourea precursor, 1-(4-nitrophenyl)-3-phenylthiourea (3e), was used to make CdS NCs.

## 2.6.References

(1) Zebibula, A.; Alifu, N.; Xia, L.; Sun, C.; Yu, X.; Xue, D.; Liu, L.; Li, G.; Qian, J. Ultra-stable and Biocompatible NIR-II Quantum Dots for Functional Bioimaging. *Advanced Functional Materials.* **2018**, *28*, 1703451-1703465.

(2) Hong, G.; Robinson, J. T.; Zhang, Y.; Diao, S.; Antaris, A. L.; Wang, Q.; Dai, H. In Vivo Fluorescence Imaging with $Ag_2S$ Quantum Dots in the Second Near-Infrared Region. *Angewandte Chemie International Edition.* **2012**, *51*, 9818-9821.

(3) Zhang, Y.; Hong, G.; Zhang, Y.; Chen, G.; Li, F.; Dai, H.; Wang, Q. $Ag_2S$ Quantum Dot: A Bright and Biocompatible Fluorescent Nanoprobe in the Second Near-Infrared Window. *ACS Nano.* **2012**, *6* , 3695-3702.

(4) Gu, Y.-P.; Cui, R.; Zhang, Z.-L.; Xie, Z.-X.; Pang, D.-W. Ultrasmall Near-Infrared $Ag_2Se$ Quantum Dots with Tunable Fluorescence for in Vivo Imaging. *J Am Chem Soc* .**2012**, *134* , 79-82.

(5) Lim, Y. T.; Kim, S.; Nakayama, A.; Stott, N. E.; Bawendi, M. G.; Frangioni, J. v. Selection of Quantum Dot Wavelengths for Biomedical Assays and Imaging. *Molecular Imaging.* **2003**, *2* , 50-64.

(6) Hong, G.; Lee, J. C.; Robinson, J. T.; Raaz, U.; Xie, L.; Huang, N. F.; Cooke, J. P.; Dai, H. Multifunctional in Vivo Vascular Imaging Using Near-Infrared II Fluorescence. *Nature Medicine.* **2012**, *18* , 1841–1846.

(7) Welsher, K.; Sherlock, S. P.; Dai, H. Deep-Tissue Anatomical Imaging of Mice Using Carbon Nanotube Fluorophores in the Second near-Infrared Window. Proceedings of the National Academy of Sciences. **2011**, *108*, 8943-8948

(8) Resch-Genger, U.; Grabolle, M.; Cavaliere-Jaricot, S.; Nitschke, R.; Nann, T. Quantum Dots versus Organic Dyes as Fluorescent Labels. *Nature Methods*. **2008**, *5*, 763–775.

(9) Chan, W. C. W.; Maxwell, D. J.; Gao, X.; Bailey, R. E.; Han, M.; Nie, S. Luminescent Quantum Dots for Multiplexed Biological Detection and Imaging. *Current Opinion in Biotechnology*. **2002**, *13*, 40–46.

(10) Smith, A. M.; Mancini, M. C.; Nie, S. Bioimaging: Second Window for in Vivo Imaging. *Nature Nanotechnology*. Nature Publishing Group **2009**, *4*, 710–711.

(11) Haghighatzadeh, A.; Kiani, M.; Mazinani, B.; Dutta, J. Facile Synthesis of ZnS–$Ag_2S$ Core–Shell Nanospheres with Enhanced Nonlinear Refraction. *Journal of Materials Science: Materials in Electronics.* **2020**, *31*, 1283–1292.

(12) Jiang, P.; Zhu, C.-N.; Zhang, Z.-L.; Tian, Z.-Q.; Pang, D.-W. Water-Soluble $Ag_2S$ Quantum Dots for near-Infrared Fluorescence Imaging in Vivo. *Biomaterials.* **2012**, *33*, 5130-5135.

(13) Chen, G.; Tian, F.; Zhang, Y.; Zhang, Y.; Li, C.; Wang, Q. Tracking of Transplanted Human Mesenchymal Stem Cells in Living Mice Using Near-Infrared $Ag_2S$ Quantum Dots. *Advanced Functional Materials.* **2014**, *24*, 2481–2488.

(14) Gu, Y. P.; Cui, R.; Zhang, Z. L.; Xie, Z. X.; Pang, D. W. Ultrasmall Near-Infrared $Ag_2Se$ Quantum Dots with Tunable Fluorescence for in Vivo Imaging. *J Am Chem Soc* .**2012**, *134* , 79–82.

(15) Sotiriou, G. A.; Meyer, A.; Knijnenburg, J. T. N.; Panke, S.; Pratsinis, S. E. Quantifying the Origin of Released $Ag^+$ Ions from Nanosilver. *Langmuir.* **2012**, *28*, 15929–15936.

(16) He, D.; Garg, S.; Wang, Z.; Li, L.; Rong, H.; Ma, X.; Li, G.; An, T.; Waite, T. D. Silver Sulfide Nanoparticles in Aqueous Environments: Formation, Transformation and Toxicity. *Environmental Science: Nano*. Royal Society of Chemistry. **2019**, *6* , 1674–1687.

(17) Gui, R.; Sun, J.; Liu, D.; Wang, Y.; Jin, H. Retracted Article: A Facile Cation Exchange-Based Aqueous Synthesis of Highly Stable and Biocompatible $Ag_2S$ Quantum Dots Emitting in the Second near-Infrared Biological Window. *Dalton Transactions*. **2014**, *43* , 16690-16697.

(18) Ren, Q.; Ma, Y.; Zhang, S.; Ga, L.; Ai, J. One-Step Synthesis of Water-Soluble Silver Sulfide Quantum Dots and Their Application to Bioimaging. *ACS Omega*. **2021**, *6* , 6361-6367.

(19) Argueta-Figueroa, L.; Martínez-Alvarez, O.; Santos-Cruz, J.; Garcia-Contreras, R.; Acosta-Torres, L. S.; de la Fuente-Hernández, J.; Arenas-Arrocena, M. C. Nanomaterials Made of Non-Toxic Metallic Sulfides: A Systematic Review of Their Potential Biomedical Applications. *Materials Science and Engineering: C.* **2017**, *76*, 1305–1315.

(20) Ge, X.-L.; Huang, B.; Zhang, Z.-L.; Liu, X.; He, M.; Yu, Z.; Hu, B.; Cui, R.; Liang, X.-J.; Pang, D.-W. Glucose-Functionalized near-Infrared $Ag_2Se$ Quantum Dots with Renal Excretion Ability for Long-Term in Vivo Tumor Imaging. *Journal of Materials Chemistry B.* **2019**, 7, 5782-5788.

(21) Rosenthal, S. J.; Chang, J. C.; Kovtun, O.; McBride, J. R.; Tomlinson, I. D. Biocompatible Quantum Dots for Biological Applications. *Chemistry & Biology*. **2011**, *18* , 10-24.

(22) Amor-Gutiérrez, O.; Iglesias-Mayor, A.; Llano-Suárez, P.; Costa-Fernández, J. M.; Soldado, A.; Podadera, A.; Parra, F.; Costa-García, A.; de la Escosura-Muñiz, A. Electrochemical Quantification of $Ag_2S$ Quantum Dots: Evaluation of Different Surface Coating Ligands for Bacteria Determination. *Microchimica Acta.* **2020**, *187* , 24-28.

(23) Yarema, M.; Pichler, S.; Sytnyk, M.; Seyrkammer, R.; Lechner, R. T.; Fritz-Popovski, G.; Jarzab, D.; Szendrei, K.; Resel, R.; Korovyanko, O.; Loi, M. A.; Paris, O.; Hesser, G.; Heiss, W. Infrared Emitting and Photoconducting Colloidal Silver Chalcogenide Nanocrystal Quantum Dots from a Silylamide-Promoted Synthesis. *ACS Nano.* **2011**, *5* , 3758-3765.

(24) Hocaoglu, I.; Çizmeciyan, M. N.; Erdem, R.; Ozen, C.; Kurt, A.; Sennaroglu, A.; Acar, H. Y. Development of Highly Luminescent and Cytocompatible Near-IR-Emitting Aqueous $Ag_2S$ Quantum Dots. *Journal of Materials Chemistry.* **2012**, *22*, 14674–14681.

(25) Zhang, Y.; Liu, Y.; Li, C.; Chen, X.; Wang, Q. Controlled Synthesis of $Ag_2S$ Quantum Dots and Experimental Determination of the Exciton Bohr Radius. *Journal of Physical Chemistry C*. **2014**, *118*, 4918–4923.

(26) Hocaoglu, I.; Demir, F.; Birer, O.; Kiraz, A.; Sevrin, C.; Grandfils, C.; Yagci Acar, H. Emission Tunable, Cyto/Hemocompatible, near-IR-Emitting $Ag_2S$ Quantum Dots by Aqueous Decomposition of DMSA. *Nanoscale.* **2014**, *6* , 11921–11931.

(27) Sahu, A.Facile Synthesis of Silver Chalcogenide ($Ag_2E$; E = Se, S, Te) Semiconductor Nanocrystals. *J Am Chem Soc.* **2011**, *133*, 6509–6512.

(28) Gommes, C. J. Ostwald Ripening of Confined Nanoparticles: Chemomechanical Coupling in Nanopores. *Nanoscale* **2019**, *11* , 7386–7393.

(29) Tiwari, A.; Dhoble, S. J. Synthesis, Functional Properties, and Applications of $Ag_2S$ Semiconductor Nanocrystals. In *Nanoscale Compound Semiconductors and their Optoelectronics Applications*; *Elsevier.* **2022**, 5, 191–228.

(30) Kim, J.; Lee, S. W.; Kim, M. H.; Park, O. O. Zigzag-Shaped Silver Nanoplates: Synthesis via Ostwald Ripening and Their Application in Highly Sensitive Strain Sensors. *ACS Applied Materials & Interfaces*. **2018**, *10*, 39134–39143.

(31) Zhang, W.; Qiao, X.; Qiu, X.; Chen, Q.; Cai, Y.; Chen, H. Controllable Synthesis and Ostwald Ripening of Silver Nanoparticles. *Current Nanoscience*. **2013**, *9* , 753–758.

(32) Asik, D.; Yagci, M. B.; Demir Duman, F.; Yagci Acar, H. One Step Emission Tunable Synthesis of PEG Coated $Ag_2S$ NIR Quantum Dots and the Development of Receptor Targeted Drug Delivery Vehicles Thereof. *Journal of Materials Chemistry B.* **2016**, *4*, 1941-1950.

(33) Borovaya, M.; Horiunova, I.; Plokhovska, S.; Pushkarova, N.; Blume, Y.; Yemets, A. Synthesis, Properties and Bioimaging Applications of Silver-Based Quantum Dots. *International Journal of Molecular Sciences.* **2021**, *22*, 12202.

(34) Guo, Y.; Alvarado, S. R.; Barclay, J. D.; Vela, J. Shape-Programmed Nanofabrication: Understanding the Reactivity of Dichalcogenide Precursors. *ACS Nano.* **2013**, *7*, 3616–3626.

(35) Hendricks, M. P.; Campos, M. P.; Cleveland, G. T.; Plante, I. J. la; Owen, J. S. A Tunable Library of Substituted Thiourea Precursors to Metal Sulfide Nanocrystals. *Science (1979).* **2015**, *348* , 1226–1230.

(36) Campos, M. P.; Hendricks, M. P.; Beecher, A. N.; Walravens, W.; Swain, R. A.; Cleveland, G. T.; Hens, Z.; Sfeir, M. Y.; Owen, J. S. A Library of Selenourea Precursors to PbSe Nanocrystals with Size Distributions near the Homogeneous Limit. *J Am Chem Soc.* **2017**, *139* , 2296–2305.

(37) Park, J.; Jayaraman, A.; Schrader, A. W.; Hwang, G. W.; Han, H.-S. Controllable Modulation of Precursor Reactivity Using Chemical Additives for Systematic Synthesis of High-Quality Quantum Dots. *Nature Communications.* **2020**, *11*, 5748.

(38) Loghina, L.; Chylii, M.; Kaderavkova, A.; Slang, S.; Svec, P.; Rodriguez Pereira, J.; Frumarova, B.; Cieslar, M.; Vlcek, M. Highly Efficient and Controllable Methodology of the $Cd_{0.25}Zn_{0.75}Se/ZnS$ Core/Shell Quantum Dots Synthesis. *Nanomaterials.* **2021**, *11* , 2616.

(39) Hendricks, M. P.; Campos, M. P.; Cleveland, G. T.; Jen-La Plante, I.; Owen, J. S. A Tunable Library of Substituted Thiourea Precursors to Metal Sulfide Nanocrystals. *Science (1979).* **2015**, *348* , 1226–1230.

(40) Mullen, D.; Hellner, E. A Simple Refinement of Density Distributions of Bonding Electrons. IX. Bond Electron Density Distribution in Thiourea, $CS(NH_2)_2$ , at 123K. *Acta Crystallographica Section B Structural Crystallography and Crystal Chemistry*. **1978**, *34* , 2789–2794.

(41) Murray, C. B.; Norris, D. J.; Bawendi, M. G. Synthesis and Characterization of Nearly Monodisperse CdE (E = Sulfur, Selenium, Tellurium) Semiconductor Nanocrystallites. *J Am Chem Soc.* **1993**, *115*, 8706-8715.

(42) Tamang, S.; Beaune, G.; Texier, I.; Reiss, P. Aqueous Phase Transfer of InP/ZnS Nanocrystals Conserving Fluorescence and High Colloidal Stability. *ACS Nano*. **2011**, *5* , 9392–9402.

(43) Reiss, P.; Carrière, M.; Lincheneau, C.; Vaure, L.; Tamang, S. Synthesis of Semiconductor Nanocrystals, Focusing on Nontoxic and Earth-Abundant Materials. *Chemical Reviews*. **2016**, *116*, 10731-10819.

(44) Pearson, R. G. Hard and Soft Acids and Bases, HSAB, Part 1: Fundamental Principles. *Journal of Chemical Education*. **1968**, *45*, 581.

(45) Jing, L.; Kershaw, S. V.; Li, Y.; Huang, X.; Li, Y.; Rogach, A. L.; Gao, M. Aqueous Based Semiconductor Nanocrystals. *Chemical Reviews.* **2016**, *116*, 10623–10730.

(46) Jiang, P.; Chen, Z. Ligand Effect on the Synthesis of Emission-Tunable near-Infrared $Ag_2S$ Quantum Dots. *New Journal of Chemistry* **2017**, *41*, 5707–5712.

(47) Zhu, C. N.; Jiang, P.; Zhang, Z. L.; Zhu, D. L.; Tian, Z. Q.; Pang, D. W. $Ag_2Se$ Quantum Dots with Tunable Emission in the Second Near-Infrared Window. *ACS Applied Materials and Interfaces.* **2013**, *5*, 1186–1189.

(48) Li, L.; Reiss, P. One-Pot Synthesis of Highly Luminescent InP/ZnS Nanocrystals without Precursor Injection. *J Am Chem Soc.* **2008**, *130*, 11588–11589.

(49) Hocaoglu, I.; Demir, F.; Birer, O.; Kiraz, A.; Sevrin, C.; Grandfils, C.; Yagci Acar, H. Emission Tunable, Cyto/Hemocompatible, near-IR-Emitting $Ag_2S$ Quantum Dots by Aqueous Decomposition of DMSA. *Nanoscale.* **2014**, *6*, 11921–11931.

(50) Hocaoglu, I.; Çizmeciyan, M. N.; Erdem, R.; Ozen, C.; Kurt, A.; Sennaroglu, A.; Acar, H. Y. Development of Highly Luminescent and Cytocompatible Near-IR-Emitting Aqueous $Ag_2S$ Quantum Dots. *Journal of Materials Chemistry.* **2012**, *22*, 14674–14681.

(51) Zhang, Y.; Liu, Y.; Li, C.; Chen, X.; Wang, Q. Controlled Synthesis of $Ag_2S$ Quantum Dots and Experimental Determination of the Exciton Bohr Radius. *Journal of Physical Chemistry C.* **2014**, *118*, 4918–4923.

(52) Brus, L. E. Electron–Electron and Electron-hole Interactions in Small Semiconductor Crystallites: The Size Dependence of the Lowest Excited Electronic State. *The Journal of Chemical Physics.* **1984**, *80*, 4403–4409.

(53) Brelle, M. C.; Zhang, J. Z. Femtosecond Study of Photo-Induced Electron Dynamics in AgI and Core/Shell Structured AgI/$Ag_2S$ and AgBr/$Ag_2S$ Colloidal Nanoparticles. *The Journal of Chemical Physics* **1998**, *108*, 3119–3126.

(54) Hammett, L. P. Some Relations between Reaction Rates and Equilibrium Constants. *Chemical Reviews.* **1935**, *17*, 125–136.

(55) Hansch, Corwin.; Leo, A.; Taft, R. W. A Survey of Hammett Substituent Constants and Resonance and Field Parameters. *Chemical Reviews.* **1991**, *91*, 165–195.

(56) Lea, M. R.; Stavros, V. G.; Maurer, R. J. Effect of Electron Donating/Withdrawing Groups on Molecular Photoswitching of Functionalized Hemithioindigo Derivatives: A Computational Multireference Study. *ChemPhotoChem.* **2022**, *6*, 20210-20290.

(57) Poenitzsch, V. Z.; Winters, D. C.; Xie, H.; Dieckmann, G. R.; Dalton, A. B.; Musselman, I. H. Effect of Electron-Donating and Electron-Withdrawing Groups on Peptide/Single-Walled Carbon Nanotube Interactions. *J Am Chem Soc.* **2007**, *129*, 14724–14732.

(58) Choi, E. J.; Park, S. B. Unique Photophysical Properties of 9-Styryl-1,2-Dihydropyrrolo[3,4-β]Indolizin-3-One and Its Efficient Synthesis via Direct C–H Activation. *Organic & Biomolecular Chemistry*. **2015**, *13*, 5202–5208.

(59) Du, Y.; Xu, B.; Fu, T.; Cai, M.; Li, F.; Zhang, Y.; Wang, Q. Near-Infrared Photoluminescent $Ag_2S$ Quantum Dots from a Single Source Precursor. *J Am Chem Soc.* **2010**, *132*, 1470–1471.

(60) Sadovnikov, S. I.; Gusev, A. I.; Chukin, A. v.; Rempel, A. A. High-Temperature X-Ray Diffraction and Thermal Expansion of Nanocrystalline and Coarse-Crystalline Acanthite $\alpha$-$Ag_2S$ and Argentite $\beta$-$Ag_2S$. *Physical Chemistry Chemical Physics*. **2016**, *18* , 4617–4626.

(61) Du, Y.; Xu, B.; Fu, T.; Cai, M.; Li, F.; Zhang, Y.; Wang, Q. Near-Infrared Photoluminescent Ag2S Quantum Dots from a Single Source Precursor. *J Am Chem Soc.* **2010**, *132*, 1470-1471.

(62) Patterson, A. L. The Scherrer Formula for X-Ray Particle Size Determination. *Physical Review.* **1939**, *56* , 978–982.

(63) TaMang, S.; Lee, S.; Choi, H.; Jeong, S. Tuning Size and Size Distribution of Colloidal InAs Nanocrystals via Continuous Supply of Prenucleation Clusters on Nanocrystal Seeds. *Chemistry of Materials.* **2016**, *28*, 8119–8122.

(64) Dayal, S.; Burda, C. Surface Effects on Quantum Dot-Based Energy Transfer. *J Am Chem Soc.* **2007**, *129*, 7977–7981.

(65) Magro, M.; de Liguoro, M.; Franzago, E.; Baratella, D.; Vianello, F. The Surface Reactivity of Iron Oxide Nanoparticles as a Potential Hazard for Aquatic Environments: A Study on Daphnia Magna Adults and Embryos. *Scientific Reports.* **2018**, *8*, 13017–13028.

(66) Mark, L. O.; Zhu, C.; Medlin, J. W.; Heinz, H. Understanding the Surface Reactivity of Ligand-Protected Metal Nanoparticles for Biomass Upgrading. *ACS Catalysis*. **2020**, *10* , 5462–5474.

(67) Piella, J.; Merkoçi, F.; Genç, A.; Arbiol, J.; Bastús, N. G.; Puntes, V. Probing the Surface Reactivity of Nanocrystals by the Catalytic Degradation of Organic Dyes: The Effect of Size, Surface Chemistry and Composition. *Journal of Materials Chemistry A*. **2017**, *5* , 11917–11929.

(68) Thapa, S.; Bhardwaj, K.; Basel, S.; Pradhan, S.; Eling, C. J.; Adawi, A. M.; Bouillard, J. S. G.; Stasiuk, G. J.; Reiss, P.; Pariyar, A.; Tamang, S. Long-Term Ambient Air-Stable Cubic $CsPbBr_3$ Perovskite Quantum Dots Using Molecular Bromine. *Nanoscale Advances*. **2019**, *1*, 3388–3391.

(69) Pang, Z.; Zhang, J.; Cao, W.; Kong, X.; Peng, X. Partitioning Surface Ligands on Nanocrystals for Maximal Solubility. *Nature Communications*. **2019**, *10*, 2454–2459.

(70) Kazes, M.; Udayabhaskararao, T.; Dey, S.; Oron, D. Effect of Surface Ligands in Perovskite Nanocrystals: Extending in and Reaching Out. *Accounts of Chemical Research*. **2021**, *54*, 1409–1418.

(71) Almeida, G.; Goldoni, L.; Akkerman, Q.; Dang, Z.; Khan, A. H.; Marras, S.; Moreels, I.; Manna, L. Role of Acid–Base Equilibria in the Size, Shape, and Phase Control of Cesium Lead Bromide Nanocrystals. *ACS Nano.* **2018**, *12*, 1704–1711.

(72) Lees, E. E.; Gunzburg, M. J.; Nguyen, T.-L.; Howlett, G. J.; Rothacker, J.; Nice, E. C.; Clayton, A. H. A.; Mulvaney, P. Experimental Determination of Quantum Dot Size Distributions, Ligand Packing Densities, and Bioconjugation Using Analytical Ultracentrifugation. *Nano Letters*. **2008**, *8*, 2883–2890.

(73) Guerrini, L.; Alvarez-Puebla, R.; Pazos-Perez, N. Surface Modifications of Nanoparticles for Stability in Biological Fluids. *Materials.* **2018**, *11*, 1154–1163.

(74) Krueger, K. M.; Al-Somali, A. M.; Mejia, M.; Colvin, V. L. The Hydrodynamic Size of Polymer Stabilized Nanocrystals. *Nanotechnology*. **2007**, *18*, 475709–475711.

(75) Jayabharathi, J.; Sundari, G. A.; Thanikachalam, V.; Jeeva, P.; Panimozhi, S. A Dodecanethiol-Functionalized Ag Nanoparticle-Modified ITO Anode for Efficient Performance of Organic Light-Emitting Devices. *RSC Advances*. **2017**, *7*, 38923–38934.

(76) Zhang, H.; Chen, M.; Wang, D.; Xu, L.; Liu, X. Laser Induced Fabrication of Mono-Dispersed $Ag_2S$@Ag Nano-Particles and Their Superior Adsorption Performance for Dye Removal. *Optical Materials Express*. **2016**, *6*, 2573–2574.

(77) Wu, Q.; Zhou, M.; Shi, J.; Li, Q.; Yang, M.; Zhang, Z. Synthesis of Water-Soluble $Ag_2S$ Quantum Dots with Fluorescence in the Second Near-Infrared Window for Turn-On Detection of Zn(II) and Cd(II). *Analytical Chemistry*. **2017**, *89*, 6616–6623.

(78) Shi, L.-J.; Zhu, C.-N.; He, H.; Zhu, D.-L.; Zhang, Z.-L.; Pang, D.-W.; Tian, Z.-Q. Near-Infrared $Ag_2Se$ Quantum Dots with Distinct Absorption Features and High Fluorescence Quantum Yields. *RSC Advances*. **2016**, *6*, 38183–38186.

(79) Ge, J.-P.; Xu, S.; Liu, L.-P.; Li, Y.-D. A Positive-Microemulsion Method for Preparing Nearly Uniform Ag2Se Nanoparticles at Low Temperature. *Chemistry - A European Journal*. **2006**, *12*, 3672–3677.

(80) Gu, Y.-P.; Cui, R.; Zhang, Z.-L.; Xie, Z.-X.; Pang, D.-W. Ultrasmall Near-Infrared $Ag_2Se$ Quantum Dots with Tunable Fluorescence for *in Vivo* Imaging. *J Am Chem Soc*. **2012**, *134*, 79–82.

(81) Xiang, J.; Cao, H.; Wu, Q.; Zhang, S.; Zhang, X.; Watt, A. A. R. <scp>l</Scp> - Cysteine-Assisted Synthesis and Optical Properties of $Ag_2S$ Nanospheres. *The Journal of Physical Chemistry C*. **2008**, *112*, 3580–3584.

(82) Castner, D. G.; Hinds, K.; Grainger, D. W. X-Ray Photoelectron Spectroscopy Sulfur 2p Study of Organic Thiol and Disulfide Binding Interactions with Gold Surfaces. *Langmuir*. **1996**, *12*, 5083–5086.

(83) Liu, Y.; Yao, D.; Shen, L.; Zhang, H.; Zhang, X.; Yang, B. Alkylthiol-Enabled Se Powder Dissolution in Oleylamine at Room Temperature for the Phosphine-Free Synthesis of Copper-Based Quaternary Selenide Nanocrystals. *J Am Chem Soc*. **2012**, *134*, 7207–7210.

(84) Moreels, I.; Lambert, K.; de Muynck, D.; Vanhaecke, F.; Poelman, D.; Martins, J. C.; Allan, G.; Hens, Z. Composition and Size-Dependent Extinction Coefficient of Colloidal PbSe Quantum Dots. *Chemistry of Materials*. **2007**, *19*, 6101–6106.

(85) Mindl, J.; Sulzer, J.; Vecera, M. Hydrolysis Kinetics and Mechanism of Diaryldithiocarbamates in 20% Aqueous Dioxane. *Collect. Czech. Chem. Commun.* **1981**, *46*, 1970–1975.

(86) Zakrzewski, J.; Huras, B.; Kiełczewska, A. Synthesis of Isoselenocyanates. *Synthesis.* **2016**, *48*, 85–96.

# Chapter III

## *Aqueous-soluble $Ag_2S$ NCs and $Ag_2S/ZnS$ NCs*

## 3.1. Introduction

Colloidal quantum dots (CQDs) of superior quality, characterized by a small size range, near-unity quantum yield (QY), and remarkable resistance to photo-degradation, are generally produced in an organic solvent utilizing the hot injection method created by Murray and Bawendi.[1] The phase transfer of nanocrystals (NCs) synthesized in an organic medium to aqueous media is an essential step for biological application.[2–4] In the previous chapter, we demonstrated the synthesis of monodisperse NIR-II emitting $Ag_2S$ CQDs in an organic solvent. These CQDs in organic solvents must be phase transferred to the aqueous medium. Ideally, the phase-transferred CQDs in the aqueous medium should have good stability (colloidal, photo- and chemical stability) in physiological pH, high fluorescence quantum yield, low hydrodynamic diameter, and low toxicity. [5–15] In this chapter, we will discuss the phase transfer reaction of $Ag_2S$ CQDs from a non-polar solvent to an aqueous medium using L-cysteine.

## 3.2. Phase transfer

### 3.2.1. L-Cysteine as the phase transfer ligand

L-cysteine is an amino acid containing the thiol group. Depending on the pH of the solution, L-cysteine can have cationic, anionic, and even zwitterionic forms (Figure 3.1). At pH ~9 the thiol group is dissociated to thiolate ion ($pKa$~8.35),[16] which is important for strong binding with the surface of the $Ag_2S$ CQDs. Ag-S(thiolate) binding energy is 2.84 eV. It is zwitterionic when the pH of the solution reaches the isoelectric point at 5.05.[17] The zwitterionic self-assembled monolayers (SAMs) are important for evading nonspecific interaction with protein.[18] The zwitterionic nature of L-cysteine, compact size, and the ability of its thiolate group to bind with the surface of the $Ag_2S$ QDs at pH>9 make it an ideal ligand for phase transfer. *L*-cysteine has been widely used in phase transfer of various CQDs including InP/ZnS,[11] CdSe/CdZnS,[19] CdSe,[20,21] CdTe,[22] CdTe/CdS,[23] ZnS,[24] CdSeTe,[25] $CuInS_2$,[26] NCs.[17] The L-cysteine-capped CQDs has a compact size and efficient clearance *via* the kidney.[17,27,28]

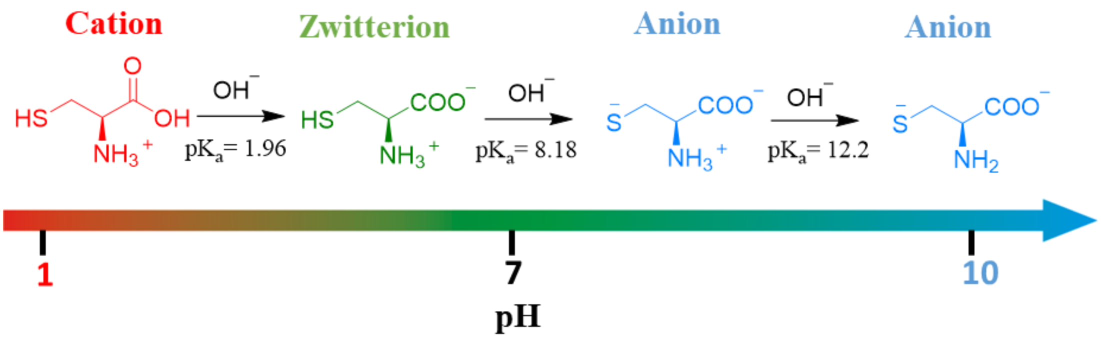
Cation
Zwitterion
Anion
Anion
HS
O
OH
NH3+
OH−
pKa= 1.96
HS
COO−
NH3+
OH−
pKa= 8.18
S−
COO−
NH3+
OH−
pKa= 12.2
S−
COO−
NH2
1
7
10
pH

**Figure 3.1:** Various forms of *L*-cysteine at different pH values.

### 3.2.2. Phase transfer reaction

The $Ag_2S$ CQDs were phase transferred from chloroform to the aqueous medium using a procedure reported for InP/ZnS core/shell CQDs.[11] The method involves vigorous stirring of a biphasic mixture containing $Ag_2S$ CQDs (in chloroform) and *L*-cysteine (in an aqueous medium) at pH~9. Figure 3.2 shows the photographs before and after the exchange reaction. The $Ag_2S$ CQDs dispersed in $CHCl_3$ were efficiently transferred to water within 2 hour.

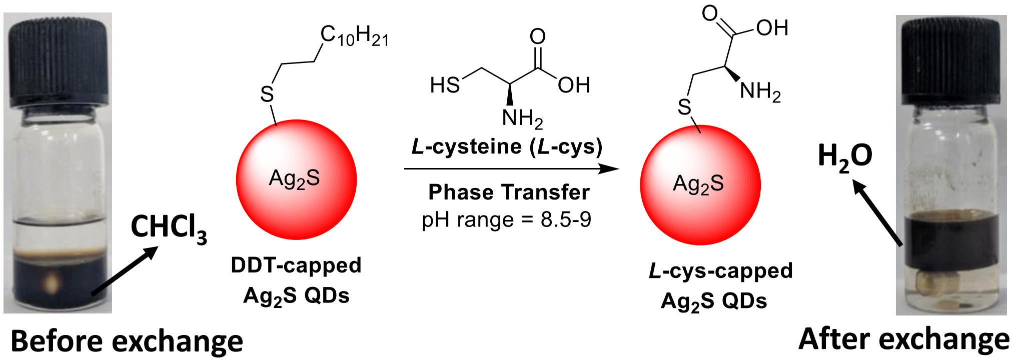
C10H21
S
Ag2S
CHCl3
DDT-capped
Ag2S QDs
Before exchange
HS
O
OH
NH2
L-cysteine (L-cys)
Phase Transfer
pH range = 8.5-9
O
OH
NH2
S
Ag2S
L-cys-capped
Ag2S QDs
H2O
After exchange

**Figure 3.2:** Phase transfer of DDT-capped $Ag_2S$ QDs from organic phase (chloroform) to aqueous phase using L-cysteine at pH ~9.

### 3.2.3. Characterization of aqueous $Ag_2S$ QDs

The successful phase transferred QDs were characterized by Fourier Transform Infrared Spectroscopy (FTIR), Photoluminescence Spectroscopy (PL spectroscopy), and X-ray Diffraction Spectroscopy (XRD).

The purified $Ag_2S$ QDs in the organic phase were phase transferred within 2 hours yielding the L-cysteine-capped $Ag_2S$ QDs in excellent yields (yield~93% and 90.0 % for QD1 and QD2 respectively). Thereafter, the aqueous QDs (QD1, $\lambda_{em}$ ~1024 nm, QD2, $\lambda_{em}$ ~1209) were characterized by IR-Spectroscopy which confirmed the successful phase transfer of the QDs from the organic phase to the aqueous phase. Figure 3.3a and 3.3b show the FTIR spectra of L-cysteine-capped $Ag_2S$ QDs (QD1 and QD2). At 2538 cm$^{-1}$ in the FTIR spectrum of pure L-cysteine, there is a distinct S-H stretching vibration signal (Figure 3.3). The lack of this signal in aqueous $Ag_2S$ QDs (Figures 3.3a and 3.3b) indicated that unbound L-cysteine was not present in the solution. The asymmetric stretching vibration of carboxylate is responsible for a strong peak at 1572 cm$^{-1}$ for QD1 and 1568 cm$^{-1}$ for QD2.

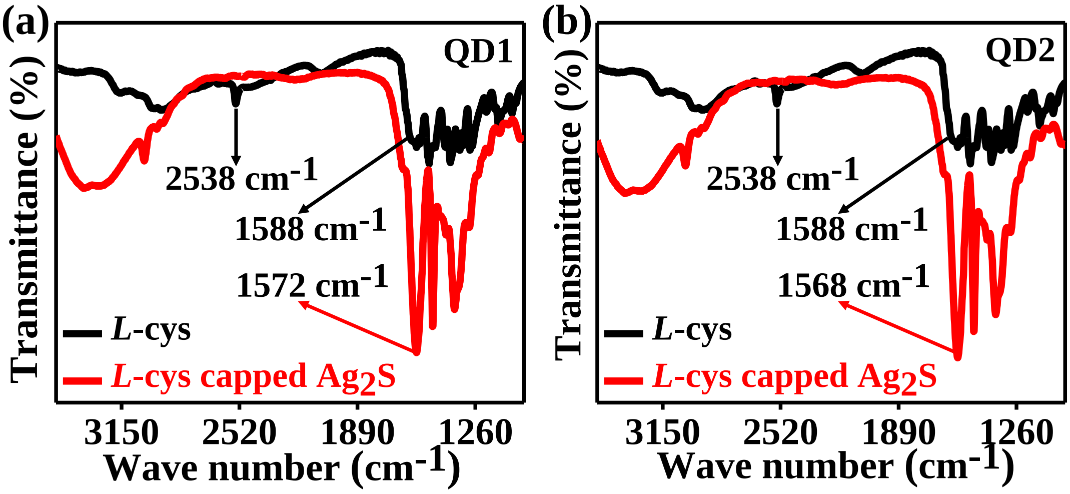

**Figure 3.3:** FTIR spectra of phase transferred QDs from organic to aqueous phase (QD1 and QD2).

Figure 3.4 shows the photoluminescence spectra of two different-sized NIR-II $Ag_2S$ QDs (QD1, size ~2.2 nm, $\lambda_{em}$ ~1024 nm, $\lambda_{abs}$ ~914 nm, and QD2, size ~4.2 nm, $\lambda_{em}$ ~1209 nm, $\lambda_{abs}$ ~1012 nm) before and after phase transfer from organic to the aqueous phase. The QDs maintained good colloidal stability in the aqueous phase and the quantum yield was well conserved (QY~5.5% and 5.6% for QD1 and QD2 respectively, Figure 3.4). The QY for other QDs emitting in the NIR-II region at $\lambda_{em}$ ~1065 nm and $\lambda_{em}$ ~1133 nm was also calculated to be at 5.6 % (*c.f.* Annexure, A3.1)

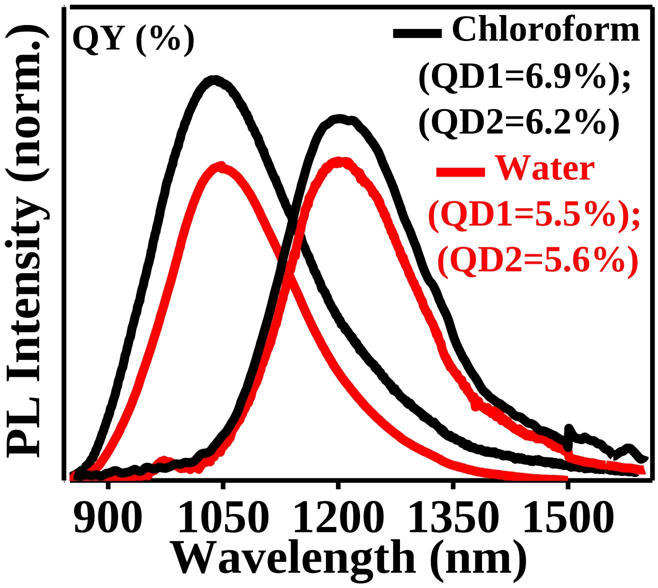

**Figure 3.4:** PL and QY results of $Ag_2S$ QDs before and after phase transfer from organic to the aqueous phase.

Due to the strong fluorescent intensity, high QY, and narrow emission bandwidth, QDs have been used as fluorophores in many imaging fields.[29–31] The QY is significantly decreased during the phase transfer, which limits the application of QDs to bioimaging.[32,33] In our case, we observed a relatively high conservation of quantum yield during the phase transfer reaction. Table 3.1 shows the detailed investigation of $Ag_2S$ QDs before and after phase transfer.

**Table 3.1:** An extensive analysis of phase transferred $Ag_2S$ QDs. The QY was determined by comparing the total fluorescence intensity of QDs in water and organic solvent (TCE) to a standard dye (IR-140, $\Phi_f = 0.167$ in ethanol)

| **NCs ($Ag_2S$)** | **Size (nm)** | **Emission (a) nm** | **Emission (b) nm** | **QY (a) %** | **QY (b) %** | **FWHM (a) nm** | **FWHM (b) nm** |
|---|---|---|---|---|---|---|---|
| **QD1** | 2.2 ± 0.52 | 1024 | 1026 | 6.9 | 5.5 | 229 | 198 |
| **QD2** | 4.2 ± 1.1 | 1209 | 1211 | 6.2 | 5.6 | 196 | 173 |

**XRD:** Figure 3.5 shows the XRD pattern of $Ag_2S$ NCs before and after the phase transfer reaction. The sample retained its monoclinic phase (JCPDS 14-0072) [34,35] NCs with space group *P2₁/c*. results of the. The measured $2\theta$ values for $Ag_2S$ are 26.3, 28.9, 31.5, 34.3, 36.8, 40.7, 43.4, and 53.2 indexed to the planes (012), (111), (-112), (-121), (121), (200), and (-213) respectively.

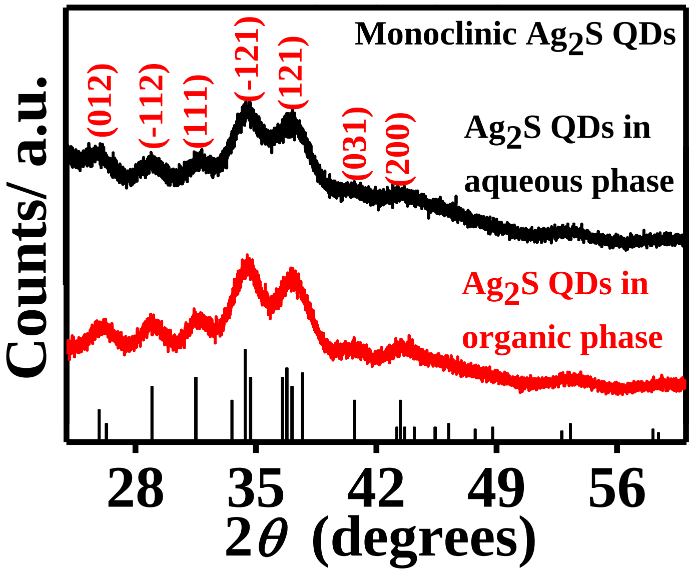

**Figure 3.5:** XRD of $Ag_2S$ NCS before and after the phase transfer from organic to the aqueous phase.

## 3.3. Stability of $Ag_2S$ QDs in aqueous medium

### 3.3.1. pH

Figure 3.6a shows that the QY of $Ag_2S$ NCs is highly sensitive to the pH of the solution. QY increased when the pH of the solution was increased, while at acidic pH we noted a decrease in quantum yield. Furthermore, at basic pH (>10) the absorption peak was also more distinct compared to that at lower pH. The decrease of QY at lower pH is also reported for other QDs such as CdSe/ZnS[36] and CdS NCs.[37,38] The reason for this observation is not clear, though it can be understood that the QY is sensitive to the species on the surface. The surface-bound thiolate-Ag (I) is expected to undergo chemical changes (reduction or oxidation) at different pH.

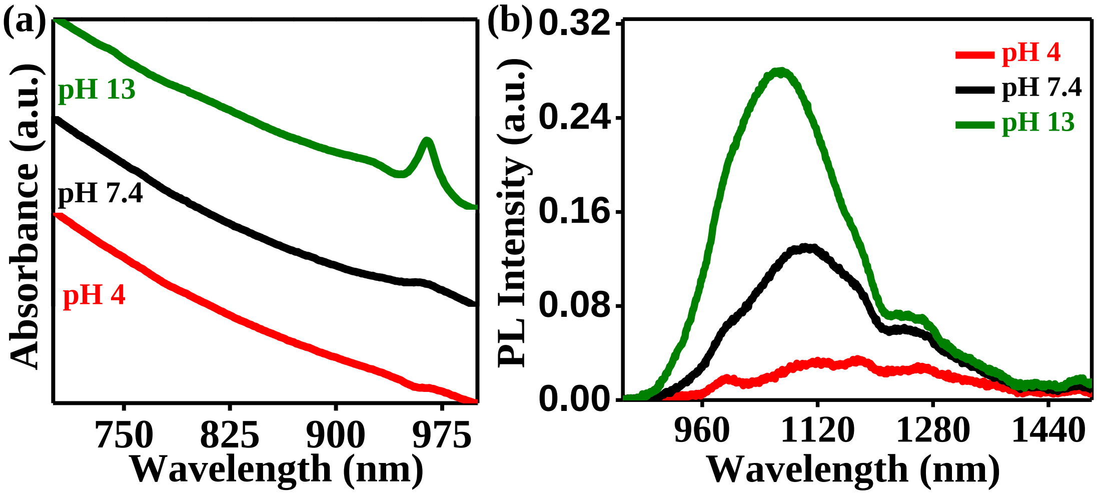

**Figure 3.6:** (a) UV-absorption spectrum of aqueous $Ag_2S$ QDs at different pH solutions (b) PL spectra of aqueous $Ag_2S$ QDs in different pH solutions.

### 3.3.2. Colloidal Stability

In our study, the absorption/emission spectra and turbidity index[39] were used to monitor the colloidal stability in the aqueous medium. The NCs were stable for up to 28 days as indicated by absorption and emission spectra (Figure 3.7a-b). The FWHM of the corresponding NCs is shown in Annexure, A3.2. Figure 3.7c is the photographs of the colloidal solution of $Ag_2S$ NCs in water taken over one month. The turbidity index of the colloidal solution maintained close to 35 NTU (nephelometric turbidity unit) for this period.

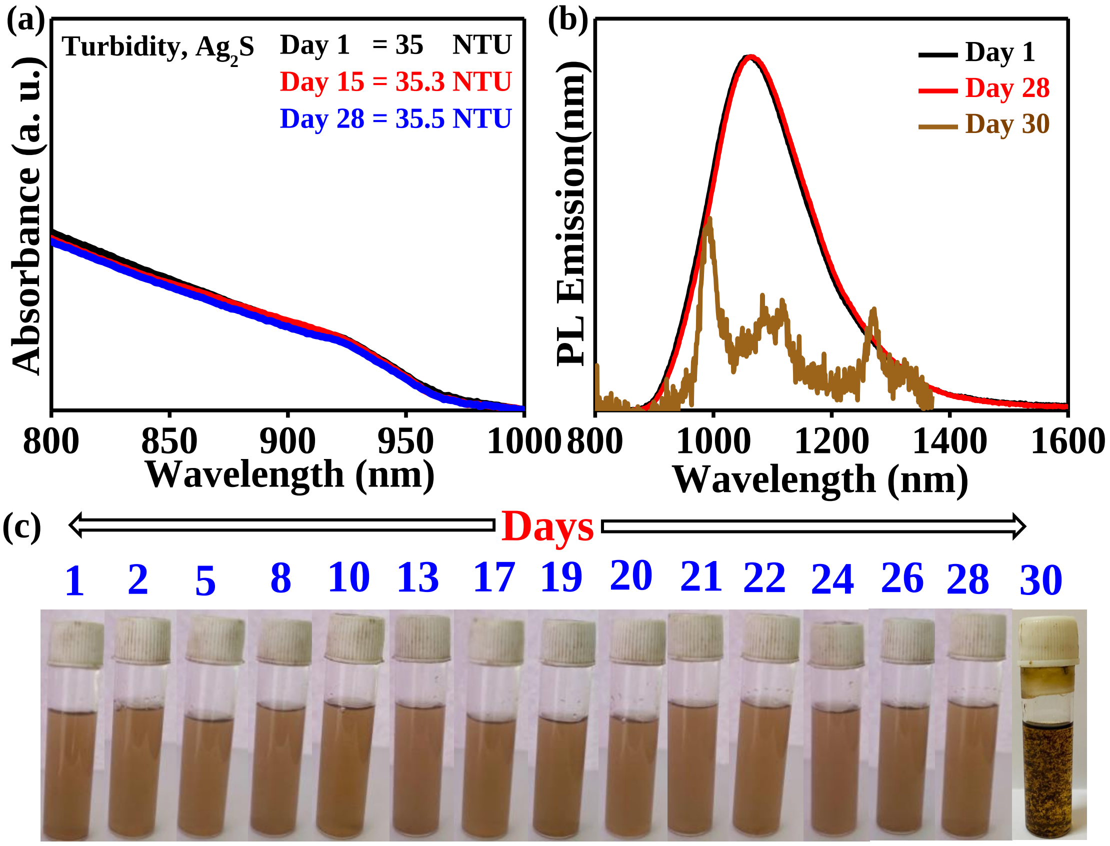

**Figure 3.7:** (a) UV-absorption spectra of aqueous $Ag_2S$ NCs ($\lambda_{em}$ ~1065 nm, $\lambda_{abs}$ ~ 921 nm) measured on days 1, 15, and 28. (b) PL emission of the same aqueous $Ag_2S$ NCs measured on days 1, 15, and 28. (c) Photographs of colloidal solutions of $Ag_2S$ NCs taken on different days.

### 3.3.3. Phase stability

XRD spectra show that the colloidal solution of $Ag_2S$ NCs retained its monoclinic phase for more than a month.

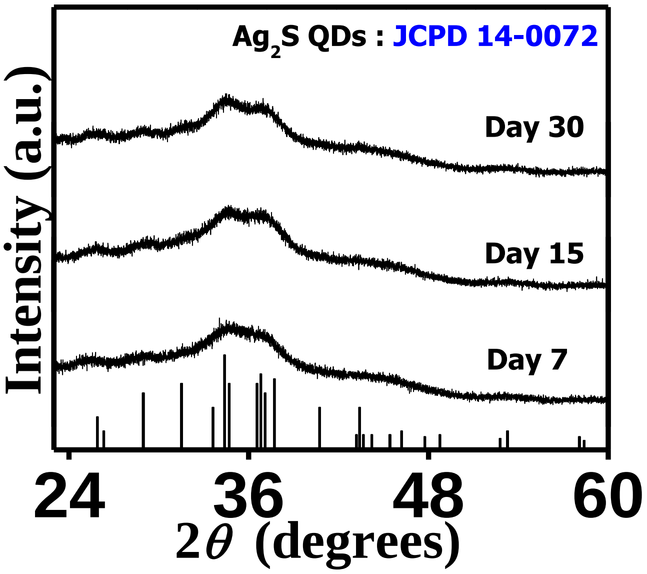

**Figure 3.8:** XRD spectra $Ag_2S$ NCs in aqueous medium monitored for 1 month.

### 3.3.4. Photostability

For photostability studies, four different-sized $Ag_2S$ NCs (From QD1 to QD2) were phase transferred to the aqueous medium using L-cysteine under the optimized condition as discussed in the previous section. Figure 3.9a-b show the absorption and emission spectra of these phase-transferred. These NCs were irradiated under blue LED (visible light) for 2 hour. The results show that larger-sized NCs (e.g. QD2) were more stable than the smaller-sized NCs (e.g. QD1). Similar results were reported for PbS NCs by Weiss and co-workers.[40] It is noteworthy that both QD1 and QD2 had nearly the same QY in water (Table 3.1) before the irradiation.

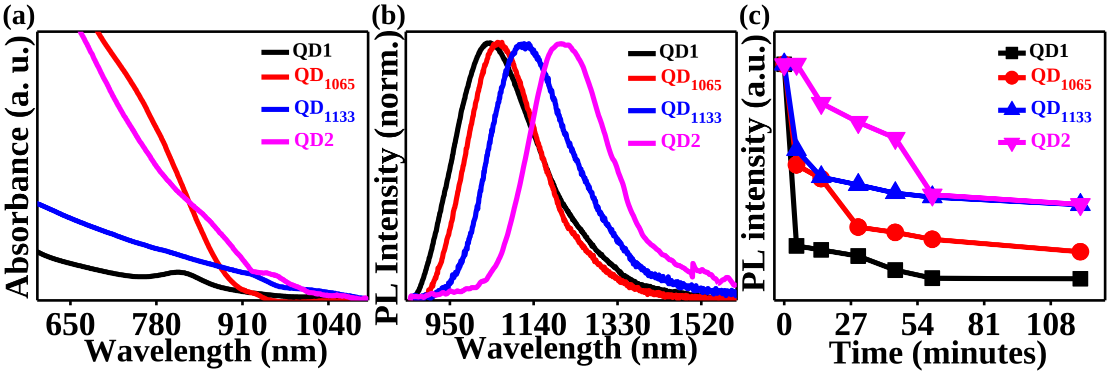

**Figure 3.9:** a) UV-visible absorption spectra of $Ag_2S$ QDs for 2 hrs. Samples QD1 and QD2 are described in section 2.1, $QD_{1065}$ and $QD_{1133}$ denote $Ag_2S$ NCs emitting at 1065 and 1133 nm respectively. (b) Corresponding PL emission spectra of the $Ag_2S$ QDs. (c) These $Ag_2S$ NCs (QD1, QD2, $QD_{1065,}$ and $QD_{1133}$) were photo-irradiated under blue LED and PL emission was monitored at a different time for 2h.

### 3.3.5. Improving photostability: synthesis and characterization of $Ag_2S$/ZnS core/shell NCs

The photostability results motivated us to further increase the photostability of aqueous $Ag_2S$ QDs. Typically, photostability can be increased either by changing the capping ligands[41] or doping various metal ions such as $Zn^{2+}$, $Pb^{2+}$, $Cd^{2+}$, $Cu^{2+}$, $Mn^{2+}$,[42–44] or by coating $Ag_2S$ QD with an insulating inorganic shell.[45] In our study, we prepared $Ag_2S$/ZnS core/shell NCs. ZnS is an ideal material for synthesizing various core/shell NCs due to its wider and direct band gap ($E_g$~3.6 eV) having exciton Bohr radius, $r_B$ = 2.5 nm. Over-coating $Ag_2S$ NCs with the ZnS shell passivates the surface defects states, prevents the core from environmental factors (oxygen, moisture, pH), and increases QY.[46–52] Some studies have also shown that in addition to photostability, growing the shell also increases the colloidal stability of the materials.[41] Preparation of $Ag_2S$ QDs is still challenging due to the large lattice mismatch (8.8%) between $(10\bar{1}0)_{ZnS}$ and $(\bar{1}11)_{Ag_2S}$.[53] Two major synthetic approaches for growing a shell on silver chalcogenide are a) successive ion layer adsorption (SILAR) and b) microwave synthesis.[54,55] In the

SILAR method, which was first applied for the synthesis of CdSe/CdS core/shell NCs,[56] the cation and anion precursors are added and adsorbed in sequence to avoid separate nucleation of ZnS in the solution. In the microwave method, the particle size of core/shell QDs synthesized is typically larger than 20 nm, with a large diameter dispersion and low monodispersity. For this reason, a shell coating technique that is quick, simple, and controlled is essential. Recently, Peng and co-workers reported a non-injection approach for synthesizing $Ag_2S$ core covered with ZnS shell, in which the ligand was used as an anion precursor (e.g., alkanethiols). The non-injection approach reduces the number of reagents used and simplifies the synthesis procedures in general.[45] $Ag_2S$/ZnS and $CuInS_2$/ZnS NCs have been successfully synthesized using this thiol-based non-injection approach.[57–59]

Synthesis of $Ag_2S$/ZnS core/shell NCs: We followed Peng's method for the synthesis of $Ag_2S$/ZnS NCs with slight modifications in our synthesis process. Briefly, zinc acetate was dissolved in oleylamine, DDT, and ODE (I-octadecene), to which a sulfur precursor (3b, *cf.* chapter II) dissolved in dimethoxymethane was added. The ZnS precursor solution was then added dropwise into the reaction solution containing pre-synthesized $Ag_2S$ NCs (*cf.* Section 2.6.3, chapter II). Control experiments confirmed that the substituted thiourea act as the sulfur precursor for both $Ag_2S$ NCs and $Ag_2S$/ZnS core/shell NCs. The NCs were purified using the centrifugation method[11] (*cf.* Section 3.9.4)

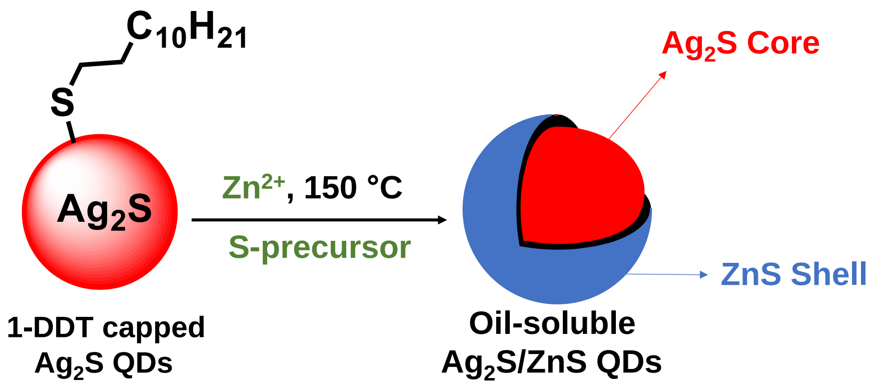
C10H21
S
Ag2S
1-DDT capped
Ag2S QDs
Zn2+, 150 °C
S-precursor
Ag2S Core
ZnS Shell
Oil-soluble
Ag2S/ZnS QDs

**Scheme 3.1:** (a) Schematic representation of the synthesis of $Ag_2S$/ZnS core/shell NCs.

**Characterization of $Ag_2S$/ZnS NCs:** The oil-soluble and aqueous $Ag_2S$/ZnS NCs are characterized by FTIR, PL spectroscopy, UV-Vis spectroscopy, TEM, and XRD spectroscopy.

**FTIR:** The presence of surface-bound DDT was confirmed by FTIR. The characteristic asymmetric and symmetric C-H stretching peaks are observed at 2916 $cm^{-1}$ and 2847 $cm^{-1}$ respectively in $Ag_2S$/ZnS NCs. A slight shift of frequencies towards lower values is due to the binding of the thiol group onto the surface of the NCs.[60] Literature shows that other alkanethiols are equally effective as the capping ligand for different sulfur (substituted thiourea,[61] thiocarbamate[62] and dithiocarbamates[62]) and selenium precursors[63].

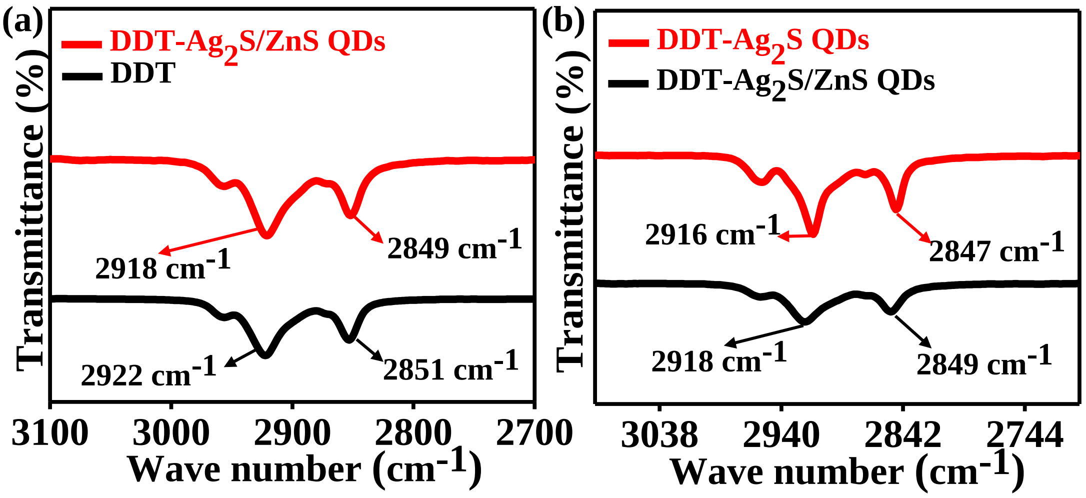

**Figure 3.10:** (a) FTIR spectra of DDT (black) and DDT-capped $Ag_2S$/ZnS core/shell

NCs (red) showing a clear shift C-H stretching frequency which confirms the surface passivation of $Ag_2S$ NCs by DDT. (b) A shift in C-H stretching frequency of $Ag_2S$ NCs (red) and $Ag_2S/ZnS$ core/shell NCs (black).

Optical properties of $Ag_2S/ZnS$ NCs: Growing a shell with a higher band gap around the core improves the PL quantum yield by passivating the surface defects[64] and preventing the influence of environmental factors (such as pH, oxygen, etc.), thus increasing the PL QY and stability of the QDs. The passivation of nonradiative recombination sites on the surface of nanocrystallites by overcoating them with higher band gap inorganic materials, such as ZnS, has been demonstrated to enhance the photoluminescence quantum yields.[64,65] Particles passivated with inorganic shell structures are more robust than organically passivated QDs and have greater tolerance to processing conditions necessary for incorporation into solid-state structures. The photoluminescence (PL) and the corresponding absorption spectra of $Ag_2S$ core NCs and the $Ag_2S/ZnS$ core/shell NCs are shown in Figures 3.11a and 3.11b. As anticipated, there is a significant improvement in PL QY as the shell growth time gradually progressed from 15 min to 60 minutes at 150 $^{o}$C. Despite a lattice mismatch of 8.8 % (between $Ag_2S$ and ZnS), a more than 2 nm thick shell could be overgrown. In small NCs, the lattice mismatch is relaxed due to short crystal facets.[66] Interestingly, the first excitonic peak also became more prominent in core/shell NCs compared to the core NCs. This is attributed to a partial leakage of excitons into the shell material, which has a larger bandgap (0.9 eV for bulk ZnS) than the core material (3.6 eV for bulk ZnS).[67,68]

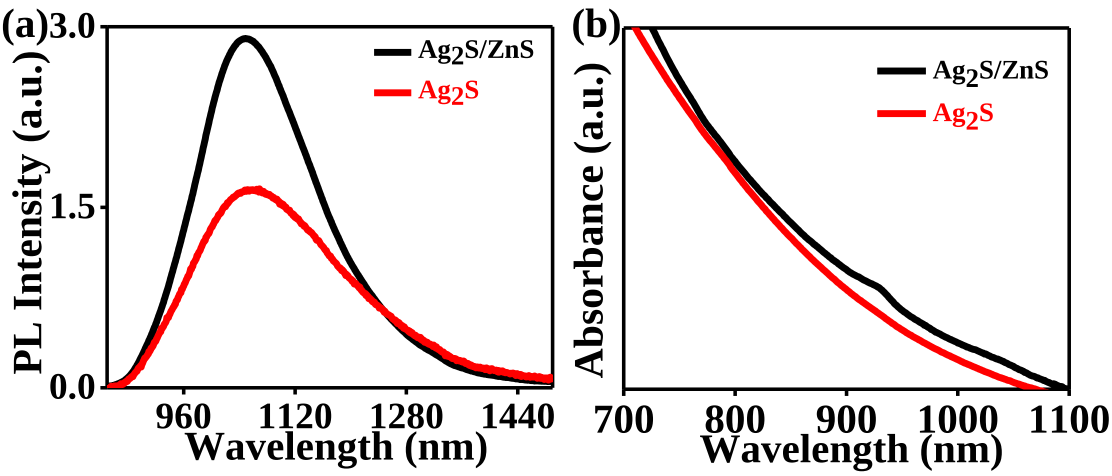

**Figure 3.11:** (a) PL emission spectra of $Ag_2S$ and $Ag_2S/ZnS$ core/shell NCs showing a 2-fold increase in QY. (b) UV-vis absorption spectra $Ag_2S$ and $Ag_2S/ZnS$ core/shell NCs showing first excitonic peak.

**TEM:** The TEM images of $Ag_2S/ZnS$ core/shell NCs are shown in Figure 3.12. The size of $Ag_2S/ZnS$ NCs is 2.5 ± 0.8 nm, which is 0.3 nm higher than the core $Ag_2S$ (2.2 ± 0.5 nm).

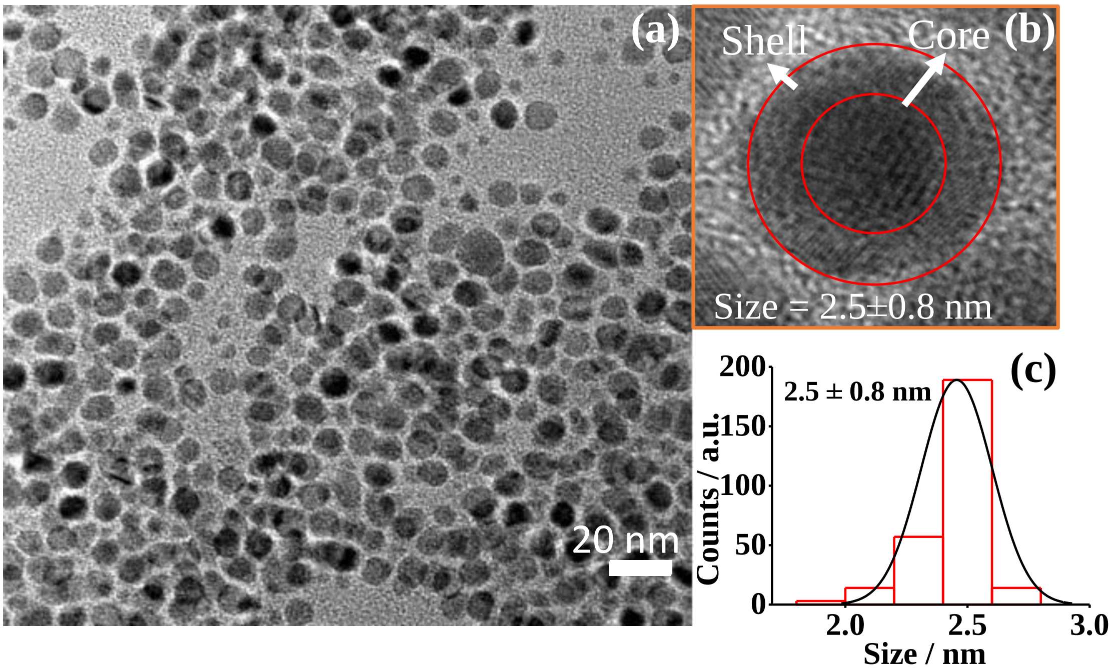
(a)
20 nm
Shell
Core
(b)
Size = 2.5±0.8 nm
(c)
2.5 ± 0.8 nm
200
150
100
50
0
Counts / a.u.
2.0
2.5
3.0
Size / nm

**Figure 3.12:** (a) TEM micrograph of 2.5 ± 0.8 nm of $Ag_2S/ZnS$ core-shell NCs (b) HRTEM image showing lattice fringes (c) the size distribution curve.

**XRD:** Figure 3.13 compares the XRD spectra of $Ag_2S$ core and $Ag_2S/ZnS$ core/shell NCs. XRD pattern of core/shell NCs is consistent with the literature report.[45] The high-intensity peak for monoclinic $Ag_2S$ NC at ~36.8 is masked by the (111) peak of wurtzite ZnS similar to the cases of previously reported core/shell structures such as $Ag_2S/ZnS$,[45] CdSe/ZnS and, CdSe/CdS QDs,[56,69,70] implying the formation of $Ag_2S/ZnS$ core/shell QDs.

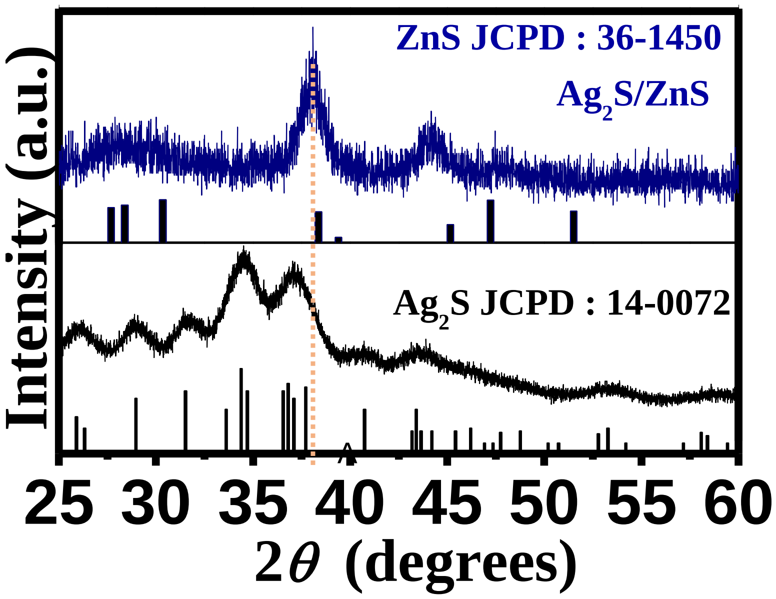

**Figure 3.13:** XRD patterns of the $Ag_2S$ QDs (black line) and $Ag_2S/ZnS$ core/shell QDs (royal blue line).

Phase transfer of $Ag_2S/ZnS$ core/shell NCs: The oil-soluble $Ag_2S/ZnS$ core/shell NCs were phase transferred into the water phase using *L*-cysteine as the transferring agent in basic pH (*cf.* section 3.5.3).[11]

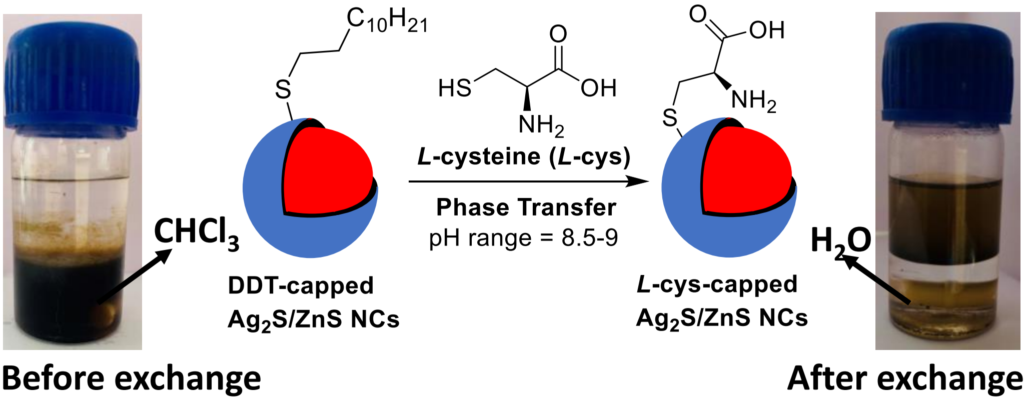
C10H21
S
HS
O
OH
NH2
L-cysteine (L-cys)
Phase Transfer
pH range = 8.5-9
O
OH
NH2
S
CHCl3
DDT-capped
Ag2S/ZnS NCs
L-cys-capped
Ag2S/ZnS NCs
H2O
Before exchange
After exchange

**Scheme 3.2:** Phase transfer of $Ag_2S$/ZnS core/shell NCs from organic (chloroform) to the aqueous phase (water) using *L*-cysteine.

Successful phase transfer is confirmed by FTIR (Figure 3.14). At 2538 $cm^{-1}$ pure L-cysteine exhibits a distinctive S-H stretching vibration signal. The lack of this signal in aqueous core/shell NCs (Figure 3.14a) indicated the absence of unbound L-cysteine in the solution. The asymmetric stretching vibration of the carboxylate ($COO^-$) group of surface-bound L-cysteine is observed at 1567 $cm^{-1}$. This peak at a lower frequency compared to the pure L-cysteine (1588 $cm^{-1}$) indicates the presence of a surface-bound ligand. The high conservation of PL QY phase-transferred core/shell NCs is attributed to the robust ZnS layer as a protective shell.

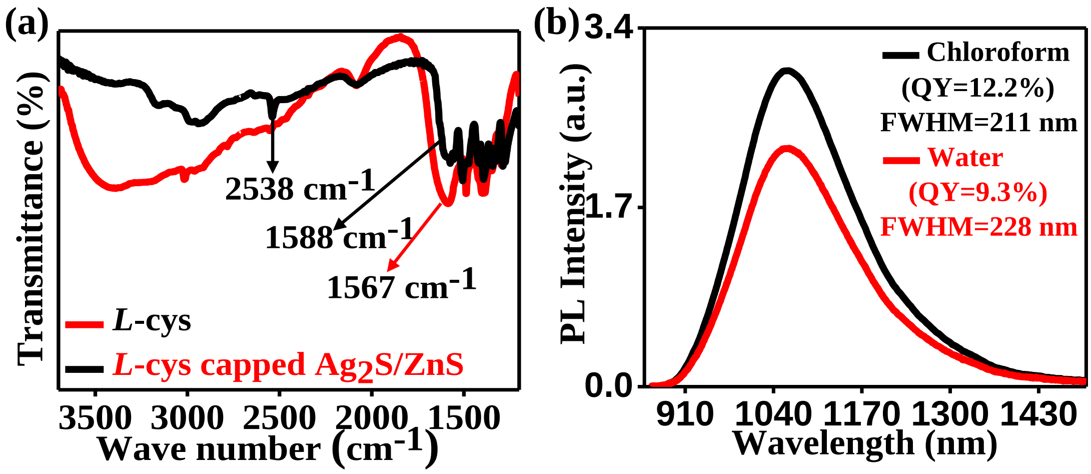

**Figure 3.14**: (a) FTIR spectra of $Ag_2S$/ZnS core/shell QDs before and after phase transfer. (b) PL spectra showing QY of $Ag_2S$/ZnS core/shell QDs before and after phase transfer.

Colloidal stability of aqueous $Ag_2S$/ZnS core/shell QDs: $Ag_2S$/ZnS core/shell NCs were stable for up to 48 days as indicated by optical (PL and absorption) and turbidity data (Figure 3.15a-b). The PL and UV did not indicate any sign of agglomeration. The turbidity index of the colloidal solution consistently remained close to ~32 NTU (nephelometric turbidity unit) for over 48 days.

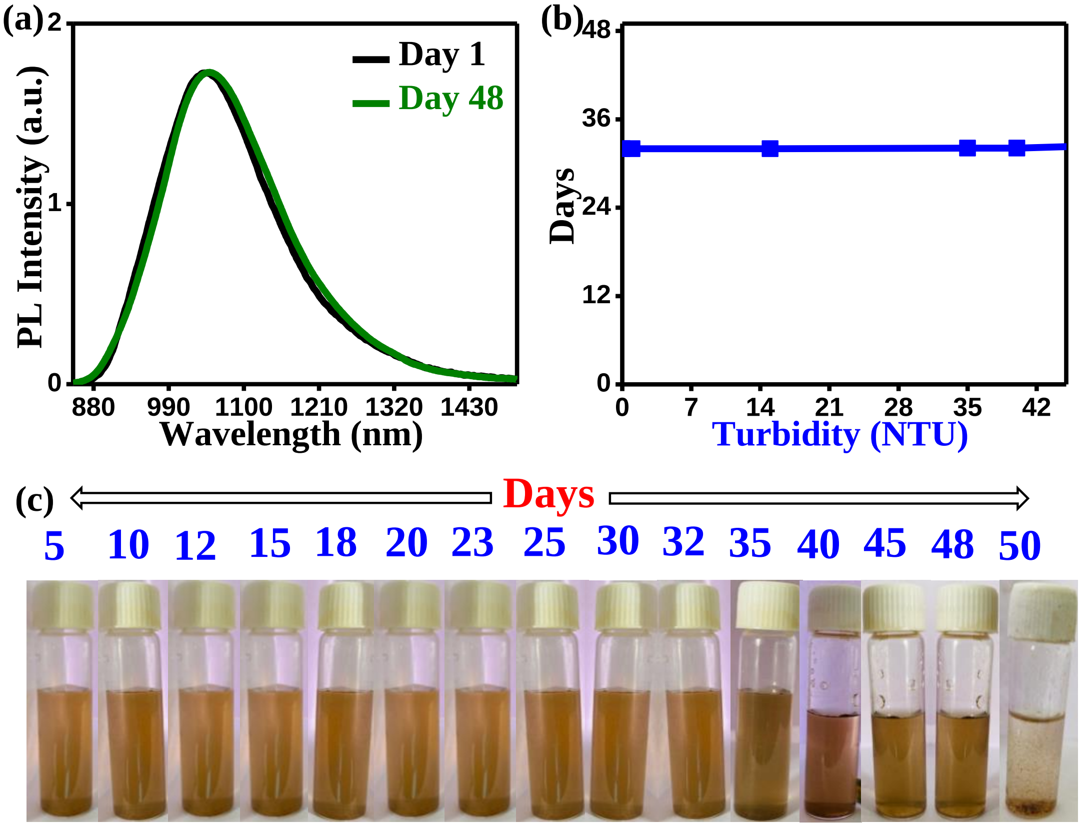

**Figure 3.15:** (a) PL emission peak for aqueous $Ag_2S/ZnS$ NCs consistent over (b) PL emission 48 days. (b) Turbidity measurement for 48 days of same aqueous $Ag_2S/ZnS$ NCs (c) Pictorial representation of colloidal solutions for 1 month (50 days after, the colloidal solution is disturbed due to agglomeration).

**pH-dependence of aqueous $Ag_2S/ZnS$ core/shell NCs:** The QY increased as the pH of the solution increased. Furthermore, in basic pH (>10), the absorption feature became more distinct compared to that at lower pH consistent with the observation in $Ag_2S$ NCs and other systems such as CdSe/ZnS[36] core/shell NCs and CdS[37,38] QDs.

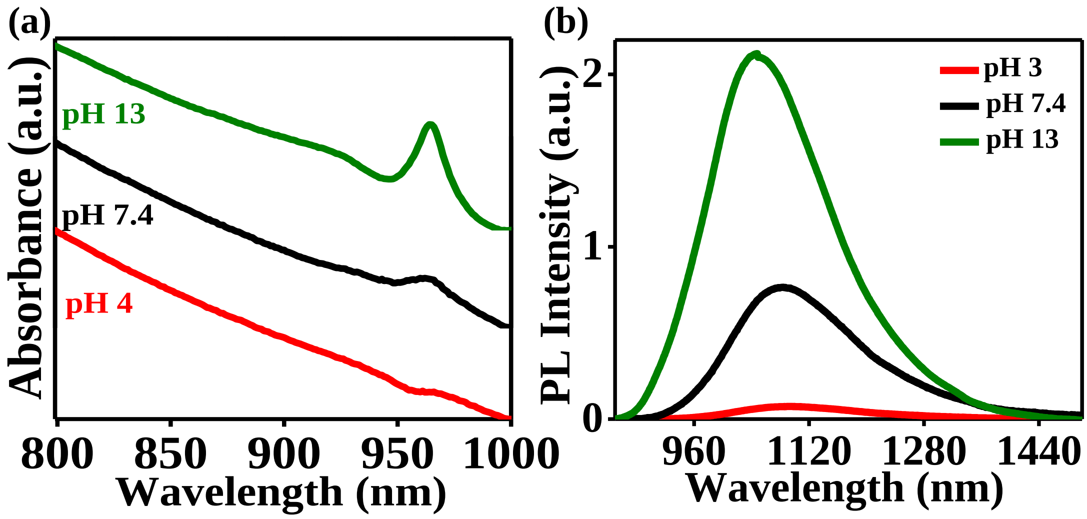

**Figure 3.16**: (a) UV-absorption spectrum of aqueous $Ag_2S/ZnS$ NCs at different pH solutions (b) PL spectra of aqueous $Ag_2S/ZnS$ NCs in different pH solutions.

**Photostability of aqueous $Ag_2S/ZnS$ core/shell NCs:** Figure 3.16 shows that not only core/shell NCs have higher PL QY but also are more photo-stable. Under continuous irradiation of the NCs with a blue LED, aqueous $Ag_2S/ZnS$ NCs retained high QY for more than 2 hour. Clearly, the protective inorganic ZnS shell is crucial for the improved photostability of $Ag_2S/ZnS$ NCs.

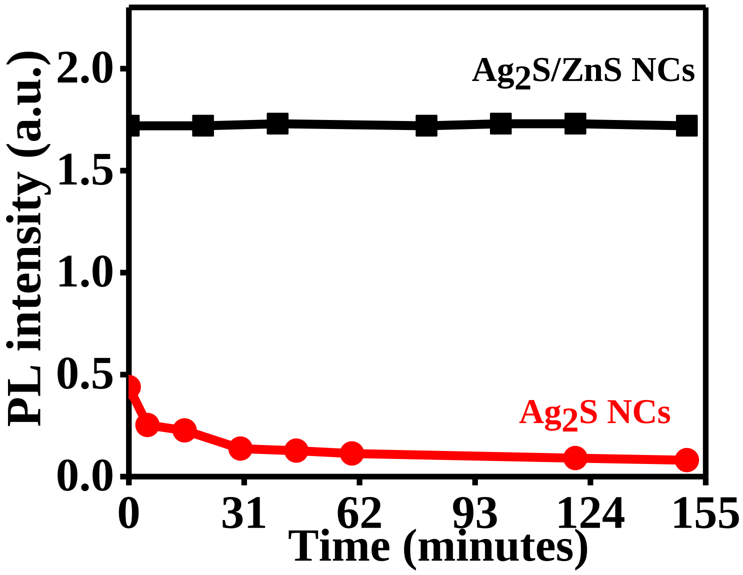

**Figure 3.17:** Comparison between PL intensities for the photostability test performed on the water-soluble $Ag_2S$ NCs and aqueous $Ag_2S/ZnS$ core/shell NCs.

## 3.4. Conclusion

In this chapter, we prepared aqueous-soluble $Ag_2S$ NCs via phase transfer reaction using *L*-cysteine as a zwitterionic ligand. Within 2 hours, the phase transfer reaction was complete, yielding *L*-cysteine-capped $Ag_2S$ NCs (QD1 and QD2) in high yield (~91-93%). The NCs exhibited QY~5.5-5.6 %, which is better than organic NIR-II dyes in water.[71,72] These NCs exhibited high colloidal stability (~1 month). The PL QY was sensitive to the pH of the solution with high QY in basic pH and vice-versa. Under blue-LED light, the NCs exhibited photostability for up to 15 minutes. The larger-sized NCs were more photostable as compared to smaller NCs.

To improve PL QY and photostability, $Ag_2S$/ZnS core-shell NCs were synthesized using substituted thiourea as a sulfur source. Overcoating $Ag_2S$ NCs with a ZnS shell of 0.3 nm thickness increased the PL QY from 6.2 % to 9.3 %. Furthermore, upon phase transfer of these core/shell NCs to an aqueous medium using L-cysteine, the NCs retained 73 % PL QY. The aqueous core/shell NCs also showed enhanced photostability under blue-LED (up to 2 hour) and colloidal stability (~48 days).

**Table 3.2:** Summary of the results.

| **NCs** | **$Ag_2S$** | **$Ag_2S/ZnS$** |
|---|---|---|
| QY(organic phase, TCE) | 6.2 % | 12.2 % |
| QY(organic phase, $H_2O$) | 5.9 % | 9.3 % |
| pH sentivity | sensitive | sensitive |
| UV-vis (1st excitonic peak) | distinct | distinct |
| Colloidal stability | stable over a month | stable for 48 days |
| Particle size (TEM) | (2.2 ± 0.52) nm | (2.5 ± 1.1) nm |
| Crystallite phase (XRD) | monoclinic | Wurtzite |
| Phase stability (XRD) | stable | stable |
| Photostability (under blue LED) | stable for 15 min | stable over 2 hours |

## 3.5. Experimental section

**3.5.1. Materials and general considerations:** The materials used were listed as follows:

| **Chemicals** | **Purity/Grade** | **Source** |
|---|---|---|
| Toluene | 95% | Sigma Aldrich |
| Dimethoxy ethane (DME) | ≥99% | Sigma Aldrich |
| Tetramethylammonium hydroxide (TMAH) | ≥99% | Sigma Aldrich |
| Tetrachloroethylene | ≥99% | Sigma Aldrich |
| 1-Octadecene | 90% | Sigma Aldrich |
| Triethylamine | ≥99% | Sigma Aldrich |
| Octylamine | 99% | Sigma Aldrich |
| Oleylamine | 70% | Sigma Aldrich |
| Phenyl isothiocyanate | 98% | Sigma Aldrich |
| L-cysteine | ≥97% | Sigma Aldrich |
| Zinc acetate | 99% | Sigma Aldrich |
| Chloroform | ≥99% | Sigma Aldrich |
| Hexane | ≥99% | Sigma Aldrich |
| Disodium hydrogen phosphate | 98% | Sigma Aldrich |
| Monopotassium phosphate | 98% | Sigma Aldrich |
| Sodium chloride | 99% | Sigma Aldrich |
| Potassium chloride | 99% | Sigma Aldrich |
| Sodium hydroxide | 98% | Sigma Aldrich |
| Hydrochloric acid | ≥97% | Sigma Aldrich |
| Silver Nitrate | 99% | Thomas Baker |
| P-toluidine | 99% | TCI |
| 4-methoxyaniline | 99% | TCI |
| 4-nitoaniline | 99% | TCI |
| p-iodoaniline | 99% | TCI |

|  |  |  |
|---|---|---|
| 1-dodecanethiol (DDT) | ≥98% | TCI |
| 1-octane thiol | ≥98% | TCI |

The UV lamp or $I_2$ stain in TLC was used to visualize the spots.

### 3.5.2. Characterization Methods

**NMR:** The Bruker ASCENDTM (400 MHz) spectrometer was used to record the $^1$H NMR, $^{13}$C NMR, with either $CDCl_3$ or $D_2O$, or DMSO-$d_6$ as the solvent. The multiplicities were indicated as *s* for singlet, *d* for doublet, *t* for triplet, *q* for quartet, and m for multiplet. The solid samples were tested for their solubility in the desired solvents and mixed in a glass vial. Using a glass Pasteur pipette, the sample was transferred to the NMR tube. The NMR tube was then labeled and scanned in the NMR instrument.

**UV-Vis spectrophotometer:** To obtain the UV-visible absorption spectra, the PerkinElmer spectrophotometer with a scan rate of 480 nm/s and Agilent Technologies Cary 100 UV-vis were employed. For these measurements, the sample was dissolved in either anhydrous hexane or anhydrous tetrachloroethylene (TCE).

**Vis-NIR spectrofluorometer:** The PL spectra of $Ag_2X$ (X=S, Se) NCs were obtained using the HORIBA Scientific spectrophotometer (Model: PTI-QM 510). The NCs were distributed in either hexane or TCE and the solution.

**TEM:** In order to obtain TEM images, the JEOL-JEM-2100 Plus electron microscope was used. HRTEM images were captured using a 200 kV electron source. To prepare the samples, a nanocrystal solution in hexane was drop-casted onto a carbon-coated surface. The copper grids, which were purchased from EMS, were stored in a vacuum desiccator overnight. The average particle size was determined using 400 particles. The lattice fringes were used to obtain the lattice plane and calculations were performed using the Image J program.

**FTIR:** The FT-IR spectra were obtained using the Bruker ALPHA E, 200396 instrument. Liquid samples are immediately dropped onto the surface of the instruments, and the spectrum was obtained. For solid samples, they were first ground in a mortar along with anhydrous potassium bromide (KBr). Then, a piece of paper was taken and a hole was cut out of it. The grounded sample was then poured into this hole, and a pallet was made using a hydraulic press. The resulting sample was inserted into the IR sample holder, attached with scotch tape, and then analyzed by running the spectrum.

**XRD:** The $Ag_2X$ (X=S, Se) NCs, which had undergone purification, were dissolved in hexane and deposited on a clean and dry glass slide using a drop-casting technique. The resulting film on the glass slide was then analyzed using the PANalytical X-Ray diffractometer, where Cu Kα (λ=1.54 Å) as the incident radiation (40 kV and 30 mA).

### 3.5.3. Synthesis

**Substituted thiourea synthesis (*Method A*):** The synthesis method used was based on previously published research, but with some minor adjustments. [35] A typical synthesis involved mixing a solution of phenyl isothiocyanate (5.0 mmol) in toluene with a solution of aniline 5.0 mmol in 10 mL toluene 10 mL. The resulting mixture was stirred for a specified duration, after which the precipitate was thoroughly dried under vacuum to remove toluene. This resulted in extremely good yields of the required precursor.

**Thiocarbamate and dithiocarbamate substitutes (*Method B*)**: The thiocarbamate and dithiocarbamate derivatives were prepared with some slight modifications to a previous study.[83] A solution of 5.0 mmol thiol or phenols in 10 mL acetonitrile was mixed with phenyl isothiocyanate (5.0 mmol) in acetonitrile. Triethylamine (5.0 mmol) was added to the mixture, and the reaction was stirred for 24 hours at 75 °C in an inert atmosphere. The solvents were then removed under vacuum in a rotating evaporator before adding n-hexane. The produced precipitates (thiocarbamate or dithiocarbamate) were filtered using a Buchner funnel and washed twice or thrice with n-hexane. The desired product (precursor) was dried in a desiccator before using it in an experiment.

**Synthesis of $Ag_2S$/ZnS core/shell NCs:** The temperature of the as-synthesized $Ag_2S$ NCs (Section 3.9.2) solution was maintained at 150 °C under an $N_2$ atmosphere. At this point, silver acetate, 0.1 mmol dissolved in oleylamine, and ODE mixed in a round button flask named A are vacuumed for 15 minutes at room temperature, RT. Meanwhile, S-precursor, 0.1 mmol dissolved in DME was mixed in Flask A. Thereafter, the cold precursor was added to the reaction solution for coating a ZnS shell on the $Ag_2S$ nanocrystals.[74] To monitor the growth of the nanoparticles, aliquots were taken at different reaction times, 5, 10, 15, and 60 minutes respectively for absorption and FL measurements. Then, the reaction mixture was quickly quenched in a cold ice bath.

**NCs purification:** The QDs were initially mixed with 4 mL of ethanol/methanol and 1 mL of hexane. After being centrifuged twice at 6000 rpm for 15 minutes, the supernatant was discarded, and the precipitate was mixed with 3 mL of ethanol/methanol, 1 mL of hexane, and 1 mL of toluene. This mixture was then centrifuged twice at 6000 rpm for 5 minutes. The resulting QDs were dispersed in 0.5 mL of toluene and centrifuged for 2 minutes at 6000 rpm. Finally, the QDs were dispersed in 1 mL of hexane/TCE and centrifuged once at 3000 rpm for further purification.

**Phase transfer of $Ag_2S$ QDs:** The $Ag_2S$ QDs emitting at 1024 nm, 1065 nm, 1133nm and 1200 nm obtained from different S-precursors *viz.,* **a, b, c, d** respectively were subjected to the phase transfer process to replace the hydrophobic ligand (DDT) with hydrophilic ligand (*L*-cysteine). The purified precipitate of $Ag_2S$ QDs (0.102g) was dispersed in 2 mL of chloroform. Simultaneously, 0.45 mg of *L*-cysteine was dissolved in 2 mL of Millipore water by dropwise addition of tetramethyl ammonium hydroxide and the pH of the system was maintained at the range of ~9.2 These two solutions were mixed and the corresponding biphasic mixtures were stirred vigorously for 2 h at 14000 rpm at room temperature. The phase transferred $Ag_2S$ QDs in water were washed three times with pure Millipore water using a micro spin-X filter (0.22 micrometre) and further, the QDs were dispersed in 1.5 ml of water.[11,73]

**Phase transfer of $Ag_2S$/ZnS core-shell QDs:** The $Ag_2S$/ZnS QDs emitting at 1065 nm obtained from S-precursor **b,** were subjected to the phase transfer process to replace the hydrophobic ligand (DDT) with hydrophilic ligand (*L*-cysteine). The purified precipitate of $Ag_2S$/ZnS QDs (0.150g) was dispersed in 2 mL of chloroform. Simultaneously, 0.65 mg of *L*-cysteine was dissolved in 2 mL of Millipore water by dropwise addition of tetramethyl ammonium hydroxide and the pH of the system was maintained at the range of ~9.2 These two solutions were mixed and the corresponding biphasic mixtures were stirred vigorously for 2 h at 14000 rpm at room temperature. The phase transferred $Ag_2S$ QDs in water were washed three times with pure Millipore water using a micro spin-X filter (0.22 micrometre) and further, the QDs were dispersed in 1.5 ml of water.[73]

**Preparation of PBS buffer:** In order to prepare 100 mL of PBS buffer, 8 g of NaCl, 0.2 g of KCl, 1.78 g of disodium hydrogen phosphate dihydrate, $Na_2HPO_4.2H_2O$, and 0.24 g of mono-potassium phosphate, $KH_2PO_4$. are mixed together and the final volume is adjusted to 100 mL Millipore water. Further, it was diluted to 1X PBS concentration to adjust the pH at 7.4. The required pH is further adjusted by adding hydrochloric acid and sodium hydroxide to the PBS solution.[76]

**Calculation of quantum yield (QY)**: The fluorescence quantum yield of QDs in water and organic solvent (TCE) was calculated using the integrated fluorescence intensity of QDs and comparing it with a standard dye called IR-140. By measuring the integrated fluorescence spectrum of $Ag_2S$ in water and TCE with five different concentrations, linear fits were used to determine the quantum yield by comparing the slopes with the reference IR-140 ($\Phi_f$ = 0.167, ethanol). To find the relative quantum yield of an unknown sample, its emission and absorption were compared with those of the QDs with known QY using a specific equation given below

$$QY_S = QY_R \times \frac{I_S \times A_R \times {n_S}^2}{I_R \times A_S \times {n_R}^2}$$

The average value was reported after performing measurements on $Ag_2S$ CQDs at five different concentrations. The measurements involved calculating the integrated PL intensity represented by the symbol $I$, the refractive index represented by the symbol $n$, and the absorbance (at the excitation wavelength) represented by the symbol $A$. The subscripts $R$ and $S$ refer to the reference and sample respectivel.[73]

**Photo-stability:** Four different $Ag_2S$ NCs samples in an aqueous medium (*Viz.*, QD1, QD2, $QD_{1065}$ and $QD_{1133}$) were photo-irradiated under blue LED (The illumination intensity of the blue LED Light are 461 nm and 0.363mW/cm$^2$ at a distance of 100 cm respectively) for 2h and PL intensity was measured at different time intervals.

**NMR Spectral Data: (*cf.* NMR spectra in Annexure, A2.1.1)**

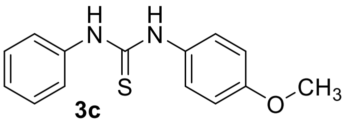
3c

**1-(4-Methoxyphenyl)-3-phenylthiourea (a).** To obtain 1-(4-methoxyphenyl)-3-phenylthiourea with a yield of 91%, a solution of 4-methoxyaniline (0.62 g, 5.0 mmol) in toluene (10 mL) and a solution of phenyl isothiocyanate (0.07 g, 5 mmol) in toluene (10 mL) were reacted using the general procedure (Method *A*). The resulting compound (a) was obtained. $^{1}$H NMR (400 MHz, $CDCl_3$) δ 7.75 (s, broad, 2H), 7.39 (d, 4H, *J*=4.2 Hz), 7.29–7.27 (m, 3H), 6.94 (d, 2H, *J*=8.8 Hz), 3.82 (s, 3H). $^{13}$C {$^{1}$H} NMR (100 MHz, $CDCl_3$) 180.7, 159.0, 129.6, 127.7, 127.0, 125.3, 115.0, 55.5.

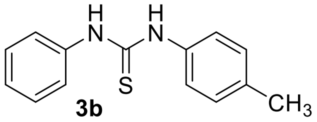
3b

**1-Phenyl-3-*p*-tolylthiourea (b).** Compound (b) was obtained in 80% yield by reacting solutions of *p*-toluidine (0.54 g, 5.0 mmol) in toluene (10 mL) and phenyl isothiocyanate (0.07 g, 5 mmol) in toluene (10 mL) according to the general procedure (Method *A*). $^{1}$H NMR (400 MHz, DMSO-$d_6$) δ 9.70 (s, 2H), 7.50 (d, 2H, *J*=7.7 Hz), 7.37–7.30 (m, 4H), 7.15–7.10 (m, 3H), 2.28 (s, 3H). $^{13}$C {$^{1}$H} NMR (100 MHz, DMSO-$d_6$) 179.6, 139.5, 136.7, 133.6, 128.3, 124.3, 123.8, 123.6, 20.5.

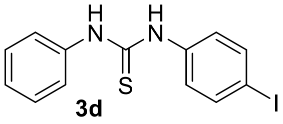
3d

**1-(4-Iodophenyl)-3-phenylthiourea (c).** The compound 1-(4-iodophenyl)-3-phenylthiourea was synthesized using the general procedure (Method *A*). This involved reacting solutions of *p*-iodoaniline (1.09 g, 5.0 mmol) in toluene (10 mL) and phenyl isothiocyanate (0.07 g, 5 mmol) in toluene (10 mL). The yield of the product (c) obtained was 60%. $^{1}$H NMR (400 MHz, DMSO-$d_6$) *δ* 9.84 (d, 2H *J*=12.8 Hz), 7.66 (d, 2H, *J*=8.5 Hz), 7.47 (d, 2H, *J*=7.9 Hz), 7.33 (*t*, 4H, *J*= 8.3 Hz), 7.13 (*t*, 1H, *J*=7.3 Hz). $^{13}$C {$^{1}$H} NMR (100 MHz, DMSO-$d_6$) 179.4, 139.3, 139.2, 137.0, 128.4, 125.6, 124.5, 123.6, 88.4.

**1-(4-Nitrophenyl)-3-phenylthiourea** (**d**). According to the standard procedure (Method *A*), a solution of *p*-nitroaniline (0.69 g, 5.0 mmol) in acetonitrile (10 mL) was reacted with a solution of phenyl isothiocyanate (0.07 g, 5 mmol) in acetonitrile (10 mL) to prepare 1-(4-nitrophenyl)-3-phenylthiourea. The reaction is refluxed for 24 h at 80 °C to give **(d)** in 41% yield. $^{1}$H NMR (400 MHz, $CDCl_3$) $\delta$ 8.09 (d, 2H, *J* = 9.0 Hz), 7.39–7.23 (m, 5H), 6.64 (d, 2H, *J*= 9.0 Hz), 4.42 (s, 2H). $^{13}$C {$^{1}$H} NMR (100 MHz, $CDCl_3$) 182.9, 147.6, 130.1, 120.8, 113.4, 109.2, 100.3.

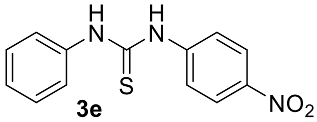

**3e**

## 3.6 References

(1) Murray, C. B.; Norris, D. J.; Bawendi, M. G. Synthesis and Characterization of Nearly Monodisperse CdE (E = Sulfur, Selenium, Tellurium) Semiconductor Nanocrystallites. *J Am Chem Soc* **1993**, *115*, 2984–2988.

(2) Chan, W. C. W.; Nie, S. Quantum Dot Bioconjugates for Ultrasensitive Non-isotopic Detection. *Science (1979)* **1998**, *281*, 2016–2018.

(3) Medintz, I. L.; Uyeda, H. T.; Goldman, E. R.; Mattoussi, H. Quantum Dot Bioconjugates for Imaging, Labelling and Sensing. *Nat Mater* **2005**, *4*, 435–446.

(4) Bruchez, M.; Moronne, M.; Gin, P.; Weiss, S.; Alivisatos, A. P. Semiconductor Nanocrystals as Fluorescent Biological Labels. *Science (1979)* **1998**, *281*, 2013–2016.

(5) Sun, H.; Zhang, H.; Ju, J.; Zhang, J.; Qian, G.; Wang, C.; Yang, B.; Wang, Z. Y. One-Step Synthesis of High-Quality Gradient CdHgTe Nanocrystals: A Prerequisite to Prepare CdHgTe−Polymer Bulk Composites with Intense Near-Infrared Photoluminescence. *Chemistry of Materials* **2008**, *20*, 20431–20456.

(6) Moreels, I.; Justo, Y.; de Geyter, B.; Haustraete, K.; Martins, J. C.; Hens, Z. Size-Tunable, Bright, and Stable PbS Quantum Dots: A Surface Chemistry Study. *ACS Nano* **2011**, *5*, 2031–2056.

(7) Ellingson, R. J.; Beard, M. C.; Johnson, J. C.; Yu, P.; Micic, O. I.; Nozik, A. J.; Shabaev, A.; Efros, A. L. Highly Efficient Multiple Exciton Generation in Colloidal PbSe and PbS Quantum Dots. *Nano Lett* **2005**, *5*, 2112–2130.

(8) Murphy, J. E.; Beard, M. C.; Norman, A. G.; Ahrenkiel, S. P.; Johnson, J. C.; Yu, P.; Mićić, O. I.; Ellingson, R. J.; Nozik, A. J. PbTe Colloidal Nanocrystals: Synthesis, Characterization, and Multiple Exciton Generation. *J Am Chem Soc* **2006**, *128*, 3241–3247.

(9) Du, Y.; Xu, B.; Fu, T.; Cai, M.; Li, F.; Zhang, Y.; Wang, Q. Near-Infrared Photoluminescent $Ag_2S$ Quantum Dots from a Single Source Precursor. *J Am Chem Soc* **2010**, *132*, 1470–1471.

(10) Aharoni, A.; Mokari, T.; Popov, I.; Banin, U. Synthesis of InAs/CdSe/ZnSe Core/Shell1/Shell2 Structures with Bright and Stable Near-Infrared Fluorescence. *J Am Chem Soc* **2006**, *128*, 257–264.

(11) Tamang, S.; Beaune, G.; Texier, I.; Reiss, P. Aqueous Phase Transfer of InP/ZnS Nanocrystals Conserving Fluorescence and High Colloidal Stability. *ACS Nano* **2011**, *5*, 9392–9402.

(12) Zhang, X.; Liu, M.; Liu, H.; Zhang, S. Low-Toxic $Ag_2S$ Quantum Dots for Photoelectrochemical Detection Glucose and Cancer Cells. *Biosens Bioelectron* **2014**, *56*, 307–312.

(13) Brevig, T.; Krühne, U.; Kahn, R. A.; Ahl, T.; Beyer, M.; Pedersen, L. H. Hydrodynamic Guiding for Addressing Subsets of Immobilized Cells and Molecules in Microfluidic Systems. *BMC Biotechnol* **2003**, *3*, 3–10.

(14) Gui, R.; Sun, J.; Liu, D.; Wang, Y.; Jin, H. Retracted Article: A Facile Cation Exchange-Based Aqueous Synthesis of Highly Stable and Biocompatible $Ag_2S$ Quantum Dots Emitting in the Second near-Infrared Biological Window. *Dalton Transactions* **2014**, *43*, 16690–16697.

(15) Xie, R.; Chen, K.; Chen, X.; Peng, X. InAs/InP/ZnSe Core/Shell/Shell Quantum Dots as near-Infrared Emitters: Bright, Narrow-Band, Non-Cadmium Containing, and Biocompatible. *Nano Res* **2008**, *1*, 457–464.

(16) Tamang, S.; Beaune, G.; Texier, I.; Reiss, P. Aqueous Phase Transfer of InP/ZnS Nanocrystals Conserving Fluorescence and High Colloidal Stability. *ACS Nano* **2011**, *5*, 9392–9402.

(17) di Zhang. Syntheses and Characterizations of Cysteine-Derived Compounds and Polymers, *ACS Nano* **2017**, *4*, 1381–1385.

(18) Muro, E.; Pons, T.; Lequeux, N.; Fragola, A.; Sanson, N.; Lenkei, Z.; Dubertret, B. Small and Stable Sulfobetaine Zwitterionic Quantum Dots for Functional Live-Cell Imaging. *J Am Chem Soc* **2010**, *132*, 4556–4557.

(19) Liu, W.; Choi, H. S.; Zimmer, J. P.; Tanaka, E.; Frangioni, J. v.; Bawendi, M. Compact Cysteine-Coated CdSe(ZnCdS) Quantum Dots for in Vivo Applications. *J Am Chem Soc* **2007**, *129*, 14530–14531.

(20) Singh, A.; Kunwar, A.; Rath, M. C. L-Cysteine Capped CdSe Quantum Dots Synthesized by Photochemical Route. *J Nanosci Nanotechnol* **2018**, *18*, 3419–3426.

(21) Tang, B.; Liu, B.-H.; Liu, Z.-Y.; Luo, M.-Y.; Shi, X.-H.; Pang, D.-W. Quantum Dots with a Compact Amphiphilic Zwitterionic Coating. *ACS Appl Mater Interfaces* **2022**, *14*, 28097–28104.

(22) Li, J.; Yang, T.; Chan, W. H.; Choi, M. M. F.; Zhao, D. Synthesis of High-Quality *N* -Acetyl-Cysteine-Capped CdTe Quantum Dots by Hydrothermal

Route and the Characterization through MALDI-TOF Mass Spectrometry. *The Journal of Physical Chemistry C* **2013**, *117*, 19175–19181.

(23) Zhang, H.; Sun, P.; Liu, C.; Gao, H.; Xu, L.; Fang, J.; Wang, M.; Liu, J.; Xu, S. L-Cysteine Capped CdTe-CdS Core-Shell Quantum Dots: Preparation, Characterization and Immuno-Labeling of HeLa Cells. *Luminescence* **2011**, *26*, 86–92.

(24) Sarangi, S. N.; Hussain, A. M. P.; Sahu, S. N. Strong UV Absorption and Emission from L-Cysteine Capped Monodispersed Gold Nanoparticles. *Appl Phys Lett* **2009**, *95*, 073109–073115.

(25) Liang, G.-X.; Gu, M.-M.; Zhang, J.-R.; Zhu, J.-J. Preparation and Bioapplication of High-Quality, Water-Soluble, Biocompatible, and near-Infrared-Emitting CdSeTe Alloyed Quantum Dots. *Nanotechnology* **2009**, *20*, 415103–415107.

(26) Bu, H.-B.; Yokota, H.; Shimura, K.; Takahasi, K.; Taniguchi, T.; Kim, D. Hydrothermal Synthesis of *N*-Acetyl-L-Cysteine-Capped $CuInS_2$ Nanoparticles. *Chem Lett* **2015**, *44*, 200–202.

(27) Liu, W.; Choi, H. S.; Zimmer, J. P.; Tanaka, E.; Frangioni, J. v.; Bawendi, M. Compact Cysteine-Coated CdSe(ZnCdS) Quantum Dots for in Vivo Applications. *J Am Chem Soc* **2007**, *129*, 14530–14531.

(28) Liu, W.; Hak, S. C.; Zimmer, J. P.; Tanaka, E.; Frangioni, J. v.; Bawendi, M. Compact Cysteine-Coated CdSe(ZnCdS) Quantum Dots for in Vivo Applications. *J Am Chem Soc* **2007**, *129*, 14530–14531.

(29) Liu, X.; Braun, G. B.; Qin, M.; Ruoslahti, E.; Sugahara, K. N. In Vivo Cation Exchange in Quantum Dots for Tumor-Specific Imaging. *Nat Commun* **2017**, *8*, 343–346.

(30) Jin, S.; Hu, Y.; Gu, Z.; Liu, L.; Wu, H.-C. Application of Quantum Dots in Biological Imaging. *J Nanomater* **2011**, *2011*, *6*, 1–13.

(31) Matea, C.; Mocan, T.; Tabaran, F.; Pop, T.; Mosteanu, O.; Puia, C.; Iancu, C.; Mocan, L. Quantum Dots in Imaging, Drug Delivery and Sensor Applications. *Int J Nanomedicine* **2017**, *12*, 5421–5431.

(32) Gil, H. M.; Price, T. W.; Chelani, K.; Bouillard, J.-S. G.; Calaminus, S. D. J.; Stasiuk, G. J. NIR-Quantum Dots in Biomedical Imaging and Their Future. *iScience* **2021**, *24*, 102189–102190.

(33) Martynenko, I. v.; Litvin, A. P.; Purcell-Milton, F.; Baranov, A. v.; Fedorov, A. v.; Gun'ko, Y. K. Application of Semiconductor Quantum Dots in Bioimaging and Biosensing. *J Mater Chem B* **2017**, *5*, 6701–6727.

(34) Sadovnikov, S. I.; Gusev, A. I.; Chukin, A. v.; Rempel, A. A. High-Temperature X-Ray Diffraction and Thermal Expansion of Nanocrystalline and Coarse-Crystalline Acanthite α-$Ag_2S$ and Argentite β-$Ag_2S$. *Physical Chemistry Chemical Physics* **2016**, *18*, 4617–4626.

(35) Du, Y.; Xu, B.; Fu, T.; Cai, M.; Li, F.; Zhang, Y.; Wang, Q. Near-Infrared Photoluminescent $Ag_2S$ Quantum Dots from a Single Source Precursor. *J Am Chem Soc* **2010**, *132*, 1470–1471.

(36) Gao, X.; Chan, W. C. W.; Nie, S. Quantum-Dot Nanocrystals for Ultrasensitive Biological Labeling and Multicolor Optical Encoding. *J Biomed Opt* **2002**, *7*, 532–534.

(37) Baral, S.; Fojtik, A.; Weller, H.; Henglein, A. Photochemistry and Radiation Chemistry of Colloidal Semiconductors. 12. Intermediates of the Oxidation of Extremely Small Particles of Cadmium Sulfide, Zinc Sulfide, and Tricadmium Diphosphide and Size Quantization Effects (a Pulse Radiolysis Study). *J Am Chem Soc* **1986**, *108*, 375–378.

(38) Spanhel, L.; Haase, M.; Weller, H.; Henglein, A. Photochemistry of Colloidal Semiconductors. 20. Surface Modification and Stability of Strong Luminescing CdS Particles. *J Am Chem Soc* **1987**, *109*, 5649–5655.

(39) Ren, Q.; Ma, Y.; Zhang, S.; Ga, L.; Ai, J. One-Step Synthesis of Water-Soluble Silver Sulfide Quantum Dots and Their Application to Bioimaging. *ACS Omega* **2021**, *6*, 6361–6367.

(40) Schwabacher, J. C.; Kodaimati, M. S.; Weiss, E. A. Origin of the PH Dependence of Emission of Aqueous Dihydrolipoic Acid-Capped PbS Quantum Dots. *The Journal of Physical Chemistry C* **2019**, *123*, 17574–17579.

(41) Wang, Y.; Hu, R.; Lin, G.; Law, W.-C.; Yong, K.-T. Optimizing the Aqueous Phase Synthesis of CdTe Quantum Dots Using Mixed-Ligands System and Their Applications for Imaging of Live Cancer Cells and Tumors in Vivo. *RSC Adv* **2013**, *3*, 8899–8901.

(42) Rajabi, H. R.; Karimi, F.; Kazemdehdashti, H.; Kavoshi, L. Fast Sonochemically-Assisted Synthesis of Pure and Doped Zinc Sulfide Quantum

Dots and Their Applicability in Organic Dye Removal from Aqueous Media. *J Photochem Photobiol B* **2018**, *181*, 98–105.

(43) Liu, M.; Wang, L.; Guan, Z.; Liu, Z.; Zhu, Y.; Tang, A. Doping of Cu Ions into CdS/ZnS Core/Shell Nanocrystals through a Cation Exchange Strategy. *J Mater Chem C Mater* **2019**, *7*, 15285–15289.

(44) Bear, J. C.; Hollingsworth, N.; Roffey, A.; McNaughter, P. D.; Mayes, A. G.; Macdonald, T. J.; Nann, T.; Ng, W. H.; Kenyon, A. J.; Hogarth, G.; Parkin, I. P. Doping Group IIB Metal Ions into Quantum Dot Shells via the One-Pot Decomposition of Metal-Dithiocarbamates. *Adv Opt Mater* **2015**, *3,* 704–712.

(45) Jiang, P.; Wang, R.; Chen, Z. Thiol-Based Non-Injection Synthesis of near-Infrared $Ag_2S$/ZnS Core/Shell Quantum Dots. *RSC Adv* **2015**, *5*, 56789–56793.

(46) Mirahmadi, F. S.; Marandi, M.; Karimipour, M.; Molaei, M. Microwave Activated Synthesis of $Ag_2S$ and $Ag_2S$@ZnS Nanocrystals and Their Application in Well-Performing Quantum Dot Sensitized Solar Cells. *Solar Energy* **2020**, *202*, 155–163.

(47) Ghosh Chaudhuri, R.; Paria, S. Optical Properties of Double-Shell Hollow ZnS-$Ag_2S$ Nanoparticles. *Journal of Physical Chemistry C* **2013**, *117*, 23385–23390.

(48) Haghighatzadeh, A.; Kiani, M.; Mazinani, B.; Dutta, J. Facile Synthesis of ZnS–$Ag_2S$ Core–Shell Nanospheres with Enhanced Nonlinear Refraction. *Journal of Materials Science: Materials in Electronics* **2020**, *31*, 1283–1292.

(49) Ovchinnikov, O.; Aslanov, S.; Smirnov, M.; Perepelitsa, A.; Kondratenko, T.; Selyukov, A.; Grevtseva, I. Colloidal $Ag_2S$/SiO 2 Core/Shell Quantum Dots with IR Luminescence . *Opt Mater Express* **2021**, *11*, 89–95.

(50) Karimipour, M.; Moradi, N.; Molaei, M. Strong NIR Luminescent $Ag_2S$@ZnS Core-Shells Synthesized by a Novel One Pot Pulsed Microwave Irradiation. *J Lumin* **2017**, *182*, 91–97.

(51) Ovchinnikov, O. v.; Perepelitsa, A. S.; Smirnov, M. S.; Latyshev, A. N.; Grevtseva, I. G.; Vasiliev, R. B.; Goltsman, G. N.; Vitukhnovsky, A. G. Luminescence of Colloidal $Ag_2S$/ZnS Core/Shell Quantum Dots Capped with Thioglycolic Acid. *J Lumin* **2020**, *220*, 117008–117009.

(52) Reiss, P.; Protière, M.; Li, L. Core/Shell Semiconductor Nanocrystals. *Small* **2009**, *5*, 154–168.

(53) Zhu, G.; Xu, Z. Controllable Growth of Semiconductor Heterostructures Mediated by Bifunctional $Ag_2S$ Nanocrystals as Catalyst or Source-Host. *J Am Chem Soc* **2011**, *133*, 148–157.

(54) Ovchinnikov, O.; Aslanov, S.; Smirnov, M.; Perepelitsa, A.; Kondratenko, T.; Selyukov, A.; Grevtseva, I. Colloidal $Ag_2S/SiO_2$ Core/Shell Quantum Dots with IR Luminescence. *Opt Mater Express* **2021**, *11*, 411432–411434.

(55) Jiang, P.; Zhu, D.-L.; Zhu, C.-N.; Zhang, Z.-L.; Zhang, G.-J.; Pang, D.-W. A Highly Reactive Chalcogenide Precursor for the Synthesis of Metal Chalcogenide Quantum Dots. *Nanoscale* **2015**, *7*, 1039–1041.

(56) Li, J. J.; Wang, Y. A.; Guo, W.; Keay, J. C.; Mishima, T. D.; Johnson, M. B.; Peng, X. Large-Scale Synthesis of Nearly Monodisperse CdSe/CdS Core/Shell Nanocrystals Using Air-Stable Reagents via Successive Ion Layer Adsorption and Reaction. *J Am Chem Soc* **2003**, *125*, 363563–363571.

(57) Li, L.; Pandey, A.; Werder, D. J.; Khanal, B. P.; Pietryga, J. M.; Klimov, V. I. Efficient Synthesis of Highly Luminescent Copper Indium Sulfide-Based Core/Shell Nanocrystals with Surprisingly Long-Lived Emission. *J Am Chem Soc* **2011**, *133*, 1176–1179

(58) Chen, B.; Zhong, H.; Zhang, W.; Tan, Z.; Li, Y.; Yu, C.; Zhai, T.; Bando, Y.; Yang, S.; Zou, B. Highly Emissive and Color-Tunable $CuInS_2$-Based Colloidal Semiconductor Nanocrystals: Off-Stoichiometry Effects and Improved Electroluminescence Performance. *Adv Funct Mater* **2012**, *22*, 7611–7615.

(59) Deng, D.; Chen, Y.; Cao, J.; Tian, J.; Qian, Z.; Achilefu, S.; Gu, Y. High-Quality $CuInS_2$/ZnS Quantum Dots for In Vitro and In Vivo Bioimaging. *Chemistry of Materials* **2012**, *24*, 3029–3037.

(60) Jayabharathi, J.; Sundari, G. A.; Thanikachalam, V.; Jeeva, P.; Panimozhi, S. A Dodecanethiol-Functionalized Ag Nanoparticle-Modified ITO Anode for Efficient Performance of Organic Light-Emitting Devices. *RSC Adv* **2017**, *7*, 38923–38934.

(61) Hendricks, M. P.; Campos, M. P.; Cleveland, G. T.; Plante, I. J.-L.; Owen, J. S. A Tunable Library of Substituted Thiourea Precursors to Metal Sulfide Nanocrystals. *Science (1979)* **2015**, *348*, 1226–1230.

(62) Mindl, J.; Sulzer, J.; Vecera, M. Hydrolysis Kinetics and Mechanism of Diaryldithiocarbamates in 20% Aqueous Dioxane. *Collect. Czech. Chem. Commun.* **1981**, *46*, 1970–1975.

(63) Pfeiffer, W. D.; Ahlers, K. D.; Falodun, A.; Villinger, A.; Langer, P. Synthesis and Spectroscopic Characterization of Arylated Selenoureas. *Phosphorus Sulfur Silicon Relat Elem* **2014**, *189*, 324–332.

(64) Wang, S.; Jarrett, B. R.; Kauzlarich, S. M.; Louie, A. Y. Core/Shell Quantum Dots with High Relaxivity and Photoluminescence for Multimodality Imaging. *J Am Chem Soc* **2007**, *129*, 3848–3856.

(65) Vinh, N. D.; Tan, P. M.; Do, P. v.; Bharti, S.; Hoa, V. X.; Hien, N. T.; Luyen, N. T.; Ca, N. X. Effect of Dopant Concentration and the Role of ZnS Shell on Optical Properties of $Sm^{3+}$ Doped CdS Quantum Dots. *RSC Adv* **2021**, *11*, 7961–7971.

(66) Hines, M. A.; Guyot-Sionnest, P. Synthesis and Characterization of Strongly Luminescing ZnS-Capped CdSe Nanocrystals. *J Phys Chem* **1996**, *100*, 468–471.

(67) Kima, S. H.; Manb, M. T.; Leea, H. S. Size and Shell Effects on CdSe Quantum Dots in Binary Ligand System. *Applied Science and Convergence Technology* **2020**, *29*, 87–90.

(68) Sadovnikov, S. I.; Gusev, A. I. Recent Progress in Nanostructured Silver Sulfide: From Synthesis and Nonstoichiometry to Properties. *J Mater Chem A Mater* **2017**, *5*, 17676–17704.

(69) Dabbousi, B. O.; Rodriguez-Viejo, J.; Mikulec, F. v.; Heine, J. R.; Mattoussi, H.; Ober, R.; Jensen, K. F.; Bawendi, M. G. (CdSe)ZnS Core−Shell Quantum Dots: Synthesis and Characterization of a Size Series of Highly Luminescent Nanocrystallites. *J Phys Chem B* **1997**, *101*, 9463–9475.

(70) Peng, X.; Schlamp, M. C.; Kadavanich, A. v.; Alivisatos, A. P. Epitaxial Growth of Highly Luminescent CdSe/CdS Core/Shell Nanocrystals with Photostability and Electronic Accessibility. *J Am Chem Soc* **1997**, *119*, 7019–7029.

(71) Zhu, S.; Yung, B. C.; Chandra, S.; Niu, G.; Antaris, A. L.; Chen, X. Near-Infrared-II (NIR-II) Bioimaging *via* Off-Peak NIR-I Fluorescence Emission. *Theranostics* **2018**, *8*, 4141–4151.

(72) Chang, Z.; Liu, F.; Wang, L.; Deng, M.; Zhou, C.; Sun, Q.; Chu, J. Near-Infrared Dyes, Nanomaterials and Proteins. *Chinese Chemical Letters* **2019**, *30*, 1856–1882.

(73) Bhardwaj, K.; Pradhan, S.; Basel, S.; Clarke, M.; Brito, B.; Thapa, S.; Roy, P.; Borthakur, S.; Saikia, L.; Shankar, A.; Stasiuk, G. J.; Pariyar, A.; Tamang, S. Tunable NIR-II Emitting Silver Chalcogenide Quantum Dots Using Thio/Selenourea Precursors: Preparation of an MRI/NIR-II Multimodal Imaging Agent. *Dalton Transactions* **2020**, *49*, 15425–15432.

(74) Jiang, P.; Wang, R.; Chen, Z. Thiol-Based Non-Injection Synthesis of near-Infrared $Ag_2$S/ZnS Core/Shell Quantum Dots. *RSC Adv* **2015**, *5*, 56789–56792.

(75) Tamang, S.; Beaune, G.; Texier, I.; Reiss, P. Aqueous Phase Transfer of InP / ZnS Nanocrystals Conserving Fluorescence. *ACS Nano* **2011**, *5*, 9392–9402.

(76) Zhou, L.; Ionescu, R. E. Influence of Saline Buffers over the Stability of High-Annealed Gold Nanoparticles Formed on Coverslips for Biological and Chemosensing Applications. *Bioengineering* **2020**, *7*, 7030068–7030069.

# Chapter IV

## *Design of MRI/NIR-II Multimodal Imaging Agent:*
## *Application of $Ag_2S$ QDs*

## 4.1. Introduction

$^1$H is the most commonly studied nucleus in Nuclear Magnetic Resonance (NMR) spectroscopy and magnetic resonance imaging (MRI). It has a non-zero spin quantum number (S=1/2) and uniform charge distribution.[1] The other nuclei include $^{13}$C and $^{14}$N as shown in Table 4.1.[2,3]

**Table 4.1:** The common nuclei and their nuclear spin.

| Nuclide | Atomic Mass | Atomic Number | Spin (*s*) |
|---|---|---|---|
| **$^1$H** | odd | odd | ½ |
| **$^{13}$C** | odd | even | ½ |
| **$^{14}$N** | even | odd | 1 |
| **$^{12}$C** | even | even | 0 |

2S+1 represents the total number of orientations a nucleus assumes under an external magnetic field. Thus, for $^1$H the total number of orientations is 2. In other words, under an external magnetic field ($B_0$), there are two spin states present viz., +1/2 (α) and -1/2 (β) as shown below. The energy difference ($\Delta E$) between these two states is given by

$$\Delta E = \frac{h\gamma}{2\pi} B_0 \tag{4.1}$$

where $h$ is the Planck constant, $\gamma$ is the magnetogyric ratio which is related to spin and magnetic moment as follows:

$$\gamma = \frac{2\pi}{hS} \mu \tag{4.2}$$

When the applied radiofrequency radiation is in resonance with the energy gap, $\Delta E$ the absorption of energy by the atomic nuclei under a magnetic field takes place, giving rise to an NMR spectrum. For example, in a 21 Tesla magnetic field $^1$H nuclei resonate at 900 MHz.[4]

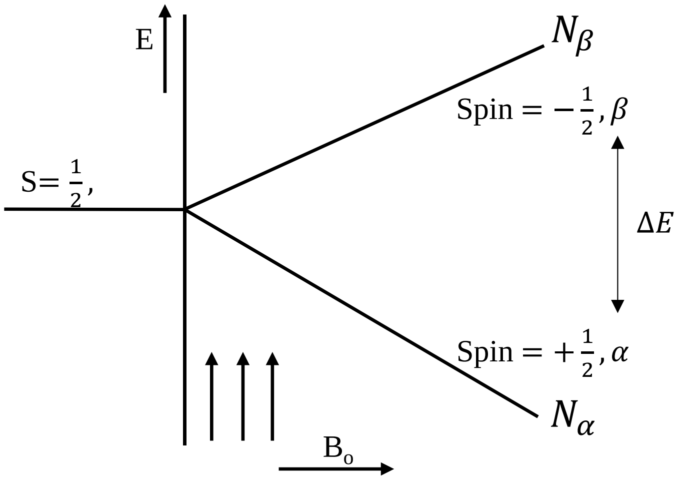

**Figure 4.1:** Alignment of magnetic moments, $\mu_z$, in a magnetic field, $B_o$.

MRI is non-radiative and non-invasive imaging of soft body tissues which is also based on the nuclear magnetic resonance phenomenon. MRI generates an image by directly exploiting the magnetic properties of $^1$H present in water inside the human body. 75 % of body weight in infants to 55% in the elderly is water.[5] When a human body is placed under a magnetic field ($B_o$), the $^1$H nuclei assume two spin states as mentioned above, one parallel to and another antiparallel to the magnetic field. RF pulses are then applied which excites the parallel lower energy state to the antiparallel higher energy state. Once the RF pulse is stopped, the nuclei relax to the ground state (parallel) and the relaxation re-emits RF radiation at their Larmor frequency.[6] Consequently, the signal is detected and converted into an image. The faster the longitudinal relaxation rate ($T_1$), the stronger is the signal intensity.[7] $T_1$ is inversely related to the relaxation rate ($R_1 = 1/T_1$). To improve the signal/noise ratio, a contrast agent is commonly injected intravenously.[3] Approximately one-third of clinical scans use a contrast agent.[8] The $T_1$-contrast agent works by interacting with the $H_2O$ protons, either by modifying their $R_1$ ($i.e.,\ T_1$) or by directly influencing the level of $H_2O$ magnetization. $Mn^{2+,}$ $Mn^{3+}$, $Fe^{3+}$, $Cu^{2+}$, and $Gd^{3+}$ are all paramagnetic metal ions that can be used to enhance contrast. $Gd^{3+}$ is the most commonly used $T_1$-contrast agents because its strong paramagnetic nature.[9,10] Solomon, Bloembergen, and Morgan (SBM) equation can be used to describe the mechanism of longitudinal (also, latitudinal) relaxation in the presence of paramagnetic ions.[11] The observed longitudinal relaxation time ($1/T_{1,obs}$) of $H_2O$ is related to both the diamagnetic ($1/T_{1,dia}$) and the paramagnetic ($1/T_{1,para}$) components:

$$\frac{1}{T_{1,obs}} = \frac{1}{T_{1,dia}} + \frac{1}{T_{1,para}} \qquad 4.3$$

$1/T_{1,para}$is directly proportional to the concentration of Gd (III) contrast agent [Gd]. Therefore, $\frac{1}{T_{1,obs}} = \frac{1}{T_{1,dia}} + r_1[Gd]$ 4.4

where $r_1$ [$mM^{-1}s^{-}1$] is the proportionality constant known as relaxivity. Furthermore, ($R_{1,para}$) is related to both the relaxation rates in inner-sphere and outer sphere. [12]

$$\frac{1}{T_{1,para}} = \left(\frac{1}{T_1}\right)_{inner-sphere} + \left(\frac{1}{T_i}\right)_{outer-sphere} \qquad 4.5$$

The longitudinal inner-sphere relaxation rate ($R_{1p}^{IS}$) due to paramagnetic contribution is given by

$$R_{1para}^{IS}\ or\ \left(\frac{1}{T_{1_{inner-sphere}}}\right) = \frac{Cq}{55.5}\,\frac{1}{T_{1M} + \tau_m} \qquad 4.6$$

where $C$ is the concentration of the Gd (III) ions, $q$ is the number of coordinated water molecule, $\tau_m$ is the water exchange lifetime, $T_{1M}$ corresponds to relaxation time of water molecule(s) directly coordinated to metal ion in the first coordination sphere and given by the following equation:[13]

$$\frac{1}{T_{1M}} = \frac{2}{15}\frac{\gamma_H^2 g_e^2 \mu_B^2 S(S+1)}{r_{GdH}^6}\left[\frac{7\tau_{c2}}{1+\omega_S^2\tau_{c2}^2} + \frac{3\tau_{c1}}{1+\omega_H^2\tau_{c1}^2}\right] \qquad 4.7$$

where $\gamma_H$ is the proton gyromagnetic ratio, S is 7/2 for $Gd^{3+}$ , $r_{GdH}$ is Gd-H distance, $\omega_H$ is proton Larmor frequency, $\omega_s$ (658. $\omega_s$) is the electron Larmor frequency, $\mu_B$ is the Bohr magneton, $g_e$ is the electron g-factor, $\tau_R$is the rotational correlation time ($\tau_R$), $\tau_m$is the water exchange lifetime ($\tau_m$), $T_{1e}$is the electronic relaxation time of the $Gd^{3+}$ metal ion and $\tau_{c1}$ is given by [13]

$$\frac{1}{\tau_{ci}} = \frac{1}{\tau_m} + \frac{1}{\tau_R} + \frac{1}{T_{1e}} \qquad 4.8$$

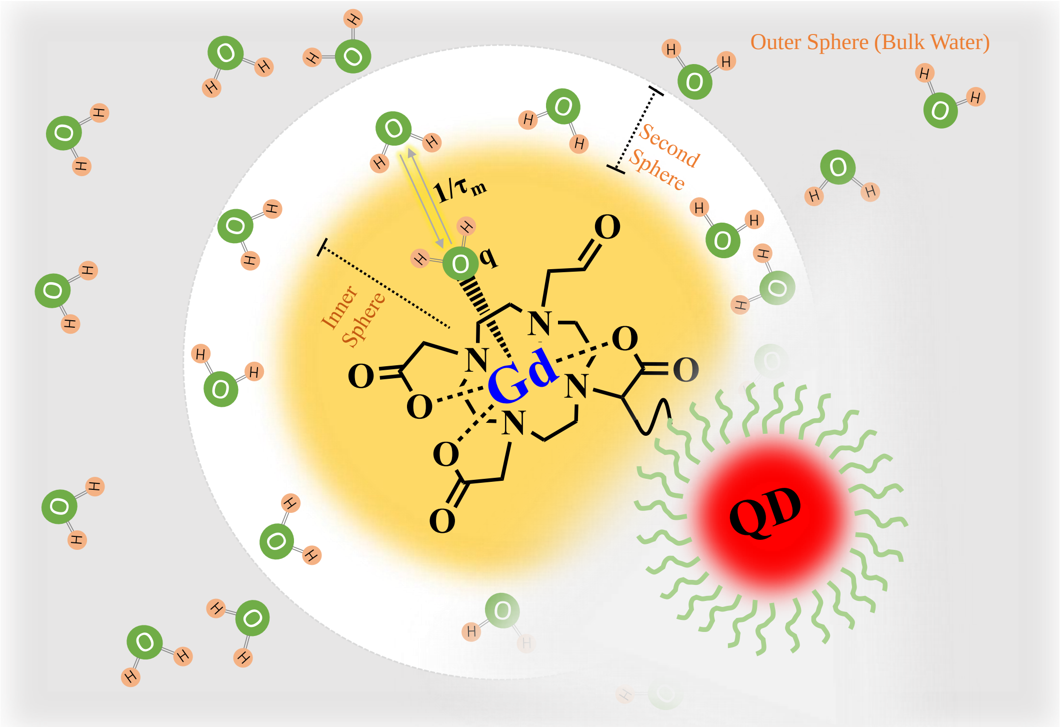

**Figure 4.2:** Schematic representation of a $Gd^{3+}$ chelate with inner and outer sphere water molecule, surrounded by bulk water.

The commercially accessible contrast agents have relaxivities that are significantly lower than theoretically achievable levels; their rotational correlation time (~100 ps) and proton exchange rate (~$10^6$ $s^{-1}$) are far from ideal.[3] As seen in the Equation 4.6 there are many factors affecting the proton relaxivity rate in the presence of a contrast agent and hence the intensity of the MRI signal. Precisely, the MRI signal/noise ration depends on hydration number (q), the separation between the gadolinium ion and a proton on the coordinated water ($r_{GdH)}$, the rotational correlation time ($\tau_r$), the residence time of coordinated waters ($\tau_m$) and the electron relaxation time ($\tau_{1e}$ ). By rationally designing the contrast agent we can control most of these factors.[11,12] In this chapter, we describe functionalisation of $Ag_2S$ quantum dots (size ~2.2 and 4.2 nm) by an MRI contrast agent and the significant improvement in $T_1$-relaxivity of water due to decrease in $\tau_r$ and increase in $\tau_m$.

## 4.2. Bio-functionalization of $Ag_2S$ QDs as MRI/NIR-II Multimodal Imaging Agent

**4.2.1. Gd-complex synthesis:** $Gd^{3+}$ based complex is the most commonly used $T_1$-contrast agents due its strong paramagnetic nature (S=7/2) and high stability.[9,10] For example, the stability constant, log $K_{ML}$ for commercially available Gd(III)-DOTA complex is 25.3.[14] We synthesized a stable Gd (III) complex Gd-L (Figure 4.3) following a previously reported method.[15]

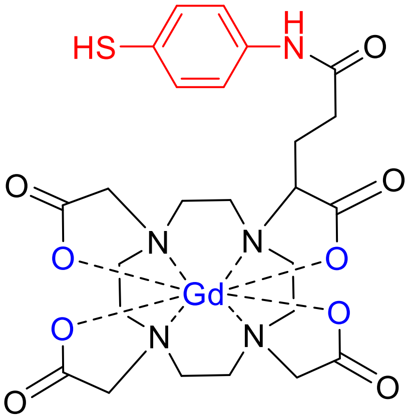

**Figure 4.3:** Structural representation of Gd-L

Gd-L is a monoaqua complex. The presence of SH group is important for grafting of this compound on to the surface of the $Ag_2S$ NCs. To synthesise the ligand, DOTA-GA $(tBu)_4$ (1) is first coupled with 4-aminothiophenol *via a* simple amide bond formation reaction using a dehydrating agent, NN-(DCC) to form compound 2. The next step is the deprotection of four carboxylic groups to form compound 3, followed by metalation.

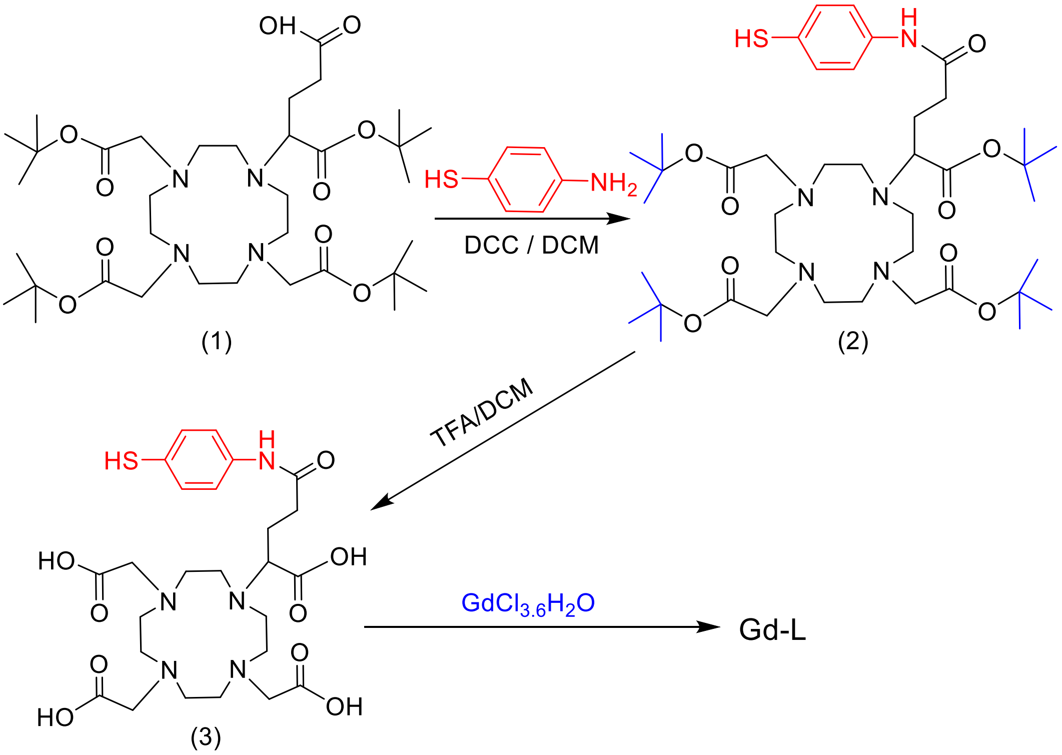

**Scheme 4.1:** Synthesis of the ligand for biofunctionalization.

Products 2 and Gd-L were thoroughly characterized using $^1$H NMR, $^{13}$C NMR and HRMS (*c.f.* Experimental section 4.5.3.2 and spectra's in Annexure, A4.1.1 ). The successful metalation i.e., the formation of Gd-L was confirmed by FTIR (1610 $cm^{-1}$ and 1676 $cm^{-1}$) and susceptibility measurement. Chemical shifts of bulk and bound water ($\Delta\delta$) in the presence of paramagnetic Gd-L is 0.3917 ppm (Figure 4.7a). Using Evan's method, the calculated molar susceptibility of the Gd-L is $2.6412.64 \times 10^{-2}$ $m^3$/mol.[16] The longitudinal relaxivity of water in the presence of the free Gd-L was 5.36 $mM^{-1}s^{-1}$.

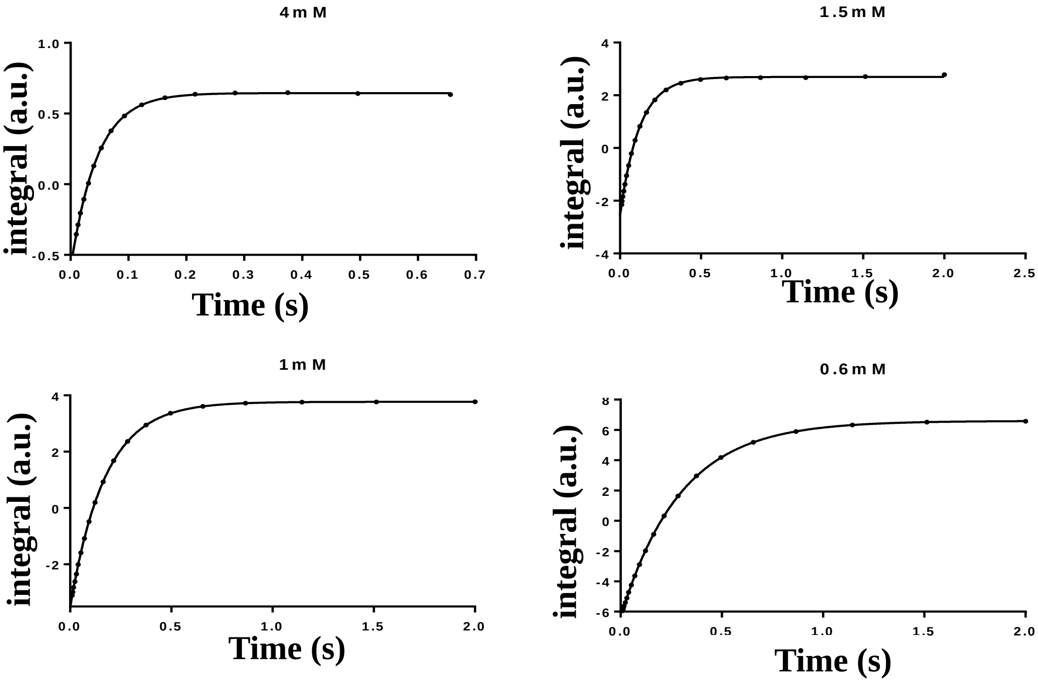

**Figure 4.4:** Relaxivity plot of Gd-L at four different concentrations.

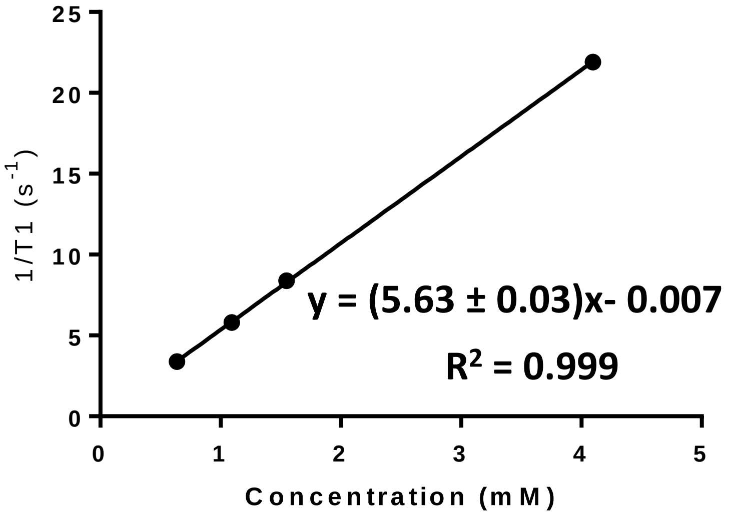

**Figure 4.5:** Plot of $1/T_1$ versus different concentrations of Gd-L.

### 4.2.2. Functionalization of $Ag_2S$ QDs with Gd-L

$Ag_2S$ QDs of two distinct sizes, QD1 (Size ~2.2 nm) and QD2 (Size ~4.2 nm) were functionalised using Gd-L to produce Gd-QD1 and Gd-QD2 (see experimental section) following a previously reported method for InP/ZnS QDs.[17]

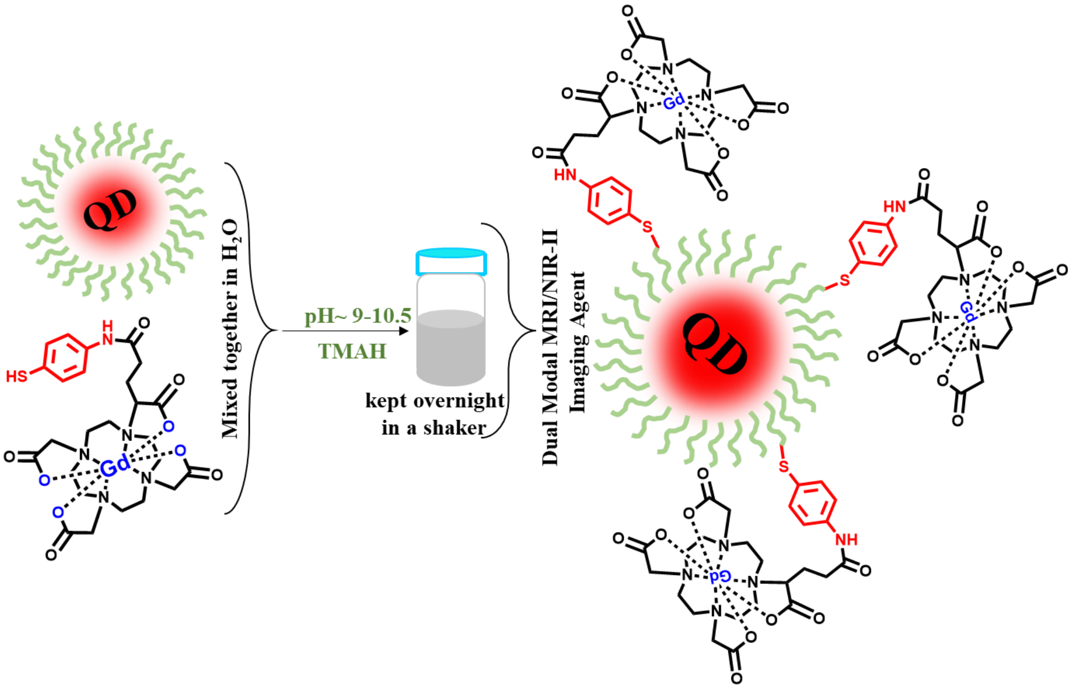
QD
HS
H
N
Gd
Mixed together in $H_2O$
pH~ 9-10.5
TMAH
kept overnight
in a shaker
Dual Modal MRI/NIR-II
Imaging Agent
QD
S
HN
NH
Gd

**Scheme 4.2:** Biofunctionalization of $Ag_2S$ QDS with Gd-L to form a dual-modal MRI/NIR-II Imaging agent.

In this method, the basic pH of 9-10.5 is crucial to deprotonate the thiol group and subsequent grafting of Gd-L on to the surface of $Ag_2S$ QDs *via* thiolate-Ag bond. TCEP is used to preserve the competitive reaction i.e., the disulphide bond formation. The conjugation of NIR-II emitting $Ag_2S$ QDs with an MRI contrast agent (Gd-L) results in the formation of a multimodal contrast agent (Gd-QD) capable of exhibiting both the fluorescence and MRI properties. The conjugation of $Ag_2S$ QDs with Gd-L is confirmed by FTIR. The asymmetric stretching vibration of the $COO^-$ group and the bending vibration of the N-H group, respectively, can be seen as peaks at 1647 $cm^{-1}$ and 1593 $cm^{-1}$ in the FTIR spectrum of the Gd-QD (Figure 4.6b). These values are at a lower frequency compared to that of the Gd-L. The O-H and N-H stretching vibrations appear in the 3000–3500 $cm^{-1}$ region.[18]

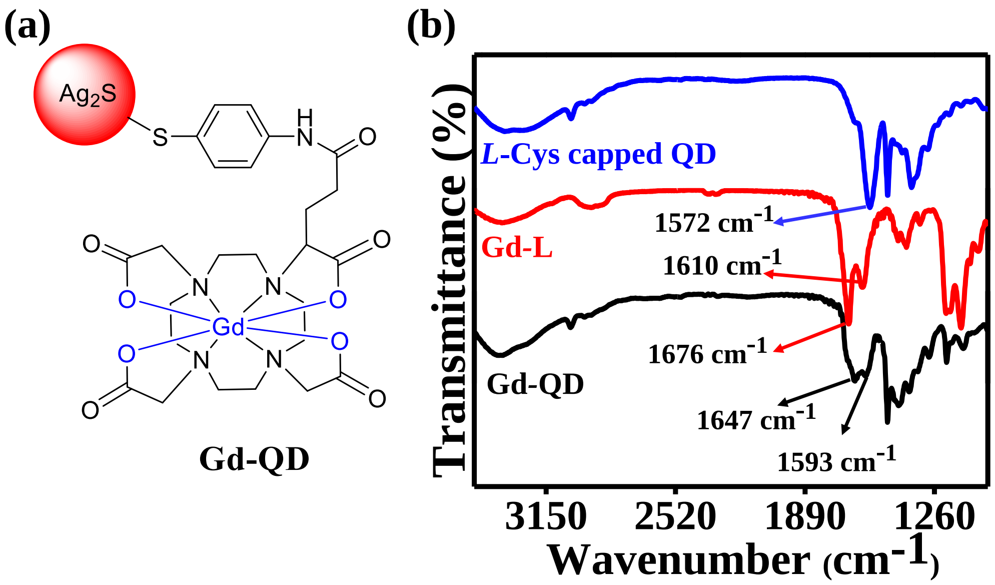

**Figure 4.6:** (a) Schematic representation of $Gd^{3+}$ complex-capped $Ag_2S$ QDs (Gd-QD) obtained by functionalization of L-cysteine capped $Ag_2S$ QDs with $Gd^{3+}$ complex (Gd-L); (b)FTIR spectra of L-cysteine-capped $Ag_2S$ QDs (blue), Gd-L (red) and Gd-QD (black).

### 4.3. Properties of NIR-II/MRI (Gd-QD) multimodal contrast agent.

#### 4.3.1. Molar extinction coefficient

Gd-QD1 (radius~2.2 nm) emits at 1024 nm, while Gd-QD2 (radius~4.2 nm) emits at 1209 nm. These mission wavelengths are in NIR-II regions, ideal for deep tissue imaging. During the grafting the loss of fluorescence was negligible. For biological application it is important to know the dose/concentration of the Gd-QD. The molar extinction coefficient was determined at 450 nm, using the Ricard equation.[19]

The molar extinction coefficient (expressed as $M^{-1}cm^{-1}$) is related to absorption cross section (expressed in $cm^2$) and Avogadro's number (N),

$$\epsilon = \frac{\sigma_{QD} \times N}{2303} \qquad 4.9$$

The absorption cross section was determined using Ricard equation,

$$\sigma_{QD} = \frac{\omega}{n_s c}\left(\frac{4}{3}\pi R^3\right)|f(\omega)|^2 2 n_{QD} k_{QD} \qquad 4.10$$

where,

$\omega$ =angular frequency

$n_s$ = refractive index of solvent matrix

$n_{QD}$ = real part of refractive index of quantum dots

$k_{QD}$ = imaginary part of refractive index of quantum dots and $f(\omega)$ is Local field factor which is calculated using the following equation,

$$f(\omega) = \frac{3\varepsilon_s}{\varepsilon_{QD} + 2\varepsilon_s} \quad 4.11$$

Where, $\varepsilon_s$ is diectric constant of solvent and $\varepsilon_{QD}$ is dielectric constant of $Ag_2S$. During the calculation, the optical constants (bulk dielectric constants and the refractive index) for monoclinic $Ag_2S$ QDs with a band gap of 1.08 eV are required, which were theoretically calculated using DFT. The details of the DFT calculation is provided in the experimental section 4.5.3.4.

### 4.3.2. Enhancement of water relaxivity by MRI/NIR-II contrast agent

Clinical MRI scanners these days mostly run at magnetic field strengths of 0.5-1.5T (20- 60MHz); at these frequencies the bound, $T_{1M}$ longitudinal relaxation time of the water molecules is dominated by the molecular reorientation (rotational correlation) time, $\tau_r$. The correlation time is longer when the Gd(III) complex tumbles more slowly, which increases the relaxation rates and decreases the relativities. Several approaches have been taken to lengthen $\tau_r$. Most commonly, a slowly tumbling macromolecule is attached to a Gd(III) complex. Examples include, binding the Gd-complex to a bulky protein or a polysaccharide or *via* aggregation of amphiphilic complexes.[20] Binding the Gd(III) complex with QDs also increases the relaxivity rate due to slowing of $\tau_r$.[21] $Gd^{3+}$-based complex decrease the longitudinal relaxation ($T_1$) of bound water protons, hence enhancing localized signal intensity[22] and image contrast.[23–32] we used nuclear magnetic resonance (NMR, 400 MHz) spectroscopy to calculate the longitudinal water relaxivity, $r_1$. QD1 and QD2 after bio-functionalisation had a distinct change in Δδ value for both GdQD1 (Δδ = 0.102, Figure 4.7c) and Gd-QD2 (Δδ = 0.0301, Figure 4.7b) respectively. This result confirms the effective grafting of $Ag_2S$ with Gd-L. Furthermore, the FTIR data of GdQD1 and GDQD2 showed absence of free Gd-L. Notably, the smaller-sized Gd-QD1 exhibited a lower longitudinal relaxivity ($r_1$) of 7.78 mM$^{-1}$s$^{-1}$ per Gd-L while the larger-sized Gd-QD2 ($r_1$=8.27 mM$^{-1}$s$^{-1}$ per Gd-L). This is an increase from Gd-L, which demonstrates a $r_1$ = 5.36 mM$^{-1}$s$^{-1}$ when taken alone. The higher relaxivity of Gd-QD compared to Gd-L is attributed to the restricted rotation of QD bound Gd-complex in solution.[15] This is much higher than the $r_1$ of the free Gd-L (5.36 mM$^{-1}$s$^{-1}$). The relaxivity per-QD for Gd-QD1 and Gd-QD2 at 400 MHz were 407.8 mM$^{-1}$s$^{-1}$ and 990.3 mM$^{-1}$s$^{-1}$, respectively.

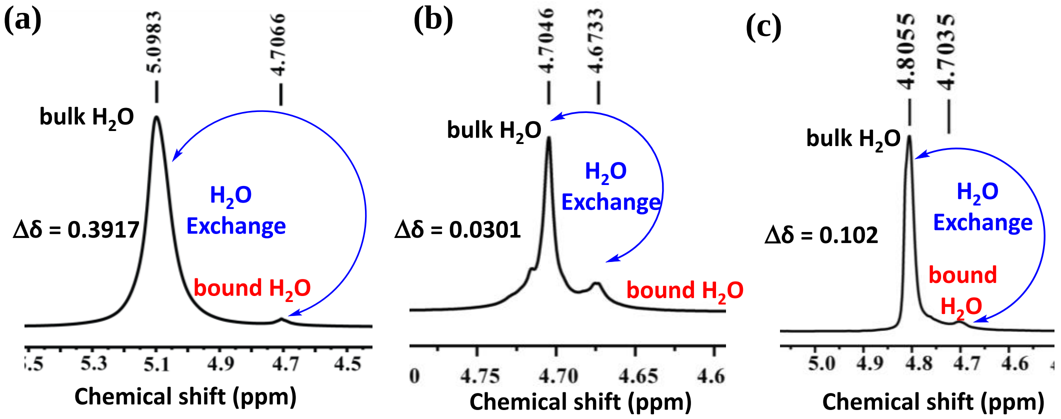

**Figure 4.7:** (a) $^1$HNMR spectrum (400 MHz) of Gd-L; (b) $^1$HNMR spectrum (400 MHz) of Gd-QD2 and (c) $^1$HNMR spectrum (400 MHz) of Gd-QD1 demonstrating the exchange of water protons between bound and bulk water of surrounding respectively.

## 4.4. Conclusion

$Ag_2S$ QDs exhibiting fluorescence in NIR-II window were functionalised with a Gd-based MRI contrast agent (Gd-L). The relaxivity values obtained are significantly higher than those reported for smaller complexes and commercially available MRI contrast agents[25]. Table 4.2 compares the longitudinal relaxivity values of Gd-QD1/Gd-QD2 with those of other MRI contrast agents. The high longitudinal relaxivity values for both Gd-QD1 and Gd-QD2 offer excellent possibility to use them as the MRI contrast agent in bioimaging applications. Since these QDs have emission in the NIR-II window, they form an efficient dual model contrast agent with high NIR-II quantum yield (~5-6 %) and MRI $T_1$ water relaxivity (408-990 $mM^{-1}s^{-1}$ per QD) depending upon the size of the QDs.

**Table:4.2:** Longitudinal relaxivity values of Gd-QD1/Gd-QD1 and other nanoprobes.

| nanoprobe | longitudinal relaxivity (r) |
|---|---|
| **Gd-QD1** | $r_1 = 7.75\ mM^{-1}s^{-1}$ |
| **Gd-QD2** | $r_1 = 8.27\ mM^{-1}s^{-1}$ |
| **Gd-L** | $r_1 = 5.36\ mM^{-1}s^{-1}$ |
| **Gadovist**[25] | $r_1 = 4.34\ mM^{-1}s^{-1}$ |
| **Gd-doped QDs**[18,26,33] | $r_1 = 5.5–6.4\ mM^{-1}s^{-1}$ |
| **Gd2O3 nanoparticles**[34] | $r_1 = 6.9\ mM\text{-}1s^{-1}$ |

## 4.5. Experimental Details

### 4.5.1. General Information

**Materials and general considerations:** Chemicals used are listed below

| Chemicals | Purity/Grade | Company Name |
|---|---|---|
| Tetramethylammonium hydroxide (TMAH) | ≥99% | Sigma Aldrich |
| Tris(2-carboxyethyl)phosphine (TCEP) | 99% | Sigma Aldrich |
| Tetrachloroethylene | ≥99% | Sigma Aldrich |
| 1-Octadecene | 90% | Sigma Aldrich |
| Triethylamine | ≥99% | Sigma Aldrich |
| Octylamine | 99% | Sigma Aldrich |
| Oleylamine | 70% | Sigma Aldrich |
| Phenyl isothiocyanate | 98% | Sigma Aldrich |
| L-cysteine | ≥97% | Sigma Aldrich |
| Oleic acid | 70% | Sigma Aldrich |
| Toluene | 95% | Sigma Aldrich |
| Dimethoxy ethane (DME) | ≥99% | Sigma Aldrich |
| Diglyme | ≥99% | Sigma Aldrich |
| Silver Nitrate | 99% | Thomas baker |
| Aniline | 99% | TCI |
| N,N′-Dicyclohexylcarbodiimide (DCC) | 99% | TCI |
| DOTA-GA (tBu)4 | 99% | TCI |
| Amino-thiophenol | ≥99% | TCI |
| Trifluoroacetic acid (TFA) | ≥99% | TCI |
| 4-Dimethylaminopyridine (DMAP) | ≥99% | TCI |
| Selenium powder | ≥98% | TCI |
| 1-Dodecanethiol (DDT) | ≥98% | TCI |
| 1-Octanethiol | ≥98% | TCI |

|  |  |  |
|---|---|---|
| Cadmium chloride | ≥98% | Thomas Baker |
| Gadolinium (III) Chloride | ≥98% | Thomas Baker |
| Deuterated solvents | ≥99% | Sigma Aldrich |

We used thin layer chromatography (TLC) to monitor the progress of the reactions by using plates coated with silica gel 60 $F_{254}$. To see the results, we used a UV lamp or $I_2$ stain. For synthesizing starting materials, we purified the chemicals using column chromatography with silica gel of 60-120 mesh size and a mixture of ethyl acetate and petroleum ether as the eluent.

### 4.5.2. Characterization Methods

**NMR:** The Bruker ASCENDTM (400 MHz) spectrometer was used to record the $^{1}H$ NMR, $^{13}C$ NMR, with either $CDCl_3$ or $D_2O$, or DMSO-$d_6$ as the solvent. The multiplicities were indicated as *s* for singlet, *d* for doublet, *t* for triplet, *q* for quartet, and m for multiplet. The solid samples were tested for their solubility in the desired solvents and mixed in a glass vial. Using a glass Pasteur pipette, the sample was transferred to the NMR tube. The NMR tube was then labeled and scanned in the NMR instrument.

**UV-Vis spectrophotometer:** To obtain the UV-visible absorption spectra, the PerkinElmer spectrophotometer with a scan rate of 480 nm/s and Agilent Technologies Cary 100 UV-vis were employed. For these measurements, the sample was dissolved in either anhydrous hexane or anhydrous tetrachloroethylene (TCE).

**Vis-NIR spectrofluorometer:** The PL spectra of $Ag_2X$ (X=S, Se) NCs were obtained using the HORIBA Scientific spectrophotometer (Model: PTI-QM 510). The NCs were distributed in either hexane or TCE and the solution.

**FTIR:** The FT-IR spectra were obtained using the Bruker ALPHA E, 200396 instrument. Liquid samples are immediately dropped onto the surface of the instruments, and the spectrum was obtained. For solid samples, they were first ground in a mortar along with anhydrous potassium bromide (KBr). Then, a piece of paper was taken and a hole was cut out of it. The grounded sample was then poured into this hole, and a pallet was made using a hydraulic press. The resulting sample was inserted into the IR sample holder, attached with scotch tape, and then analyzed by running the spectrum.

### 4.5.3. Synthesis

#### 4.5.3.1. General Procedures synthesis of Sulphur Precursor and $Ag_2S$ NCs

**Substituted thiourea synthesis (*Method A):*** The synthesis method used was based on previously published research, but with some minor adjustments. [35] A typical synthesis involved mixing a solution of phenyl isothiocyanate (5.0 mmol) in toluene with a solution of aniline 5.0 mmol in 10 mL toluene 10 mL. The resulting mixture was stirred for a specified duration, after which the precipitate was thoroughly dried under vacuum to remove toluene. This resulted in extremely good yields of the required precursor.

**Synthesis of silver sulfide ($Ag_2S$) NCs:** To prepare the sulfur precursor, 0.2 mmol of it was dissolved in 1 mL of dimethoxymethane and left to degas for 30 minutes at room temperature in a double-necked round bottom flask (A) under a nitrogen environment for another 30 minutes. Meanwhile, in another 50 mL three-necked round bottom flask (B), a combination of silver nitrate (0.034 g, 0.2 mmol), 1-octadecene (3.5 mL), and 1-dodecanethiol (DDT) was vacuumed for 30 minutes at ambient temperature and then for 15 minutes at 120 °C to obtain a pale-yellow solution. The temperature of the reaction mixture was then raised to 150 °C while maintaining a nitrogen environment. Depending on the substituents in the *p*-position to the precursors, the reaction mixture was allowed to turn black from red quickly after injecting the cold precursor solution of flask A into the hot solution of flask B. The reaction mixture was then rapidly cooled in an ice bath.

**NCs purification:** The QDs were initially mixed with 4 mL of ethanol/methanol and 1 mL of hexane. After being centrifuged twice at 6000 rpm for 15 minutes, the supernatant was discarded, and the precipitate was mixed with 3 mL of ethanol/methanol, 1 mL of hexane, and 1 mL of toluene. This mixture was then centrifuged twice at 6000 rpm for 5 minutes. The resulting QDs were dispersed in 0.5 mL of toluene and centrifuged for 2 minutes at 6000 rpm. Finally, the QDs were dispersed in 1 mL of hexane/TCE and centrifuged once at 3000 rpm for further purification.

**Phase transfer of $Ag_2S$ QDs:** The $Ag_2S$ quantum dots (QDs) obtained from precursor **3c** and **3e** that emit at 1039 nm and 1200 nm, respectively, were transformed through the phase transfer method to replace the hydrophobic ligand (DDT) with a hydrophilic ligand (L-cysteine). The purified $Ag_2S$ QDs (0.102 g) were dispersed in 2 mL of chloroform. Meanwhile, 0.45 mg of *L*-cysteine was dissolved in 2 mL of Millipore water by gradually adding tetramethyl ammonium hydroxide to maintain the pH of the solution at around 9.36. The two solutions were mixed and stirred vigorously for 2 hours at 14000 rpm at room temperature to produce biphasic mixtures. The phase transferred $Ag_2S$ QDs were then washed three times with pure Millipore water using a micro spin-X filter (0.22 micrometre) and finally dispersed in 1.5 mL of water.

### 4.5.3.2. Synthesis of Gadolinium Complex (Gd-L) and Conjugation with Colloidal $Ag_2S$ QDs for MRI Contrast Agent

We synthesized the gadolinium complex (Gd-L) and chelated it with colloidal $Ag_2S$ QDs by replicating a previously published method by one of the authors, which was reported in reference.[37]

**Synthesis of functionalized DOTA-GA (*t*Bu)$_4$ with 4-aminothiophenol (I)**: In this experiment, DOTA-GA (tBu)$_4$ (0.57 mmol, 0.4 g) and 4-aminothiophenol (1.14 mmol, 0.14 g) were mixed together in 15 mL of DCM (dichloromethane) as a solvent. To this mixture, N, N′-dicyclohexylcarbodiimide (DCC, 0.57 mmol, 0.12 g) and 4-dimethylaminopyridine (DMAP, 0.06 mmol, 0.007 g) were added and stirred for 24 hours at room temperature. The progress of the reaction was monitored using thin layer chromatography (TLC) and the product was purified using column chromatography, which resulted in the formation of a white solid product (I) in 78% yield

**Deprotection of BOC group in compound I:** To a solution of (I), (130 mg, 0.172 mmol) in TFA (3 mL) and DCM (1.5 mL), the reaction mixture was stirred at room temperature for 18 hours. The solvents were then removed by vacuum evaporation. The resulting residue was dissolved in DCM and the solvent was again removed in vacuo for three cycles. The obtained solid was washed thrice with dichloromethane followed by thrice with diethyl ether. As a result, a brown solid product (II) was obtained in 65 % yield

**Synthesis of gadolinium complex (Gd-L):** In this experiment, a solution of 0.076 mmol of deprotected product (II) in 2 mL of water was prepared, and the pH was adjusted to 5.5 by adding small amounts of 1.0 M NaOH. Next, a solution of $GdCl_3.6H_2O$ (0.076 mmol) in 1 mL of water was prepared while maintaining the pH at

5.5. The two solutions were mixed and the pH was readjusted to 5.5, followed by stirring for 30 minutes. The solvent was then removed under vacuum to obtain a hygroscopic white powder, **Gd-L**. The product was further purified using a Sephadex G-25 resin to remove any inorganic salts. The final yield of the white hygroscopic solid was 69% (Gd).

**Complexation of the ligands (Gd-L) with QDs:** In this experiment, we aimed to complex the ligands (Gd-L) with QDs. To do so, we added tris-(2-carboxyethyl) phosphine hydrochloride (TCEP) and QDs (QD1 and QD2) to degassed water (2 mL). We then adjusted the pH of the mixture between 9 to 10.5 using 0.5 M tetramethylammonium hydroxide and stirred the solution vigorously for 24 hours in the dark. After 24 hours, we obtained the products (Gd-QD1 and Gd-QD2) by subjecting the mixture to spin filtration through centrifugation. To measure the relaxivity of the Gd-QD1 and Gd-QD2, we subjected them to NMR studies. The absence of free Gd was confirmed by a xylenol orange test.[38] We adjusted the pH of the Gd-capped QDs to 7.4 for the relaxivity measurements.

### 4.5.3.3. Relaxivity measurements

Gd-QD1 and Gd-QD2 were placed in a capillary tube and sealed with parafilm. The tube was then put into an NMR tube containing $D_2O$. $1/T_1$ measurements were carried out using a Bruker Avance III (400 MHz). The effectiveness of a contrast agent can be assessed by measuring its water relaxivity, $r_1$ which is expressed in units of $mM^{-1}s^{-1}$ per Gd complex and depends on the field strength and temperature.

As it is known[39],

$$\frac{1}{T_{1(obs)}} = \frac{1}{T_{1(H2O)}} + \frac{1}{T_{1(para)}} \qquad 4.12$$

where, $T_1$(obs) represents the measured longitudinal relaxation time of a substance in seconds. $T_1$($H_2O$) and $T_1$(*para*) respectively refer to the relaxation time contribution of diamagnetic water, in the absence of paramagnetic ions and paramagnetic water.[39]

Furthermore,

$$\frac{1}{T_{1(obs)}} = \frac{1}{T_{1(H2O)}} + r_1[M] \qquad 4.13$$

where $[M]$ is given by molar concentration of the paramagnetic substance obtained from the NMR shift of water proton when the paramagnetic substance is present. Evan's formula is used to calculate the overall concentration of Gd ions.[40]

$$[M] = \frac{3\times\Delta\delta}{4\pi\times\chi_M\ 10^3} \qquad 4.14$$

where, the difference in chemical shift (ppm) between the shifted resonance of the solvent in the presence of paramagnetic material and the pure solvent is given by $\Delta\delta$. $\chi_M$ is magnetic (molar) susceptibility which is estimated using Curie equation[41] $\mu_{eff} = 2.83\sqrt{(\chi_M \times T)}$ where, $\mu_{eff}$ is magnetic moment (for $Gd^{3+}$ , $\mu_{eff}$ =7.94)[42,43] and T is the temperature. The concentration of QD is required in order to calculate relaxivity per **QD**. We determined the concentration of CQDs i.e., [**QD**] using Lambert-Beer's law, A=$\varepsilon\ [\boldsymbol{QD}]\ l$ where A is absorbance (determined from UV-Vis spectroscopy) and $\epsilon$ molar extinction coefficient of $Ag_2S$ CQDs.

### 4.5.3.4. Determination of Optical constants of $Ag_2S$ using DFT

Monoclinic $Ag_2S$ exhibits anisotropic nature and hence their refractive index and dielectric values are different for X and Z directions (Table 4.3). The optical constants of $Ag_2S$ have been determined from the first principles calculation based on full potential linearized augmented plane wave (FP-LAPW) method.[44] The monoclinic phase (space group $P2_1/m$) with optimized lattice parameters of $a$ = 4.22 Å, $b$ = 7.56 Å, $c$ = 4.24 Å and $\beta$ = 110.55° has been considered. The effect of exchange correlation of electrons are treated with Perdew-Burke-Ernzerhof generalised gradient approximations (PBE-GGA)[45] and modified Becke-Johnson (mBJ) potential is included to match the energy band gap with experimental report. $Ag_2S$ is an indirect energy band gap semiconductor with gap value (1.12 eV) consistent to experimental data (1.1 eV).[46] The frequency dependent complex dielectric constant $\varepsilon(\omega)$ describes the optical response of a materials against photon radiation and can be expressed as $\varepsilon(\omega) = \varepsilon_1(\omega) + i\varepsilon_2(\omega)$, where $\varepsilon_1(\omega)$ and $\varepsilon_2(\omega)$ are real and imaginary parts, respectively. The refractive index and the extinction coefficient along the three independent directions of an anisotropic monoclinic symmetric unit cell of bulk sample are further estimated from the complex dielectric constants using following relations.

$$k = \frac{\left(-\varepsilon_1 + \left(\varepsilon_1^2 + \varepsilon_2^2\right)^{1/2}\right)^{1/2}}{\sqrt{2}} \qquad 4.15$$

$$n = \frac{\left(\varepsilon_1 + \left(\varepsilon_1^2 + \varepsilon_2^2\right)^{1/2}\right)^{1/2}}{\sqrt{2}} \qquad 4.16$$

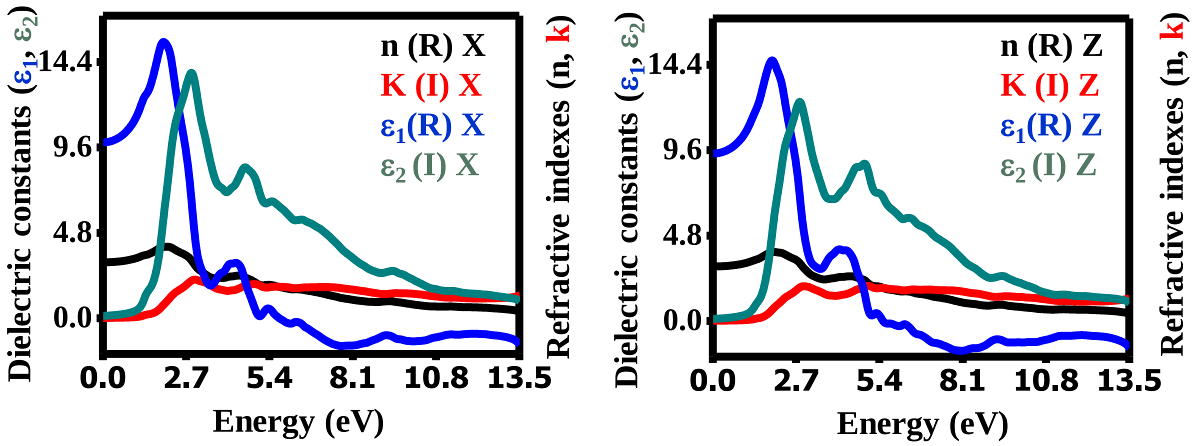

**Figure 4.8** : Optical constants of monoclinic $Ag_2S$ (X and Z directions)

**Table 4.3**: Optical constants of monoclinic $Ag_2S$ (X and Z directions); Note, I = imaginary and R = real parts of dielectric constants ($\varepsilon_1$ and $\varepsilon_2$) and refractive indexes (n and k).

| **Energy (eV)** | **$\varepsilon_1$(R) X** | **$\varepsilon_2$ (I) X** | **n (R) X** | **k(I) X** | **$\varepsilon_1$ (R) Z** | **$\varepsilon_2$ (I) Z** | **n (R) Z** | **k(I) Z** |
|---|---|---|---|---|---|---|---|---|
| 1.37418 | 3.54E+00 | 1.76E-01 | 1.25E+01 | 1.25E+00 | 3.43E+00 | 1.27E-01 | 1.18E+01 | 8.75E-01 |
| 1.40139 | 3.55E+00 | 1.90E-01 | 1.26E+01 | 1.35E+00 | 3.45E+00 | 1.37E-01 | 1.19E+01 | 9.45E-01 |
| 1.4286 | 3.56E+00 | 2.02E-01 | 1.26E+01 | 1.44E+00 | 3.46E+00 | 1.46E-01 | 1.20E+01 | 1.01E+00 |
| 1.45581 | 3.57E+00 | 2.12E-01 | 1.27E+01 | 1.51E+00 | 3.48E+00 | 1.54E-01 | 1.21E+01 | 1.07E+00 |
| 1.48302 | 3.59E+00 | 2.20E-01 | 1.28E+01 | 1.58E+00 | 3.50E+00 | 1.63E-01 | 1.22E+01 | 1.14E+00 |
| 1.51023 | 3.60E+00 | 2.28E-01 | 1.29E+01 | 1.64E+00 | 3.52E+00 | 1.72E-01 | 1.24E+01 | 1.21E+00 |
| 1.53744 | 3.62E+00 | 2.36E-01 | 1.30E+01 | 1.71E+00 | 3.55E+00 | 1.82E-01 | 1.25E+01 | 1.29E+00 |
| 1.56466 | 3.64E+00 | 2.45E-01 | 1.32E+01 | 1.78E+00 | 3.57E+00 | 1.95E-01 | 1.27E+01 | 1.39E+00 |
| 1.59187 | 3.66E+00 | 2.55E-01 | 1.34E+01 | 1.87E+00 | 3.60E+00 | 2.10E-01 | 1.29E+01 | 1.51E+00 |
| 1.61908 | 3.69E+00 | 2.69E-01 | 1.35E+01 | 1.98E+00 | 3.63E+00 | 2.28E-01 | 1.31E+01 | 1.65E+00 |
| 1.64629 | 3.72E+00 | 2.85E-01 | 1.37E+01 | 2.12E+00 | 3.66E+00 | 2.50E-01 | 1.33E+01 | 1.83E+00 |
| 1.6735 | 3.74E+00 | 3.04E-01 | 1.39E+01 | 2.27E+00 | 3.68E+00 | 2.75E-01 | 1.35E+01 | 2.03E+00 |
| 1.70071 | 3.77E+00 | 3.25E-01 | 1.41E+01 | 2.45E+00 | 3.71E+00 | 3.03E-01 | 1.37E+01 | 2.25E+00 |
| 1.72792 | 3.80E+00 | 3.49E-01 | 1.43E+01 | 2.65E+00 | 3.74E+00 | 3.33E-01 | 1.39E+01 | 2.49E+00 |
| 1.75513 | 3.83E+00 | 3.75E-01 | 1.45E+01 | 2.87E+00 | 3.76E+00 | 3.66E-01 | 1.40E+01 | 2.75E+00 |
| 1.78235 | 3.86E+00 | 4.05E-01 | 1.47E+01 | 3.12E+00 | 3.79E+00 | 4.01E-01 | 1.42E+01 | 3.04E+00 |
| 1.80956 | 3.88E+00 | 4.38E-01 | 1.49E+01 | 3.41E+00 | 3.81E+00 | 4.39E-01 | 1.43E+01 | 3.35E+00 |
| 1.83677 | 3.91E+00 | 4.76E-01 | 1.51E+01 | 3.73E+00 | 3.83E+00 | 4.80E-01 | 1.44E+01 | 3.68E+00 |
| 1.86398 | 3.94E+00 | 5.19E-01 | 1.52E+01 | 4.09E+00 | 3.85E+00 | 5.24E-01 | 1.45E+01 | 4.03E+00 |
| 1.89119 | 3.96E+00 | 5.65E-01 | 1.54E+01 | 4.48E+00 | 3.87E+00 | 5.71E-01 | 1.46E+01 | 4.42E+00 |

| | | | | | | | | |
|---|---|---|---|---|---|---|---|---|
| 1.9184 | 3.98E+00 | 6.14E-01 | 1.55E+01 | 4.89E+00 | 3.88E+00 | 6.21E-01 | 1.46E+01 | 4.81E+00 |
| 1.94561 | 3.99E+00 | 6.65E-01 | 1.55E+01 | 5.31E+00 | 3.88E+00 | 6.71E-01 | 1.46E+01 | 5.22E+00 |
| 1.97283 | 4.00E+00 | 7.15E-01 | 1.55E+01 | 5.73E+00 | 3.89E+00 | 7.22E-01 | 1.46E+01 | 5.61E+00 |
| 2.00004 | 4.01E+00 | 7.65E-01 | 1.55E+01 | 6.14E+00 | 3.88E+00 | 7.70E-01 | 1.45E+01 | 5.98E+00 |
| 2.02725 | 4.02E+00 | 8.15E-01 | 1.55E+01 | 6.55E+00 | 3.88E+00 | 8.16E-01 | 1.44E+01 | 6.33E+00 |
| 2.05446 | 4.02E+00 | 8.64E-01 | 1.54E+01 | 6.95E+00 | 3.87E+00 | 8.59E-01 | 1.42E+01 | 6.65E+00 |
| 2.08167 | 4.02E+00 | 9.13E-01 | 1.53E+01 | 7.34E+00 | 3.86E+00 | 8.99E-01 | 1.41E+01 | 6.94E+00 |
| 2.10888 | 4.02E+00 | 9.64E-01 | 1.52E+01 | 7.75E+00 | 3.86E+00 | 9.38E-01 | 1.40E+01 | 7.23E+00 |
| 2.13609 | 4.02E+00 | 1.02E+00 | 1.51E+01 | 8.17E+00 | 3.85E+00 | 9.77E-01 | 1.39E+01 | 7.53E+00 |
| 2.16331 | 4.02E+00 | 1.07E+00 | 1.50E+01 | 8.60E+00 | 3.85E+00 | 1.02E+00 | 1.38E+01 | 7.83E+00 |
| 2.19052 | 4.01E+00 | 1.13E+00 | 1.48E+01 | 9.04E+00 | 3.84E+00 | 1.06E+00 | 1.36E+01 | 8.15E+00 |
| 2.21773 | 3.99E+00 | 1.18E+00 | 1.45E+01 | 9.45E+00 | 3.83E+00 | 1.11E+00 | 1.35E+01 | 8.48E+00 |
| 2.24494 | 3.97E+00 | 1.24E+00 | 1.42E+01 | 9.83E+00 | 3.82E+00 | 1.15E+00 | 1.33E+01 | 8.81E+00 |
| 2.27215 | 3.95E+00 | 1.29E+00 | 1.39E+01 | 1.02E+01 | 3.80E+00 | 1.20E+00 | 1.30E+01 | 9.13E+00 |
| 2.29936 | 3.92E+00 | 1.33E+00 | 1.36E+01 | 1.05E+01 | 3.78E+00 | 1.24E+00 | 1.28E+01 | 9.41E+00 |
| 2.32657 | 3.89E+00 | 1.38E+00 | 1.33E+01 | 1.07E+01 | 3.76E+00 | 1.29E+00 | 1.25E+01 | 9.66E+00 |
| 2.35379 | 3.87E+00 | 1.41E+00 | 1.30E+01 | 1.09E+01 | 3.73E+00 | 1.32E+00 | 1.22E+01 | 9.88E+00 |
| 2.381 | 3.84E+00 | 1.45E+00 | 1.26E+01 | 1.11E+01 | 3.70E+00 | 1.36E+00 | 1.19E+01 | 1.01E+01 |
| 2.40821 | 3.81E+00 | 1.49E+00 | 1.23E+01 | 1.13E+01 | 3.68E+00 | 1.39E+00 | 1.16E+01 | 1.02E+01 |
| 2.43542 | 3.78E+00 | 1.52E+00 | 1.20E+01 | 1.15E+01 | 3.65E+00 | 1.42E+00 | 1.13E+01 | 1.04E+01 |
| 2.46263 | 3.76E+00 | 1.55E+00 | 1.17E+01 | 1.16E+01 | 3.63E+00 | 1.45E+00 | 1.11E+01 | 1.05E+01 |
| 2.48984 | 3.73E+00 | 1.58E+00 | 1.14E+01 | 1.18E+01 | 3.61E+00 | 1.47E+00 | 1.08E+01 | 1.06E+01 |
| 2.51705 | 3.71E+00 | 1.61E+00 | 1.12E+01 | 1.19E+01 | 3.59E+00 | 1.50E+00 | 1.06E+01 | 1.08E+01 |
| 2.54427 | 3.69E+00 | 1.64E+00 | 1.09E+01 | 1.21E+01 | 3.57E+00 | 1.53E+00 | 1.04E+01 | 1.09E+01 |
| 2.57148 | 3.67E+00 | 1.67E+00 | 1.07E+01 | 1.22E+01 | 3.55E+00 | 1.56E+00 | 1.01E+01 | 1.11E+01 |
| 2.59869 | 3.64E+00 | 1.70E+00 | 1.04E+01 | 1.24E+01 | 3.53E+00 | 1.59E+00 | 9.89E+00 | 1.12E+01 |
| 2.6259 | 3.62E+00 | 1.73E+00 | 1.01E+01 | 1.25E+01 | 3.50E+00 | 1.63E+00 | 9.63E+00 | 1.14E+01 |
| 2.65311 | 3.60E+00 | 1.77E+00 | 9.85E+00 | 1.27E+01 | 3.48E+00 | 1.66E+00 | 9.36E+00 | 1.16E+01 |
| 2.68032 | 3.58E+00 | 1.80E+00 | 9.55E+00 | 1.29E+01 | 3.46E+00 | 1.70E+00 | 9.07E+00 | 1.17E+01 |
| 2.70753 | 3.55E+00 | 1.84E+00 | 9.22E+00 | 1.31E+01 | 3.43E+00 | 1.74E+00 | 8.74E+00 | 1.19E+01 |
| 2.73475 | 3.52E+00 | 1.88E+00 | 8.87E+00 | 1.32E+01 | 3.40E+00 | 1.78E+00 | 8.37E+00 | 1.21E+01 |
| 2.76196 | 3.49E+00 | 1.92E+00 | 8.48E+00 | 1.34E+01 | 3.36E+00 | 1.82E+00 | 7.97E+00 | 1.22E+01 |
| 2.78917 | 3.45E+00 | 1.96E+00 | 8.08E+00 | 1.35E+01 | 3.31E+00 | 1.85E+00 | 7.53E+00 | 1.23E+01 |
| 2.81638 | 3.41E+00 | 2.00E+00 | 7.64E+00 | 1.37E+01 | 3.26E+00 | 1.89E+00 | 7.06E+00 | 1.23E+01 |
| 2.84359 | 3.37E+00 | 2.04E+00 | 7.16E+00 | 1.38E+01 | 3.20E+00 | 1.92E+00 | 6.59E+00 | 1.23E+01 |
| 2.8708 | 3.31E+00 | 2.08E+00 | 6.65E+00 | 1.38E+01 | 3.14E+00 | 1.94E+00 | 6.13E+00 | 1.22E+01 |
| 2.89801 | 3.25E+00 | 2.11E+00 | 6.12E+00 | 1.38E+01 | 3.08E+00 | 1.95E+00 | 5.71E+00 | 1.20E+01 |
| 2.92522 | 3.19E+00 | 2.14E+00 | 5.61E+00 | 1.37E+01 | 3.03E+00 | 1.96E+00 | 5.34E+00 | 1.18E+01 |
| 2.95244 | 3.13E+00 | 2.16E+00 | 5.11E+00 | 1.35E+01 | 2.97E+00 | 1.96E+00 | 5.01E+00 | 1.16E+01 |

| | | | | | | | | |
|---|---|---|---|---|---|---|---|---|
| 2.97965 | 3.06E+00 | 2.17E+00 | 4.66E+00 | 1.33E+01 | 2.92E+00 | 1.95E+00 | 4.72E+00 | 1.14E+01 |
| 3.00686 | 2.99E+00 | 2.17E+00 | 4.24E+00 | 1.30E+01 | 2.87E+00 | 1.95E+00 | 4.45E+00 | 1.12E+01 |
| 3.03407 | 2.93E+00 | 2.17E+00 | 3.89E+00 | 1.27E+01 | 2.82E+00 | 1.94E+00 | 4.20E+00 | 1.10E+01 |
| 3.06128 | 2.87E+00 | 2.16E+00 | 3.59E+00 | 1.24E+01 | 2.78E+00 | 1.93E+00 | 3.98E+00 | 1.08E+01 |
| 3.08849 | 2.82E+00 | 2.15E+00 | 3.35E+00 | 1.21E+01 | 2.73E+00 | 1.92E+00 | 3.78E+00 | 1.05E+01 |
| 3.1157 | 2.77E+00 | 2.13E+00 | 3.15E+00 | 1.18E+01 | 2.69E+00 | 1.91E+00 | 3.61E+00 | 1.03E+01 |
| 3.14292 | 2.73E+00 | 2.11E+00 | 2.99E+00 | 1.15E+01 | 2.65E+00 | 1.89E+00 | 3.47E+00 | 1.00E+01 |
| 3.17013 | 2.69E+00 | 2.09E+00 | 2.86E+00 | 1.13E+01 | 2.62E+00 | 1.87E+00 | 3.36E+00 | 9.77E+00 |
| 3.19734 | 2.66E+00 | 2.08E+00 | 2.75E+00 | 1.10E+01 | 2.59E+00 | 1.85E+00 | 3.28E+00 | 9.54E+00 |
| 3.22455 | 2.63E+00 | 2.06E+00 | 2.64E+00 | 1.08E+01 | 2.56E+00 | 1.82E+00 | 3.22E+00 | 9.33E+00 |
| 3.25176 | 2.59E+00 | 2.05E+00 | 2.52E+00 | 1.06E+01 | 2.53E+00 | 1.80E+00 | 3.17E+00 | 9.14E+00 |
| 3.27897 | 2.56E+00 | 2.04E+00 | 2.41E+00 | 1.04E+01 | 2.51E+00 | 1.78E+00 | 3.13E+00 | 8.97E+00 |
| 3.30618 | 2.53E+00 | 2.03E+00 | 2.28E+00 | 1.03E+01 | 2.49E+00 | 1.77E+00 | 3.09E+00 | 8.80E+00 |
| 3.3334 | 2.49E+00 | 2.01E+00 | 2.16E+00 | 1.00E+01 | 2.47E+00 | 1.75E+00 | 3.05E+00 | 8.64E+00 |
| 3.36061 | 2.46E+00 | 2.00E+00 | 2.06E+00 | 9.82E+00 | 2.45E+00 | 1.73E+00 | 3.02E+00 | 8.49E+00 |
| 3.38782 | 2.43E+00 | 1.98E+00 | 1.98E+00 | 9.60E+00 | 2.43E+00 | 1.71E+00 | 2.99E+00 | 8.34E+00 |
| 3.41503 | 2.40E+00 | 1.96E+00 | 1.92E+00 | 9.37E+00 | 2.42E+00 | 1.70E+00 | 2.97E+00 | 8.20E+00 |
| 3.44224 | 2.37E+00 | 1.93E+00 | 1.87E+00 | 9.15E+00 | 2.40E+00 | 1.68E+00 | 2.94E+00 | 8.05E+00 |
| 3.46945 | 2.34E+00 | 1.91E+00 | 1.85E+00 | 8.93E+00 | 2.38E+00 | 1.66E+00 | 2.93E+00 | 7.90E+00 |
| 3.49666 | 2.32E+00 | 1.88E+00 | 1.84E+00 | 8.71E+00 | 2.37E+00 | 1.64E+00 | 2.93E+00 | 7.75E+00 |
| 3.52388 | 2.30E+00 | 1.85E+00 | 1.85E+00 | 8.51E+00 | 2.35E+00 | 1.61E+00 | 2.94E+00 | 7.60E+00 |
| 3.55109 | 2.28E+00 | 1.82E+00 | 1.88E+00 | 8.32E+00 | 2.34E+00 | 1.59E+00 | 2.97E+00 | 7.45E+00 |
| 3.5783 | 2.27E+00 | 1.79E+00 | 1.93E+00 | 8.14E+00 | 2.34E+00 | 1.56E+00 | 3.01E+00 | 7.31E+00 |
| 3.60551 | 2.26E+00 | 1.77E+00 | 1.99E+00 | 7.98E+00 | 2.33E+00 | 1.54E+00 | 3.08E+00 | 7.19E+00 |
| 3.63272 | 2.25E+00 | 1.74E+00 | 2.06E+00 | 7.83E+00 | 2.34E+00 | 1.52E+00 | 3.15E+00 | 7.08E+00 |
| 3.65993 | 2.25E+00 | 1.71E+00 | 2.14E+00 | 7.71E+00 | 2.34E+00 | 1.50E+00 | 3.24E+00 | 7.00E+00 |
| 3.68714 | 2.25E+00 | 1.69E+00 | 2.22E+00 | 7.61E+00 | 2.35E+00 | 1.48E+00 | 3.32E+00 | 6.94E+00 |
| 3.71436 | 2.26E+00 | 1.67E+00 | 2.30E+00 | 7.53E+00 | 2.36E+00 | 1.46E+00 | 3.41E+00 | 6.90E+00 |
| 3.74157 | 2.26E+00 | 1.65E+00 | 2.38E+00 | 7.47E+00 | 2.36E+00 | 1.45E+00 | 3.48E+00 | 6.87E+00 |
| 3.76878 | 2.26E+00 | 1.64E+00 | 2.44E+00 | 7.43E+00 | 2.37E+00 | 1.44E+00 | 3.55E+00 | 6.86E+00 |
| 3.79599 | 2.27E+00 | 1.63E+00 | 2.49E+00 | 7.39E+00 | 2.38E+00 | 1.44E+00 | 3.60E+00 | 6.85E+00 |
| 3.8232 | 2.27E+00 | 1.62E+00 | 2.53E+00 | 7.36E+00 | 2.39E+00 | 1.43E+00 | 3.65E+00 | 6.85E+00 |
| 3.85041 | 2.27E+00 | 1.61E+00 | 2.55E+00 | 7.33E+00 | 2.40E+00 | 1.43E+00 | 3.69E+00 | 6.85E+00 |
| 3.87762 | 2.27E+00 | 1.61E+00 | 2.57E+00 | 7.29E+00 | 2.40E+00 | 1.43E+00 | 3.73E+00 | 6.85E+00 |
| 3.90484 | 2.27E+00 | 1.60E+00 | 2.60E+00 | 7.23E+00 | 2.41E+00 | 1.42E+00 | 3.77E+00 | 6.85E+00 |
| 3.93205 | 2.27E+00 | 1.58E+00 | 2.64E+00 | 7.17E+00 | 2.41E+00 | 1.42E+00 | 3.81E+00 | 6.85E+00 |
| 3.95926 | 2.27E+00 | 1.57E+00 | 2.70E+00 | 7.12E+00 | 2.42E+00 | 1.42E+00 | 3.86E+00 | 6.86E+00 |
| 3.98647 | 2.28E+00 | 1.56E+00 | 2.78E+00 | 7.09E+00 | 2.43E+00 | 1.42E+00 | 3.91E+00 | 6.89E+00 |
| 4.01368 | 2.29E+00 | 1.55E+00 | 2.86E+00 | 7.08E+00 | 2.44E+00 | 1.42E+00 | 3.96E+00 | 6.93E+00 |

| | | | | | | | | |
|---|---|---|---|---|---|---|---|---|
| 4.04089 | 2.30E+00 | 1.54E+00 | 2.93E+00 | 7.10E+00 | 2.45E+00 | 1.42E+00 | 4.00E+00 | 6.98E+00 |
| 4.0681 | 2.32E+00 | 1.54E+00 | 2.99E+00 | 7.13E+00 | 2.46E+00 | 1.43E+00 | 4.02E+00 | 7.04E+00 |
| 4.09531 | 2.33E+00 | 1.54E+00 | 3.04E+00 | 7.18E+00 | 2.47E+00 | 1.44E+00 | 4.03E+00 | 7.11E+00 |
| 4.12253 | 2.34E+00 | 1.55E+00 | 3.07E+00 | 7.24E+00 | 2.48E+00 | 1.45E+00 | 4.03E+00 | 7.17E+00 |
| 4.14974 | 2.34E+00 | 1.56E+00 | 3.08E+00 | 7.29E+00 | 2.48E+00 | 1.46E+00 | 4.02E+00 | 7.23E+00 |

### 4.5.3.5. Calculation of quantum yield (QY)

The fluorescence quantum yield of QDs in water and organic solvent (TCE) was calculated using the integrated fluorescence intensity of QDs and comparing it with a standard dye called IR-140. By measuring the integrated fluorescence spectrum of $Ag_2S$ in water and TCE with five different concentrations, linear fits were used to determine the quantum yield by comparing the slopes with the reference IR-140 ($\Phi_f$ = 0.167, ethanol). To find the relative quantum yield of an unknown sample, its emission and absorption were compared with those of the QDs with known QY using a specific equation given below

$$QY_S = QY_R \times \frac{I_S \times A_R \times {n_S}^2}{I_R \times A_S \times {n_R}^2}$$

The average value was reported after performing measurements on $Ag_2S$ CQDs at five different concentrations. The measurements involved calculating the integrated PL intensity represented by the symbol *I*, the refractive index represented by the symbol *n*, and the absorbance (at the excitation wavelength) represented by the symbol *A*. The subscripts *R* and *S* refer to the reference and sample respectively.

### 4.5.3.6. Spectral Data

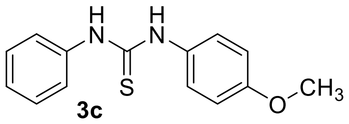
3c

**1-(4-Methoxyphenyl)-3-phenylthiourea** (**3c**). To synthesize 1-(4-methoxyphenyl)-3-phenylthiourea, the general procedure (Method *A*) was followed. In this method, solutions of 4-methoxyaniline (2c, 0.62 g, 5.0 mmol) in toluene (10 mL) and phenyl isothiocyanate (1, 0.07 g, 5 mmol) in toluene (10 mL) were reacted. The reaction led to the formation of 1-(4-methoxyphenyl)-3-phenylthiourea (**3c**) in 91% yield. 1H NMR (400 MHz, $CDCl_3$) δ 7.75 (s, broad, 2H), 7.39 (d, 4H, *J*=4.2 Hz), 7.29–7.27 (m, 3H), 6.94 (d, 2H, *J*=8.8 Hz), 3.82 (s, 3H). $^{13}C$ {$^1H$} NMR (100 MHz, $CDCl_3$) 180.7, 159.0, 129.6, 127.7, 127.0, 125.3, 115.0, 55.5.

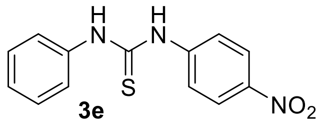
3e

**1-(4-Nitrophenyl)-3-phenylthiourea (3e).**The chemical compound 1-(4-nitrophenyl)-3-phenylthiourea was synthesized using a standard method (Method A) by combining separate solutions of *p*-nitroaniline (2e, 0.69 g, 5.0 mmol) in acetonitrile (10 mL) and phenyl isothiocyanate (1, 0.07 g, 5 mmol) in acetonitrile (10 mL). The mixture was then heated under reflux for 24 hours at 80°C, which resulted in the formation of 3e with a yield of 41%. $^1H$ NMR (400 MHz, $CDCl_3$) $\delta$ 8.09 (d, 2H, *J* = 9.0 Hz), 7.39–7.23 (m, 5H), 6.64 (d, 2H, *J*= 9.0 Hz), 4.42 (s, 2H). $^{13}C$ {$^1H$} NMR (100 MHz, $CDCl_3$) 182.9, 147.6, 130.1, 120.8, 113.4, 109.2, 100.3.

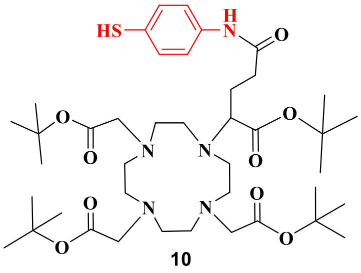
10

**tri-*tert*-Butyl2,2',2''-(10-(1-(*tert*-butoxy)-5-((4-mercaptophenyl)amino)-1,5-dioxopentan-2-yl)-1,4,7,10-tetraazacyclododecane-1,4,7-triyl)triacetate (10):** The general procedure for its synthesis is described above in (***Method D***). $^1H$ NMR ($CDCl_3$, 400 MHz) δ 6.91 (d, 2H, *J*=6.8 Hz), 6.61 (d, 2H, *J*=8.5 Hz), 5.18 (s, 1H), 4.37 (s, 1H), 3.32–3.31 (m, 3H), 2.91–2.60 (m, 12H), 2.38–1.96 (m, 12H), 1.39–1.35 (m, 8H), 1.31–1.28 (m, 28 H). $^{13}$C {1H} NMR (100 MHz, $CDCl_3$) $\delta$ 200.0, 174.5, 172.7, 149.1, 135.7, 115.6, 113.9, 113.3, 82.7, 82.1, 59.6, 55.8, 53.6, 52.6, 52.4, 48.4, 48.0, 47.1, 44.2, 41.1, 37.8, 20.1. ESI-MS calculated for $C_{41}H_{69}N_5NaO_9S$ $(M+Na)^+$ 830.4713, found 831.0001.

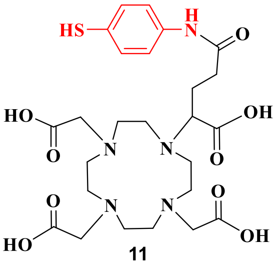

11

**2,2',2''-(10-(1-Carboxy-4-((4-mercaptophenyl)amino)-4-oxobutyl)-1,4,7,10-tetraazacyclododecane-1,4,7-triyl)triacetic acid (11):** The general procedure for its synthesis is described above in (***Method E***). $^1$H NMR ($D_2O$, 400 MHz) δ 7.55 (s, 1H), 7.46 (d, 2H, *J*=8.3 Hz), 7.34 (d, 2H, *J*=8.6 Hz), 4.81 (s, 1H), 3.90–3.84 (m, 4H), 3.36–3.30 (m, 5H), 3.02–2.82 (m, 12H), 1.95–1.88 (m, 3H), 1.31–1.11 (m, 3H). ESI-MS calculated for $C_{25}H_{38}N_5O_9S$ $(M+H)^+$ 584.239, found 584.001.

### 4.6. References

(1) Grover, V. P. B.; Tognarelli, J. M.; Crossey, M. M. E.; Cox, I. J.; Taylor-Robinson, S. D.; McPhail, M. J. W. Magnetic Resonance Imaging: Principles and Techniques: Lessons for Clinicians. *J Clin Exp Hepatol* **2015**, *5*, 246–255.

(2) Cui, L.; Rao, J. Chemical Methodology for Labelling and Bioconjugation. In *The Chemistry of Molecular Imaging*; John Wiley & Sons, Inc: Hoboken, NJ, **2014**, *6*, 25–53.

(3) P. W. Atkins. Physical Chemistry, 6th Edition. *Oxford University Press* **1998**.

(4) Markiewicz, W. D.; Brey, W. W.; Cross, T. A.; Dixon, I. R.; Gor’kov, P. L.; Grant, S. C.; Marks, E. L.; Painter, T. A.; Schepkin, V. D.; Swenson, C. A. A Decade of Experience With the UltraWide-Bore 900-MHz NMR Magnet. *IEEE Transactions on Applied Superconductivity* **2015**, *25*, 1–5.

(5) Jéquier, E.; Constant, F. Water as an Essential Nutrient: The Physiological Basis of Hydration. *Eur J Clin Nutr* **2010**, *64*, 115–123.

(6) Plewes, D. B.; Kucharczyk, W. Physics of MRI: A Primer. *Journal of Magnetic Resonance Imaging* **2012**, *35*, 1038–1054.

(7) Li, W.; Grgac, K.; Huang, A.; Yadav, N.; Qin, Q.; van Zijl, P. C. M. Quantitative Theory for the Longitudinal Relaxation Time of Blood Water. *Magn Reson Med* **2016**, *76*, 270–281.

(8) Welker, M. E.; Kulik, G. Recent Syntheses of PI3K/Akt/MTOR Signaling Pathway Inhibitors. *Bioorg Med Chem* **2013**, *21*, 4063–4091.

(9) Mahmoudi, M.; Serpooshan, V.; Laurent, S. Engineered Nanoparticles for Biomolecular Imaging. *Nanoscale* **2011**, *3*, 3007–3010.

(10) Caravan, P.; Ellison, J. J.; McMurry, T. J.; Lauffer, R. B. Gadolinium(III) Chelates as MRI Contrast Agents: Structure, Dynamics, and Applications. *Chem Rev* **1999**, *99*, 2293–2352.

(11) Solomon, I. Relaxation Processes in a System of Two Spins. *Physical Review* **1955**, *99*, 559–565.

(12) Bloembergen, N.; Morgan, L. O. Proton Relaxation Times in Paramagnetic Solutions. Effects of Electron Spin Relaxation. *J Chem Phys* **1961**, *34*, 842–850.

(13) Wahsner, J.; Gale, E. M.; Rodríguez-Rodríguez, A.; Caravan, P. Chemistry of MRI Contrast Agents: Current Challenges and New Frontiers. *Chem Rev* **2019**, *119*, 957–1057.

(14) Kumar, K.; Jin, T.; Wang, X.; Desreux, J. F.; Tweedle, M. F. Effect of Ligand Basicity on the Formation and Dissociation Equilibria and Kinetics of Gd3+ Complexes of Macrocyclic Polyamino Carboxylates. *Inorg Chem* **1994**, *33*, 3823–3829.

(15) Stasiuk, G. J.; Tamang, S.; Imbert, D.; Poillot, C.; Giardiello, M.; Tisseyre, C.; Barbier, E. L.; Fries, P. H.; de Waard, M.; Reiss, P.; Mazzanti, M. Cell-Permeable Ln(III) Chelate-Functionalized InP Quantum Dots As Multimodal Imaging Agents. *ACS Nano* **2011**, *5*, 8193–8201.

(16) Evans, D. F. The Determination of the Paramagnetic Susceptibility of Substances in Solution by Nuclear Magnetic Resonance. *Journal of the Chemical Society* **1959**, *1*, 2003–2005.

(17) Tamang, S.; Beaune, G.; Texier, I.; Reiss, P. Aqueous Phase Transfer of InP/ZnS Nanocrystals Conserving Fluorescence and High Colloidal Stability. *ACS Nano* **2011**, *5*, 9392–9402.

(18) Chen, H.; Wang, L.; Fu, H.; Wang, Z.; Xie, Y.; Zhang, Z.; Tang, Y. Gadolinium Functionalized Carbon Dots for Fluorescence/Magnetic Resonance Dual-Modality Imaging of Mesenchymal Stem Cells. *J Mater Chem B* **2016**, *4*, 7472–7480.

(19) Ricard, D.; Ghanassi, M.; Schanne-Klein, M. C. Dielectric Confinement and the Linear and Nonlinear Optical Properties of Semiconductor-Doped Glasses. *Opt Commun* **1994**, *108*, 4–6.

(20) Hanaoka, K.; Kikuchi, K.; Kojima, H.; Urano, Y.; Nagano, T. Development of a Zinc Ion-Selective Luminescent Lanthanide Chemosensor for Biological Applications. *J Am Chem Soc* **2004**, *126*, 12470–12476.

(21) Gil, H. M.; Price, T. W.; Chelani, K.; Bouillard, J.-S. G.; Calaminus, S. D. J.; Stasiuk, G. J. NIR-Quantum Dots in Biomedical Imaging and Their Future. *iScience* **2021**, *24*, 102189–102191.

(22) Tan, L.; Liu, S.; Li, X.; Chronakis, I. S.; Shen, Y. A New Strategy for Synthesizing AgInS2 Quantum Dots Emitting Brightly in Near-Infrared Window for in Vivo Imaging. *Colloids Surf B Biointerfaces* **2015**, *125*, 222–229.

(23) McAdams, S. G.; Lewis, D. J.; McNaughter, P. D.; Lewis, E. A.; Haigh, S. J.; O'Brien, P.; Tuna, F. High Magnetic Relaxivity in a Fluorescent CdSe/CdS/ZnS Quantum Dot Functionalized with MRI Contrast Molecules. *Chemical Communications* **2017**, *53*, 10500–10503.

(24) Marangoni, V. S.; Neumann, O.; Henderson, L.; Kaffes, C. C.; Zhang, H.; Zhang, R.; Bishnoi, S.; Ayala-Orozco, C.; Zucolotto, V.; Bankson, J. A.; Nordlander, P.; Halas, N. J. Enhancing T $_1$ Magnetic Resonance Imaging Contrast with Internalized Gadolinium(III) in a Multilayer Nanoparticle. *Proceedings of the National Academy of Sciences* **2017**, *114* (27), 6960–6965.

(25) Caravan, P.; Ellison, J. J.; McMurry, T. J.; Lauffer, R. B. Gadolinium(III) Chelates as MRI Contrast Agents:  Structure, Dynamics, and Applications. *Chem Rev* **1999**, *99*, 2293–2352.

(26) Ren, X.; Liu, L.; Li, Y.; Dai, Q.; Zhang, M.; Jing, X. Facile Preparation of Gadolinium(III ) Chelates Functionalized Carbon Quantum Dot-Based Contrast Agent for Magnetic Resonance/Fluorescence Multimodal Imaging. *J. Mater. Chem. B* **2014**, *2*, 5541–5549.

(27) Stasiuk, G. J.; Minuzzi, F.; Sae-Heng, M.; Rivas, C.; Juretschke, H.-P.; Piemonti, L.; Allegrini, P. R.; Laurent, D.; Duckworth, A. R.; Beeby, A.; Rutter, G. A.; Long, N. J. Dual-Modal Magnetic Resonance/Fluorescent Zinc Probes for Pancreatic β-Cell Mass Imaging. *Chemistry - A European Journal* **2015**, *21*, 5023–5033.

(28) Keasberry, N. A.; Bañobre-López, M.; Wood, C.; Stasiuk, Graeme. J.; Gallo, J.; Long, Nicholas. J. Tuning the Relaxation Rates of Dual-Mode $T_1/T_2$ Nanoparticle Contrast Agents: A Study into the Ideal System. *Nanoscale* **2015**, *7*, 16119–16128.

(29) Rivas, C.; Stasiuk, G. J.; Sae-Heng, M.; J. Long, N. Towards Understanding the Design of Dual-Modal MR/Fluorescent Probes to Sense Zinc Ions. *Dalton Transactions* **2015**, *44*, 4976–4985.

(30) Stasiuk, G. J.; Long, N. J. The Ubiquitous DOTA and Its Derivatives: The Impact of 1,4,7,10-Tetraazacyclododecane-1,4,7,10-Tetraacetic Acid on Biomedical Imaging. *Chemical Communications* **2013**, *49*, 2732–2740.

(31) Chabloz, N. G.; Wenzel, M. N.; Perry, H. L.; Yoon, I.; Molisso, S.; Stasiuk, G. J.; Elson, D. S.; Cass, A. E. G.; Wilton-Ely, J. D. E. T. Polyfunctionalised Nanoparticles Bearing Robust Gadolinium Surface Units for High Relaxivity Performance in MRI. *Chemistry – A European Journal* **2019**, *25*, 10895–10906.

(32) Stasiuk, G. J.; Tamang, S.; Imbert, D.; Gateau, C.; Reiss, P.; Fries, P.; Mazzanti, M. Optimizing the Relaxivity of Gd(Iii) Complexes Appended to InP/ZnS Quantum Dots by Linker Tuning. *Dalton Transactions* **2013**, *42*, 8197–8199.

(33) Tang, T.; Sun, X.; Xu, X.; Bian, Y.; Ma, X.; Chen, N. Development of Hollow Ferrogadolinium Nanonetworks for Dual-Modal MRI Guided Cancer Chemotherapy. *RSC Adv* **2019**, *9*, 2559–2566.

(34) Ahrén, M.; Selegård, L.; Söderlind, F.; Linares, M.; Kauczor, J.; Norman, P.; Käll, P.-O.; Uvdal, K. A Simple Polyol-Free Synthesis Route to Gd2O3 Nanoparticles for MRI Applications: An Experimental and Theoretical Study. *Journal of Nanoparticle Research* **2012**, *14*, 1006–1010.

(35) Hendricks, M. P.; Campos, M. P.; Cleveland, G. T.; Plante, I. J.-L.; Owen, J. S. A Tunable Library of Substituted Thiourea Precursors to Metal Sulfide Nanocrystals. *Science (1979)* **2015**, *348*, 1226–1230.

(36) Tamang, S.; Beaune, G.; Texier, I.; Reiss, P. Aqueous Phase Transfer of InP / ZnS Nanocrystals Conserving Fluorescence. *ACS Nano* **2011**, *5*, 9392–9402.

(37) Stasiuk, G. J.; Tamang, S.; Imbert, D.; Poillot, C.; Giardiello, M.; Tisseyre, C.; Barbier, E. L.; Fries, P. H.; De Waard, M.; Reiss, P.; Mazzanti, M. Cell-Permeable Ln(III) Chelate-Functionalized InP Quantum Dots as Multimodal Imaging Agents. *ACS Nano,* **2011**, *5*, 8193–8201.

(38) Brunisholz, G.; Randin, M. Sur La Separation Des Terres Rares B l’aide de l’acide 6thylBnediamine-Tktraacetique. IX. Procbde En Cycle Pour Le Fractionnement Des Terres Yttriques. *Helvetica Chimica Acta* **1959**, *42*, 1927–1938.

(39) Gutiérrez-Mejía, F.; Ruiz-Suárez, J. C. AC Magnetic Susceptibility at Medium Frequencies Suggests a Paramagnetic Behavior of Pure Water. *Journal of Magnetism and Magnetic Materials* **2012**, *324*, 1129–1132.

(40) Evans, D. F. The Determination of the Paramagnetic Susceptibility of Substances in Solution by Nuclear Magnetic Resonance. *J. Chem. Soc.* **1959**, *6*, 2003–2005.

(41) Malerich, C.; Ruff, P. K. Demonstrating and Measuring Relative Molar Magnetic Susceptibility Using a Neodymium Magnet. *Journal of Chemical Education* **2004**, *81*, 1155–1160.

(42) Sitharaman, B.; Jacobson, B. D.; Wadghiri, Y. Z.; Bryant, H.; Frank, J. The Magnetic, Relaxometric, and Optical Properties of Gadolinium-Catalyzed Single Walled Carbon Nanotubes. *Journal of Applied Physics* **2013**, *113*, 134308–134309.

(43) Si, P. Z.; Škorvánek, I.; Kováč, J.; Geng, D. Y.; Zhao, X. G.; Zhang, Z. D. Structure and Magnetic Properties of Gd Nanoparticles and Carbon Coated Gd/GdC2 Nanocapsules. *Journal of Applied Physics* **2003**, *94*, 6779–6784.

(44) Blaha, P.; Schwarz, K.; Sorantin, P.; Trickey, S. B. Full-Potential, Linearized Augmented Plane Wave Programs for Crystalline Systems. *Computer Physics Communications* **1990**, *59*, 399–415.

(45) Perdew, J. P.; Burke, K.; Ernzerhof, M. Generalized Gradient Approximation Made Simple. *Physical Review Letters* **1996**, *77*, 3865–3868.

(46) Prabhune, V. B.; Shinde, N. S.; Fulari, V. J. Studies on Electrodeposited Silver Sulphide Thin Films by Double Exposure Holographic Interferometry. *Applied Surface Science* **2008**, *255*, 1819–1823.

# *Annexure A: Supplementary Information*

# *Annexure A2: Supplementary information from Chapter II*

## **A2.1:** $^{1}$H and $^{13}$C NMR for all synthesized precursors (**3a-9b**) for the synthesis of NIR-II NCs.

### **A2.1.1** Copies of NMR spectra:

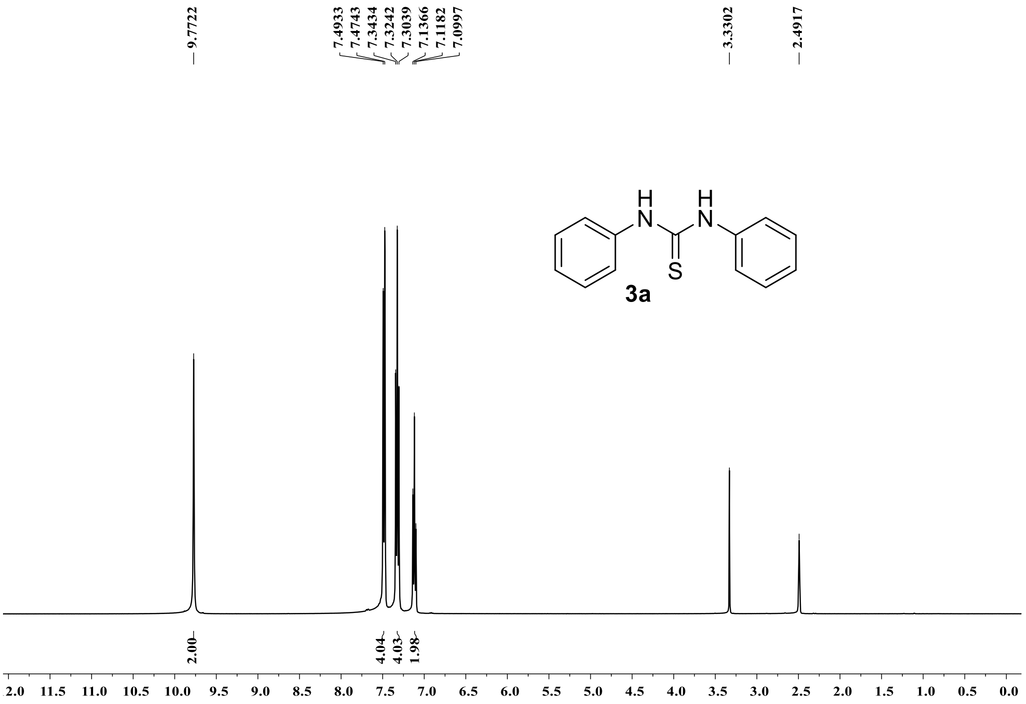

**Figure A2.1**: $^{1}$H NMR of **3a** (400 MHz, DMSO-d$_6$)

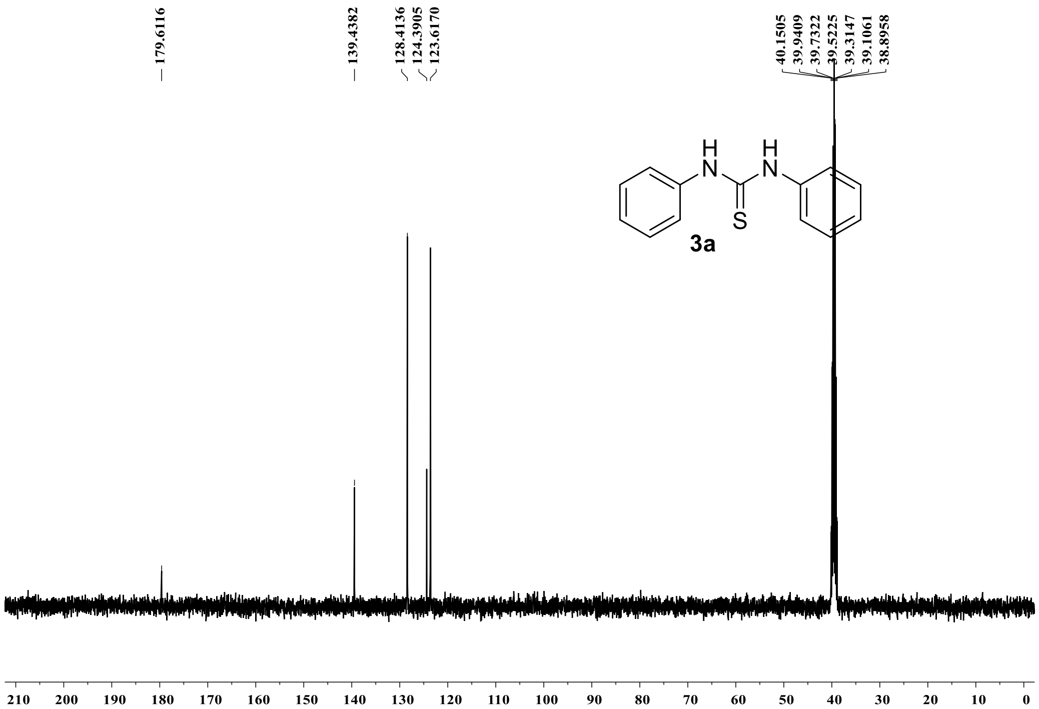

**Figure A2.2:** $^{13}$C NMR of **3a** (400 MHz, DMSO-d$_6$)

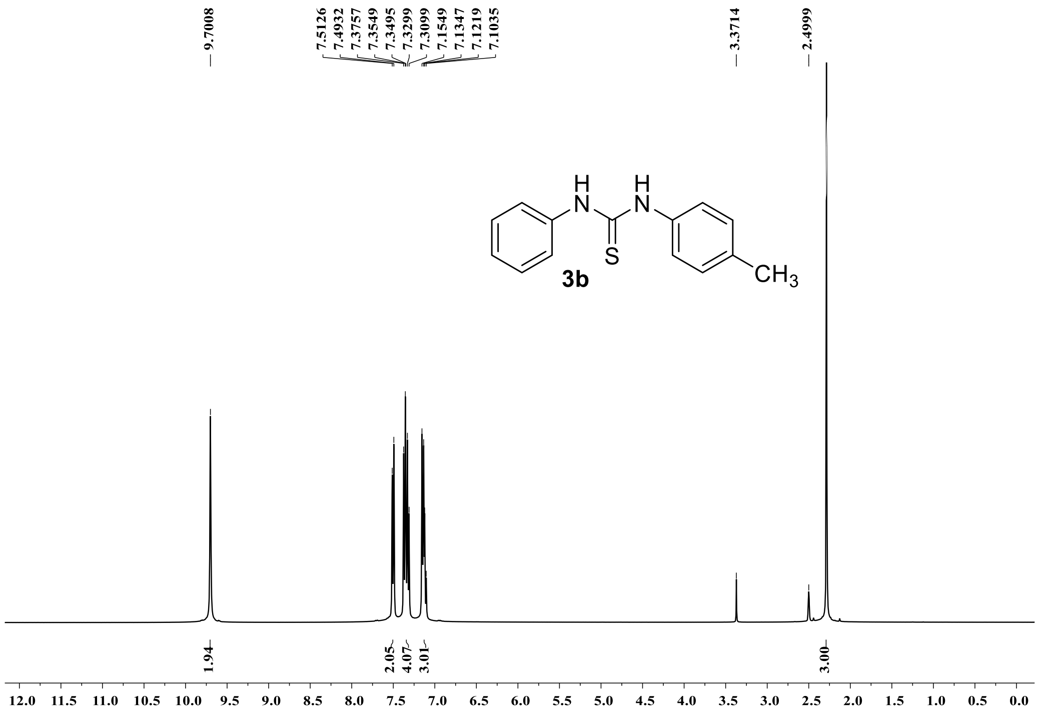

**Figure A2.3**: $^1$H NMR of **3b** (400 MHz, DMSO-d$_6$)

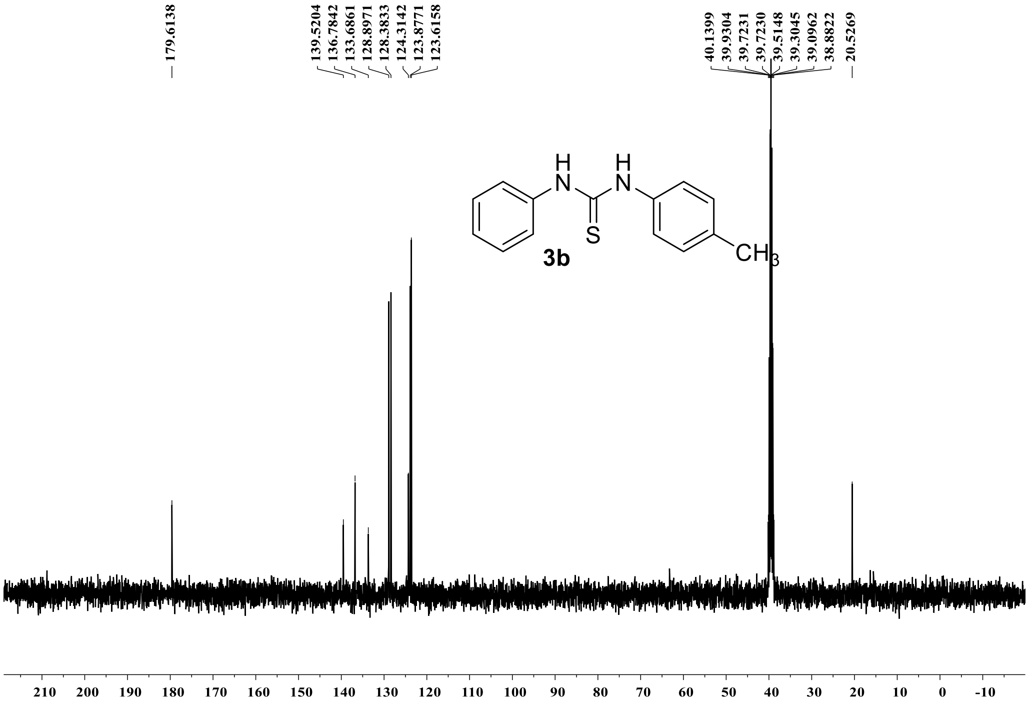

Figure A2.4: $^{13}$C NMR of **3b** (400 MHz, DMSO-d6)

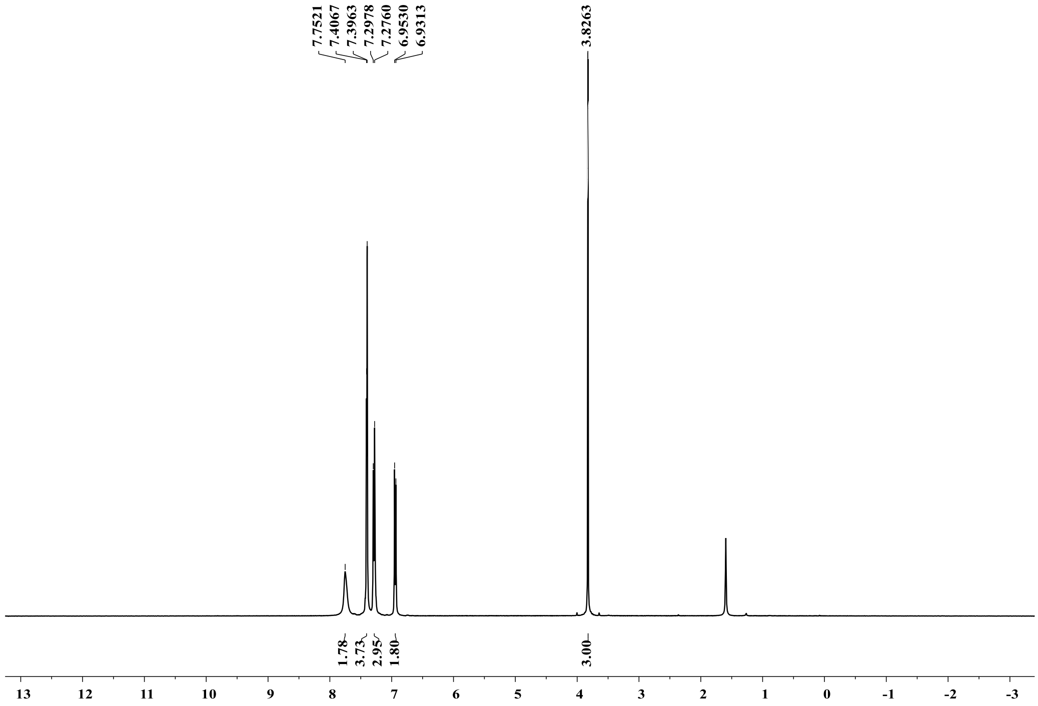

**Figure A2.5**: $^1$H NMR of **3c** (400 MHz, CDCl$_3$)

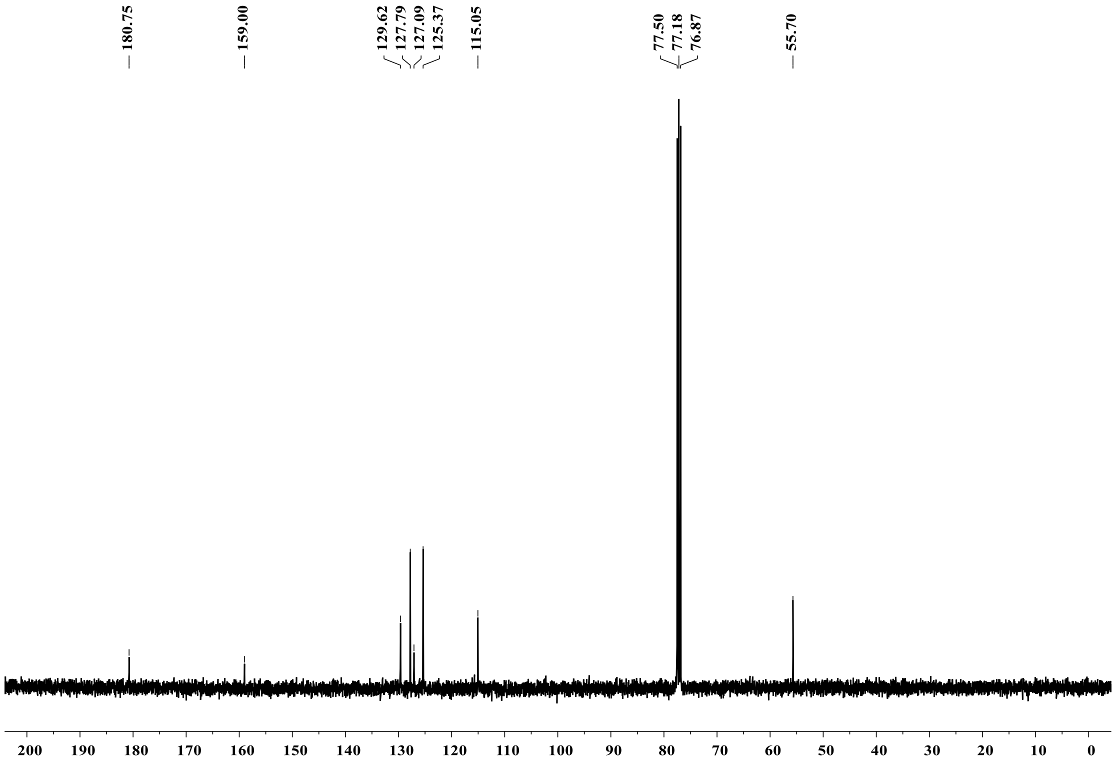

**Figure A2.6:** $^{13}$C NMR of **3c** (400 MHz, $CDCl_3$)

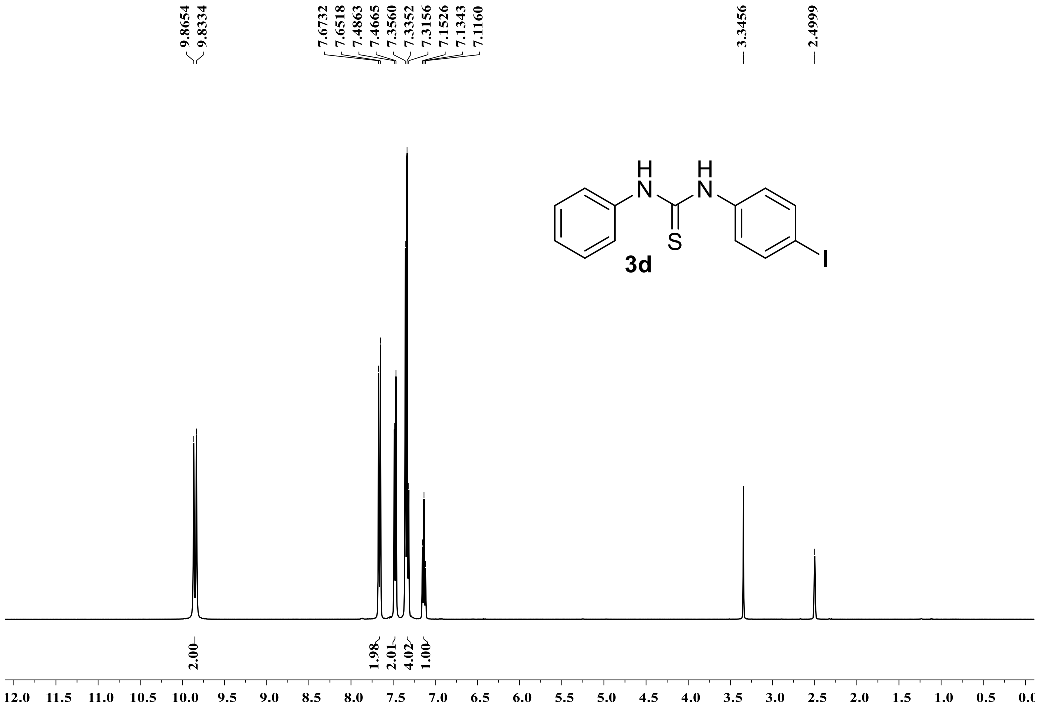

**Figure A2.7**: $^{1}$H NMR of **3d** (400 MHz DMSO-$d_6$)

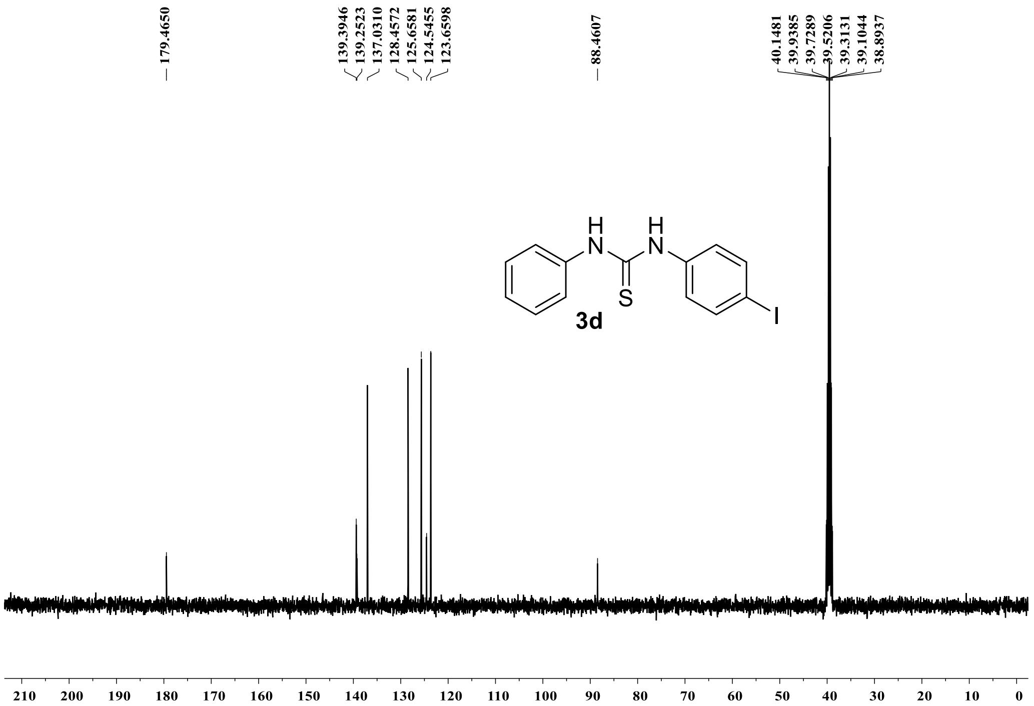

**Figure A2.8:** $^{13}$C NMR of **3d** (400 MHz, DMSO-d$_6$)

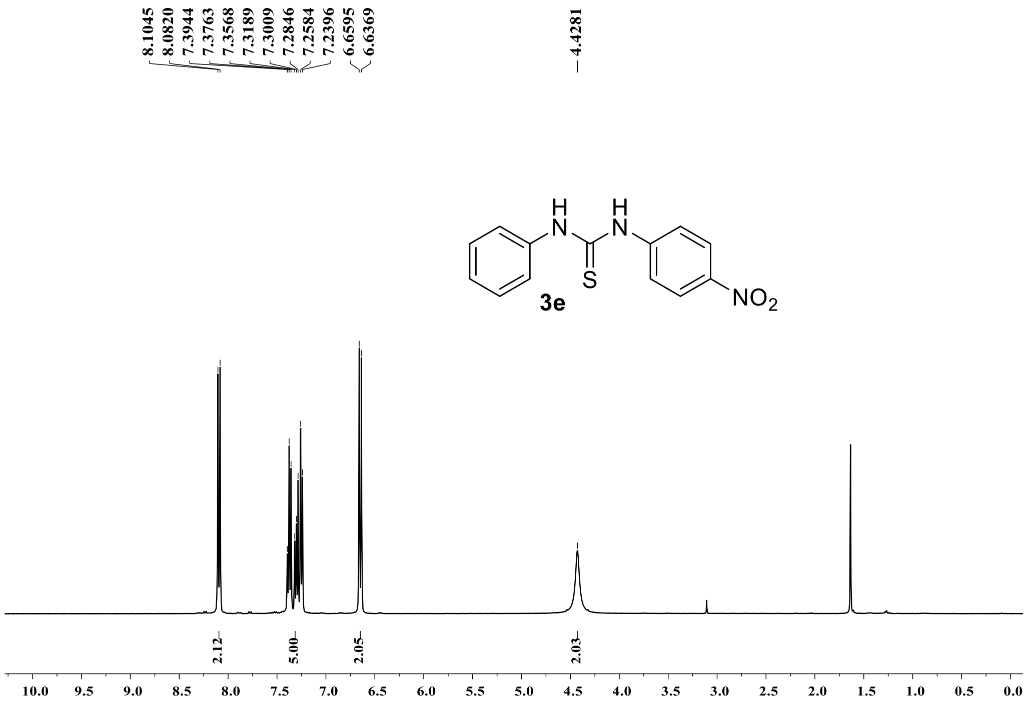

**Figure A2.9**: $^{1}$H NMR of **3e** (400 MHz, CDCl$_3$)

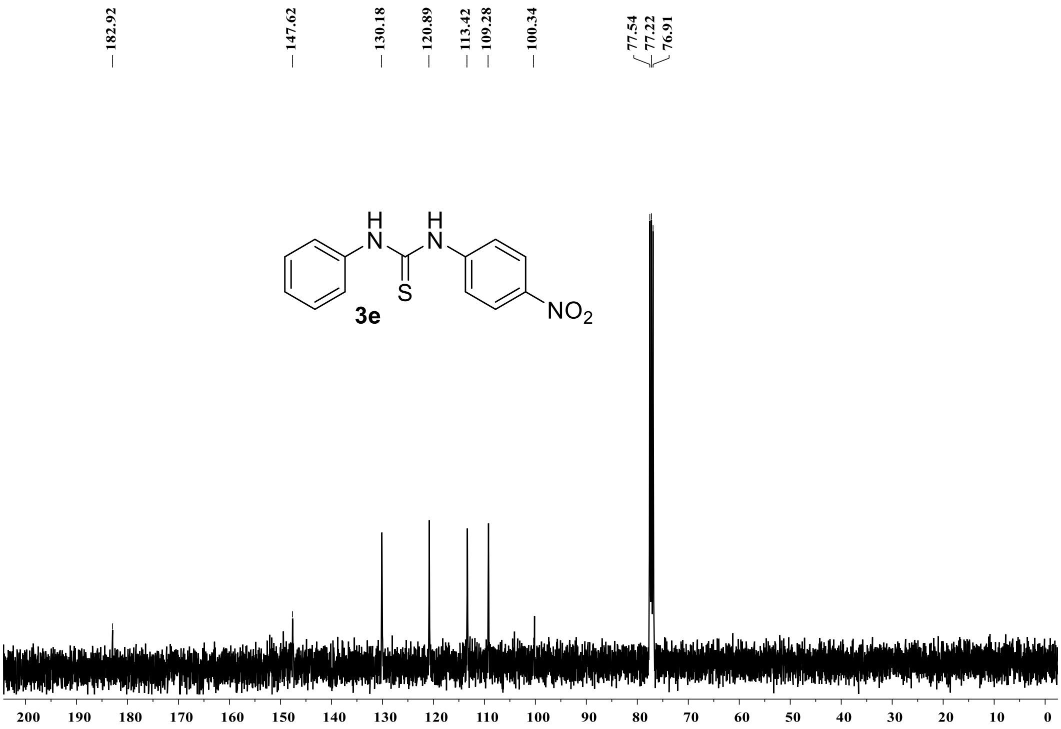

**Figure A2.10:** $^{13}$C NMR of **3e** (400 MHz, CDCl$_3$)

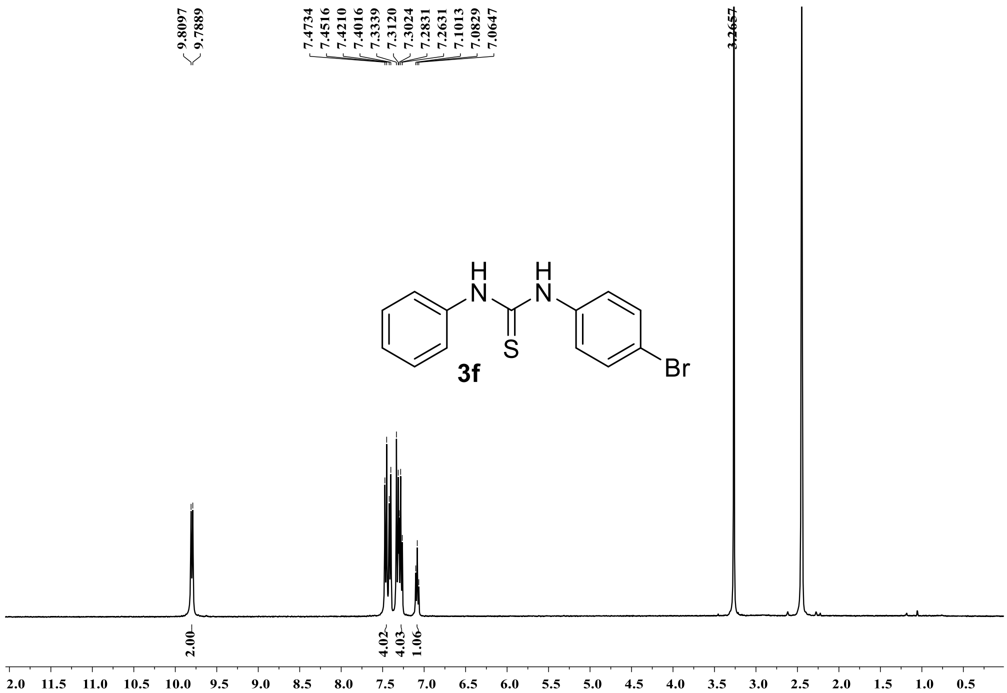

**Figure A2.11**: $^{1}$H NMR of **3f** (400 MHz DMSO-d$_6$)

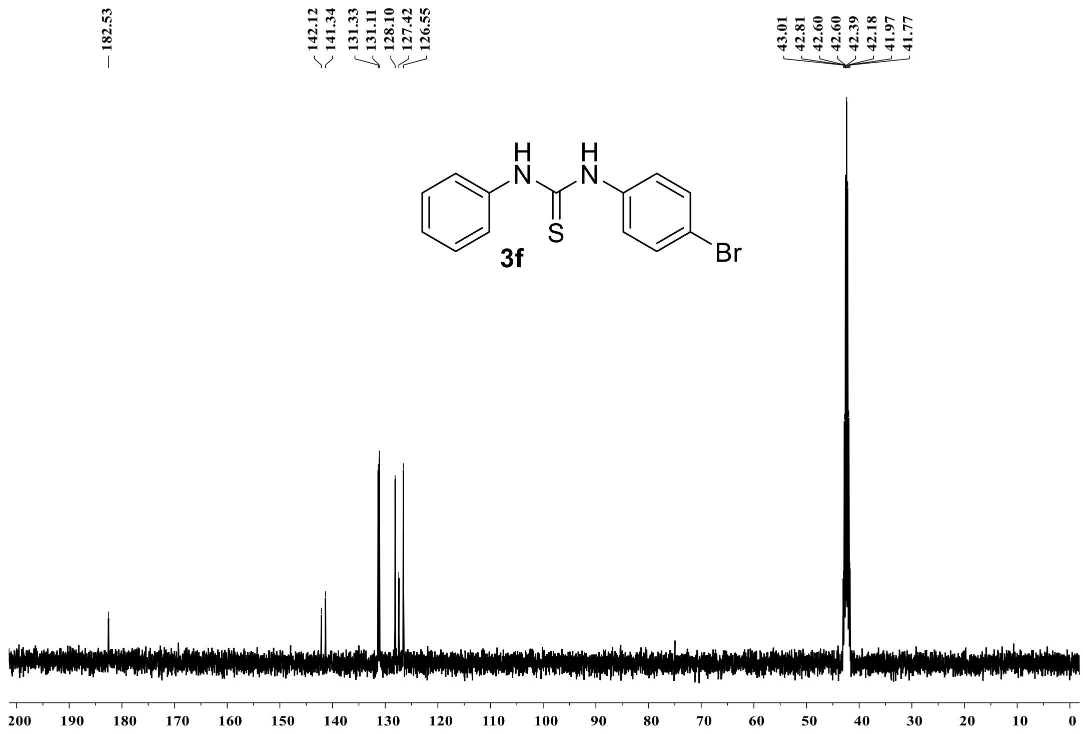

**Figure A2.12:** $^{13}$C NMR of **3f** (400 MHz, DMSO-d$_6$)

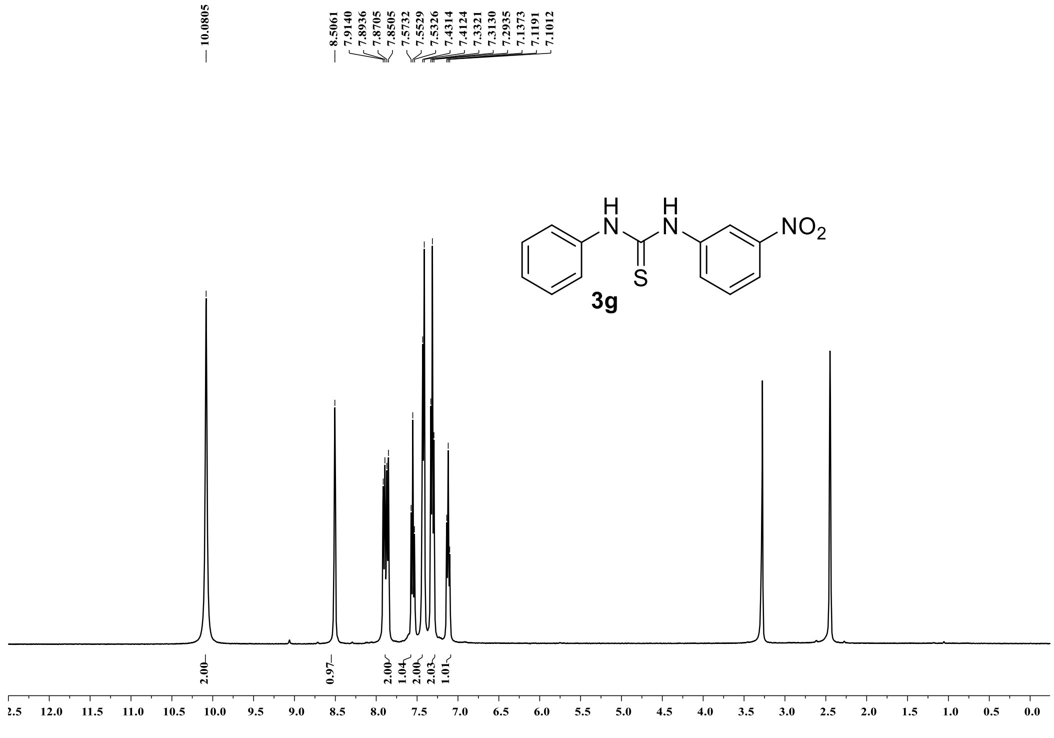

**Figure A2.13**: $^1$H NMR of **3g** (400 MHz DMSO-d6)

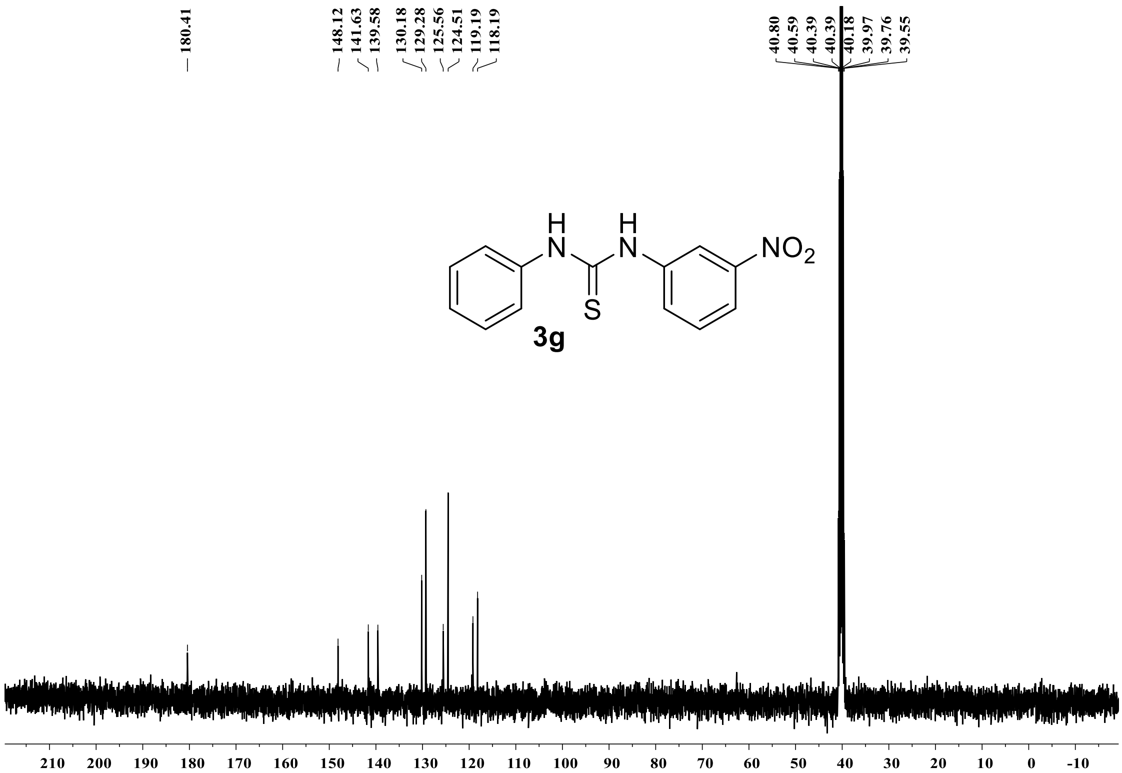

**Figure A2.14:** $^{13}$C NMR of **3g** (400 MHz, DMSO-d6)

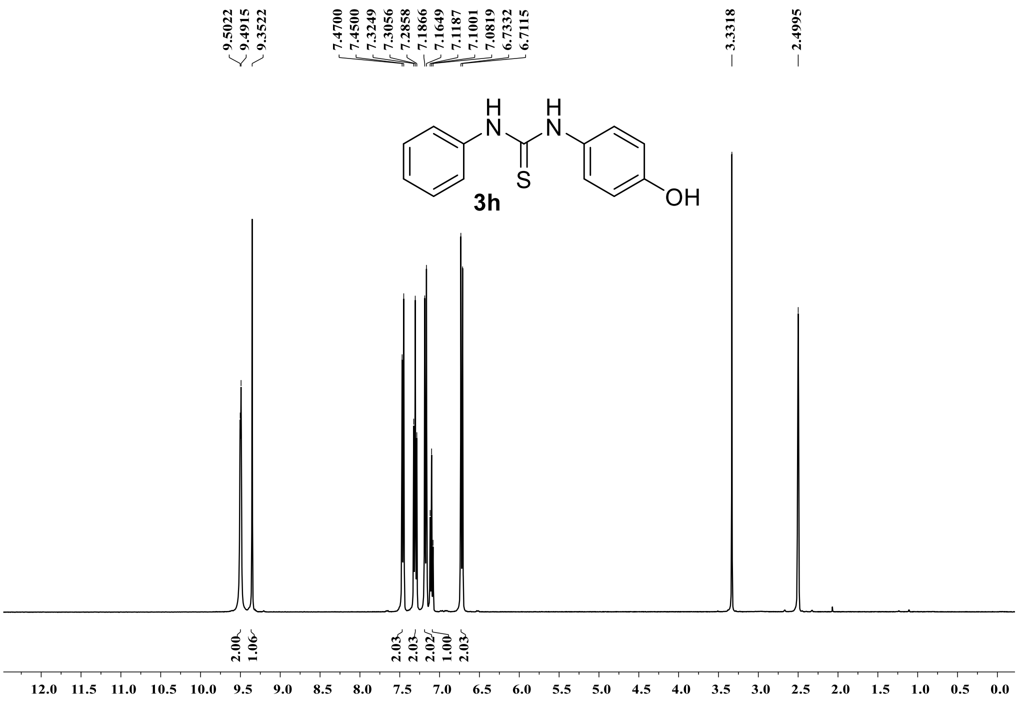

**Figure A2.15:** $^{1}$H NMR of **3h** (400 MHz DMSO-d6)

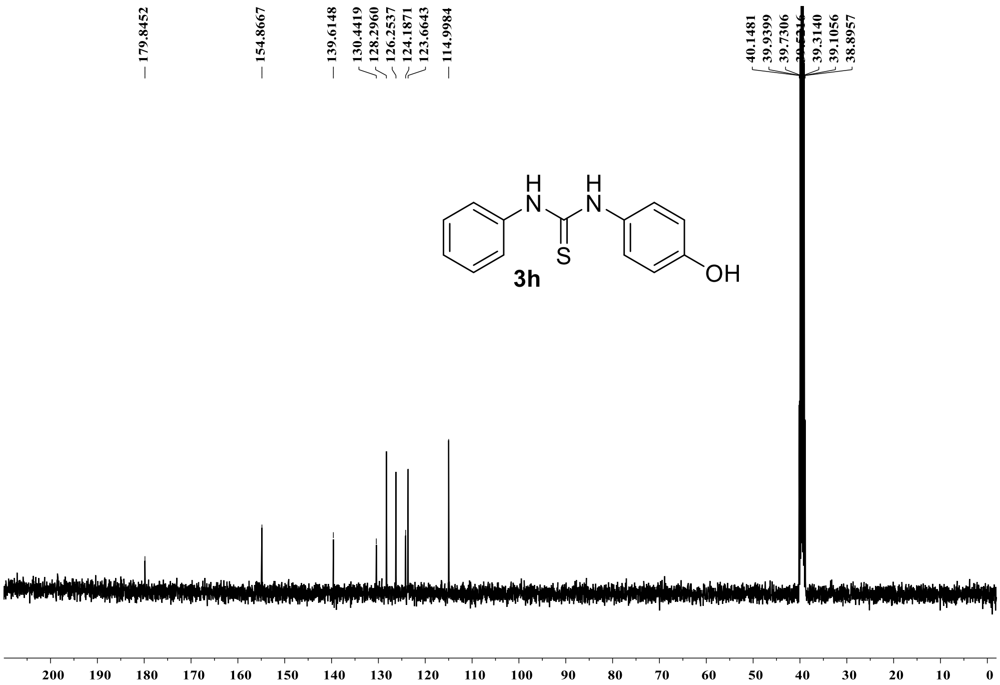

**Figure A2.16:** $^{13}$C NMR of **3h** (400 MHz, DMSO-d$_6$)

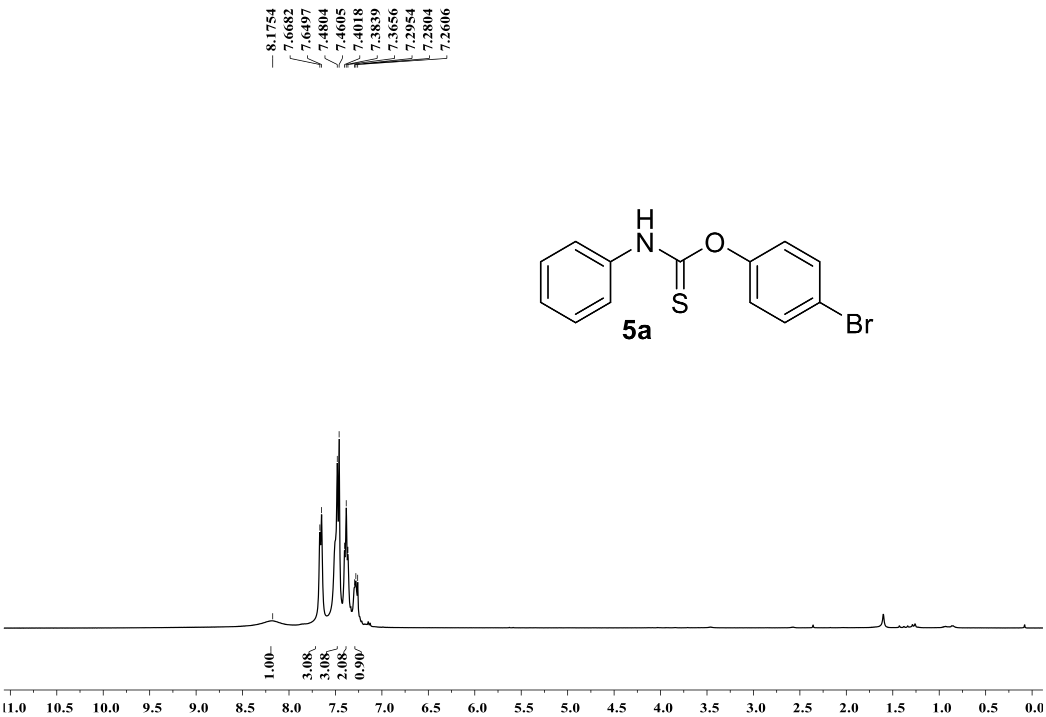

**Figure A2.17:** $^{1}$H NMR of **5a** (400 MHz, CDCl$_3$)

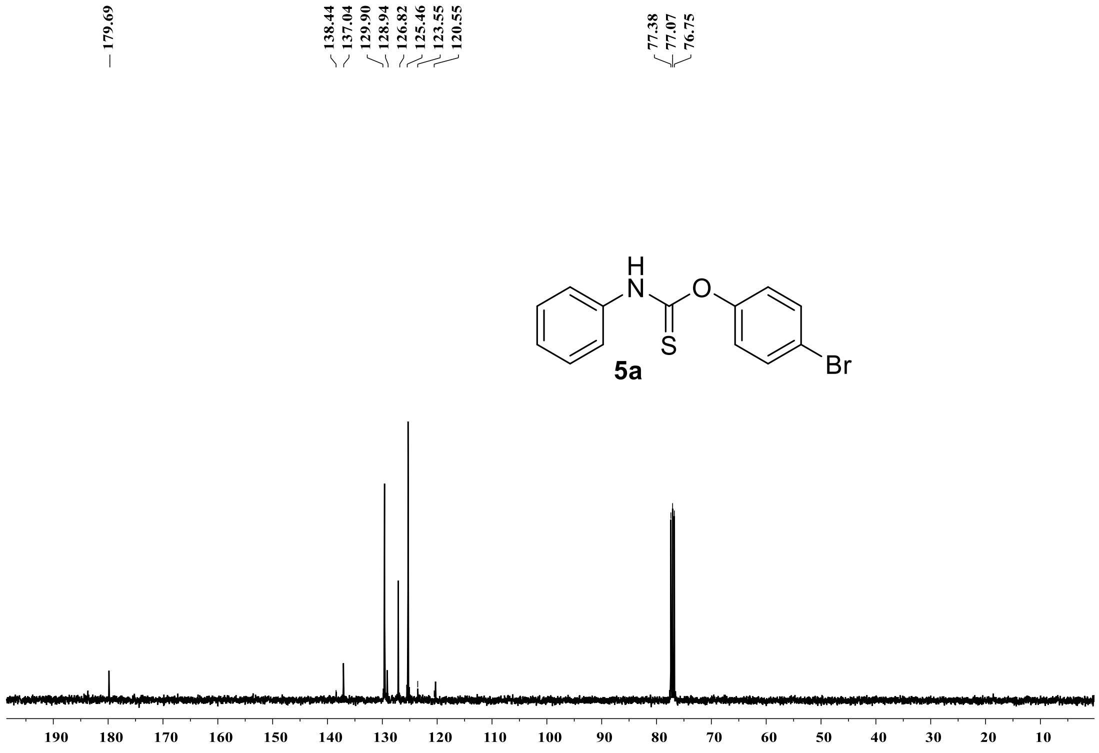

**Figure A2.18:** $^{13}$C NMR of **5a** (100 MHz, CDCl$_3$)

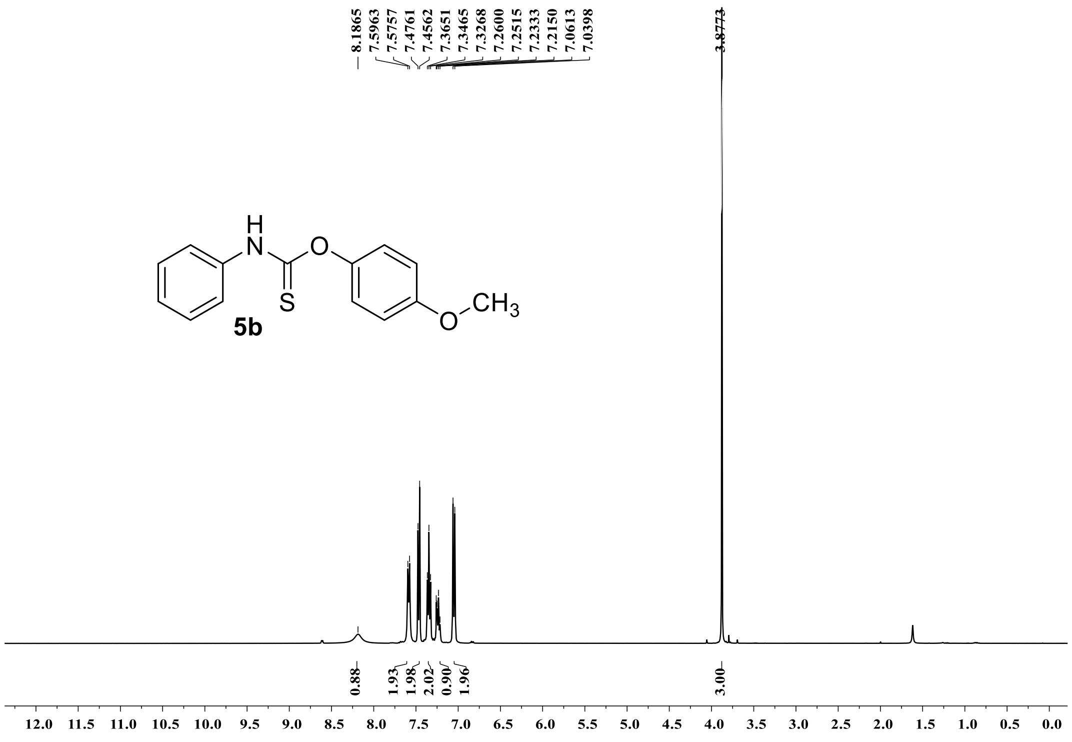

**Figure A2.19:** $^{1}$H NMR of **5b** (400 MHz, CDCl$_3$)

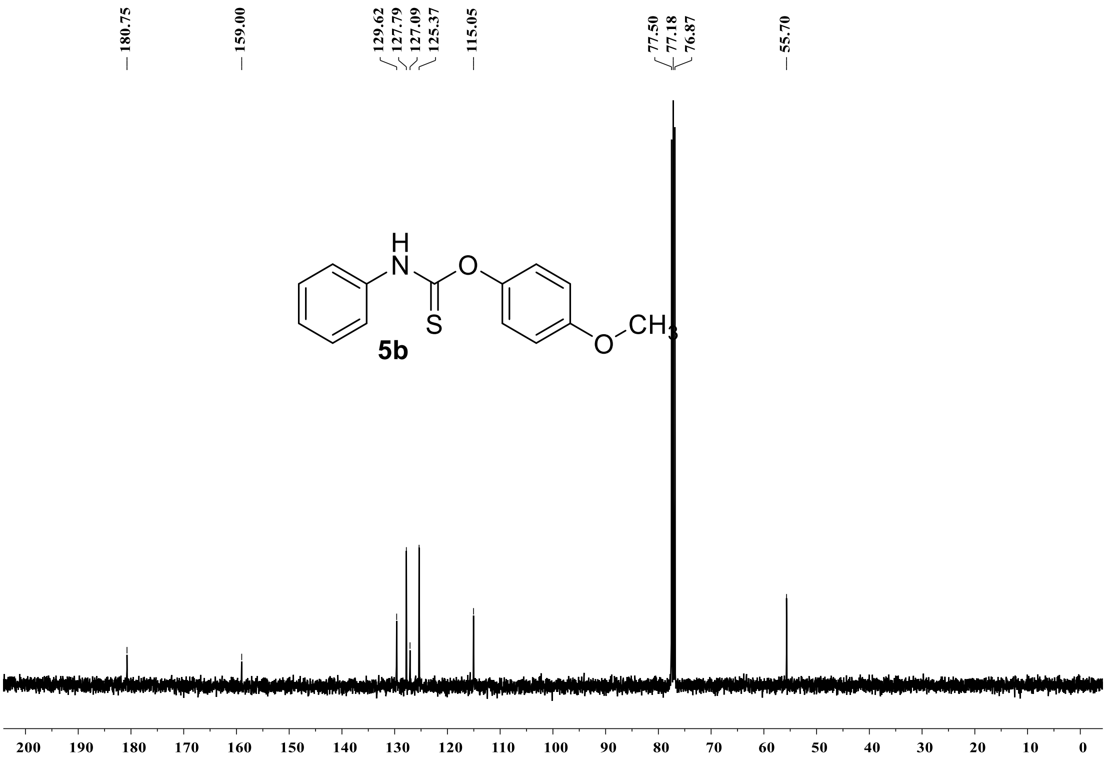

**Figure A2.20:** $^{13}$C NMR of **5b** (100 MHz, CDCl$_3$)

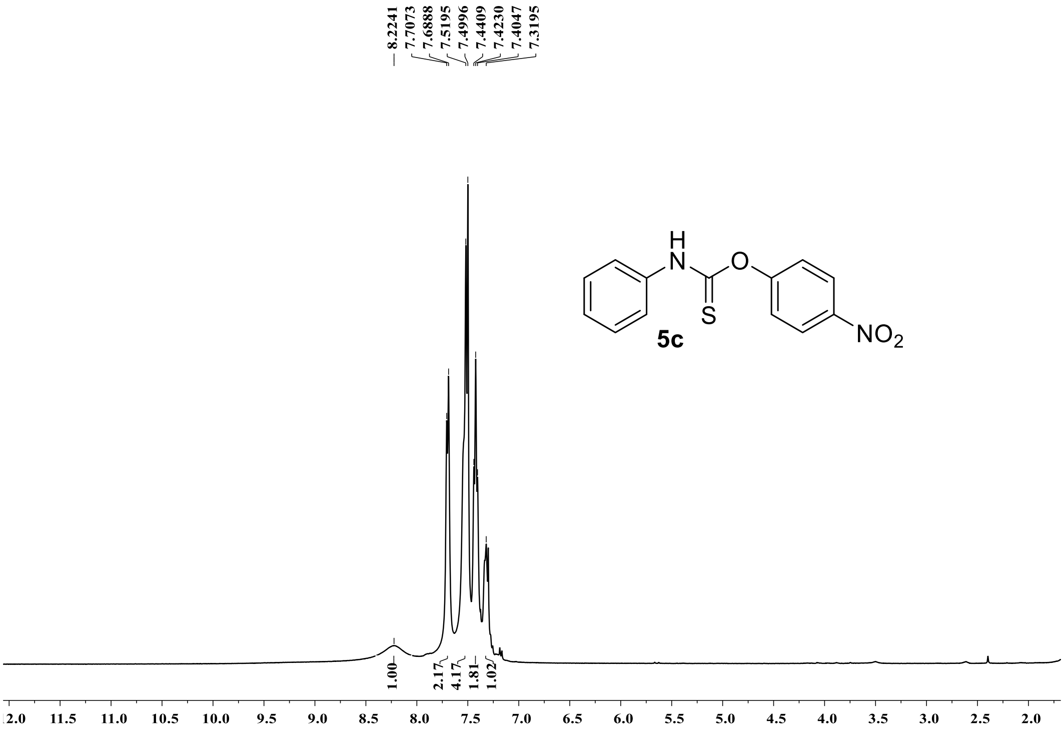

**Figure A2.21:** $^{1}$H NMR of **5c** (400 MHz, CDCl$_3$)

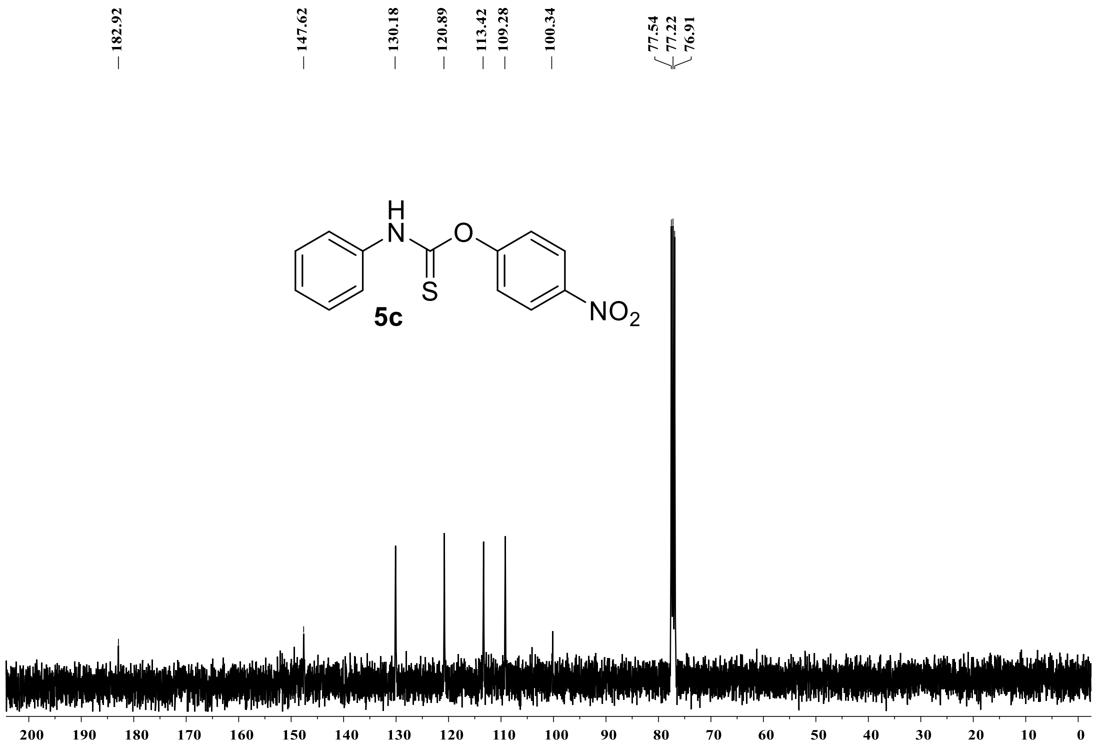

**Figure A2.22:** $^{13}$C NMR of **5c** (100 MHz, CDCl$_3$)

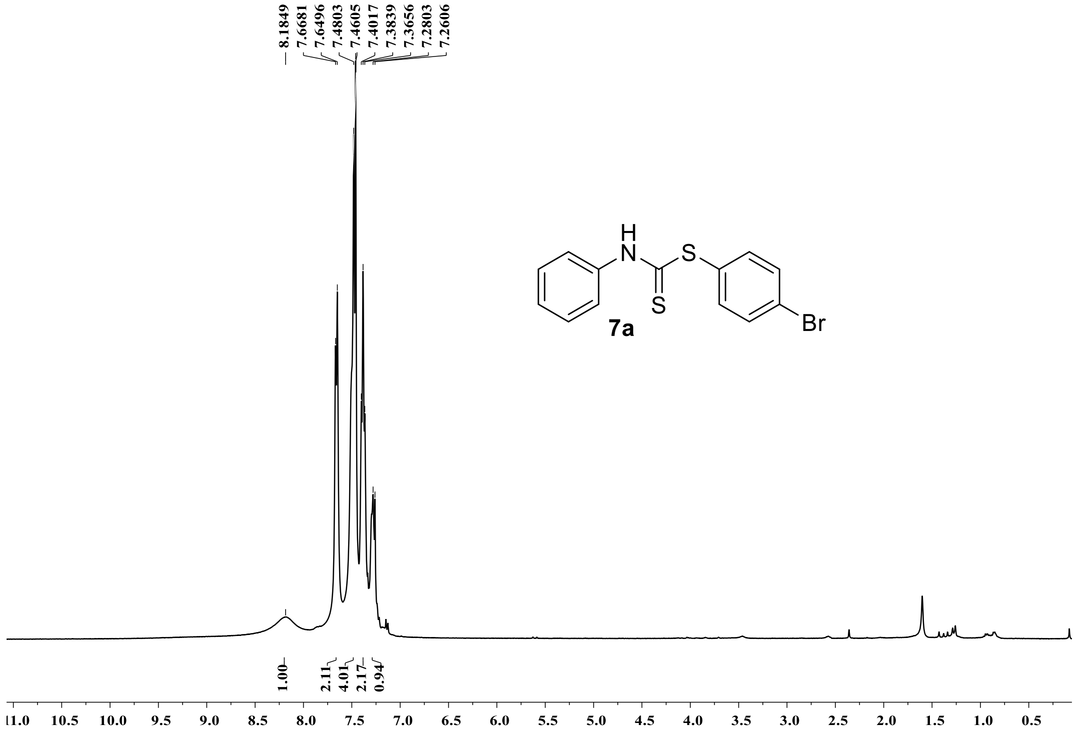

**Figure A2.23:** $^{1}$H NMR of **7a** (400 MHz, CDCl$_3$)

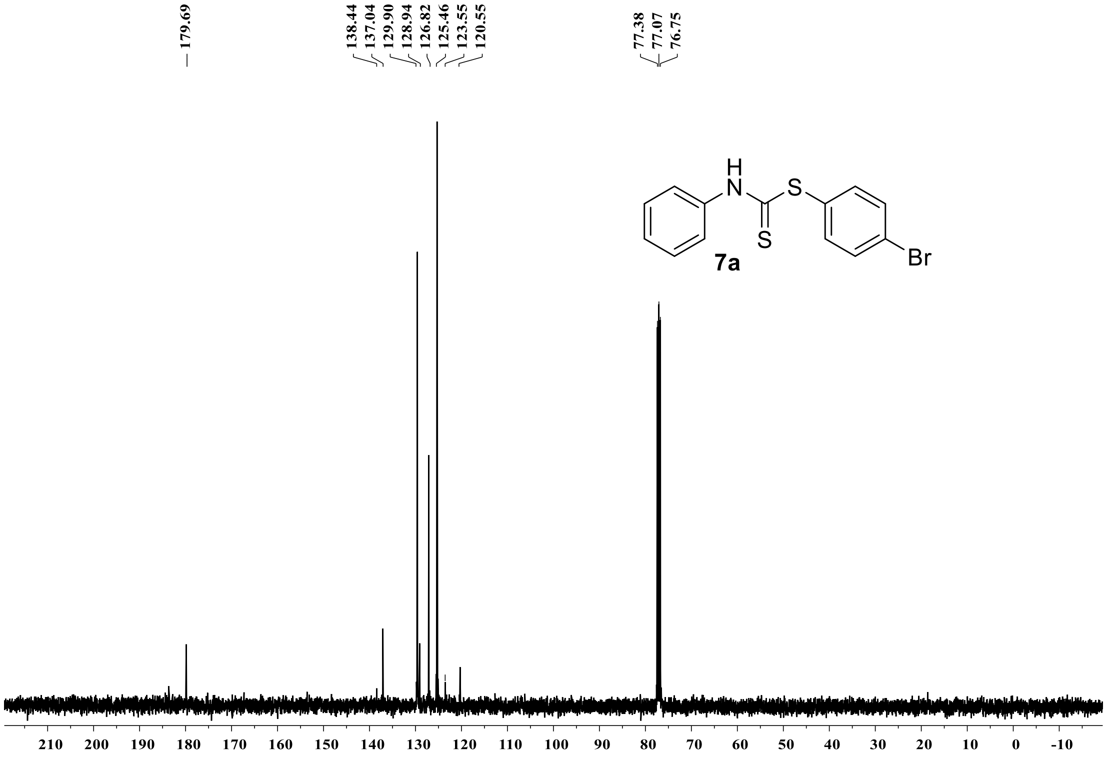

Figure A2.24: $^{13}$C NMR of **7a** (100 MHz, CDCl$_3$)

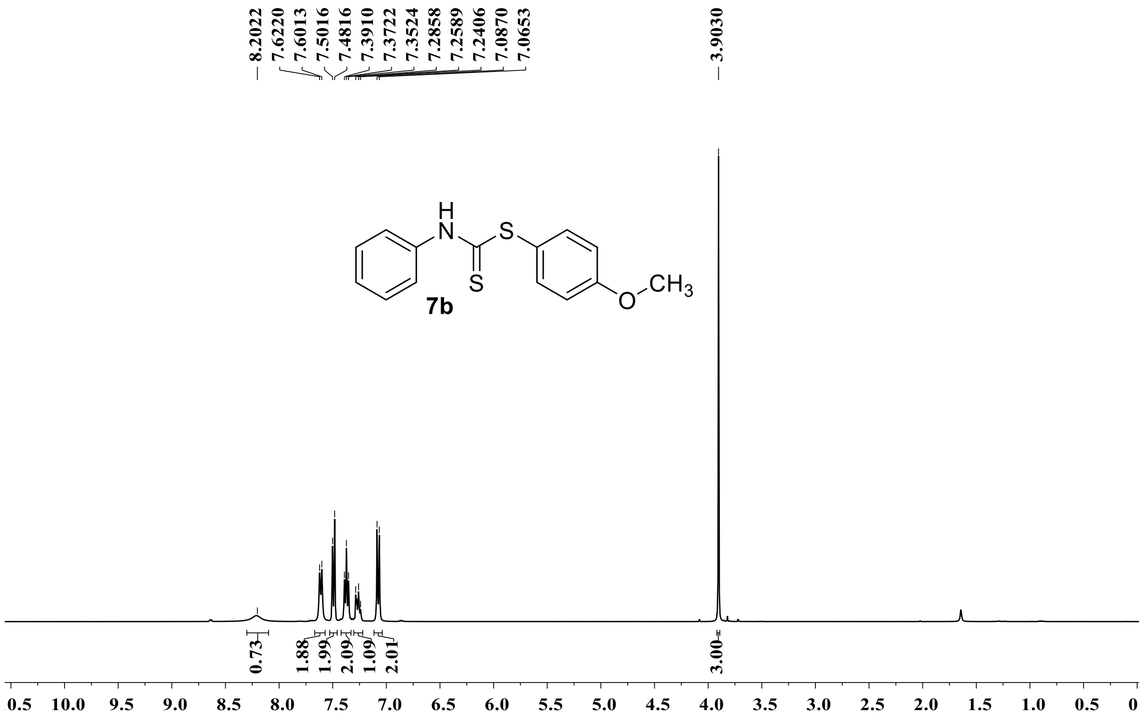

Figure A2.25: $^{1}$H NMR of **7b** (400 MHz, CDCl$_3$)

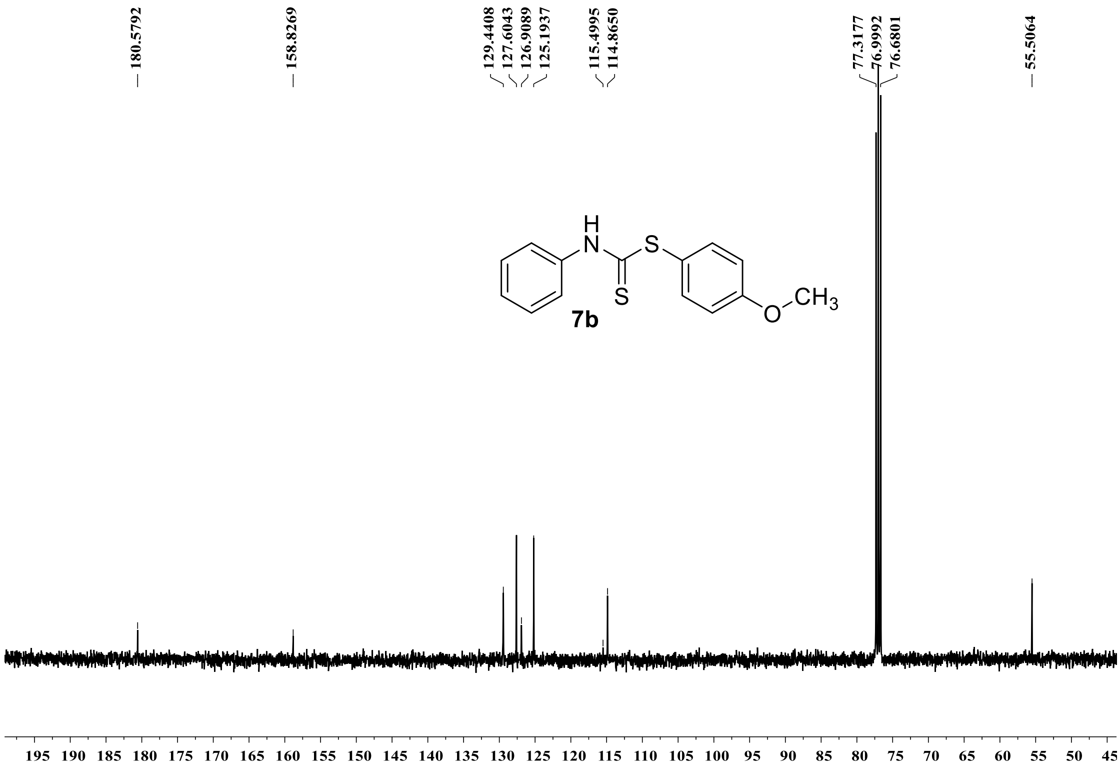

**Figure A2.26**: $^{13}$C NMR of **7b** (100 MHz, $CDCl_3$)

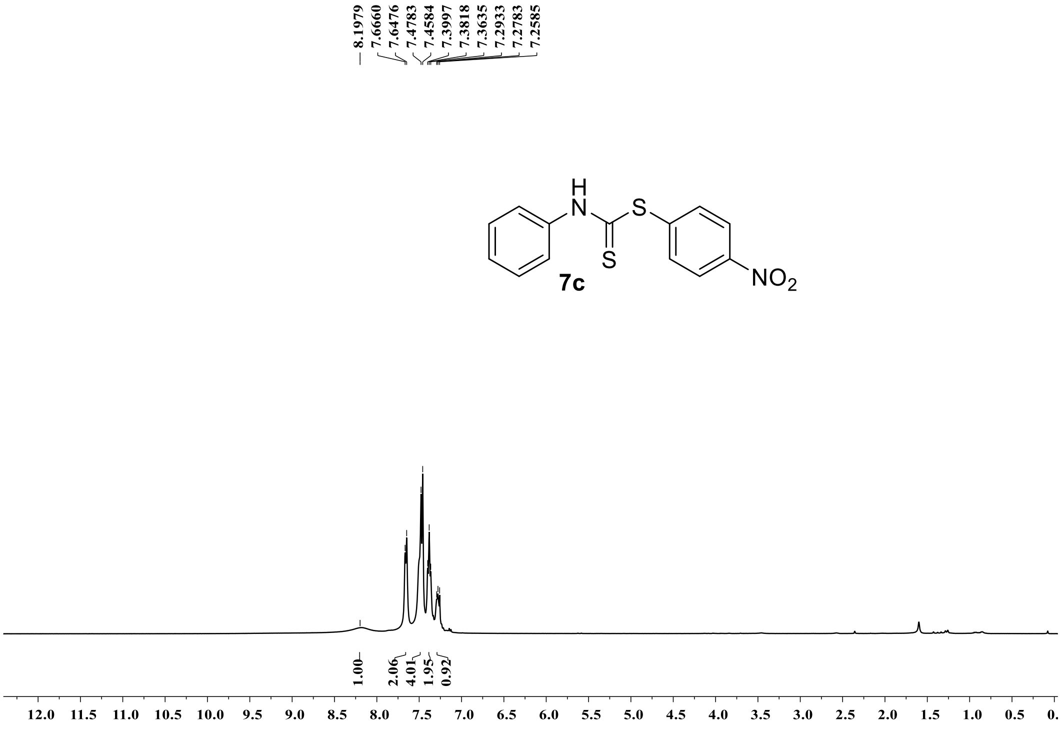

**Figure A2.27:** $^{1}$H NMR of **7c** (400 MHz, $CDCl_3$)

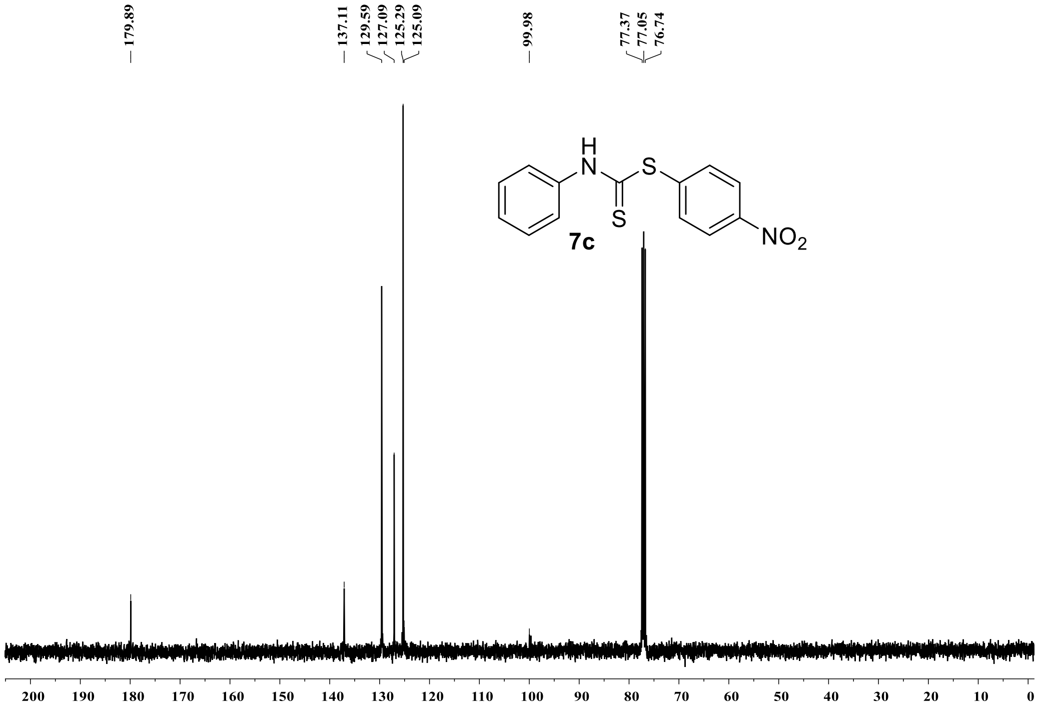

**Figure A2.28:** $^{13}$C NMR of **7c** (100 MHz, $CDCl_3$)

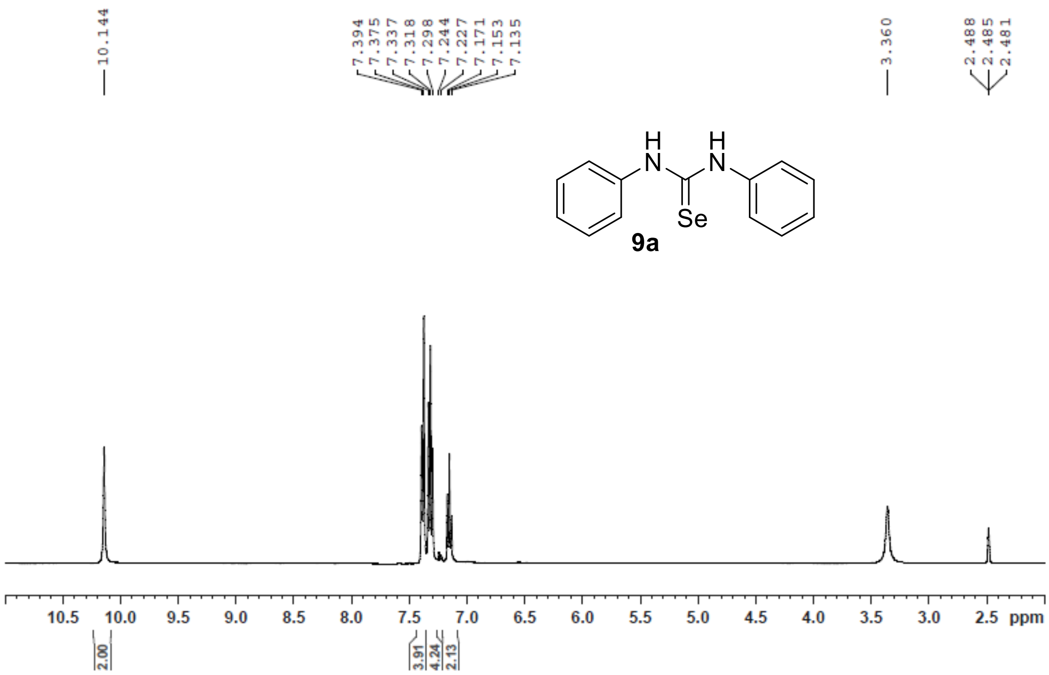

**Figure A2.29:** $^{1}$H NMR of **9a** (400 MHz, DMSO-$d_6$)

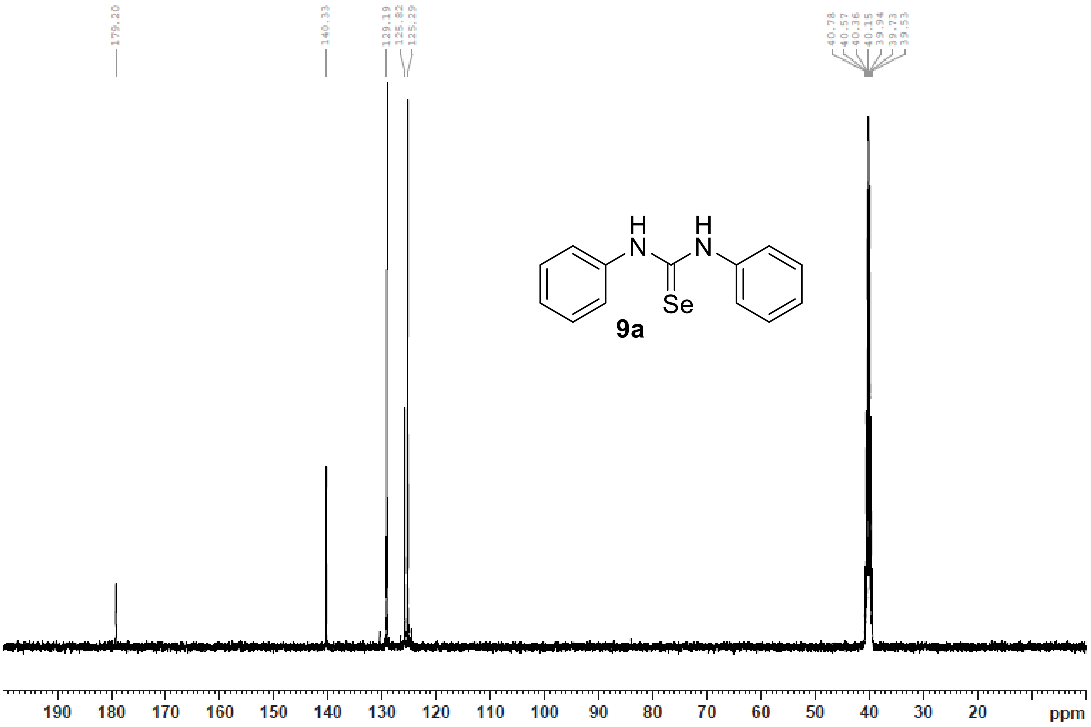

**Figure A2.30:** $^{13}$C NMR of **9a** (400 MHz, DMSO-$d_6$)

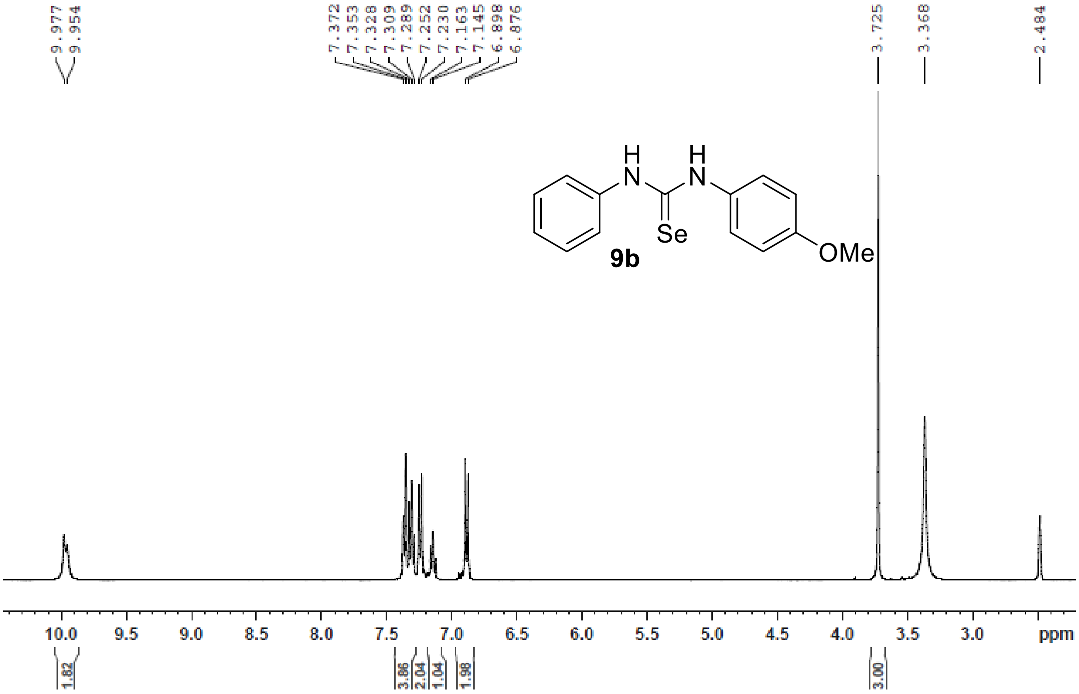

**Figure A2.31:** $^{1}$H NMR of **9b** (400 MHz, DMSO-$d_6$)

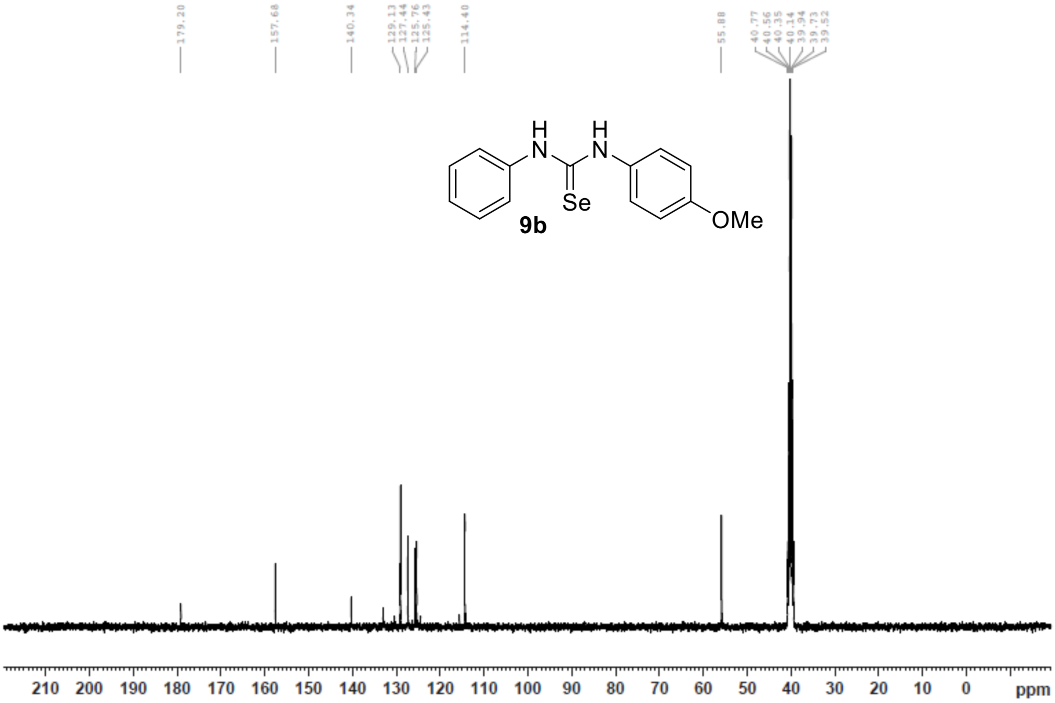

**Figure A2.32:** $^{13}$C NMR of **9b** (400 MHz, DMSO-$d_6$)

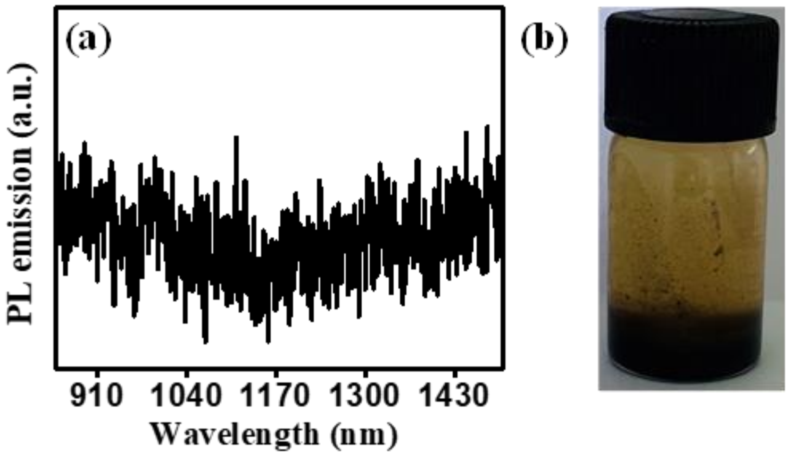

**Figure A2.33:** (a) The photoluminescence (PL) spectrum observed when oleic acid was used to synthesize $Ag_2S$ NCs. No PL emission found (excitation: 800 nm). As shown in figure, the colloidal stability was also poor (b).

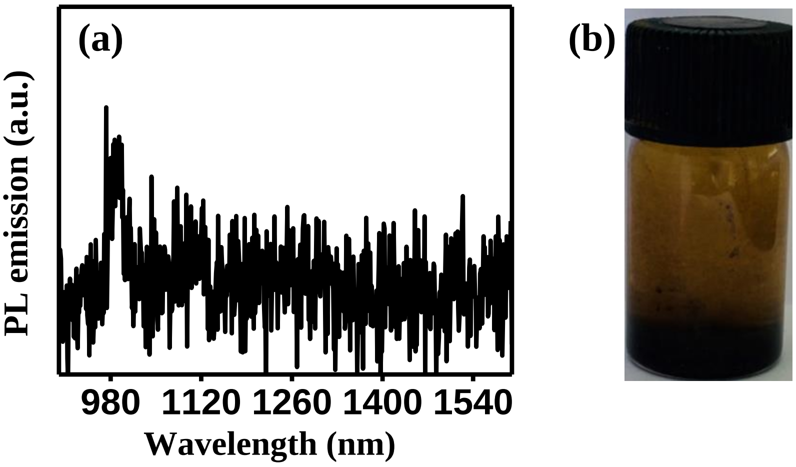

**Figure A2.34:** (a) Photoluminescence (PL) spectrum recorded when oleic acid and oleyl amine were used as capping ligands to synthesize $Ag_2S$ QDs. No PL emission was found (excitation: 600 or 800 nm). Figure (b) shows that the colloidal stability was poor as the particles settled to the bottom of the vial.

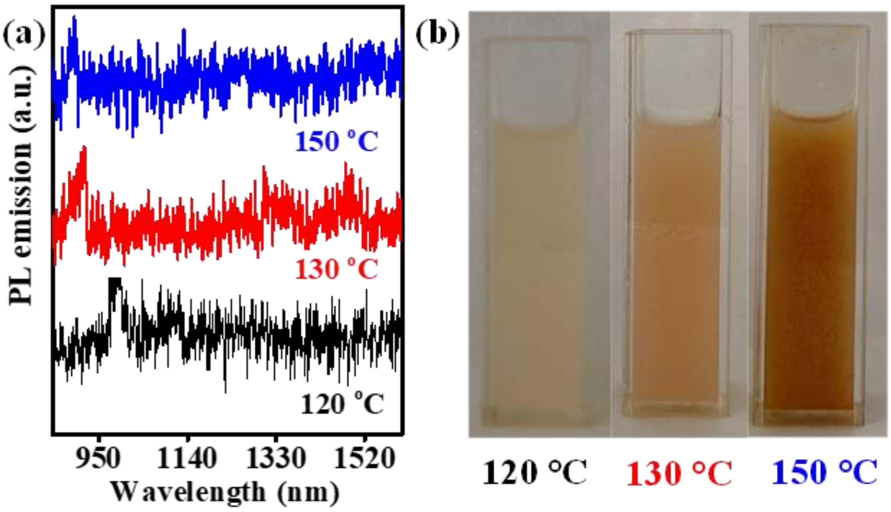

**Figure A2.35:** (a) Photoluminescence (PL) spectra recorded for the synthesis of $Ag_2S$ QDs after the reaction of thiourea (**3a**) with DDT at 120 °C, 130 °C and 150 °C showing no characteristic emission peak of $Ag_2S$ QDs; (b) Photographs of the concentrated aliquots taken from the reaction mixture of $Ag_2S$ QDs at 120 °C, 130 °C and 150 °C.

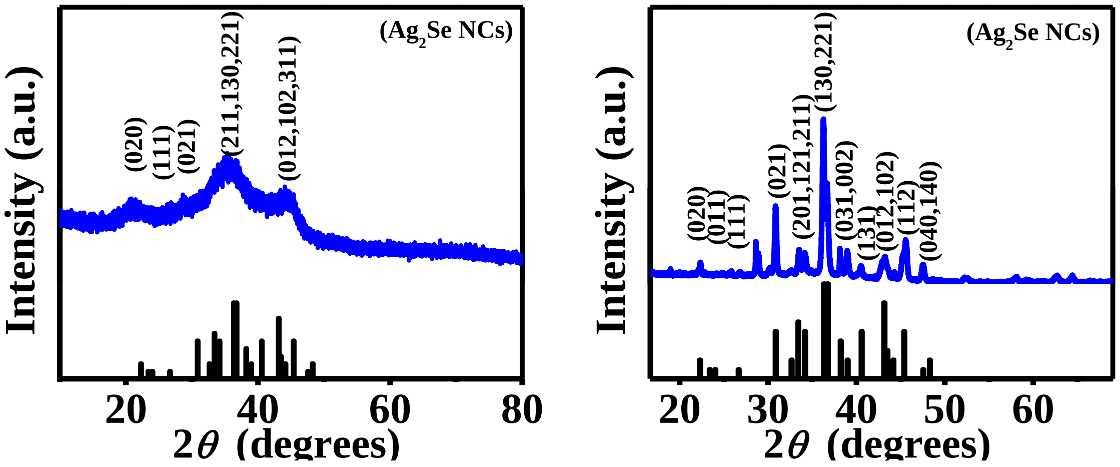

**Figure A2.36:** (a)The XRD results of orthorhombic (*β*-form) $Ag_2Se$ (JCPDS 024-1041)[64] NCs with space group *P2221E*. (b) $Ag_2Se$ NCs after annealing at 180° for 1 hours.

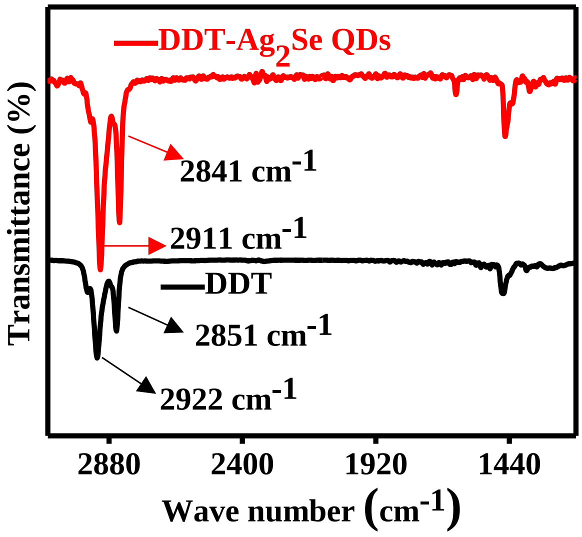

**FigureA2.37:** FTIR spectra of purified $Ag_2Se$ and 1-DDT.

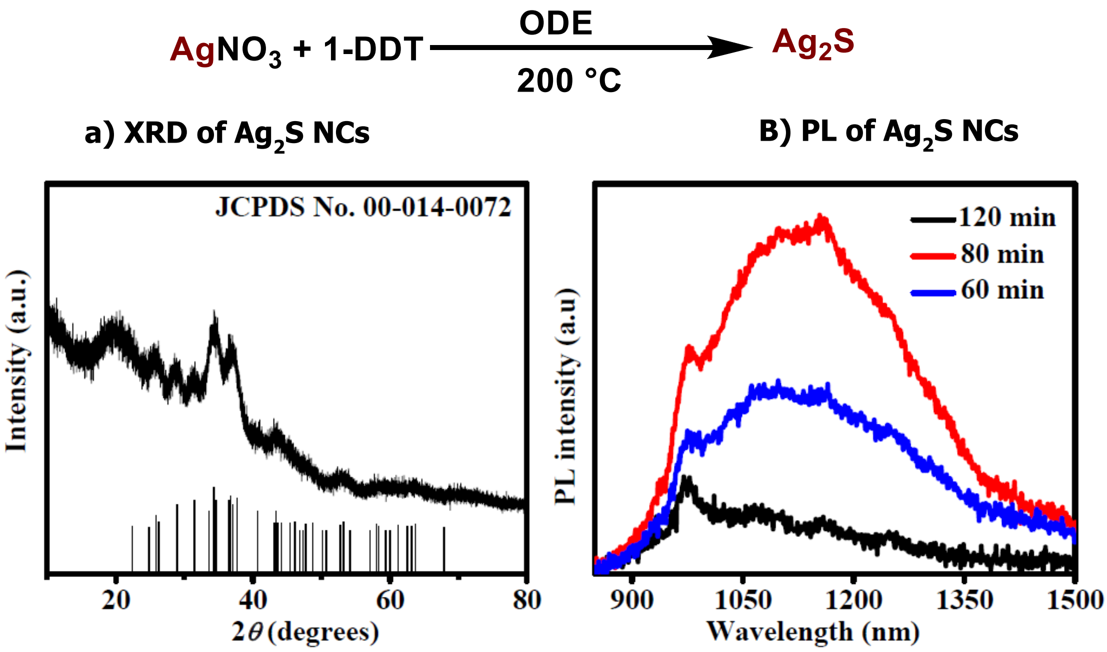

**Figure A2.38:** (a) XRD and (b) PL spectra of $Ag_2S$ QDs synthesized with DDT only without adding the S-precursor.

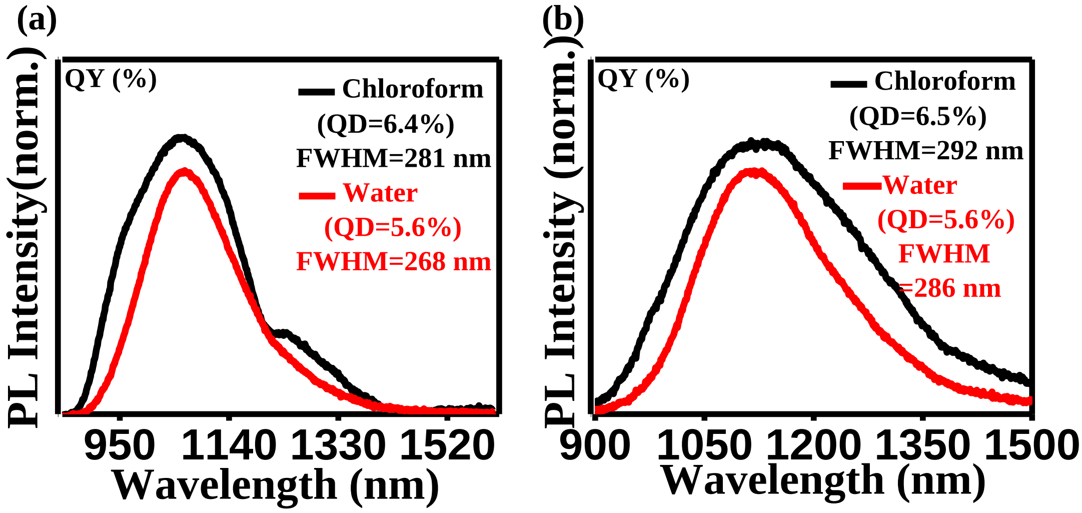

**Figure A3.1:** The QY for NIR-II emitting NCs with emission at $\lambda_{em}$ ~1065 nm and $\lambda_{em}$ ~1133 nm was calculated to be 5.6 %.

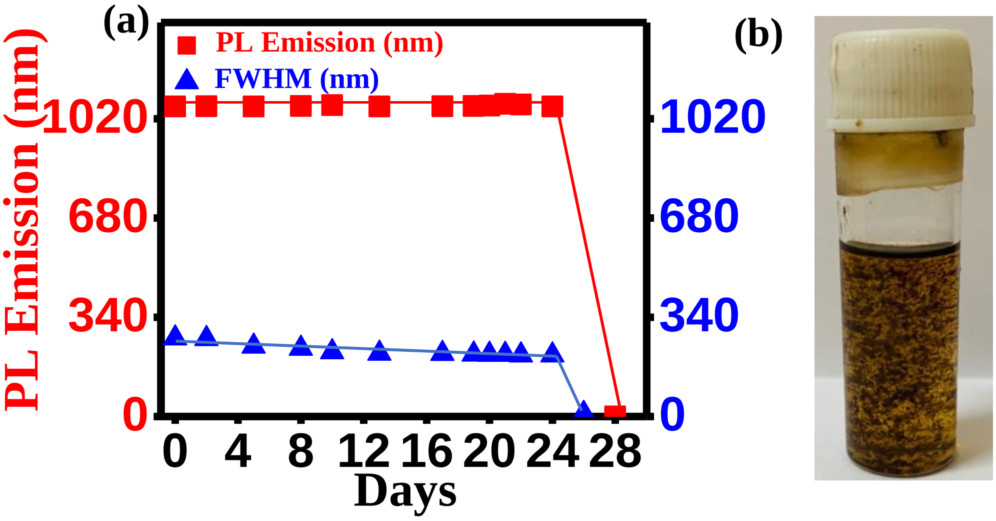

**Figure A3.2: (a)** The FWHM of the colloidally stable $Ag_2S$ NCs (~1065 nm) for 28 days. **(b)** After 28 days, the colloidal solutions were disturbed due to agglomeration

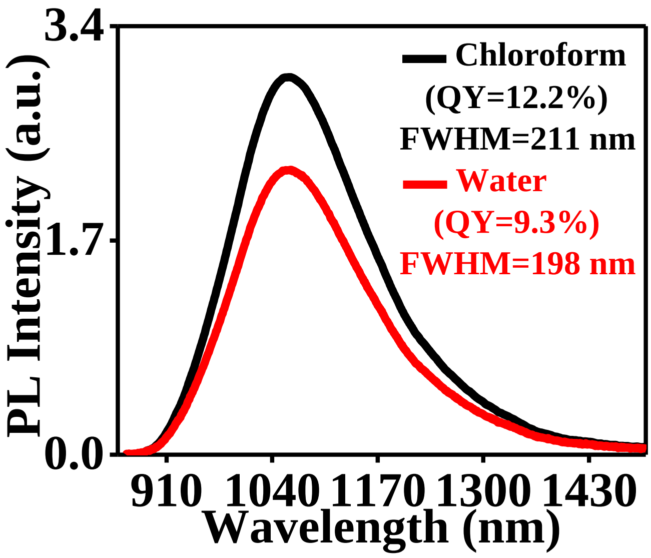

**Figure A3.3:** QY measurement shows that the QY was increased 2-fold from $Ag_2S$ to $Ag_2S$/ZnS core/shell QDs

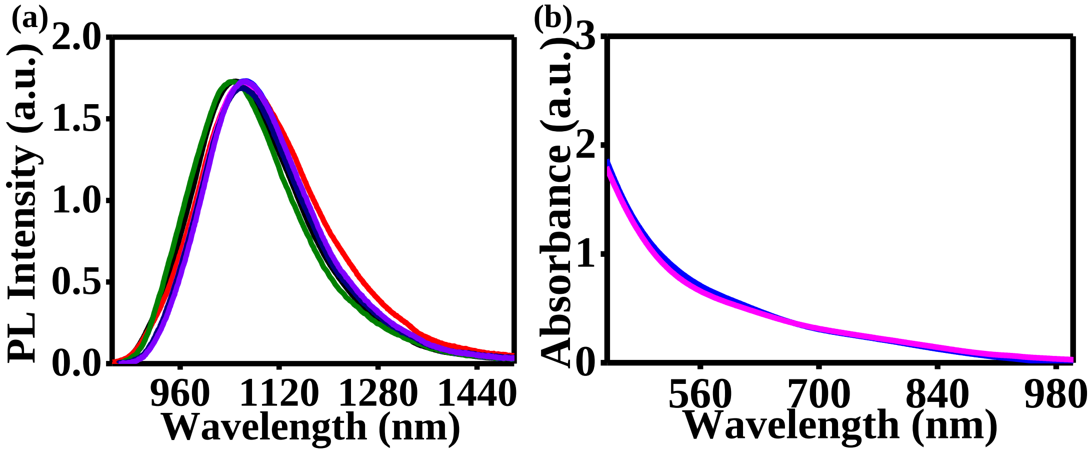

**Figure A3.4: (a)** Photoluminescence (~1065 nm) and absorption (~921 nm) spectra for the photostability test of aqueous $Ag_2S$/ZnS core/shell NCs

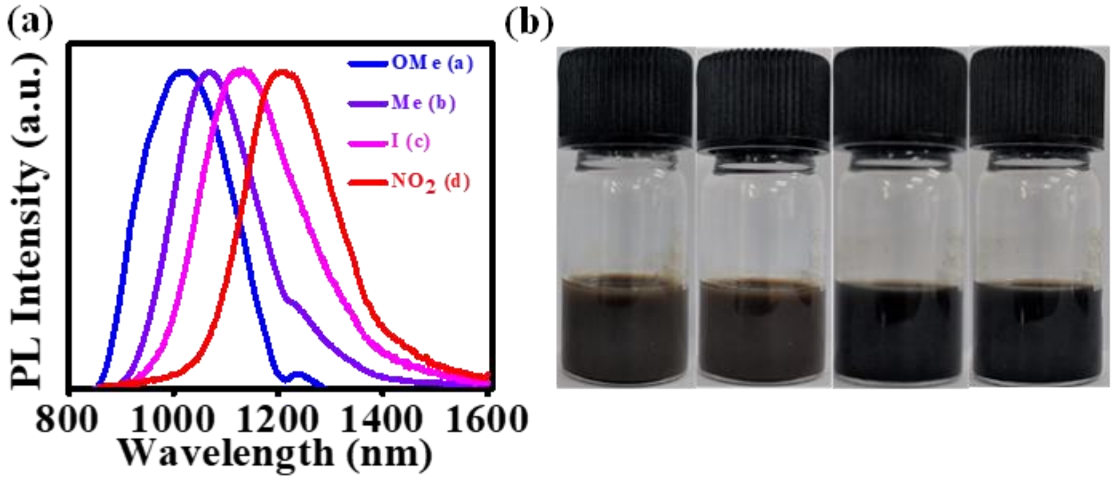

**Figure A3.5:** (a) PL spectra of $Ag_2S$ QDs synthesized from thiourea precursors (**a-d**) bearing various substituents at the *para* position of phenyl ring (*p*-OMe, *p*-Me, *p*-I, and *p*-$NO_2$) with PL emission ~1024 nm, 1065 nm, 1133 nm and 1209 nm; (b) Picture representation of different $Ag_2S$ QDs.

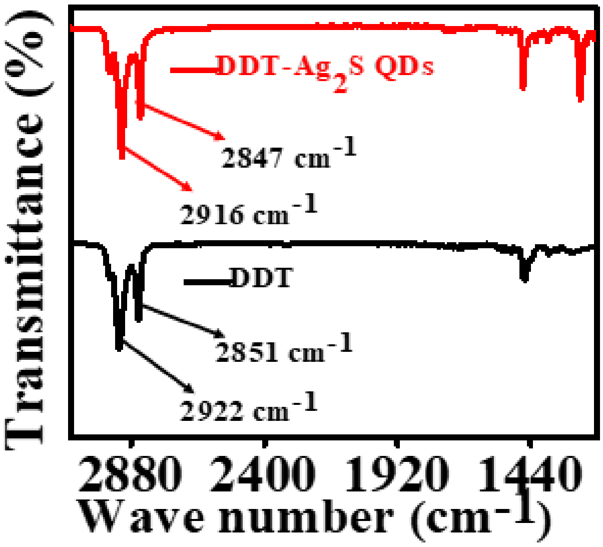

**Figure A3.6:** FTIR spectra of dodecanthiol (1-DDT) and DDT-capped $Ag_2S$ QDs (red color) showing distinct shift of C-H stretching frequency confirming the surface passivation of $Ag_2S$ QDs by DDT.

# *Annexure A4: Supplementary information from Chapter III*

## **A4.1.** $^{1}H$ and $^{13}C$ NMR

### **A4.1.1.** Copies of NMR spectra:

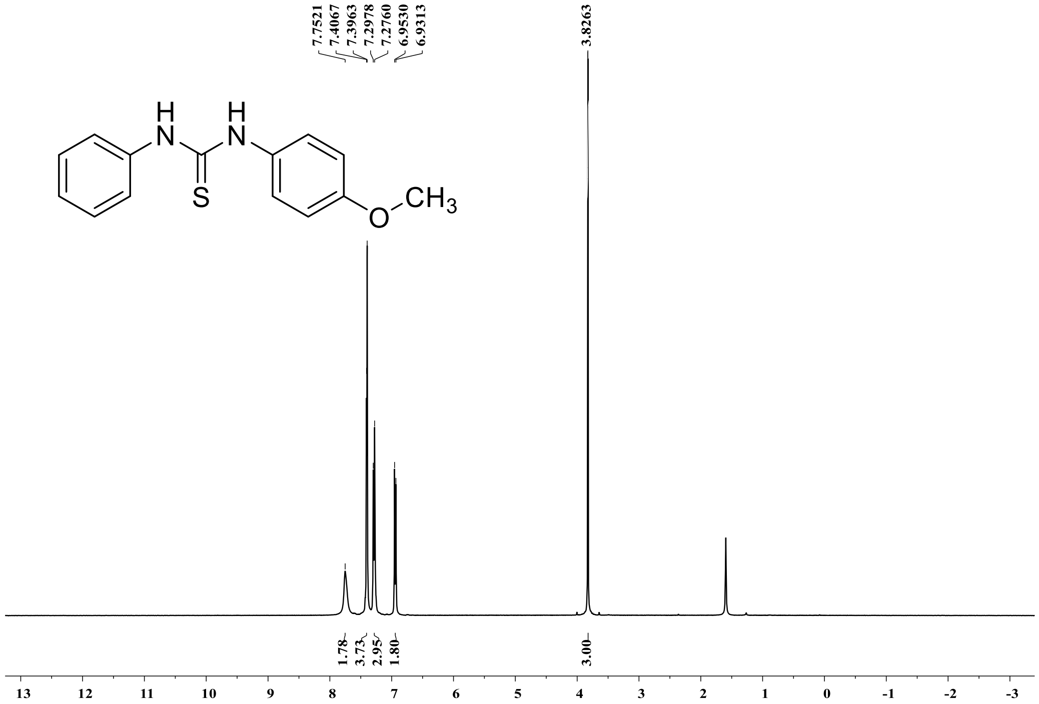

**Figure A4.1:** $^{1}H$ NMR of 1-(4-Methoxyphenyl)-3-phenylthiourea (400 MHz, $CDCl_3$)

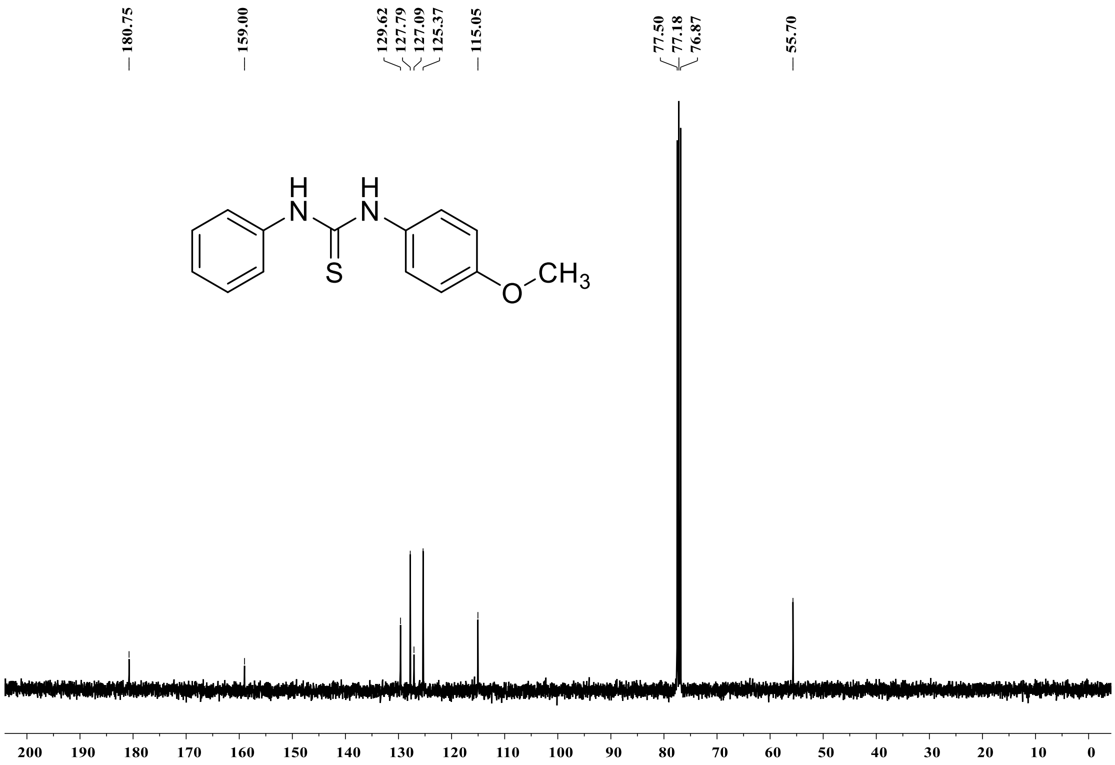

**Figure A4.2:** $^{13}$C NMR of 1-(4-Methoxyphenyl)-3-phenylthiourea (400 MHz, $CDCl_3$)

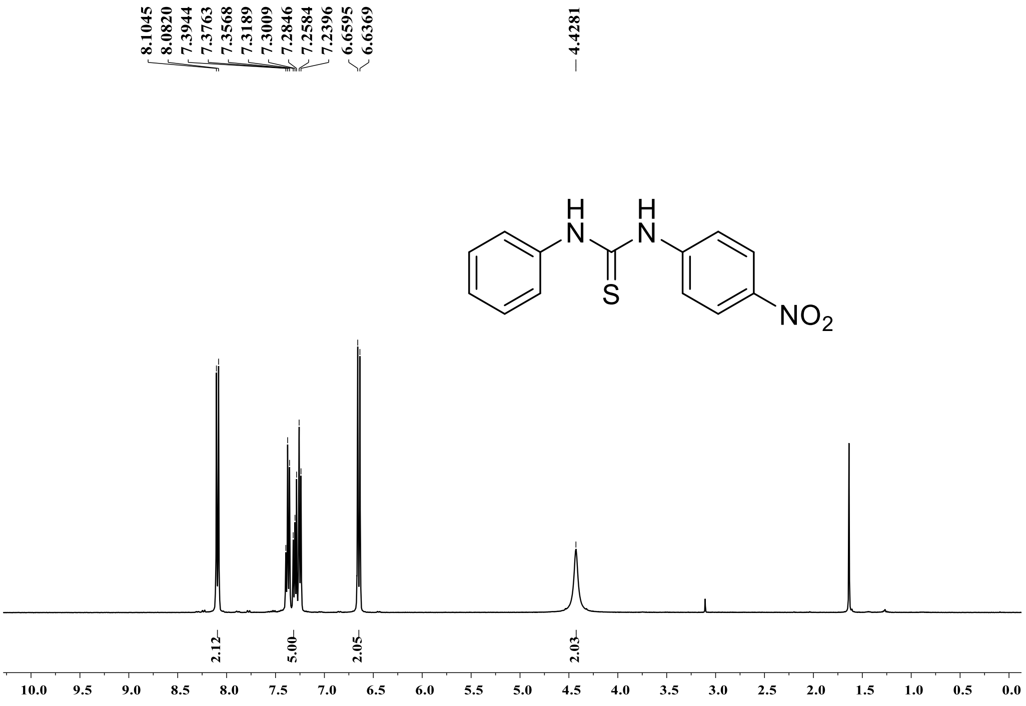

**Figure A4.3:** $^{1}$H NMR of 1-(4-Nitrophenyl)-3-phenylthiourea (400 MHz, $CDCl_3$)

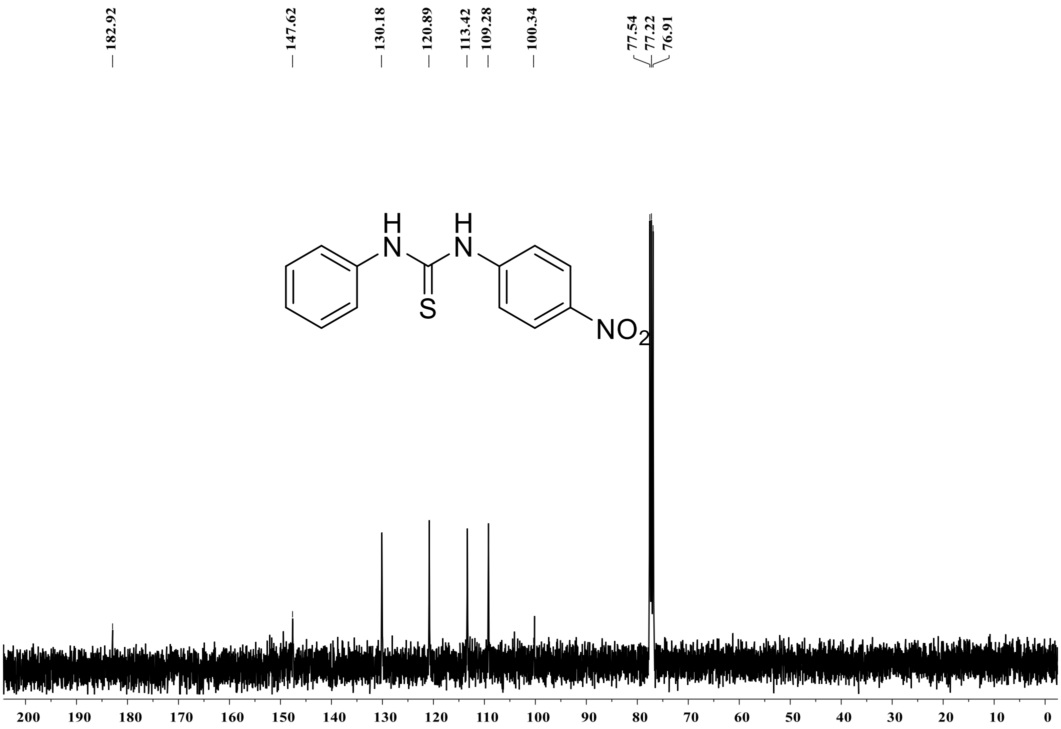

Figure A4.4: $^{13}$C NMR of 1-(4-Nitrophenyl)-3-phenylthiourea (400 MHz, $CDCl_3$)

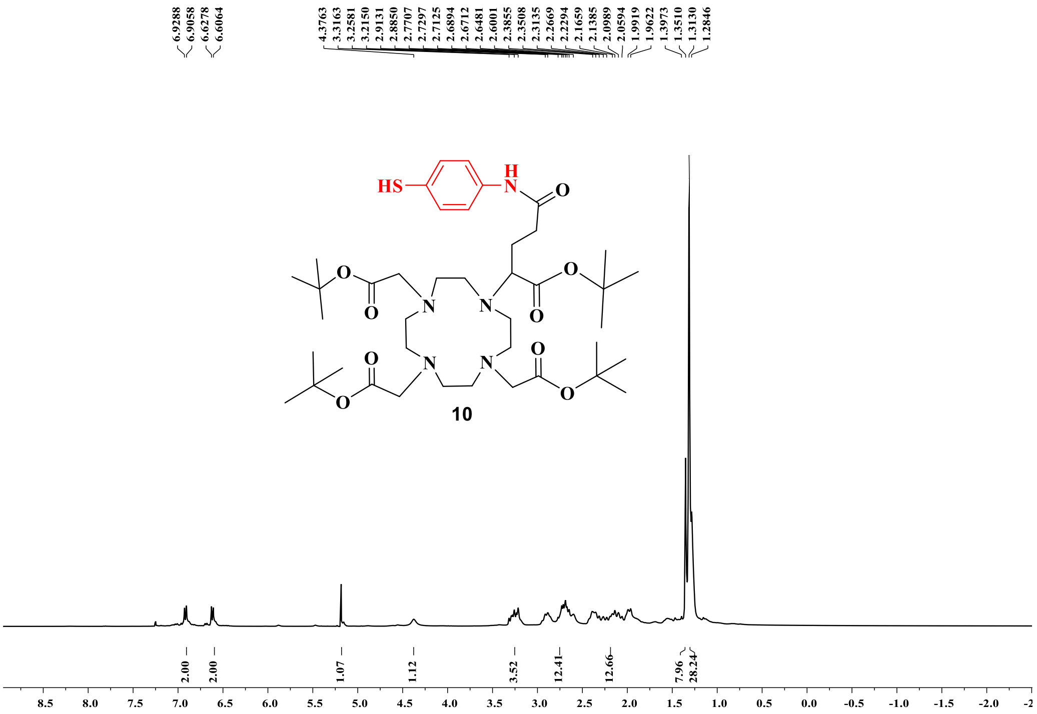

**Figure A4.5:** $^{1}$H NMR of **10** (400 MHz, $CDCl_3$)

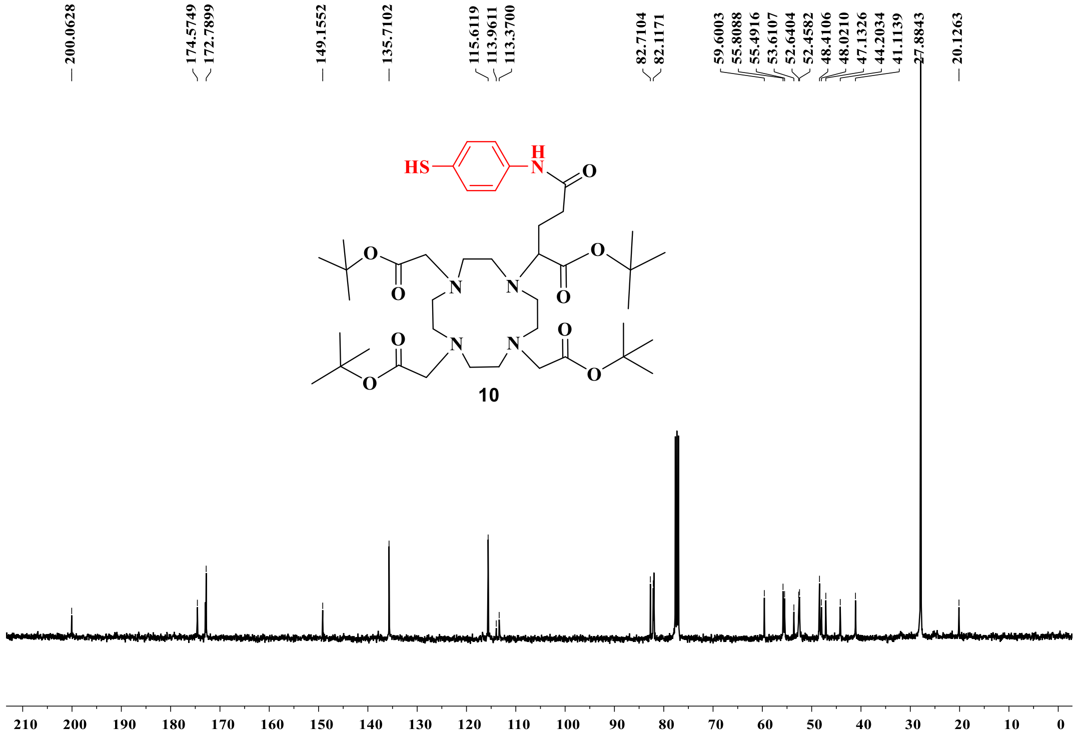

**Figure A4.6:** $^{13}$C NMR of **10** (100 MHz, CDCl$_3$)

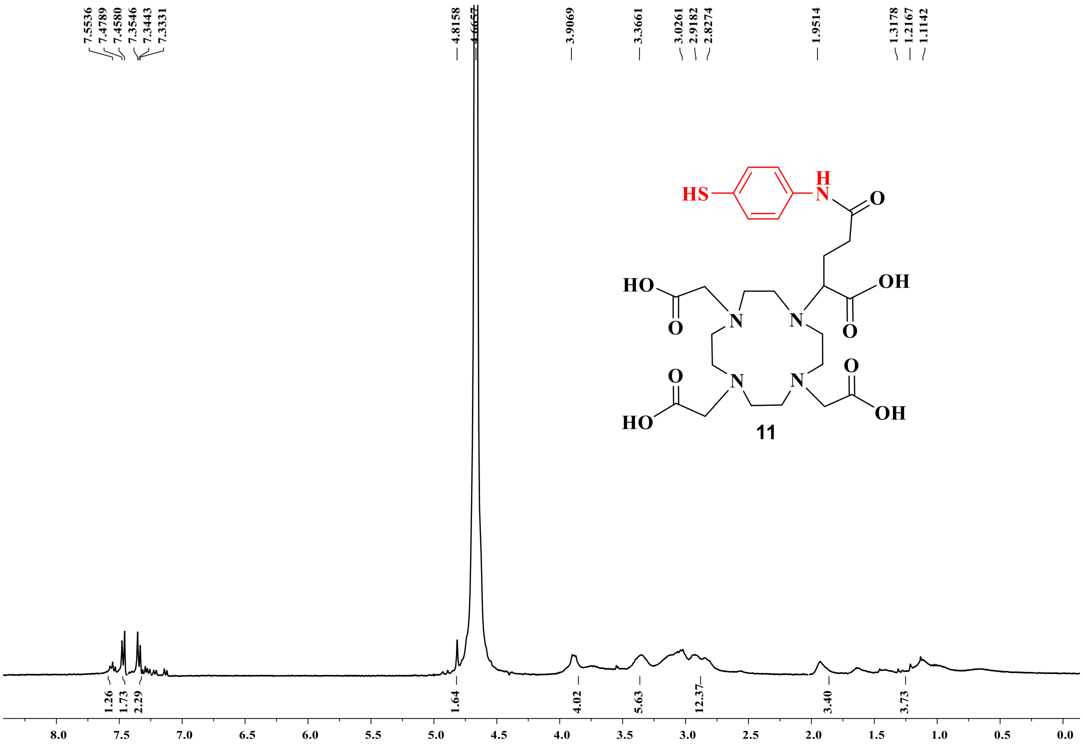

**Figure A4.7:** $^{1}$H NMR of **11** (400 MHz, D$_2$O)

## A4.1.2. Copies of Mass Spectra

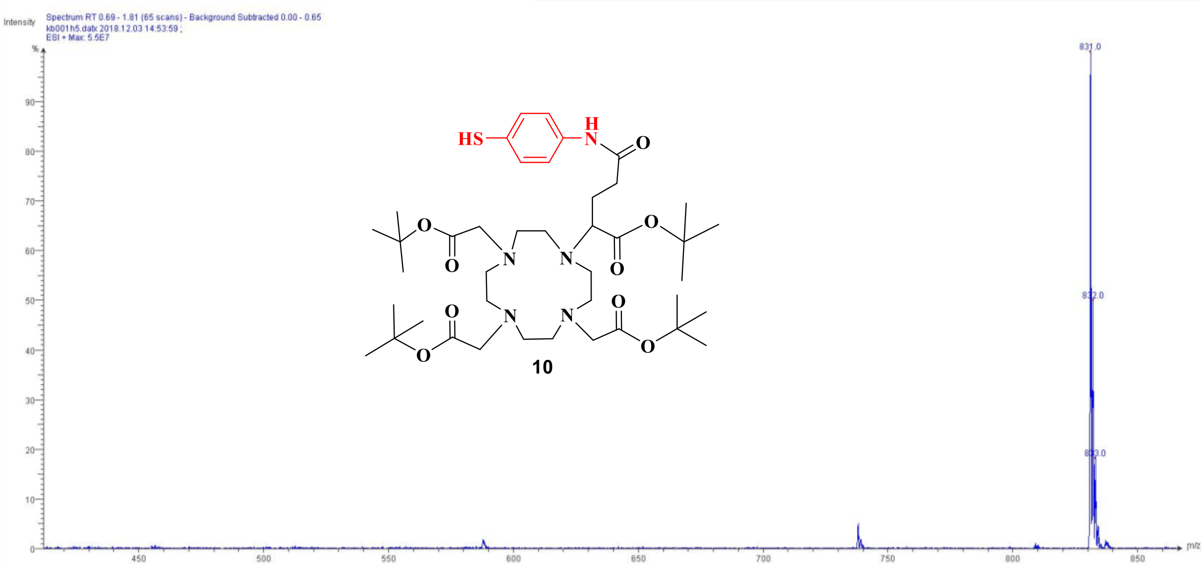

**Figure A4.8:** ESI-Mass spectrum of product **10** (Functionalised DOTA-Ga(tBu)4 with 4-aminothiophenol

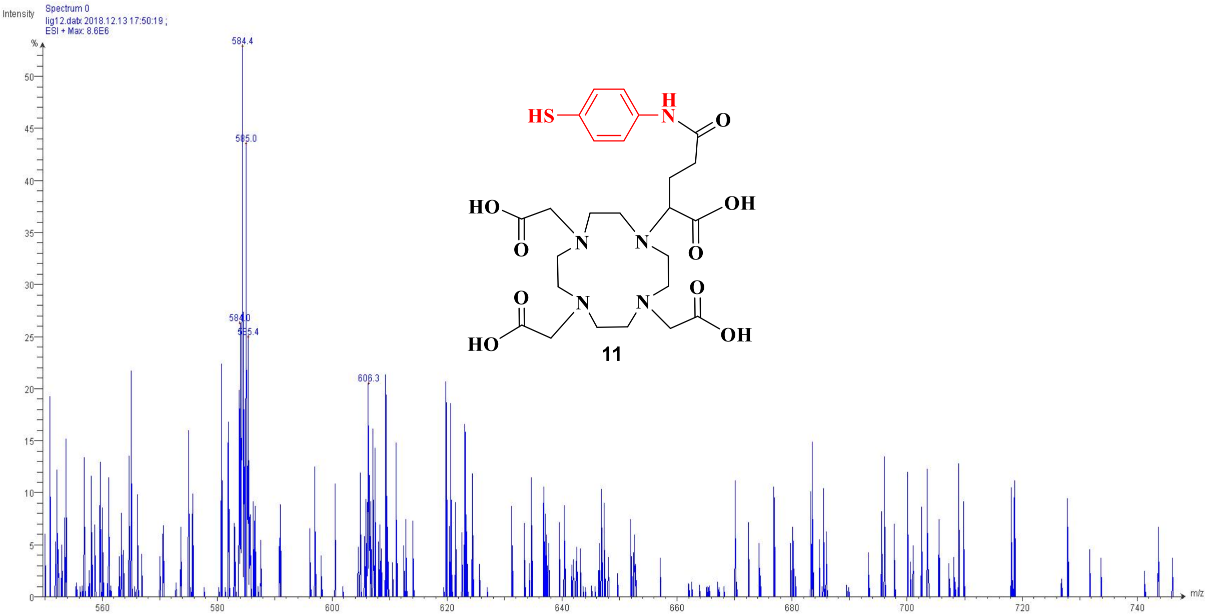

**Figure A4.9:** ESI-Mass spectrum of product BOC-deprotected product (**11)**

# *Annexure B: Instrumentation and technique*

## B1. Absorption spectroscopy.

### B1.1. Basic principle

Ultraviolet/Visible/Near-infrared (UV/Vis/NIR) spectroscopy examines the intensity of the light that is absorbed by a sample to obtain insight into the electronic energy levels of the sample.[1] In the case of colloidal semiconductor NCs, it is a useful technique to obtain information about the excitonic energies, band gap, extinction coefficient, and even size.[2] Typically, a sample dispersed as colloids in a suitable solvent or solution form or thin film is subjected to a variable light source, and a change in its intensity is measured using a detector. The data is typically plotted as absorbance *vs.* wavelength of the light as shown below (Figure B1.1), with absorbance being, $A = log_{10}\,(I_o/I)$ where $I_o$is the intensity of light at source and $I$ is the transmitted intensity of light.

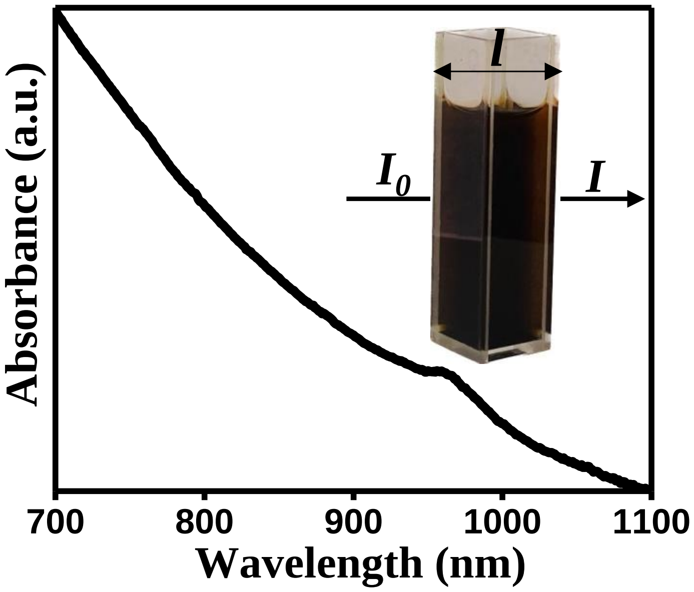

**Figure B1.1:** Absorption *Vs* wavelength spectra of $Ag_2S$ NCs

The concentration of the absorbing species in the solution may be calculated quantitatively using Lambert-Beer's law,[3] $c = \times l$, where ε is the molar extinction coefficient ($M^{-1}cm^{-1}$) and $l$ is the path length (cm). The background is corrected using a "blank"– a quartz cuvette filled with only the dispersing medium – to ensure that no contribution from the solvent is included in the sample absorbance. The spectrum is usually characterized by a sharp absorption corresponding to the specific electronic transition in the sample.

## B1.2. Absorption peak and its origin

QDs are small particles of a semiconductor material that are typically a few nanometres in size.[4] They have known for their unique size-dependent optical and electrical properties due to the confinement of the electrons in all three spatial dimensions.[4] One of the important optical properties of QDs its characteristic absorption bands in the absorption spectrum, which is typically a sharp peak. This peak originates due to the transition of an electron from the valence band to the conduction band of the QDs upon absorption of a photon.[5,6,7] The first excitonic absorption peak corresponds to the lowest-energy transition between the electron and hole states, while the second excitonic absorption peak corresponds to the corresponding higher-energy transition. Figure B1.2 shows the absorption spectrum of PbS QDs in colloidal form for illustration. The main absorption peak at 1420 nm (or 0.87 eV ) corresponds to the transition of electrons from the highest occupied molecular orbital (HOMO) to the lowest unoccupied molecular orbital (LUMO) and is also referred to as the $1S_h$-$1S_e$ HOMO-LUMO transition. The second peak, at the lower wavelength (1024 nm), is attributed to the $1P_h$-$1P_e$ transition. The absorbance at a shorter wavelength tends to be higher due to the increasing density of states as the energy moves further from the maximum valence and minimum conductance bands.[7]

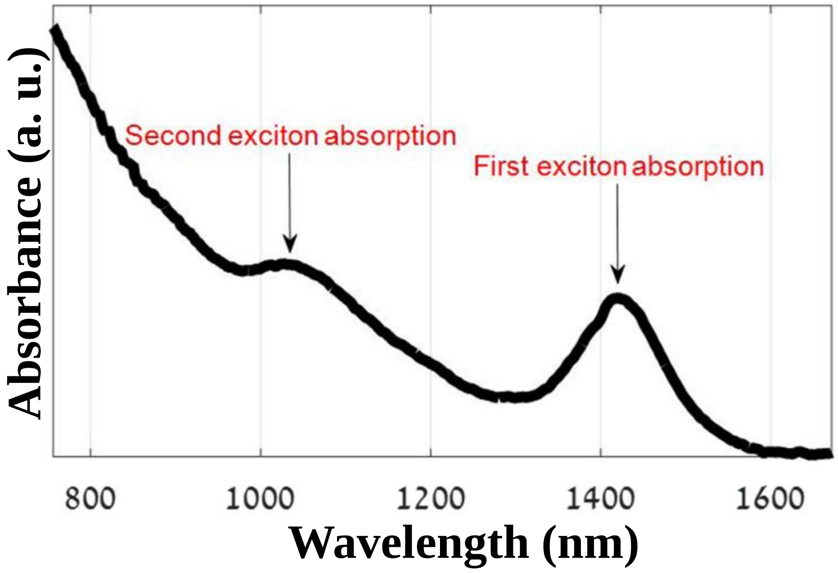

**Figure B1.2:** Absorption spectrum of PbS colloidal QDs. Adapted with permission from Hechster *et al.* Copyright 2016, AIP Advances[7]

The bandgap diagrams shown in Figure B1.3 can help us visualize energy transitions within the material. Unlike the standard bulk semiconductor, QDs have discrete energy levels near the band edges due to the confinement of charge carriers in all three dimensions.[8] Promotion of electrons from the valence band to the conduction band will leave a hole and they form an exciton, the coulombically interacting electron-hole pair.[8]

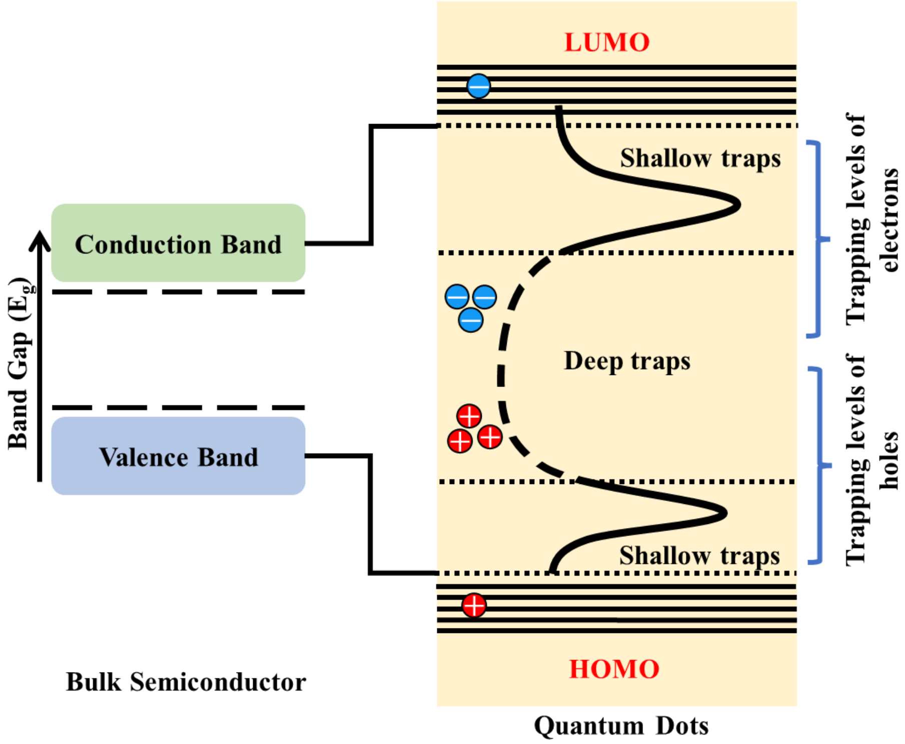
LUMO
Shallow traps
Trapping levels of electrons
Conduction Band
Band Gap ($E_g$)
Deep traps
Valence Band
Trapping levels of holes
Shallow traps
HOMO
Bulk Semiconductor
Quantum Dots

**Figure B1.3:** Graphically representation of band gaps in bulk semiconductors and QDs.

For bulk, the natural radius within which electron-hole pair are bound together is known as exciton Bohr radius which is given by the following equation.[9]

$$a_B = \frac{4\pi\epsilon\varepsilon\hbar^2}{\mu q^2} \qquad \text{B1.1}$$

Where, $\varepsilon$ is the absolute permittivity of the vacuum, $\epsilon$ is Permittivity of the dielectric constant of the semiconductor, $\hbar = h/2$, h is Planck's constant, $\mu$ is Reduced mass, q is the charge of an electron. When the size of the QD is smaller than $a_B$ the properties of the material start to deviate from that of the bulk materials due to quantum confinement. In other words, the quantum confinement effect results from the electrons and electrons holes pair being squeezed into the dimension that approaches the quantum regime. Consequently, quantum confinement leads to a collapse of the continuous energy bands of bulk material into discrete, atomic-like energy levels.

Since the QDs have a larger surface-to-volume ratio, it is practically impossible to remove surface defects such as vacancies (missing atoms) or interstitials (extra atoms), point defects, line defects, or other crystal defects.[10] These imperfections act as traps for electrons and holes. If the traps are positioned near the conduction band (LUMO) within the energy bandgap, they are referred to as shallow traps for electrons. Conversely, if the traps are situated close to the valence band (HOMO) within the energy bandgap, they are considered shallow traps for holes,[11] as depicted in Figure B1.3. Deep traps for electrons and holes, on the other hand, are located far from the conduction (LUMO) and valence (HOMO) bands, respectively, as also illustrated in Figure B1.3. Depending on their formation energy, these traps can be shallow traps or deep traps for both electrons and holes. For example, formation energy for the vacancy is smaller than the interstitial defect and hence generally forms shallow traps. These traps can also leave a signature peak or hump in the absorption spectrum.[10]

### B1.3. Effective Mass Approximation Model (EMA)

The EMA model, developed by Brus in 1986, is an effective model to quantify the change in energy levels due to quantum confinement. Considering only coulombic interaction between the electron and hole pair, the Hamiltonian for the EMA model is given by:

$$\hat{\mathrm{H}} = 2\frac{-\hbar^2}{2m_h}\nabla_e^2 - \frac{\hbar^2}{2m_h^*}\nabla_h^2 - \frac{e^2}{\epsilon_0|r_e-r_h|} \qquad \text{B1.2}$$

Solving the corresponding Schrodinger equation, the equation for effective band gap energy ($E_{BG}^{QD}$ ) of the QDs is obtained:

$$E_{BG}^{QD} = E_{BG}^{B} + \frac{h^2\pi^2}{2}\left[\frac{1}{m_e} + \frac{1}{m_h}\right]\frac{1}{R^2} - \frac{1.8e^2}{4\pi\varepsilon_0\varepsilon_B}\cdot\frac{1}{R} \qquad \text{B1.3}$$

Where, $E_{BG}^{B}$ is the bandgap of the bulk material, h = Planck's constant, 6.63 x $10^{-34}$ Js, R is the radius of the QD, $m_e$ is the effective mass of an electron, for CdS, 0.21 m, $m_h$

is the effective mass of a hole, for CdS, 0.81 m, m is the mass of the electron, 9. 11 x $10^{-31}$ kg, e is the elementary charge, 1.60 x $10^{-19}$ C, $\varepsilon_0$ is Permittivity of free space, 8.85 × $10^{-12}$ $C^2J^2M^{-1}$,$\varepsilon_B$ is electric constant of the bulk material, for CdS it is 5.6, 1 eV = 1.60 × $10^{-19}$ J. Some of the modified versions of the Brus Equation[12] also include polarization terms:

$$E_{BG}^{QD} = E_{BG}^{B} + \frac{\hbar^2\pi^2}{2\mu R} - 1.786\,\frac{e^2}{\epsilon\, R} - 0.248\, E_{gr}^{*} \qquad \text{B1.4}$$

Where $E_{gr}^{*}$ is the effective Rydberg energy. EMA fits fairly well with experimental data for larger sized QDs but deviates for smaller QDs.[8] To account for this, the Density Functional Theory (DFT) for QDs was developed.[13]

The size of QDs can be approximated from the first exciton peak wavelength. Empirical relationships relating the diameter of the QDs to the wavelength of the first exciton peak have been determined for various QDs using UV-Vis and TEM data.[14] For example, for CdSe QDs diameter (D, nm) is related to λ (nm, the wavelength of the first excitonic absorption peak of the corresponding sample) as follows.[14,15]

$$D = (1.6122 \text{ x } 10{-}7)\, \lambda^3 - (2.6575 \text{ x } 10{-}3)\, \lambda^2 + (1.6242)\, \lambda - 41.57 \qquad \text{B1.5}$$

Similarly, the molar extinction coefficient (ε, $M^{-1}cm^{-1}$) can be determined experimentally[16] or using Ricard equation[17]

$$\sigma_{QD} = \frac{\omega}{n_s c}\left(\frac{4}{3}\pi R^3\right) |f(\omega)|^2 2 n_{QD} k_{QD} \qquad \text{B1.6}$$

ω is the angular frequency, $n_s$is the refractive index of solvent matrix, $n_{QD}$is the real part of refractive index of QDs, $k_{QD}$ is the imaginary part of refractive index of QDs and $f(\omega)$ is Local field factor which is calculated using the following equation,

$$f(\omega) = \frac{3\varepsilon_S}{\varepsilon_{QD} + 2\varepsilon_S} \qquad \text{B1.7}$$

where, $\varepsilon_S$ is diectric constant of solvent and $\varepsilon_{QD}$ is dielectric constant of $Ag_2S$.

It is worth-noting that, ε is size-dependent at first excitonic peak and hence lower wavelength or higher photon energy where absorbance is size-independent is considered for its determination.[18,19]

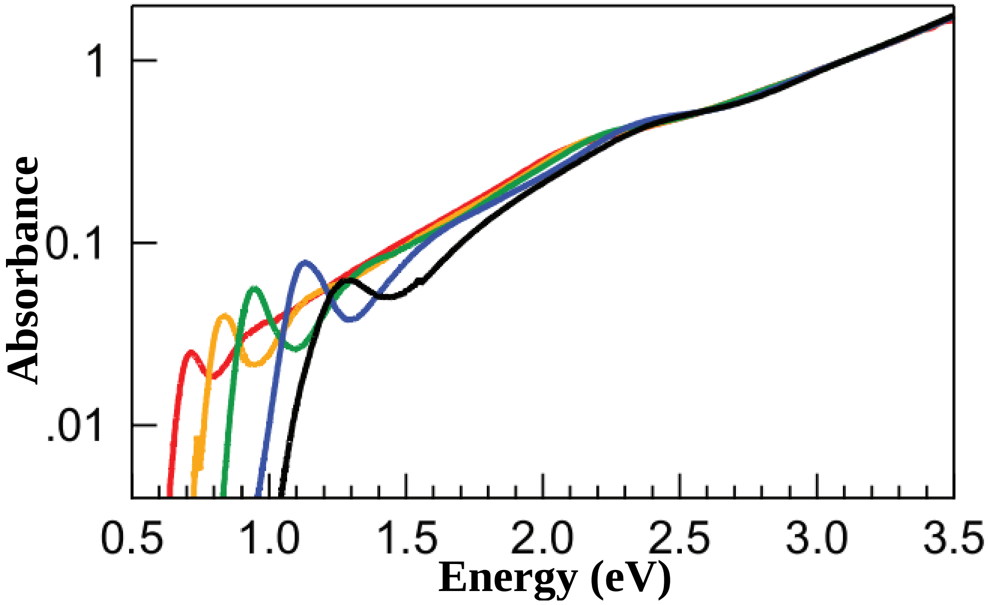

**Figure B1.4:** Series of absorbance spectra of PbS QDs suspended in tetrachloroethylene, normalized at 3.1 eV. All spectra coincide at high energies and are size-independent. Adapted with permission from Moreels *et al.* Copyright 2009, ACS Nano [19]

### B1.4. Determination of band gap using UV-Vis spectroscopy

A typical absorption spectrum of the CdS colloidal QDs synthesized in this thesis work is shown in Figure B1.5.

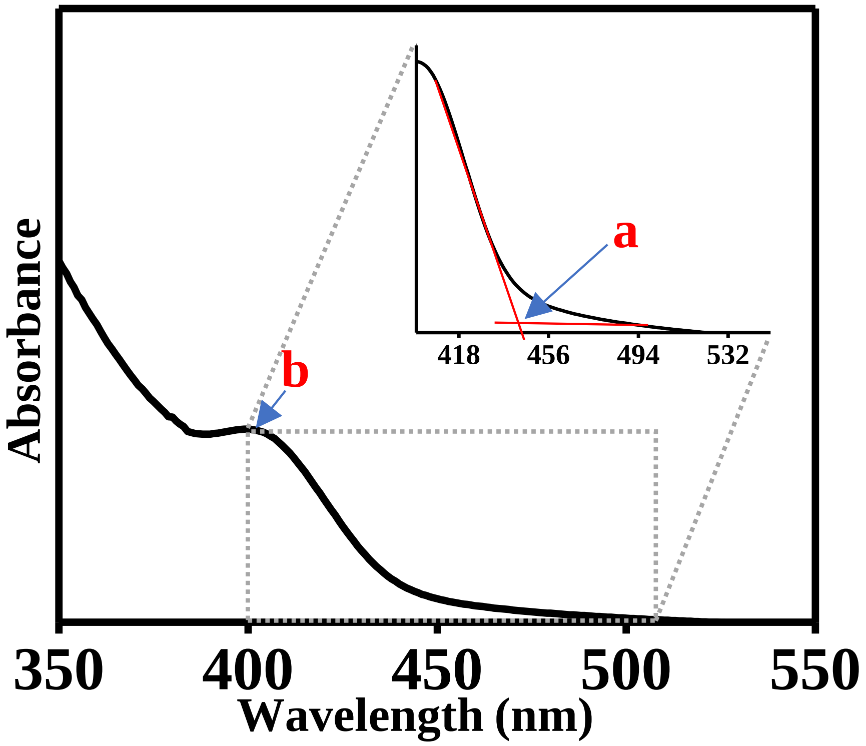

**Figure B1.5:** UV−vis absorption spectra CdS QDs.

The band-gap energy is determined by either finding a cut-off wavelength/absorption onset (a)[20] or from absorption maxima value (b).[8] In crystalline semiconductors, a correlation between the absorption coefficient and incident photon energy has been established through the derivation of a correlative Equation B1.8 given as[8,21,22]

$$\alpha(\nu)\mathrm{h\nu} = B(\mathrm{h\nu} - E_{gap})^{m} \tag{B1.8}$$

where, $B$, hν and $E_{gap}$ are the constant, incident photon energy and optical gap respectively; $\alpha(\nu)$ is the absorption coefficient defined by the Beer-Lambert's law as the Equation B2.9 given by

$$\alpha(\nu) = \frac{2.303\times\mathrm{Abs}(\lambda)}{d} \tag{B1.9}$$

where, d and Abs are the film thickness and film absorbance, respectively. The Absorption Spectrum Fitting (ASF) method can be understood by reformulating the Equation B1.9 as a function of wavelength (λ) as Equation B1.10 as

$$\alpha\,(\lambda)=\mathrm{B}(hc)^{1-m}\lambda\left(\frac{1}{\lambda}-\frac{1}{\lambda_g}\right)^m \qquad \text{B1.10}$$

where, $\lambda_g$, c and h are wavelengths corresponding to the optical band gap, velocity of light and Planck's constant respectively. The Equation B1.10 above can be rewritten as the Equation B1.11 as $\mathrm{Abs}\,(\lambda)=\mathrm{B}_1\lambda\left(\frac{1}{\lambda}-\frac{1}{\lambda_g}\right)^m+\mathrm{B}_2$ B1.11

where, $\mathrm{B}_1=\mathrm{B}(hc)^{1-m}\times\frac{d}{2.303}$ and $\mathrm{B}_2$ is a constant that accounts for reflection. By utilizing Equation B1.11, the optical band gap can be determined through absorbance spectrum fitting (ASF) without the requirement of film thickness information. This allows the band gap to be determined in electron volt and can be calculated from the parameter $\lambda_g$ using $E_{\mathrm{gap}}^{\mathrm{ASF}}=\frac{1239.83}{\lambda_g}$. In simple terms, the value of $\lambda_g$ can be estimated by extrapolating the linear portion of the $\left(\frac{\mathrm{Abs}(\lambda)}{\lambda}\right)^{\frac{1}{m}} vs.\frac{1}{\lambda}$ curve at $\left(\frac{Abs(\lambda)}{\lambda}\right)^{\frac{1}{m}}=0$. The best fit was found to occur when using the least squares technique and m = $\frac{1}{2}$ .The values for $E_{\mathrm{gap}}^{\mathrm{ASF}}$(eV) can be determined by extrapolating the straight-line portion of the plots in Figure B1.6 to the point where Abs(λ) = 0. The relationship between the optical gap and the deposition time for as-deposited thin films is shown in Figure B1.6 which demonstrates that the optical gap decreases as the deposition time increases. This is due to the growth of particle size over time, leading to a decrease in the energy band gap.[8]

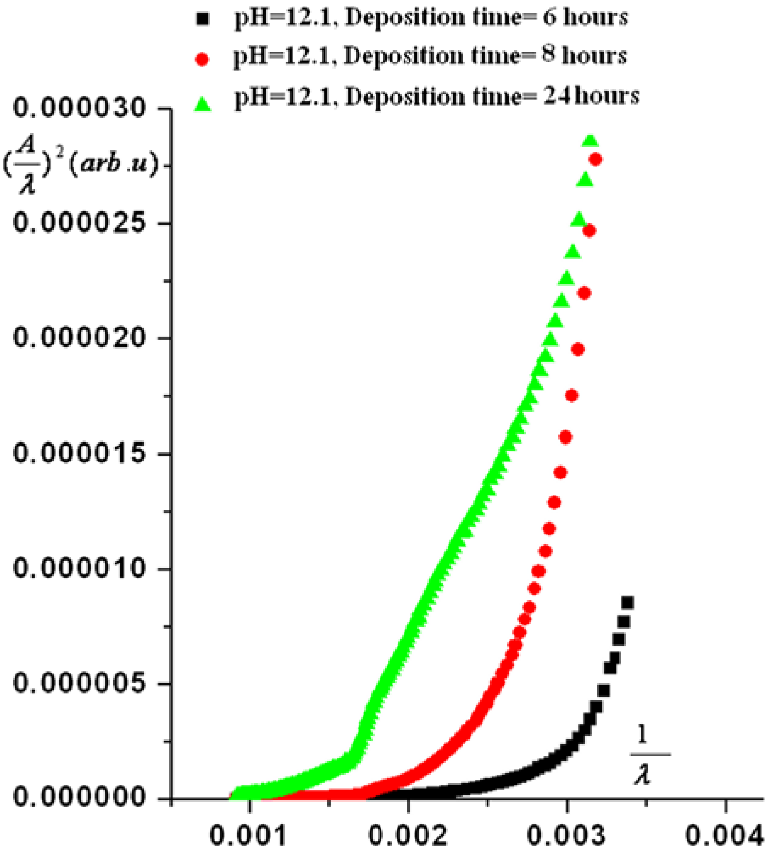

**Figure B1.6:** The absorption spectrum fitting (ASF) plot showing $\left(\frac{Abs(\lambda)}{\lambda}\right)^2$ $vs. \frac{1}{\lambda}$ and $\left(\frac{Abs(\lambda)}{\lambda}\right)^2 = 0$.Adapted with permission from Ghobadi *et al.* Copyright 2013, Interface Nano Letters.[8]

### B1.5. Specification and sample preparation

For the studies reported in this thesis, the UV-Visible absorption spectra were run in a Perkin Elmer spectrophotometer and Agilent Technologies Cary 100 UV-vis. A quartz cuvette with a width ($L$) of 1 cm is utilized for all measurements. The former has the spectral range of 200-800 nm, while the latter has the range of 190-1100 nm. The Ultraviolet/Visible/Near-infrared (UV/Vis/NIR) spectroscopy were collected using Perkin Elmer spectrophotometer and Agilent Technologies Cary 750 UV-vis with spectral range of 190-1400nm.

UV-VIS
SPECTROMETER

**Figure B1.7:** Photograph of a Perkin Elmer spectrophotometer (Range: 190-1100 nm)

In our studies, the samples are dispersed either in anhydrous hexane, water, chloroform, ethanol or in anhydrous tetrachloroethylene (TCE) for measurements depending upon the choice of the solvents and the solution is made up to the mark.

## B2. Photoluminescence (PL) Spectroscopy

### B2.1: Basic Principle

The transition of an electron from the valence band to the conduction band of the QDs takes place upon absorption of photon energy. The excited electron relaxes back to the ground state, which results in emission of photon energy (lower than the absorbed photon energy), known as photoluminescence (PL).[23–25]

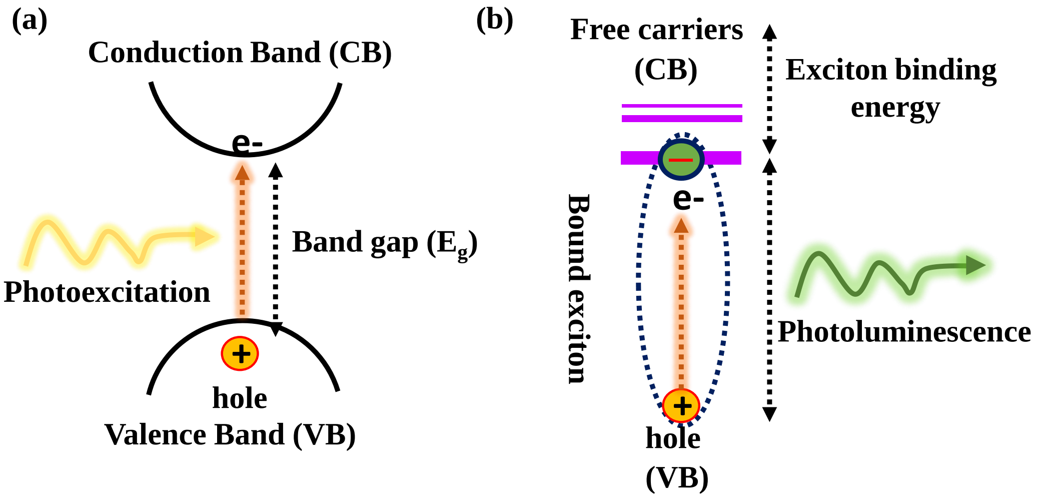
(a)
Conduction Band (CB)
e-
Band gap ($E_g$)
Photoexcitation
+
hole
Valence Band (VB)
(b)
Free carriers
(CB)
Exciton binding
energy
Bound exciton
e-
Photoluminescence
+
hole
(VB)

**Figure B1.8:** (a) Photoexcitation promotes electrons from the valence band to the conduction band by leaving a hole in the valence band. (b) The electron in the conduction band relaxes quickly *via* radiatively or non-radiatively.

PL can be either be fluorescence or phosphorescence depending on symmetry of the state and emission pathways (Figure B1.9). In semiconductors colloidal QDs, absorption and fluorescence emission take place within a few nanoseconds ($10^{-30}$ ns). The phosphorescence takes place slower due to the unfavourable symmetry of the state (triplet to singlet).

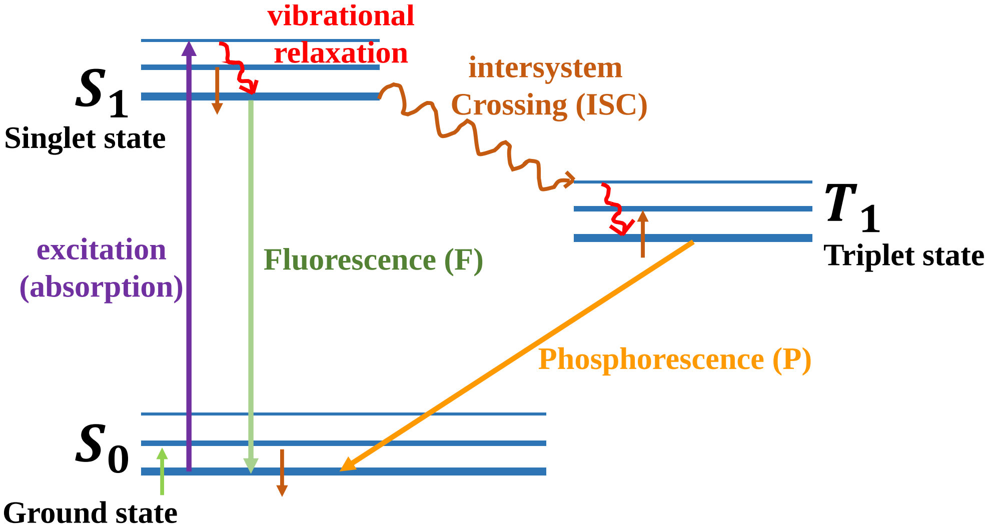
vibrational
relaxation
$S_1$
Singlet state
intersystem
Crossing (ISC)
$T_1$
Triplet state
excitation
(absorption)
Fluorescence (F)
Phosphorescence (P)
$S_0$
Ground state

**Figure B1.9:** Energy diagram showing the principle of luminescence.

PL is a radiative relaxation process i.e., an electron emits a photon. In a non-radiative relaxation, phonons are emitted whose combined energy is equal to the energy of the photon.[26]The emission of phonons is a result of surface defects, impurities, and dopants between the conduction and valence bands.[27]In nonradiative relaxation, there are two types of recombination. When an electron passes its energy to the phonons, it is called Shockley Read Hall recombination. When a relaxing electron passes its energy to another electron or hole is called Auger recombination. Both processes lead to decrease in PL intensity. Only in radiative recombination, emitted photon energy is equal to the bandgap energy. In PL spectroscopy, a monochromatic light is passed through the sample and the emission wavelength is detected. The intensity vs. wavelength plot obtained is referred to as the photoluminescence, PL emission spectrum.[3] The PL emission spectrum gives a broad range of information including quantum yield, size, recombination mechanism, surface defects and trap states. A typical PL emission spectrum of $Ag_2S$ QDs is shown below (Figure B1.10). while the PL maximum is related to the size of the NCs, the line-width of the is often used to understand the size-distribution of the NCs-smaller the width, smaller the size distribution. Furthermore, the higher PL intensity using means low defect density.

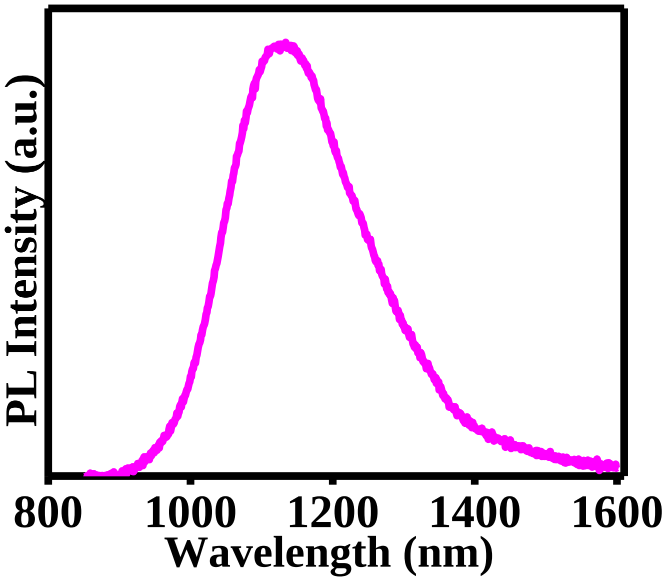

**Figure B2.10:** Photoluminescence spectra of $Ag_2S$ NCs emitting at 1133 nm

### B2.2. Determination of Band-gap

PL emission peak can also be used to determine the band of the materials. However, following limitations must be taken into consideration.[28,29]

- **(a)** The method works only for direct bandgap materials since the indirect bandgap materials lose their energy in the form of phonons instead of photons.
- **(b)** PL emissions do not give an exact bandgap, as the emissions are not 100% radiative in nature. Consequently, the bandgap calculated by the PL study will always be less than the original bandgap. Therefore, it is better to calculate it from the absorbance i.e., UV-vis data.
- **(c)** Emission spectra are highly sensitive to solvent polarity.

### B2.3. Crystal defects

Defects in QDs can affect the PL properties of the material in several ways. For example, defects can cause the emission of the QDs to shift or alter the intensity of the emitted light. Defects can also cause quenching of the photoluminescence, where the emission light is suppressed. Overall, photoluminescence is a powerful tool for studying defects in QDs, and defects in QDs are deviations from the ideal crystal structure of the material, which can significantly impact the properties of the QDs. There are several types of defects that occur in QDs, including:

1. Point defects: These are defects that occur at a single point in the crystal structure, such as vacancies (missing atoms) or interstitials (extra atoms). Point defects can affect the electronic and optical properties of the QDs. Point defects are also due to impurities of atoms and molecules that are present in the QD crystal but are not part of the regular lattice. Impurities can be intentional

(doping) or unintentional (contamination). Impurities can affect the electronic and optical properties of QDs. The presence of point defects in QDs has been reported for a wide range of QD materials such as CdSe, CdS, CdTe, GaAs, InAs, InP, and Si, as well as metal QDs such as Au, Ag, and Cu.[30–34]

2. Strain: Strain is the deformation of the crystal lattice due to external forces or mismatched lattice constants. Strain can affect the electronic and optical properties of QDs.[30–34]
3. Line defects: These are defects that occur along a line or plane in the crystal structure that include dislocations, grain boundaries, and stacking faults, among others. Line defects can affect the structural integrity and stability of the QDs.[30,34]
4. Surface defects: These are defects that occur at the surfaces of the QDs, such as steps, pits, or roughness. Surface defects can affect the stability and reactivity of the QDs.[30–32]

Defects in QDs can be introduced during the synthesis process, or they can occur naturally as the QDs are exposed to the environment. They can also be intentionally introduced to tune the properties of the QDs for specific applications.[35]

### B2.4. Quantum Yield measurements

The fluorescence quantum yield (QY) is the ratio of the number of photons emitted to the number absorbed.[36]

$$QY = \frac{photons_{em}}{photons_{abs}} \qquad \text{B1.12}$$

One way to determine the relative quantum yield ($QY_S$) of an unidentified sample is by using the equation that compares the integrated photoluminescence of the sample with that of a standard dye with a known quantum yield ($QY_R$)

$$QY_s = QY_R \times \frac{I_S \times A_R \times n_S^2}{I_R \times A_S \times n_R^2} \qquad \text{B1.13}$$

where I is integrated PL intensity, n is the refractive index, and A is the absorbance.

Equation B1.13 can be written as follows

$$QY_s = QY_R \times \frac{\frac{I_S}{A_S}}{\frac{I_R}{A_R}} \times \frac{n_S^2}{n_S^2} \qquad \text{B1.14}$$

If we take multiple measurements and obtain the gradient of *I* vs *A*. Then, the above equation can be written as

$$QY_s = QY_R \times \frac{Gradient_s}{Gradient_R} \times \frac{n_S^2}{n_S^2} \qquad \text{B1.15}$$

## B2.5. Instrumentation and sample preparation

The photoluminescent (PL) spectra of our synthesized NCs were collected using a HORIBA Scientific spectrophotometer (Model: PTI-QM 510) with spectral range of 400-1700 nm. Fluorescence spectra were measured in a quartz cell of 1 cm. The samples were dispersed either in anhydrous hexane, water, chloroform, ethanol or in anhydrous tetrachloroethylene (TCE) for measurements. Except otherwise noted, all the measurements were performed with instrument parameters that are mentioned in Table B1.1 below:

**Table B1.1:** Typical instrument parameters used for PL spectroscopy

| Parameters | Set |
|---|---|
| **Scan mode** | Emission |
| **Data mode** | Fluorescence |
| **Scan Speed** | 1200 nm/min |
| **Delay** | 0 s |
| EX Slit | 5.0 nm |
| EM Slit | 5.0 nm |
| PMT Voltage | 700 V |
| Response | 2.0 s |

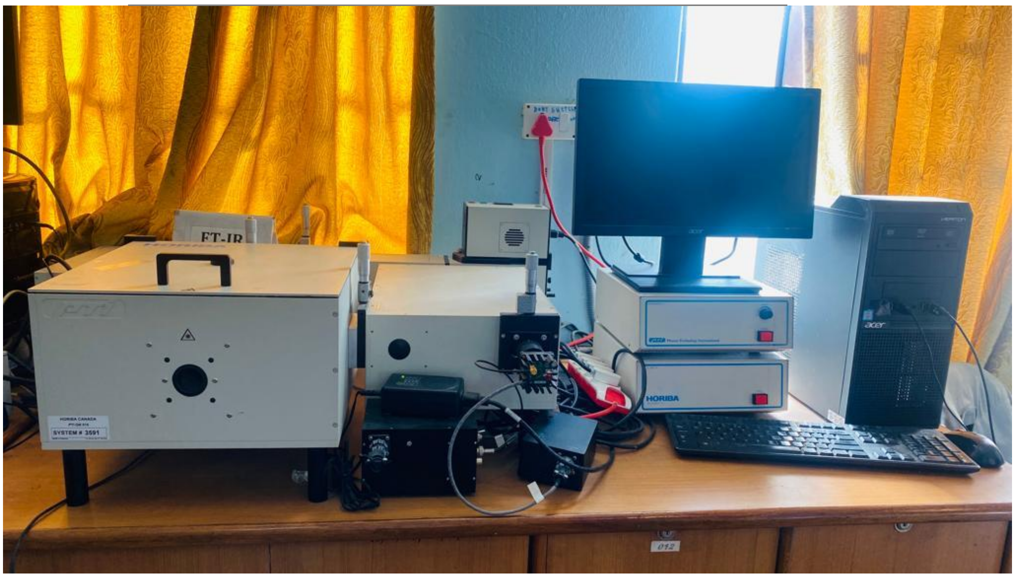

**Figure B1.11:** Photograph of HORIBA Scientific spectrophotometer (Model: PTI-QM 510)

## B3. X-Ray Diffraction

### B3.1: Basic principle

X-ray diffraction (XRD) is a powerful technique to study the internal structure of materials. In 1912 Max von Laue first suggested that X-ray might be diffracted when passed through a crystal which was confirmed by Walter Friedrich and Paul Knipping.[37,38] This discovery, which was later expanded upon by Bragg and Bragg, opened up a new field of research called X-ray crystallography. In the mid-90s XRD studies were first used to confirm the crystalline nature of the QDs.[39] Now its routeinely used to determine the crystal phase and crystallite size of the QDs.[40–42]

X-ray are electromagnetic radiation in the wavelength range of ~1-2 Å, which is comparable to interatomic distances. X-rays are used for investigating the molecular and atomic structure of a wide variety of materials.[43] Primarily X-rays interacts with electrons in atoms. When certain geometric requirements are met, X-rays scattered from a crystalline solid can constructively interfere, producing a diffracted beam. The intensities of peaks and the positions can be used to identify the underlying crystal structure of the material. W.L. Bragg in 1912 recognized the following equation[41,42,44]

$$n\lambda = 2d\sin\theta \qquad \text{B1.16}$$

where n is the diffraction order, $\lambda$ is the wavelength of X-rays, $d$ is the interplanar distance and $\theta$ is the X-ray scattering angle. There are 7 primitive crystal systems[41,45] namely: cubic, tetragonal, orthorhombic, hexagonal, rhombohedral, triclinic and monoclinic. Depending upon the type of crystal system $d$ is related to the corresponding crystal plane in the set of ($h\ k\ l$) represented by Miller indices as follows:

Cubic: $\frac{1}{d^2} = \frac{h^2+k^2+l^2}{a^2}$, (edges $a = b = c$, angle $\alpha = \beta = \gamma = 90°C$) B1.17

Tetragonal: $\frac{1}{d^2} = \frac{h^2 + k^2}{a^2} + \frac{l^2}{c^2}$, (edges $a = b \neq c$, angle $\alpha = \beta = \gamma = 90°C$ B2.18

Hexagonal: $\frac{1}{d^2} = \frac{4}{3}\left(\frac{h^2 + hk + k^2}{a^2}\right) + \frac{l^2}{c^2}$, (edges $a = b \neq c$, angle $\alpha = \beta = 90°C$, $\gamma = 120°C$) B1.19

Rhombohedral: $\frac{1}{d^2} = \frac{(h^2 + k^2 + l^2) sin^2 \alpha + 2(hk + kl + hl)(cos^2 \alpha - \cos \alpha)}{a^2(1-3 Cos^2 \alpha + 2 Cos^3 \alpha)}$, (edges $a = b = c$, angle $\alpha = \beta = \gamma \neq 90°C$) B1.20

Orthorhombic: $\frac{1}{d^2} = \frac{h^2}{a^2} + \frac{k^2}{b^2} + \frac{l^2}{c^2}$, (edges $a \neq b \neq c$, B1.21

angle $\alpha = \beta = \gamma = 90°C$)

Triclinic: $\frac{1}{d^2} = \frac{1}{V^2}$ $(S_{11}h^2 + S_{22}k^2 + S_{33}l^2 + 2S_{12}hk + 2S_{23}kl + 2S_{13}hl)$, (edges $a \neq b \neq c$, angle $\alpha \neq \beta \neq \gamma \neq 90°C$) B1.22

Monoclinic: $\frac{1}{d^2} = \frac{1}{Sin^2\beta}\left(\frac{h^2}{a^2} + \frac{k^2 sin^2 \beta}{b^2} + \frac{l^2}{c^2} - \frac{2\, hl \cos\beta}{ac}\right)$, (edges $a \neq b \neq c$, angle $\alpha = \gamma = 90°C, \beta \neq 90°C$) B1.23

Combining the above equation of any of the seven primitive crystal planes (For example, Equation B1.17 for cubic) with Bragg's equation (Equation B1.16), we obtained the equation (Equation B1.25) where the Bragg's theta is solely dependent on the type of crystalline:

$$\left(\frac{n\lambda}{2a}\right)^2 = \frac{sin^2\theta}{h^2 + k^2 + l^2} \qquad \text{B1.24}$$

$$\theta = sin^{-1}\left(\frac{\lambda}{2a}\sqrt{(h^2 + k^2 + l^2)}\right) \qquad \text{B1.25}$$

In Powder-XRD (PXRD), a plot of 2 theta ($\theta$) vs Intensity [$I(\theta)$] is generated. The Intensity of the peak is related to the structure factor, $F(\theta)$.

$$I(\theta) = F(\theta) * F(\theta) \qquad \text{B1.26}$$

The structure factor is related to scattering factor, $f_i$ ; number of atoms per unit cell, n; atom coordinates $(x_i, y_i, z_i)$ and miller indices (h k l) as follows

$$F(\theta) = \sum_i^n f_i e^{2\pi(hx_i + ky_i + lz_i)} \qquad \text{B1.27}$$

Let us comprehend each term by first understanding how to calculate the number of atoms per unit cell.

Thus, in case of simple cubic, $n = 8(\text{corners}) \times \frac{1}{8} = 1$, meaning there is only one atom per unit cell due to the sharing of 8 corner atoms among 8-unit cells.

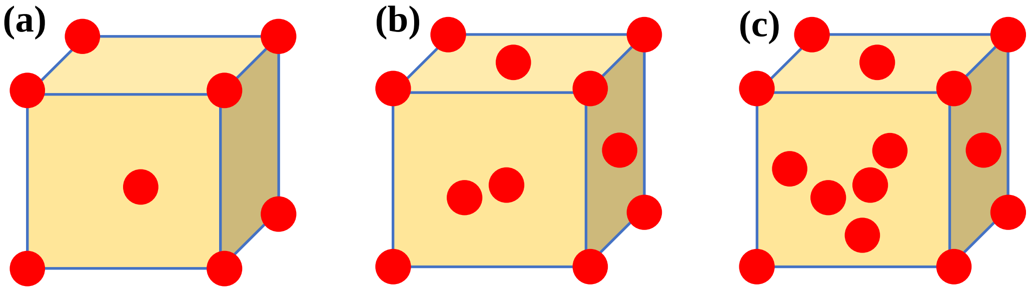

**Figure B1.12:** A unit cell **(a)** Simple cubic **(b)** bcc **(c)** fcc

The second term $f_i$, is dependent on atomic number, X-ray wavelength and $\theta$ and is primarily determined by type of atom. The atom coordinates $(x_i, y_i, z_i)$ for simple cubic unit cell are (0,0,0) since all the atoms are located at the corners. For bcc, it has two atoms ($n = 2$) and for one of them the atom coordinates are (0,0,0) and $\left(\frac{1}{2}, \frac{1}{2}, \frac{1}{2}\right)$. Similarly, for fcc where there are 4 atoms/unit cell ($n = 4$), the atom coordinates are (0,0,0), $\left(\frac{1}{2}, \frac{1}{2}, 0\right)$, $\left(0, \frac{1}{2}, \frac{1}{2}\right)$ and , $\left(0, \frac{1}{2}, \frac{1}{2}\right)$. Using these values one can obtain:

$$F(\theta) = f_1 e^0 = f_1 \text{ for simple cubic} \qquad \text{B1.28}$$

$$F(\theta) = 2f_1 e^{\frac{\pi}{2}i(h+k+l)} \cos\left[\frac{\pi}{2}(h+k+l)\right] \text{ for bcc and} \qquad \text{B1.29}$$

$$F(\theta) = 4f_1 e^{\frac{\pi}{2}i(h+k+l)} \cos^2\left[\frac{\pi}{2}(h+k)\right] \cos^2\left[\frac{\pi}{2}(h+l)\right] \text{ for fcc} \qquad \text{B1.30}$$

Which implies that:

For QDs, the broadening of XRD peak is observed due to finite size effect. Scherrer's equation[46] is used to calculate the size of the particle using the equation below.

$$D = \frac{k\lambda}{B\cos\theta} \qquad \text{B1.31}$$

where *K* is the shape factor, λ is the wavelength of the X-ray, B is the full width at half maximum (FWHM) in radians, and θ is the Bragg angle can be used to relate the crystallite size with the XRD line-width.

### B3.2. Sample preparation and instrumentation:

The purified NCs were evenly distributed in hexane and then deposited onto a clean and dry glass slide through drop-casting. After the deposition, the film on the glass slide was subjected to X-ray diffraction analysis using Cu $K_\alpha$ ($\lambda$= 1.54 Å) as the incident radiation, with 40 kV and 30 mA as the operating conditions. The beta filter used was Ni.

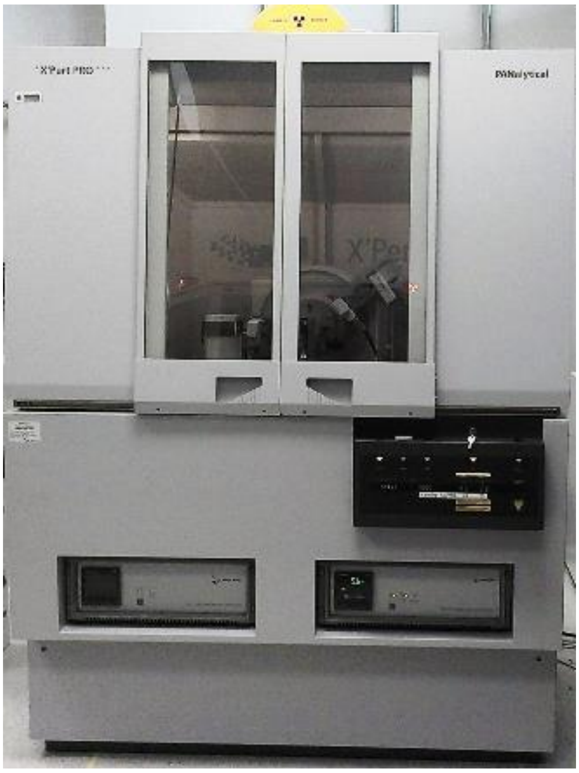

**Figure B1.13:** Photograph of PANalytical X-Ray diffractometer.

## B4. Fourier-transform Infrared Spectroscopy (FTIR)

### B4.1. Basic Principle

FTIR is a well-established technique that is commonly used in materials science and chemistry. FT-IR spectroscopy determines the functional groups present in a molecule. In this spectroscopic method, absorption of light causes molecular vibration. In order to cause the bonds in a molecule to vibrate, it is necessary to supply the molecule with energy at a frequency that is exactly equal to the vibrational frequency of the molecule. It is mainly based on the vibration of chemical bonds in mid infrared region (400 to 4000 $cm^{-1}$) only. The two fingerprints region lies in 400-1600 $cm^{-1}$ and the functional groups region which lies in 1600-4000 $cm^{-1}$. The vibrational spectra are determined using Hooke's equation[47–49]

$$\bar{\upsilon} = \frac{1}{2\pi c}\sqrt{\frac{k}{\mu}}cm^{-1} \qquad \text{B1.32}$$

where, $\bar{\upsilon}$ is wavenumber ($cm^{-1}$), c is speed of light ($cm\ sec^{-1}$), k is the force constant ($dyne\ cm^{-1}$) and μ is the reduced mass of atoms (g).

Different types of vibrational modes possible are stretching and bending.[50–52] In stretching mode, the interatomic distance and bond length changes and in bending mode, the bond angle changes. Furthermore, stretching mode is classified in two types- symmetric and anti-symmetric stretching. When a molecule has at least two or three identical groups, symmetric and asymmetric stretching occur, as seen in molecules such as $CH_2$, $CH_3$, $CCl_2$, anhydride, $NO_2$, and $NH_2$. The asymmetric stretch has a higher energy compared to the symmetric stretch. In symmetric stretching, the bond lengths of the participating atoms either both increase or decrease, while in asymmetric stretching, one bond length increases and the other decreases. For example, the $CH_3$ symmetric stretch occurs at approximately 2872 $cm^{-1}$, while its asymmetric stretch, at a higher energy, appears at 2962 $cm^{-1}$. Similarly, the symmetric stretch of the $NH_2$ group is at 3300 $cm^{-1}$, while its asymmetric stretch is at 3400 $cm^{-1}$. Bending mode is classified into four types- rocking, scissoring, wagging and twisting. In rocking, the two atoms moves clockwise or anticlockwise; in scissoring, the two atoms move towards or away from the central atom simultaneously; in wagging, the two atoms move in V direction back and forth and in twisting, one of the atoms moves backward where as another moves forward as shown in the Figure B1.14 below:

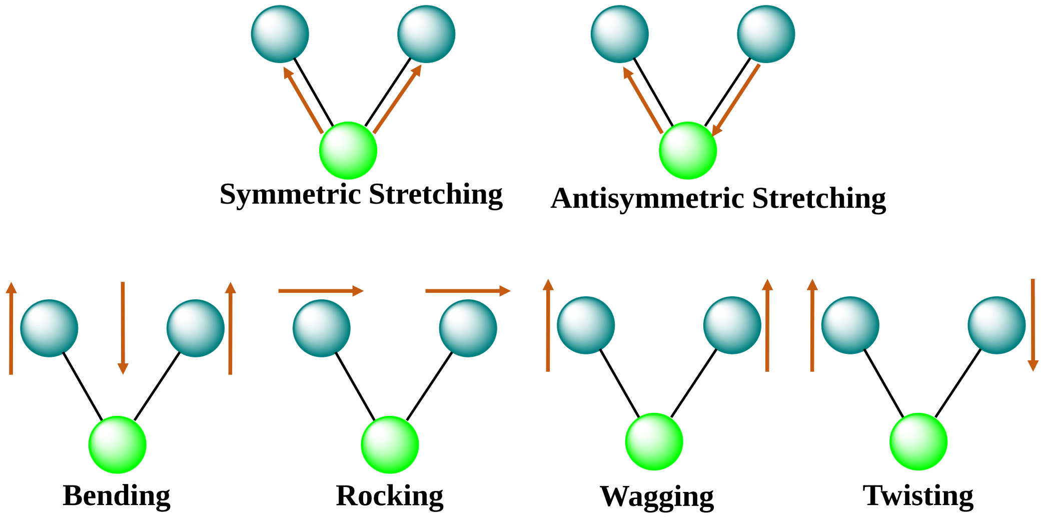

**Figure B1.14:** Different modes of vibration in IR spectroscopy.[53]

FTIR is a powerful tool for analysis surface chemistry of QDs and detecting organic impurities. It is a non-destructive technique that provides insightful information about the stabilizing ligand and nature of its bonding to the QDs. Figure B1.15 shows the difference between pure L-cysteine and L-cysteine appended on the surface of the QDs. The FTIR spectrum of pure L-cysteine displays a distinctive S-H stretching vibration signal at 2538 cm$^{-1}$, as seen in Figure B1.15. The lack of this peak in the spectrum of aqueous $Ag_2S$ QDs, confirms the absence of free L-cysteine in the solution. A notable peak at 1572 cm$^{-1}$ is attributed to the asymmetric stretching vibration of the carboxylate ($COO^{-}$) group in L-cysteine that is surface-bound. For free L-cysteine, this peak is observed at a slightly higher frequency, around 1588 cm$^{-1}$. The shift of frequency towards the lower range is attributed to the binding of L-cysteine to the surface of the QDs.[54]

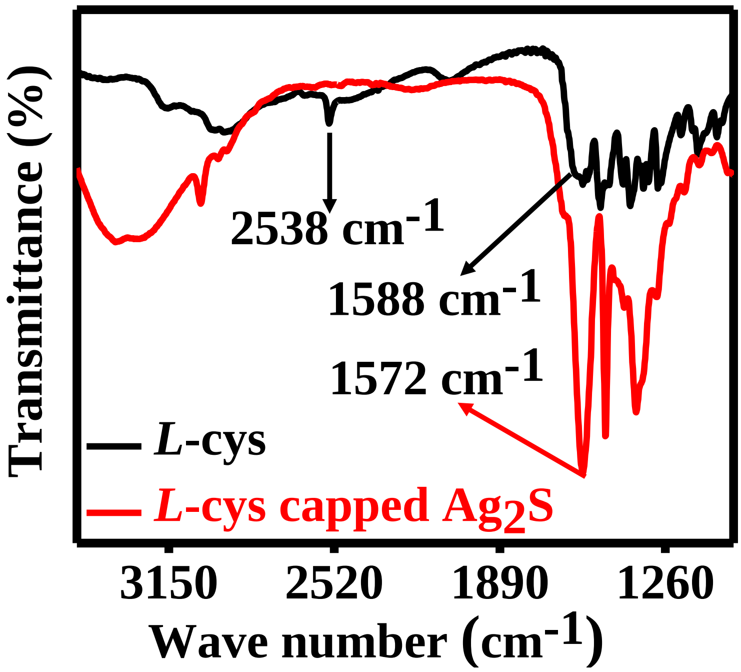

**Figure B1.15:** FTIR spectrum of pure *L*-cysteine and surface bound *L*-cysteine on QDs.[54]

### B4.2. Sample preparation and Instrumentation

FT-IR spectra were recorded using Bruker ALPHA E, 200396. The instrument consists of the following components- light source, monochromator, sample holder and the detector. The light source is basically a Nernst filament or a Globar filament which are red or white heated before analysis. The light produces are then passed further towards the sample with the help of silver layered mirror and passes through the monochromator producing desired frequency of light. The samples are held in metal sample holder (in case of solid samples) by preparing a thin film of KBr and the sample and the liquid samples are held in an ATR crystal surface. The detector then detects by sensing heating effect due to radiation or by photoconductivity.

**(a)** Liquid samples were drop-casted onto the surface of the instrument detector, and the spectrum was obtained.

**(b)** For solid samples, the samples were grounded in a mortar with anhydrous potassium bromide (KBr). A piece of paper is taken and on top of it, a cut-out hole is made. The grounded sample is poured in the hole and a pallet is made with the help of a hydraulic press. The sample is inserted in the IR sample holder and attached with scotch tape and the spectrum is run for analysis.

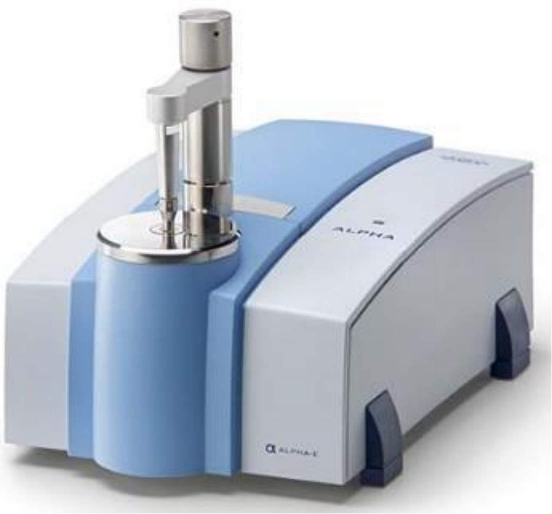

**Figure B1.16:** Bruker Alpha FT-IR Spectrophotometer.

## B5. Thermogravimetric Analyser (TGA)

### B5.1. Basic Principle

Any simple molecule undergoes various transformation when heated or cooled. Some of the transformations such as vaporisation, decomposition, reaction etc. leads to loss or gain of weight. TGA works by measuring the change in mass of a sample as a function of temperature. By exposing the QDs to a controlled heating rate, TGA can provide information on the thermal stability of the material, including the temperature at which decomposition occurs, the amount of material-both organic and inorganic- lost during degradation, and the evolution of degradation products. The TGA instrument can scan over a wide range of temperature (25 – 1200 ºC). Any change in mass due to decomposition, oxidation-reduction, dehydration, volatilisation or chemisorption are detectable.[55–57]

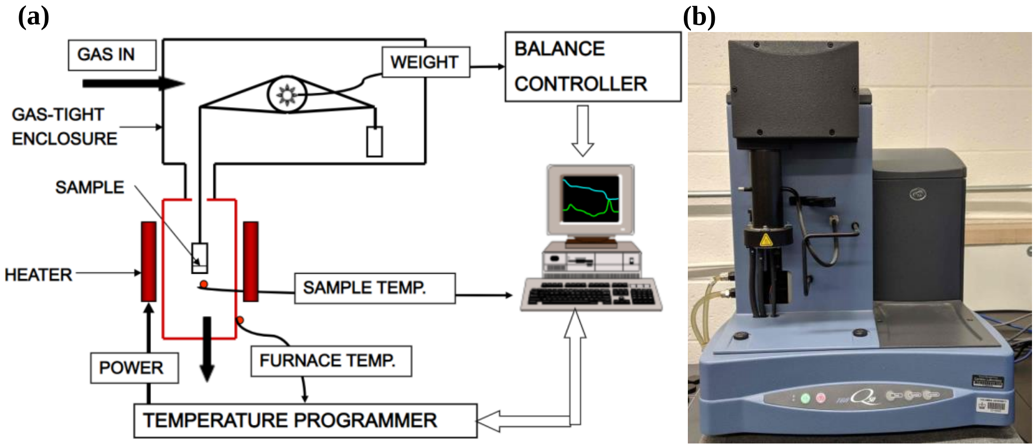

**Figure B1.17: (a)** Schematic diagram of a TGA analyser[58] **(b)** TA Instrument's Q50 TGA analyser.

TGA is a combination of a microbalance, programmable temperature controller and a PC for data acquisition.[59–61] The balance is connected to sensor which detects the deviation from a null point and measures the change in mass. They are sensitive to an order of $10^{-6}$ g. Samples are placed in a pan (platinum/aluminium/ceramics) and suspended from the microbalance down to a furnace where a highly controlled heating environment is maintained. The balance mechanism present inside the instrument is protected from causing damage due to a high temperature by using a baffle and flowing inert gas. The measurement is plotted as two ways- thermogravimetric (TG) curve or derivative thermogravimetric (DTG) curve. In the first one, the change in mass/weight *vs.* time or temperature is plotted and in the second one, the rate of change in mass/weight *vs.* time or temperature is plotted.[60,61]

Figure B1.18 shows the decomposition temperature at 140°C of an organic compound named 1-(4-Methoxyphenyl)-3-phenylthiourea. To determine the decomposition temperature, both weights lost (%) and its derivative with respect to temperature are analysed.[54] The temperature at which the sample starts to lose weight can be determined from the inflection point or the maximum rate of weight loss in the TGA curve. This temperature is considered to be the decomposition temperature material.

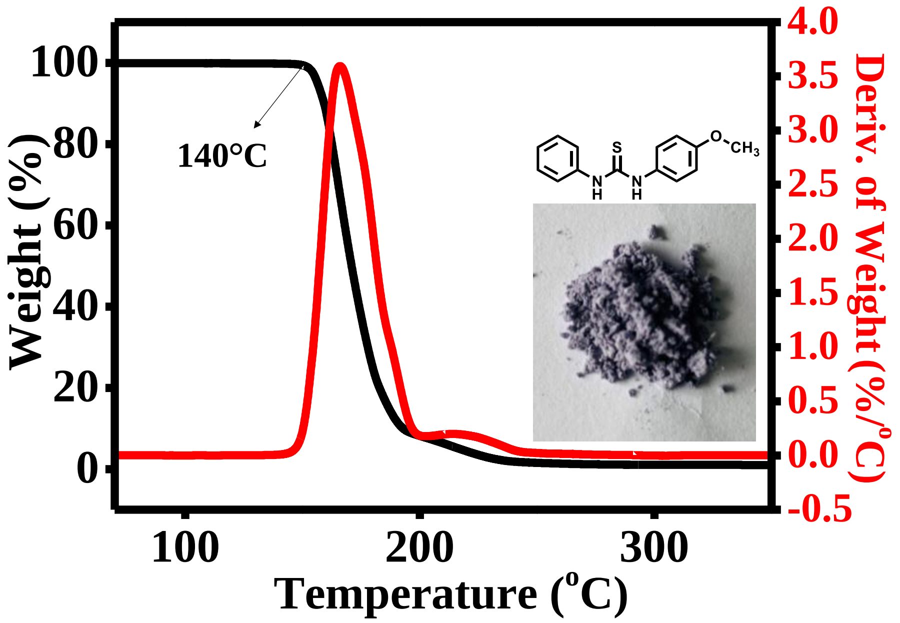

**Figure B1.18: (a)** TGA graph showing decomposition temperature of 1-(4-Methoxyphenyl)-3-phenylthiourea.[54]

## B6. Turbidimeter

### B6.1. Basic principle

Turbidimeter is an instrument that measures the optical density of a sample and is a suitable technique for characterizing QDs suspensions because they provide information about the size and distribution of the QDs. The turbidimeter measures the light transmittance of a sample in NTU's (Nephelometric Turbidity Units, a standard measure). Turbidimeters measure the intensity of light scattered in one particular direction, predominantly at right angles to the incident light. Optical turbidity, $T$, refers to the light scattered per cell length in the following equation: [62]

$$T = K\frac{I_{90}}{I_0} \qquad \text{B1.33}$$

where $I_{90}$ is the intensity of transmitted light scattered at 90° , $I_0$ is the intensity of light incident upon a suspension having negligible absorption of light and K is a constant that includes instrumental calibration factors and optical constants for the suspension being measured.[62]

### B6.2. Sample Preparation and Instrumentation

In this thesis, we used turbidity index to study the colloidal stability of the NCs in aqueous medium. The NCs were dispersed in water (aqueous system) and were analysed in turbidimeter.

**Table B1.2: Specification of the turbidimeter used**

| | |
|---|---|
| **Range** | 0 to 200 NTU 0 to 1000 NTU2 Ranges |
| **Display** | 3Half digit LED display |
| **Voltage** | 220 V |
| **Resolution** | 1 NTU |
| **Light Source** | 6.8 V |
| **Accuracy** | ±3 % S ±1 digit |
| **Power** | 230 VAC, ±10% |
| **Sample System** | m clear glass tube |

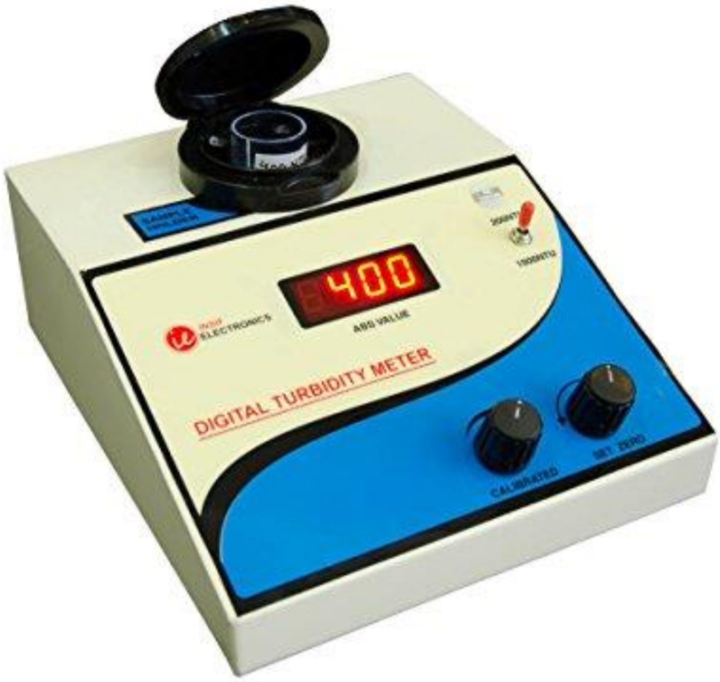

**Figure B1.19:** Photograph of a turbidity meter.

## B7. Transmission electron microscopy (TEM)

### B7.1: Basic principle

TEM provides high resolution imaging and structural analysis, allowing scientists and engineers to study and understand the properties of materials at the nanoscale. It is used to analyse microstructures of cells, nanostructures such as fibers, particles and thin films, materials such as crystal structure and compositions, phase transitions and transformation in materials, defects in materials such as voids,cracks and grain boundaries etc. TEM was invented by German physicists Max Knoll and Ernst Ruska in the 1930s.[63,64]

The basic principle of TEM is to pass a beam of electrons through a thin specimen and observe the transmitted electrons to create an image. The electrons are transmitted through the specimen and interact with the atoms, causing the electrons to diffract, scatter or be absorbed. The electrons that pass through the specimen form an image that can be captured by a screen or an electron detector, providing a high resolution representation of the specimen's internal structure. This technique enables scientists and engineers to observe materials at the nanoscale, and to study their physical, chemical, and structural properties.[65] Figure B1.20 shows photographic representation a TEM image of $Ag_2S$ QDs at 20 nm scale with size 2.2 nm.

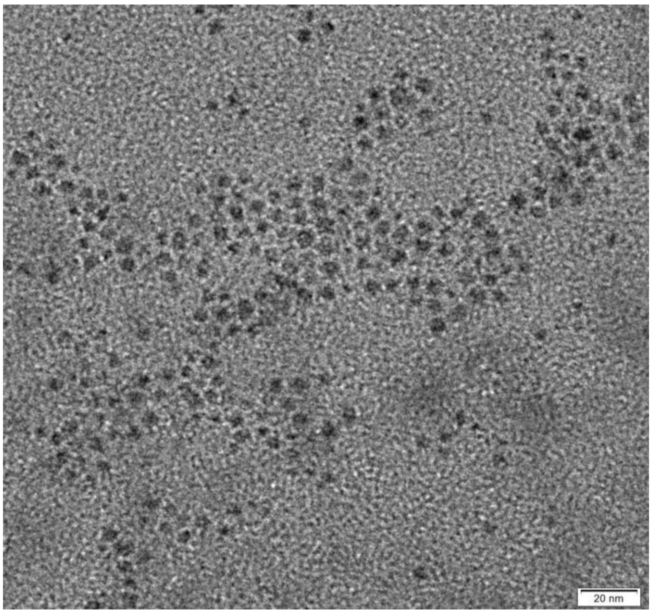

**Figure B1.20:** TEM image of $Ag_2S$ QDs.[54]

**Particle size and lattice fringes calculation:**

There are various image processing software that are used to analyse TEM images. ImageJ software is used in our studies to calculate the size of the QDs. It is a free, open-source software that is widely used in the scientific community for analyzing and processing images. [64]

To use ImageJ to analyse TEM images, it is first required to aquire the TEM images and import them into ImageJ. Then various tools can be used and plugins that are available in ImageJ to process and analyze the images. Some common tasks that has be performed include:

To calculate the size of QDs and lattice fringes using ImageJ, the following steps are followed:

1. Acquire the TEM image of the QDs or lattice fringes, and import it into Imagej.
2. Adjust the contrast and brightness of the image as needed to enhance the details and make it easier to see.
3. Use the "Line Tool" or "Polyline Tool" to draw a line along the edge of the quantum dot or lattice fringe.
4. Use the Analyse> Measure function to measure the length of the line. This will give the size of the QDs or lattice fringe.
5. Repeat the process for multiple QDs or lattice fringes to get an average size or to study the size distribution.

Thus, with the above mentioned processes, the size of the $Ag_2S$ QDs were calculated to be 2.2 nm from the TEM image shown in Figure B1.20. From the TEM image, we can also calculate the lattice fringes which are observed as regular, repeating patterns in the image and their spacing is related to the distance between crystal planes in the lattice. The fringes arise from the interference of electrons that have passed through different parts of the crystal lattice. Figure B1.21 shows lattice fringes of $Ag_2S$ QDs corresponding to the monoclinic phase (1,2,1) with d spacing measured to be 0.26 nm

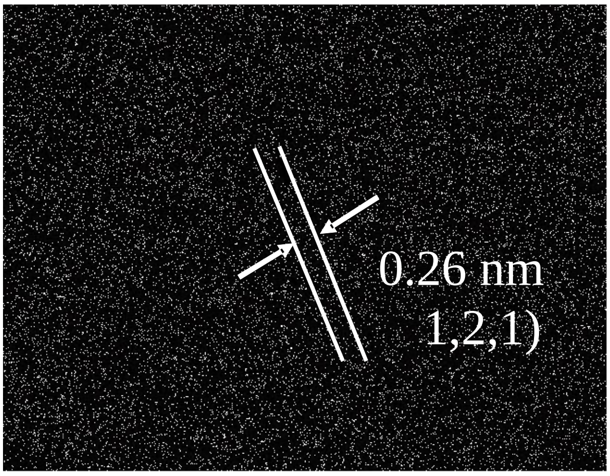

**Figure B1.21:** The lattice fringes of $Ag_2S$ QDs corresponding to the monoclinic phase.[54]

**Selected area electron diffreaction measurements (SAED):**

In SAED, a narrow electron beam is focused onto a small area of the sample, producing an electron diffraction pattern that provides information about the crystal structure of the material. The diffraction pattern consists of a series of bright spots or rings, which correspond to the various crystal planes in the lattice. The spacing between the diffraction spots provides information about the lattice constant, which can be used to identify the crystal structure and determine the orientation of the crystal. The technique can also be used to study crystalline materials at the nanoscale, and to determine the crystal structure of individual grains in a polycrystalline material.[66]

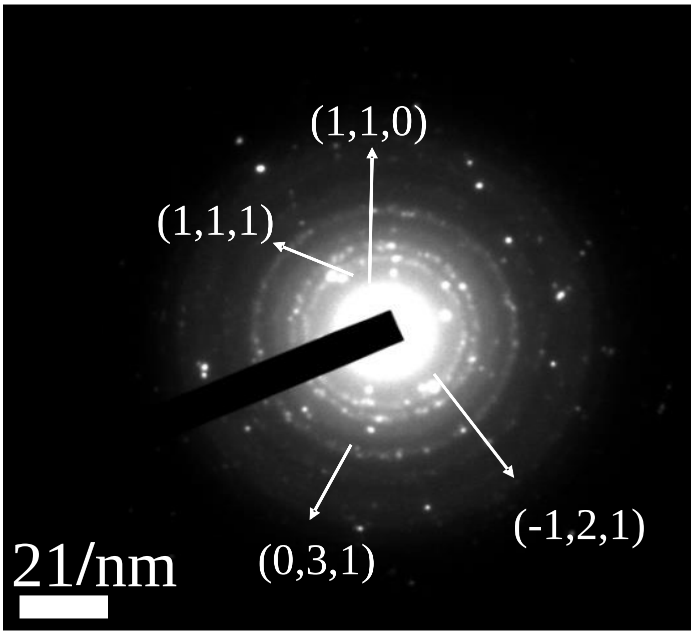

**Figure B1.22:** SAED image of $Ag_2S$ QDs corresponding to the monoclinic phase [54]

To calculate the d-spacing from the SAED image , the following steps can be followed:

1) Measure the diameter, D = 2R, R = Radius. Find the radius R = $x\left[\frac{1}{nm}\right]$
2) Find the interplaner distance d in real space as 1/R = d.
3) After calculating d, comparethe d value with the corressponding hkl values in the literature.

For example , in the case $Ag_2S$ QDs as shown in Figure B1.22 , For the first ring, 2R = 5.62$\left[\frac{1}{nm}\right]$, R = 2.81$\left[\frac{1}{nm}\right]$, d = 1/ R, d = 1/ 2.81 = 0.355 nm corressponds to (1,1,0) planes. Similarly for other rings, d = 0.308 nm (1,1,1) plane, d = 0.266 nm (-1,2,1) plane and d = 220 nm (0,3,1) plane. These results suggests that the SAED image corresponds to monoclinic phase of $Ag_2S$ QDs.[54]

**B7.2: Sample preparation and instrumentation:**

Samples were thoroughly purified prior and prepared by drop casting the sample on the carbon coated copper grids and allowing the solvent to evaporate. All TEM images presented in the thesis were recorded in JEOL-JEM-2100 Plus electron microscope. The take-off angle maintained taken was 90°. HRTEM images were obtained using 200 kV electron source. The lattice plane was obtained from lattice fringes. Image J software was used for calculation.

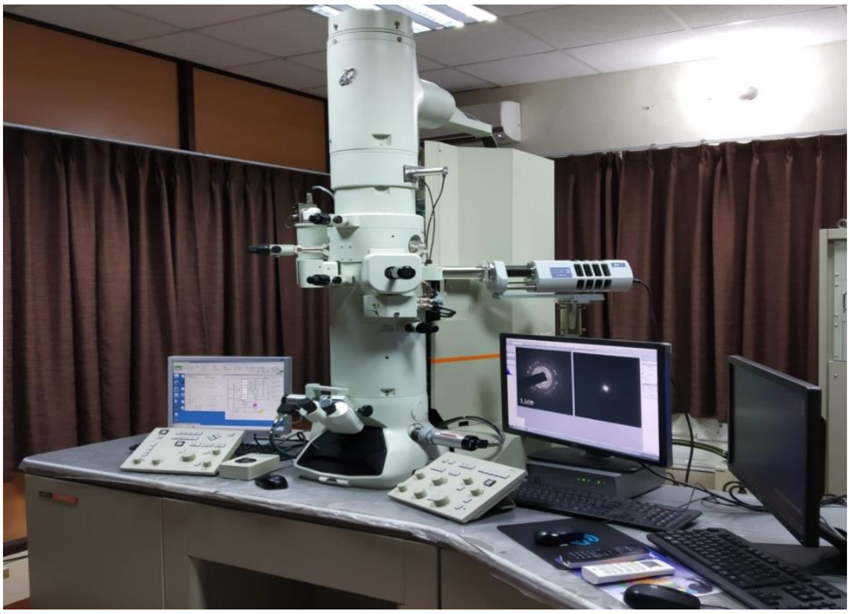

**Figure B1.23:** Photograph of a JEOL-JEM-2100 Plus electron microscope (TEM).

## B8. X-ray Photoelectron (XPS) Spectroscopy

### B8.1. Basic principle

When a material is irradiated with X-ray, three types of processes can occur: (a) emission of the electron known photoelectron (an electron ejected from an inner shell following the absorption of X-ray energy) (b) x-ray fluorescence, where the absorbed energy is re-emitted as a fluorescent X-ray with a lower energy and (c) emission of an Auger electron, where a vacancy in the inner shell is filled by an electron from an outer shell, and the excess energy is emitted as an Auger electron.[67]

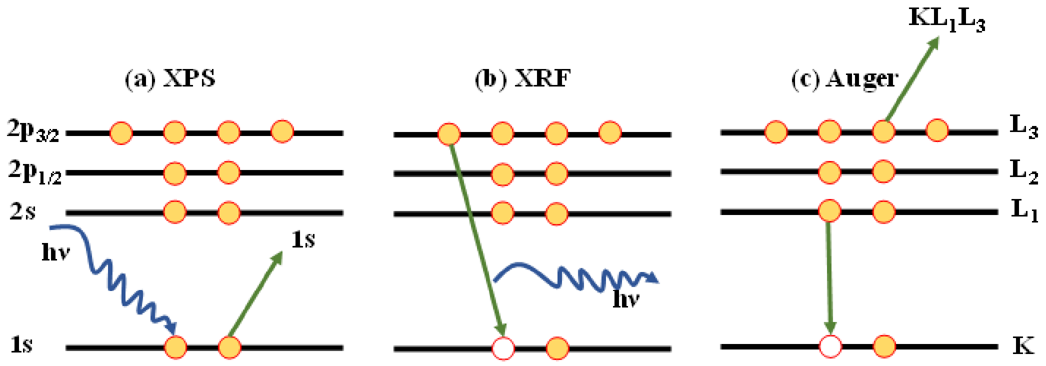

**Figure B1.24:** Processes that result from x-ray bombardment of a surface include (a) emission of a photoelectron, (b) x-ray fluorescence, and (c) emission of an Auger electron.

The release of a photoelectron occurs when the x-ray energy ($h\vartheta$) is fully transferred to a core electron, which can be represented mathematically as follows:

$$h\vartheta = BE + KE - \varphi \qquad \text{B1.34}$$

where $BE$ is the binding energy of the ejected electron, $KE$ is the kinetic energy of the ejected electron and $\varphi$ is the spectrometer work function. In X-ray photoelectron spectroscopy (XPS), the plot $BE$ vs Intensity is obtained and analysed. Since BE is highly sensitive to the type of atom, type of orbital, oxidation state, electronegativity of the adjacent atom) of the atom, XPS is a powerful technique to analyse: composition, and electronic structure of materials in QDs.[67–70] Photoelectron peaks are named according to the quantum numbers of the energy levels from which the electrons are originating. For example: An electron originating from an orbital with principal quantum number ‘n’, orbital quantum number ‘l’ and spin quantum number ‘s’ is indicated as[67]

$$\mathrm{n}l_{l+s} \qquad \text{B1.35}$$

For a non-zero orbital quantum no (l >0), spin moment is coupled with orbital moment which is also known as L-S coupling and it has a total momentum (j = l + ½) and (j = l

$-½$) and generally given by ($j = l \pm S$), each state being filled with (2j + 1) electrons.[67,71] Hence, most XPS peaks appear in doublets and the intensity ratio of the peaks is given by, $\frac{l+1}{l}$.[72] In other words, for s there will be no splitting; for p orbital ($l = 1$) splitting into $p_{1/2}$ and $p_{3/2}$ occurs (peak area ratio ~ 1:2). Similarly, for d orbital ($l = 2$), splitting into $d_{3/2}$ and $d_{5/2}$ occurs (peak area ratio ~2:3) and for f orbital ($l = 3$), splitting into $f_{5/2}$ and $f_{7/2}$ occurs (peak area ratio ~3:4).

### B8.2. Chemical environment

BE is affected by chemical environment.[73] Ti has a binding energy of 458.8 eV, which corresponds to the Ti $2p_{3/2}$ peak whereas Ti $2p_{3/2}$ peak for Ti (IV)$O_2$ will typically be observed at binding energies in the range of 464-465 eV due to change in oxidation state. Not only the oxidation state, but also the electronegativity of the adjacent (or counter ion or atom) element also affects the BE. For example, C 1s peak of C=O and $CH_3$ are substantially different. More electronegative adjacent atom increases the BE.[74] Sometimes, there are multiple specifies in the same broad peak in which case the high resolution XPS peak is obtained and deconvoluted using literature spin-orbit splitting constant and peak line-width values.[75]

### B8.3. Back ground correction:

Background correction is an important step in XPS analysis. Removing the spectral background caused by low energy electrons that are not part of the photoelectron signal is important. We used Shirley method for background correction as shown in Figure B1.25: This correction method is widely used because it is simple and quick to perform, and can produce reasonable results for many XPS spectra.[76]

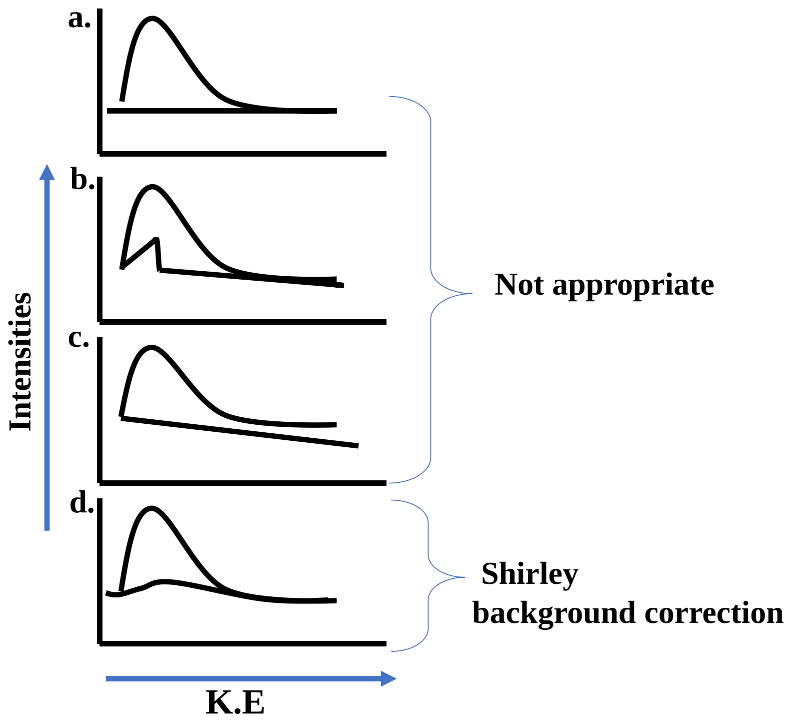

**Figure B1.25:** Representation of correct background method.

### B8.4. Elemental Analysis

Semi-quantitative analysis can be achieved by measuring the area of specific elemental core lines (l) and by utilizing the proper RSF factor through the application of an equation

$$C_x = (l_x/S_x)\sum(l_i/S_i) \qquad \text{B1.35}$$

where the atomic fraction of element x in a sample is represented by $C_x$

In XPS analysis, the relative sensitivity factor (RSF) plays a crucial role as it has the potential to alter the peak intensity for a particular element in the XPS spectrum. The RSF may differ for various elements and even for various electron subshells of a single element. For example, the RSF values for Se, Ag and Se are as follows: Se $3p_{3/2}$: $0.9 - 1.1$, Ag $3d_{5/2}$: $0.5 - 0.7$ and S 2p: 1.3.[77,78]

### B8.5. Sample preparation and Instrumentation

Thermo-Scientific ESCALAB Xi$^+$ spectrometer equipped with an X-ray source of Al K$_\alpha$ (1486.7 eV) was utilized to obtain the XPS spectra. The high resolution spectra were acquired using a constant analyzer energy (CAE) of 50 eV, while a CAE of 100 eV was employed to acquire survey spectra.

**Figure B1.26:** Photograph of Thermo-Scientific ESCALAB Xi$^+$ X-ray Photoelectron Spectrometer.

In order to prevent charging, XPS samples were created in a glovebox on silicon wafers coated with carbon. The binding energy of XPS spectra was aligned to the C 1s Band gap Energy, which is 284.8 eV. The peaks in the spectra were separated using the Gaussian-Lorentzian (SGL) function, using a fixed ratio of 80:20. Additionally, the Shirley method was utilized to correct the background of the spectrum.[72]

## B9. Nuclear Magnetic Resonance Spectroscopy (NMR)

### B9.1. Basic Principle

Nuclear magnetic resonance (NMR) spectroscopy is a powerful analytical technique used to study the structure and behavior of molecules. It is based on the principle that the nuclei of certain atoms, such as hydrogen and carbon, have a magnetic moment and can act as tiny magnets. When these nuclei are subjected to a magnetic field, they align either parallel or anti-parallel to the magnetic field, creating two energy levels.[79–81]

The following features lead to the NMR phenomenon

**(a)** A spinning charge generates a magnetic field. The resulting spin-magnet has a magnetic moment ($\mu$) proportional to the spin as shown in Figure B1.27.

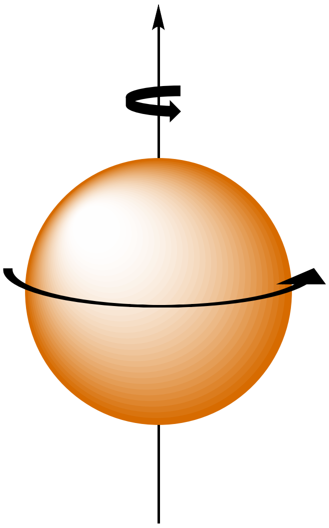

**Figure B1.27:** Spinning creates a magnetic moment

**(b)** In the presence of an external magnetic field ($B_0$), two spin states exist, $+\frac{1}{2}$ and $-\frac{1}{2}$ The magnetic moment of the lower energy $+\frac{1}{2}$ state is aligned with the external field, but that of the higher energy $-\frac{1}{2}$ spin state is opposed to the external field.

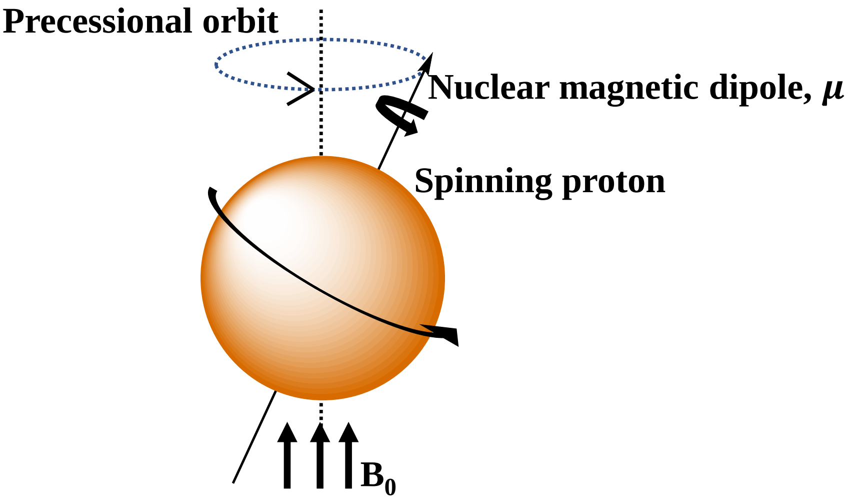
Precessional orbit
Nuclear magnetic dipole, μ
Spinning proton
B0

**Figure B1.28:** Representation of a precessing proton in a stationary magnetic field $B_0$

**(c)** The difference in energy between the two spin states is dependent on the external magnetic field strength, and is always very small. The Figure B1.29 describes that the two spin states have the same energy when the external field is zero, but diverge as the field increases.

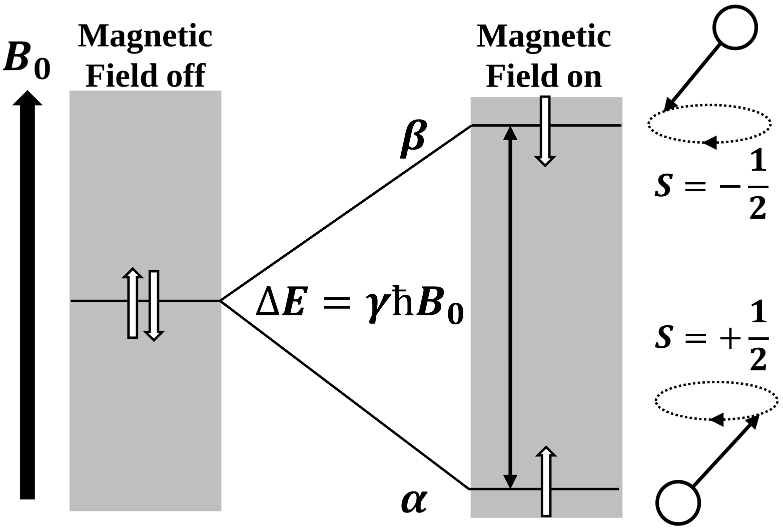
$B_0$
Magnetic Field off
Magnetic Field on
$\beta$
$\alpha$
$\Delta E = \gamma\hbar B_0$
$S = -\frac{1}{2}$
$S = +\frac{1}{2}$

**Figure B1.29:** The energy difference ΔE between the spin energy states.

The NMR spectrometer applies a short radio frequency (RF) pulse to the sample, causing the magnetic moments of the nuclei to flip from their original alignment. As the magnetic moments return to their original alignment, they emit a radio frequency signal that is detected by the spectrometer. This signal is then processed to generate an NMR spectrum, which provides information about the chemical composition, structure, and behavior of the sample.[82]

**Table B1.3:** Properties of some nuclei with non-zero spin. [83]

| Nucleus | Spin | Natural Abundance % | Magnetic moment μ | Magnetogyric ratio $\gamma/10^7$ rad T $s^{-1}$ | NMR frequency ν/MHz |
|---|---|---|---|---|---|
| **$^{1}$H** | 1/2 | 99.985 | 2.7927 | 26.7520 | 400.00 |
| **$^{2}$H** | 1 | 0.015 | 0.8574 | 4.1066 | 61.402 |
| **$^{7}$Li** | 3/2 | 92.58 | 3.2560 | 10.9375 | 155.454 |
| **$^{13}$C** | 1/2 | 1.108 | 0.7022 | 6.7283 | 100.577 |
| **$^{14}$N** | 1 | 99.63 | 0.4036 | 1.9338 | 28.894 |
| **$^{15}$N** | 1/2 | 0.37 | -0.2830 | -2.712 | 40.531 |
| **$^{17}$O** | 5/2 | 0.037 | -1.8930 | -3.6279 | 54.227 |
| **$^{19}$F** | 1/2 | 100 | 2.6273 | 25.181 | 376.308 |
| **$^{23}$Na** | 3/2 | 100 | 2.2161 | 7.08013 | 105.805 |
| **$^{27}$Al** | 5/2 | 100 | 3.6385 | 6.9760 | 104.229 |
| **$^{29}$Si** | 1/2 | 4.70 | -0.5548 | -5.3188 | 79.460 |
| **$^{31}$P** | 1/2 | 100 | 1.1305 | 10.841 | 161.923 |
| **$^{59}$Co** | 7/2 | 100 | 4.6388 | 6.317 | 94.457 |
| **$^{77}$Se** | 1/2 | 7.58 | 0.5333 | 5.12 | 76.270 |
| **$^{195}$Pt** | 1/2 | 33.8 | 0.6004 | 5.768 | 85.996 |
| **$^{199}$Hg** | 1/2 | 16.84 | 0.4993 | 4.8154 | 71.309 |

### B9.2. Chemical Shift

Not every proton resonance occurs at the same position. Because the actual magnetic field B at the nucleus is always less than the external field $B_0$, the Larmor precession frequency ($\gamma_0$) varies. This phenomenon is caused by the "superconducting" circulation of electrons in the molecule, which generates a local magnetic field $B_e$ that is opposed to $B_0$($B_e$ is proportional to $B_0$).[84,85] Therefore,

$$B = B_0 - B_e. \qquad \text{B1.36}$$

It is said therefore that the nucleus is shielded from the external magnetic field. The extent of shielding is influenced by many structural features within the molecule and hence is measured as a chemical shift. The scale used to assign peaks in an NMR spectrum is in ppm (parts per million) scale. Chemical shift (δ) is obtained as:

$$Chemical\ shift, \delta = \frac{Frequency\ of\ signal - frequency\ of\ reference}{spectrometer\ frequency} \times 10^6 \qquad \text{B1.37}$$

The relative positions of the resonances in NMR spectra are frequently convenient to describe. For example, a peak with a chemical shift, of 10 ppm is considered to be downfield or deshielded relative to a peak at 5 ppm; alternatively, the peak at 5 ppm is upfield or shielded relative to the peak at 10 ppm.

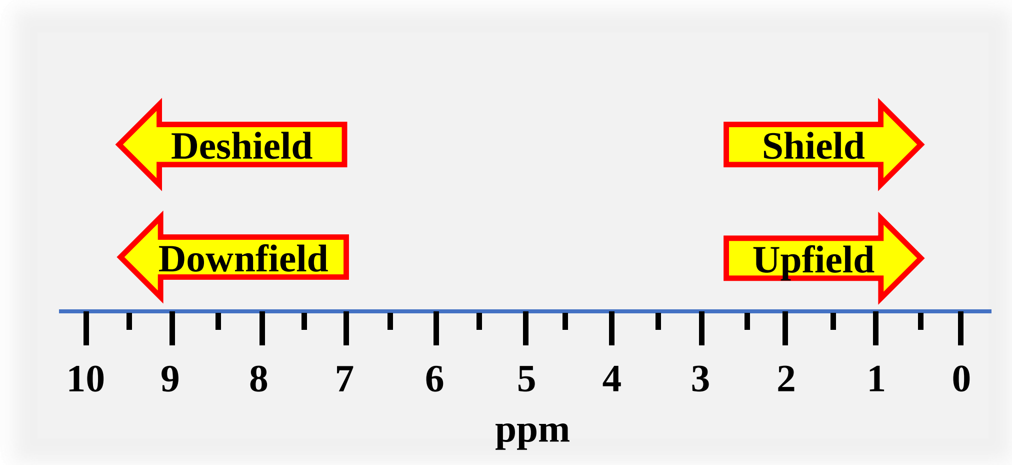

**Figure B1.30:** Representation of a chemical shift in NMR.

### B9.3. $T_1$ Relaxation (Spin-lattice relaxation)

The spin-lattice (or longitudinal) relaxation time $T_1$ is referred to the rate of transfer of energy from the nuclear spin system to the neighbouring molecules (the lattice). This is relaxation in the z-direction and leads to restoration of Boltzmann equilibrium.[86]

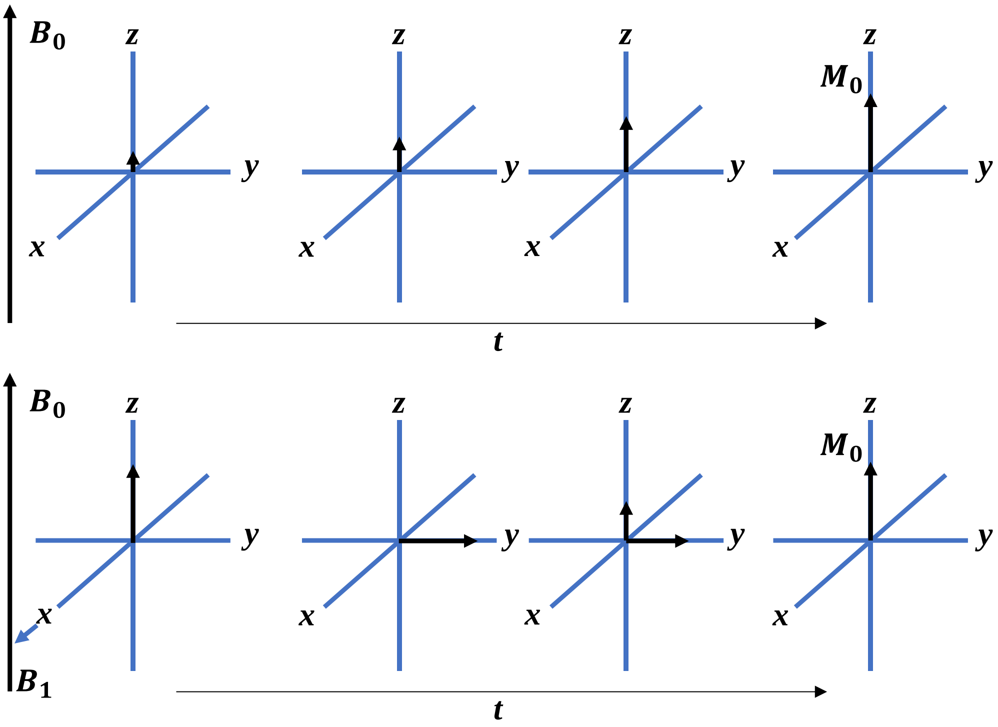

**Figure B1.31:** $T_1$ relaxation processes in NMR

### B9.4. $T_2$ Relaxation (Spin-Spin relaxation)

$T_2$ relaxation is a phenomenon that occurs in NMR spectroscopy and refers to the time it takes for the magnetic moments of the nuclei in a sample to lose their phase coherence. $T_2$ decay provides information about the interactions between the nuclei in a sample and their local environment and is an important parameter in NMR spectroscopy.[86]

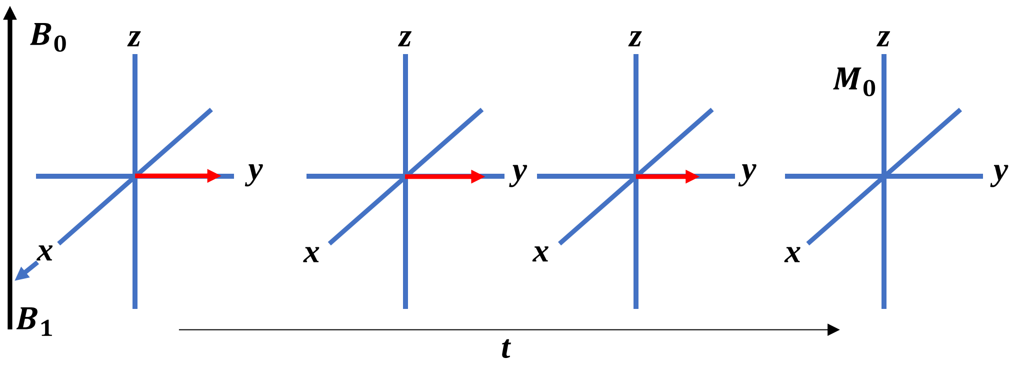

**Figure B1.32:** $T_2$ relaxation processes in NMR

### B9.5. Relaxivity Measurements

In this study, NMR instrument was utilized to examine the S-precursors used in the formation of Ag-chalcogenide QDs. This approach was taken because MRI is also based on the NMR phenomenon.[86–89] The NMR instrument was also utilized to determine the relaxivity measurements in an effort to develop a bimodal NIR-II/MRI contrast agent with tunable fluorescence and high T1 relaxivity. The formation of Gadolinium (III) complex on the surface of the QDs (Gd-QD conjugate) was confirmed through NMR spectroscopy (400 MHz) by observing the change in the chemical shift of water caused by the presence of the paramagnetic center. The difference in the chemical shifts of bulk and bound water ($\Delta\delta$) was 0.3917 ppm for pure ligand, Gd-L (Figure B1.33b)

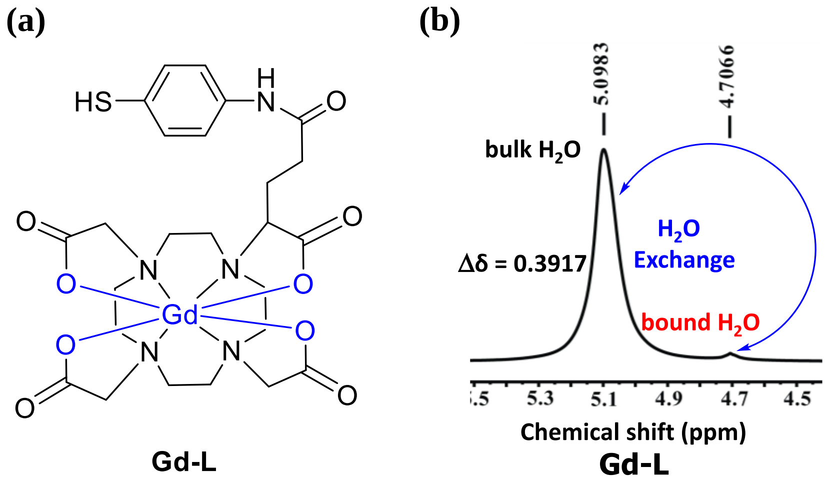
(a)
(b)
HS
H
N
O
O
O
N
N
O
O
Gd
O
O
N
N
O
O
Gd-L
5.0983
4.7066
bulk $H_2O$
$\Delta\delta$ = 0.3917
$H_2O$
Exchange
bound $H_2O$
5.5
5.3
5.1
4.9
4.7
4.5
Chemical shift (ppm)
Gd-L

**Figure B1.33**: (a) The MRI contrast agent (Gd-L) is based on gadolinium ($Gd^{3+}$ ) and has a specific structure (b) The $^1$HNMR spectrum of Gd-L indicates that there is an exchange of water protons between the bound and bulk water of the surrounding area.[54]

After functionalization with two different sized QDs (QD1 and QD2), the distinct change in $\Delta\delta$ was observed for both Gd-QD1 ($\Delta\delta = 0.102$, Figure B1.34b) and Gd-QD2 ($\Delta\delta = 0.0301$, Figure B1.34c) respectively. [54]

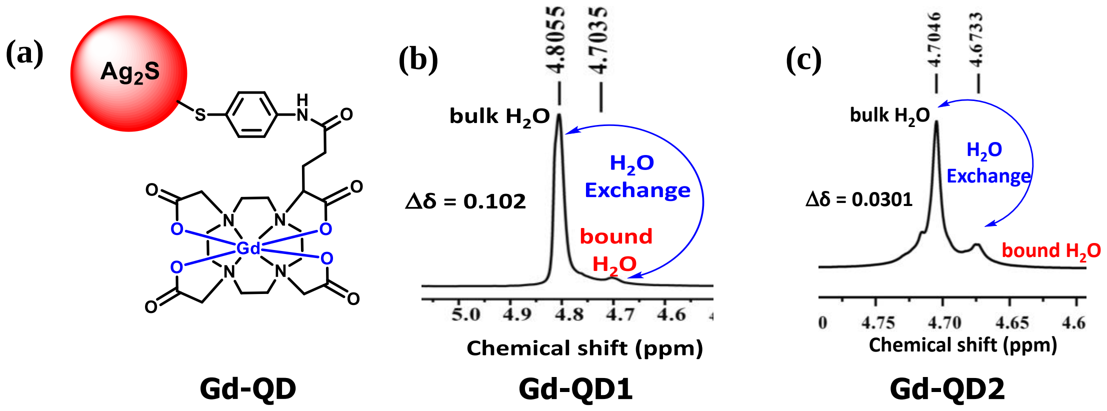
(a)
$Ag_2S$
S
H
N
O
O
O
N
N
O
O
Gd
O
O
N
N
O
O
Gd-QD
(b)
4.8055
4.7035
bulk $H_2O$
$\Delta\delta$ = 0.102
$H_2O$
Exchange
bound
$H_2O$
5.0
4.9
4.8
4.7
4.6
Chemical shift (ppm)
Gd-QD1
(c)
4.7046
4.6733
bulk $H_2O$
$\Delta\delta$ = 0.0301
$H_2O$
Exchange
bound $H_2O$
0
4.75
4.70
4.65
4.6
Chemical shift (ppm)
Gd-QD2

**Figure B1.34:** (a) The configuration of quantum dots (QDs) capped with gadolinium ($Gd^{3+}$) is depicted. (b) The $^1$HNMR spectrum of Gd-QD2 and (c) Gd-QD1 display evidence of water protons exchange between the adjoining bound and surrounding bulk water. [54]

The water relaxivity, expressed in units of $mM^{-1}s^{-1}$ per Gd complex, is a quantitative measure used to determine the efficacy of a contrast agent. This measure is subject to variations based on factors such as magnetic field strength and temperature.[90]

We know,

$$\frac{1}{T_{1(obs)}} = \frac{1}{T_{1(H2O)}} + \frac{1}{T_{1(para)}} \qquad \text{B1.38}$$

where $T_1$(obs) refers to the measured longitudinal relaxation time in seconds, while $T_1$($H_2O$) and $T_1$(para) denote the diamagnetic and paramagnetic water relaxation contributions, respectively, in the absence of paramagnetic ions.[90]

Furthermore, $\frac{1}{T_{1(obs)}} = \frac{1}{T_{1(H2O)}} + r_1[M]$ B1.39

One way to determine the molar concentration of a paramagnetic substance [M] is by analyzing the NMR shift of water protons when the substance is present. Meanwhile, to calculate the concentration of Gd ions, Evan's formula was utilized.[91]

$$[M] = \frac{3\times\Delta\delta}{4\pi\times\chi_M\ 10^3} \qquad \text{B1.40}$$

where, $\Delta\delta$ represents the disparity in chemical shift, measured in parts per million (ppm), between the resonance of the solvent in the presence of a paramagnetic material and the resonance of the pure solvent. On the other hand, magnetic susceptibility, $\chi_M$, which is estimated by employing the Curie equation, refers to the degree of magnetization of a material when subjected to an external magnetic field.[92]

$$\mu_{eff} = 2.83\sqrt{(\chi_M \times T)} \qquad \text{B1.41}$$

where, $\mu_{eff}$ is magnetic moment (for $Gd^{3+}$ , $\mu_{eff}$ =7.94)[93,94] and T is the temperature.

To calculate relaxivity per **QD** the concentration of QD is required. We determined the concentration of CQDs i.e., [**QD**] using Lambert-Beer’s law,

$$A=\varepsilon\ [\boldsymbol{QD}]\ l \qquad \text{B1.42}$$

where, the absorbance (measured through UV-vis spectroscopy) of $Ag_2S$ CQDs is denoted as A, and their molar extinction coefficient is represented by $\varepsilon$. The molar extinction coefficient was determined at a wavelength of 450 nm, using the Ricard equation.[95] To calculate the molar extinction coefficient, the optical constants of monoclinic $Ag_2S$ QDs with a band gap of 1.08 eV were required. These constants were theoretically calculated using DFT and are explained in detail in Chapter-4. The faster the longitudinal relaxation rate ($T_1$), the stronger is the signal intensity[96]. $T_1$ is inversely related to the relaxation rate ($R_1 = 1/T_1$). For Gd-L: Relaxivity $r_1 = 5.36$ $mM^{-1}s^{-1}$; Gd-QD1: $r_1 = 7.75$ $mM^{-1}s^{-1}$ and Gd-QD1: $r_1 = 8.27$ $mM^{-1}s^{-1}$.

### B9.6. Sample preparation and Instrumentation

The $^1H$ NMR, $^{13}C$ NMR of all the compounds mentioned in this thesis were recorded in solvents such $CDCl_3$ or $D_2O$, or DMSO-$d_6$. Multiplicities were shown as follows: s (singlet), d (doublet), t (triplet), q (quartet), and m (multiplet). The solid samples were tested for their solubility in the desired solvents and mixed in a glass vial. Using a glass Pasteur pipette, the sample was transferred to the NMR tube. The NMR tube was then labeled and scanned in the NMR instrument. For $T_1$ measurements, A 1mm diameter capillary tube was filled with suspensions of Gd-QD1 and Gd-QD2, sealed at the top with parafilm. This capillary tube was then placed within an NMR tube in a $D_2O$ environment. All the measurements were performed on a Bruker Avance III (400 MHz).

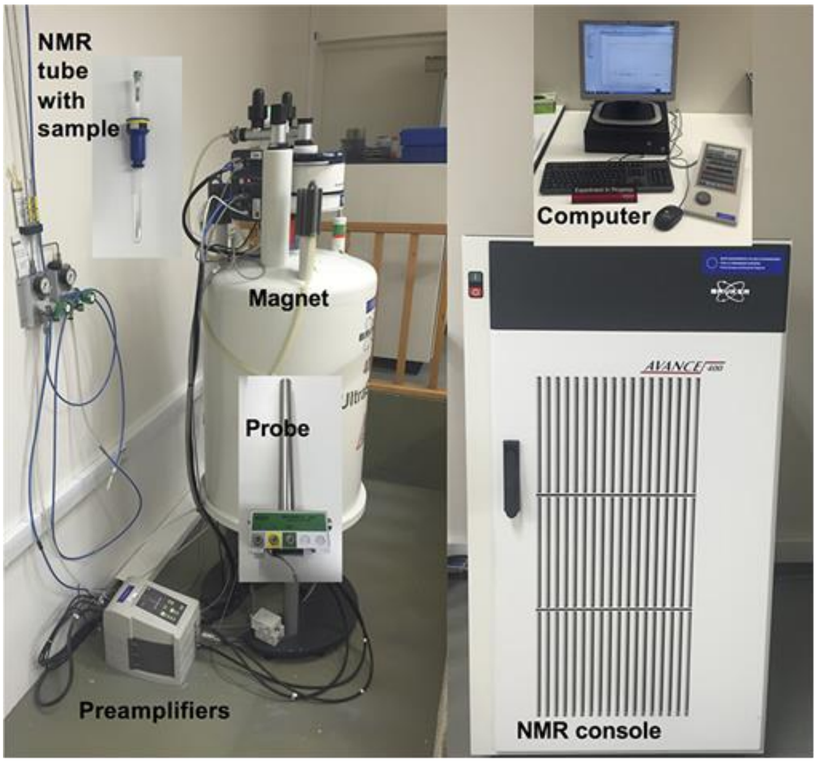
NMR
tube
with
sample
Magnet
Probe
Preamplifiers
Computer
NMR console
AVANCE 400

**Figure B1.35:** Photograph of Bruker Avance III (400 MHz) NMR instrument.

## B10. References

(1) Behzadi, S.; Ghasemi, F.; Ghalkhani, M.; Ashkarran, A. A.; Akbari, S. M.; Pakpour, S.; Hormozi-Nezhad, M. R.; Jamshidi, Z.; Mirsadeghi, S.; Dinarvand, R.; Atyabi, F.; Mahmoudi, M. Determination of Nanoparticles Using UV-Vis Spectra. *Nanoscale* **2015**, *7*, 5134–5139.

(2) Alim-Al-Razy, M.; Asik Bayazid, G. M.; Rahman, R. U.; Bosu, R.; Shamma, S. S. Silver Nanoparticle Synthesis, UV-Vis Spectroscopy to Find Particle Size and Measure Resistance of Colloidal Solution. *J Phys Conf Ser* **2020**, *1706*, 012020–012209.

(3) Tamang, S. Synthèse et Fonctionnalisation Des Nanocristaux Émettant Dans Le Proche Infrarouge Pour l’imagerie Biologique, PhD thesis, Université de Grenoble, Français., **2011**.

(4) Jiang, P.; Tian, Z.-Q.; Zhu, C.-N.; Zhang, Z.-L.; Pang, D.-W. Emission-Tunable Near-Infrared Ag2S Quantum Dots. *Chemistry of Materials* **2012**, *24*, 5137–5139.

(5) Chan, W. C. W.; Maxwell, D. J.; Gao, X.; Bailey, R. E.; Han, M.; Nie, S. Luminescent Quantum Dots for Multiplexed Biological Detection and Imaging. *Curr Opin Biotechnol* **2002**, *13*, 40–46.

(6) Pawan M.V Raja. Photoluminescence, Phosphorescence, and Fluorescence Spectroscopy. *Analytical_Chemistry/Physical Methods in Chemistry and Nano Science (Barron)* **2022,** *18*, 241–248.

(7) Ellingson, R. J.; Beard, M. C.; Johnson, J. C.; Yu, P.; Micic, O. I.; Nozik, A. J.; Shabaev, A.; Efros, A. L. Highly Efficient Multiple Exciton Generation in Colloidal PbSe and PbS Quantum Dots. *Nano Lett* **2005**, *5*, 865–871.

(8) Ghobadi, N. Band Gap Determination Using Absorption Spectrum Fitting Procedure. *Int Nano Lett* **2013**, *3*, 2015–2020

(9) Zhang, Y.; Liu, Y.; Li, C.; Chen, X.; Wang, Q. Controlled Synthesis of Ag2S Quantum Dots and Experimental Determination of the Exciton Bohr Radius. *Journal of Physical Chemistry C* **2014**, *118*, 4918–4923.

(10) Wu, X.; Trinh, M. T.; Niesner, D.; Zhu, H.; Norman, Z.; Owen, J. S.; Yaffe, O.; Kudisch, B. J.; Zhu, X.-Y. Trap States in Lead Iodide Perovskites. *J Am Chem Soc* **2015**, *137*, 2089–2096.

(11) Moiz, S. A.; Khan, I. A.; Younis, W. A.; Karimov, K. S. Space Charge–Limited Current Model for Polymers. *Conducting Polymers* **2016**, *15*, 854–860.

(12) Vatankhah, C.; Saki, M.; Jafargholinejad, S. Theoretical and Experimental Investigation of Quantum Confinement Effect on the Blue Shift in Semiconductor Quantum Dots. *Oriental Journal of Chemistry* **2015**, *31*, 907–912.

(13) I. FILIKHIN, S. G. M. A. B. V. QUANTUM MECHANICS OF SEMICONDUCTOR QUANTUM DOTS AND RINGS. *North Carolina Central University, 1801 Fayetteville St. Durham, NC 27707, USA.*

(14) Yu, W. W.; Qu, L.; Guo, W.; Peng, X. Experimental Determination of the Extinction Coefficient of CdTe, CdSe, and CdS Nanocrystals. *Chemistry of Materials* **2003**, *15*, 2854–2860.

(15) Reiss, P.; Protière, M.; Li, L. Core/Shell Semiconductor Nanocrystals. *Small* **2009**, *5*, 154–168.

(16) Parra, G. G.; Ferreira, L. P.; Gonçalves, P. J.; Sizova, S. v.; Oleinikov, V. A.; Morozov, V. N.; Kuzmin, V. A.; Borissevitch, I. E. Stimulation of Cysteine-Coated CdSe/ZnS Quantum Dot Luminescence by Meso-Tetrakis (p-Sulfonato-Phenyl) Porphyrin. *Nanoscale Res Lett* **2018**, *13*, 40–48

(17) Ricard, D.; Ghanassi, M.; Schanne-Klein, M. C. Dielectric Confinement and the Linear and Nonlinear Optical Properties of Semiconductor-Doped Glasses. *Opt Commun* **1994**, *108*, 311–318.

(18) Xia, C.; Wu, W.; Yu, T.; Xie, X.; van Oversteeg, C.; Gerritsen, H. C.; de Mello Donega, C. Size-Dependent Band-Gap and Molar Absorption Coefficients of Colloidal $CuInS_2$ Quantum Dots. *ACS Nano* **2018**, *12*, 8350–8361.

(19) Moreels, I.; Lambert, K.; Smeets, D.; de Muynck, D.; Nollet, T.; Martins, J. C.; Vanhaecke, F.; Vantomme, A.; Delerue, C.; Allan, G.; Hens, Z. Size-Dependent Optical Properties of Colloidal PbS Quantum Dots. *ACS Nano* **2009**, *3*, 3023–3030.

(20) Oskam, G.; Hu, Z.; Penn, R. L.; Pesika, N.; Searson, P. C. Coarsening of Metal Oxide Nanoparticles. *Phys Rev E* **2002**, *66*, 011403–011409.

(21) Tauc, J.; Menth, A. States in the Gap. *J Non Cryst Solids* **1972**, *8* (1), 569–585.

(22) Mott, N. D. E. Electron Processes in Non-Crystalline Materials. Clarendon. *Oxford* **1979**. *10*, 69–67.

(23) Vogel, D. J.; Kilin, D. S. First-Principles Treatment of Photoluminescence in Semiconductors. *The Journal of Physical Chemistry C* **2015**, *119* (50), 27954–27964.

(24) Teets, T. S. *Photoluminescence*; American Chemical Society: Washington, DC, USA, **2021**, *8*, 1122–1128.

(25) Weerawardene, K. L. D. M.; Aikens, C. M. Theoretical Insights into the Origin of Photoluminescence of Au $_{25}$ (SR) $_{18}$ $^{-}$ Nanoparticles. *J Am Chem Soc* **2016**, *138*, 11202–11210.

(26) Yuan, L.-D.; Deng, H.-X.; Li, S.-S.; Wei, S.-H.; Luo, J.-W. Unified Theory of Direct or Indirect Band-Gap Nature of Conventional Semiconductors. *Phys Rev B* **2018**, *98* (24), 245203–245210.

(27) Gfroerer, T. H. Photoluminescence in Analysis of Surfaces and Interfaces. In *Encyclopedia of Analytical Chemistry*; John Wiley & Sons, Ltd: Chichester, UK, **2006**, *8*, 503–510.

(28) William D. Callister, J. Materials Science and Engineering an Introduction. *Department of Metallurgical Engineering the University of Utah* **2007,** *7*, 108–145.

(29) Segets, D.; Lucas, J. M.; Klupp Taylor, R. N.; Scheele, M.; Zheng, H.; Alivisatos, A. P.; Peukert, W. Determination of the Quantum Dot Band Gap Dependence on Particle Size from Optical Absorbance and Transmission Electron Microscopy Measurements. *ACS Nano* **2012**, *6*, 9021–9032.

(30) Li, W.; Li, K.; Zhao, X.; Liu, C.; Coudert, F.-X. Defective Nature of CdSe Quantum Dots Embedded in Inorganic Matrices. *J Am Chem Soc* **2022**, *144*, 11296–11305.

(31) Carmesin, C.; Olbrich, F.; Mehrtens, T.; Florian, M.; Michael, S.; Schreier, S.; Nawrath, C.; Paul, M.; Höschele, J.; Gerken, B.; Kettler, J.; Portalupi, S. L.; Jetter, M.; Michler, P.; Rosenauer, A.; Jahnke, F. Structural and Optical Properties of InAs/(In)GaAs/GaAs Quantum Dots with Single-Photon Emission in the Telecom C-Band up to 77 K. *Phys Rev B* **2018**, *98*, 125407–125409.

(32) Haram, S. K.; Kshirsagar, A.; Gujarathi, Y. D.; Ingole, P. P.; Nene, O. A.; Markad, G. B.; Nanavati, S. P. Quantum Confinement in CdTe Quantum Dots: Investigation through Cyclic Voltammetry Supported by Density Functional Theory (DFT). *The Journal of Physical Chemistry C* **2011**, *115*, 6243–6249.

(33) Svit, K. A.; Zarubanov, A. A.; Duda, T. A.; Trubina, S. v.; Zvereva, V. v.; Fedosenko, E. v.; Zhuravlev, K. S. Crystal Structure and Predominant Defects in CdS Quantum Dots Fabricated by the Langmuir–Blodgett Method. *Langmuir* **2021**, *37*, 5651–5658.

(34) Nuntawong, N.; Huang, S.; Jiang, Y. B.; Hains, C. P.; Huffaker, D. L. Defect Dissolution in Strain-Compensated Stacked InAs⁄GaAs Quantum Dots Grown by Metalorganic Chemical Vapor Deposition. *Appl Phys Lett* **2005**, *87*, 113105–113109.

(35) Karpov, S. v.; Isaev, I. L.; Gavrilyuk, A. P.; Gerasimov, V. S.; Grachev, A. S. Defects of Colloidal Crystals. *Colloid Journal* **2009**, *71*, 329–339.

(36) Tamang, S.; Beaune, G.; Texier, I.; Reiss, P. Aqueous Phase Transfer of InP/ZnS Nanocrystals Conserving Fluorescence and High Colloidal Stability. *ACS Nano* **2011**, *5*, 9392–9402.

(37) M.A. El-Sayed, R. E. C. T. E.-Sayed. X-Ray Diffraction Studies of Colloidal CdS and CdSe Quantum Dots. *J Appl Phys* **1997**, *81*, 5244–5249.

(38) S. Link, M. A. E.-S. Structural Characterization of Colloidal Quantum Dots Using X-Ray Diffraction. *Journal of Physical Chemistry B* **1998**, *102*, 4407–4413.

(39) Eckert, M. Disputed Discovery: The Beginnings of X-Ray Diffraction in Crystals in 1912 and Its Repercussions. *Zeitschrift für Kristallographie* **2012**, *227*, 27–35.

(40) Stanjek, H.; Häusler, W. Basics of X-Ray Diffraction. *Hyperfine Interact* **2004**, *154*, 107–119.

(41) Christopher Hammond; The Basics of Crystallography and Diffraction, Second Edition. *Oxford Science Publications,* **2001,** *7,* 132–138.

(42) Vicente, R. A.; Neckel, I. T.; Sankaranarayanan, S. K. R. S.; Solla-Gullon, J.; Fernández, P. S. Bragg Coherent Diffraction Imaging for *In Situ* Studies in Electrocatalysis. *ACS Nano* **2021***, 15*, 6129–6146.

(43) Azaroff, L. v. Elements of X-Ray Crystallography, *Mc Graw Hill Book Co.,New York,* **1968**, *9*, 642–649.

(44) Bunaciu, A. A.; Udriştioiu, E. gabriela; Aboul-Enein, H. Y. X-Ray Diffraction: Instrumentation and Applications. *Crit Rev Anal Chem* **2015**, *45*, 289–299.

(45) W. I. F. David, K. S. L. B. M. Ch. B. Structure Determination from Powder Diffraction Data. *Oxford; New York: Oxford University Press*, **2001**, *5*, 179–185.

(46) Patterson, A. L. The Scherrer Formula for X-Ray Particle Size Determination. *Physical Review* **1939**, *56*, 978–982.

(47) J. Michael Hollas. Modern Spectroscopy; **2004,** *6*, 815–819.

(48) Nakamoto, K. Theory of Normal Vibrations. *Infrared Raman Spectra Inorg. Coord. Compd.* **2009**, *6*, 143–147.

(49) Ismail, A. A.; van de V. F. R.; S. J. Chapter 4 Fourier Transform Infrared Spectroscopy: Principles and Applications. *Tech. Instrum. Anal. Chem.* **1997**, *18*, 93–139.

(50) Khan, S. A.; Khan, S. B.; Khan, L. U.; Farooq, A.; Akhtar, K.; Asiri, A. M. Fourier Transform Infrared Spectroscopy: Fundamentals and Application in Functional Groups and Nanomaterials Characterization. In *Handbook of Materials Characterization*; Springer International Publishing: Cham, **2018,** *5*, 317–344.

(51) Harris, D. C., and M. D. Bertolucci. Ymmetry and Spectroscopy: An Introduction to Vibrational and Electronic Spectroscopy. *New York: Dover Publications* **1989,** *55*, 213–220.

(52) Housecroft, C. E., and A. G. Sharpe. Inorganic Chemistry. *Harlow: Pearson Education* **2008,** *6*, 109–115.

(53) Javadzadeh, Y.; Hamedeyaz, S. Floating Drug Delivery Systems for Eradication of Helicobacter Pylori in Treatment of Peptic Ulcer Disease. In *Trends in Helicobacter pylori Infection*; InTech, **2014**, *57*, 9178–9182.

(54) Bhardwaj, K.; Pradhan, S.; Basel, S.; Clarke, M.; Brito, B.; Thapa, S.; Roy, P.; Borthakur, S.; Saikia, L.; Shankar, A.; Stasiuk, G. J.; Pariyar, A.; Tamang, S. Tunable NIR-II Emitting Silver Chalcogenide Quantum Dots Using Thio/Selenourea Precursors: Preparation of an MRI/NIR-II Multimodal Imaging Agent. *Dalton Transactions* **2020**, *49*, 15425–15432.

(55) Bottom, R. Thermogravimetric Analysis. In *Principles and Applications of Thermal Analysis*; Blackwell Publishing Ltd: Oxford, UK, **2018**, *9*, 817–828.

(56) Ng, H. M.; Saidi, N. M.; Omar, F. S.; Ramesh, K.; Ramesh, S.; Bashir, S. Thermogravimetric Analysis of Polymers. In *Encyclopedia of Polymer Science and Technology*; John Wiley & Sons, Inc.: Hoboken, NJ, USA, **2018**, *4*, 1–29.

(57) Prof Dr. Zahraa Salim. Al-Garawi. The Principle of Thermogravimetric analysis and Its Applications. *Biochemistry, Biophysics* **2001**, *49*, 17–22.

(58) Saadatkhah, N.; Carillo Garcia, A.; Ackermann, S.; Leclerc, P.; Latifi, M.; Samih, S.; Patience, G. S.; Chaouki, J. Experimental Methods in Chemical Engineering: Thermogravimetric Analysis—TGA. *Can J Chem Eng* **2020**, *98,* 34–43.

(59) Sharp, J. H.; Manley, T. R. Thermal Analysis. *Proceedings of the Society for Analytical Chemistry* **1971**, *8*, 112–119.

(60) Coats, A. W.; Redfern, J. P. Thermogravimetric Analysis. A Review. *Analyst* **1963**, *88* 1053–1058.

(61) Simon, J. Introduction to Thermal Analysis Techniques and Applications; *Brown, M. E., Ed.; Kluwer Academic Publishers* **2001**, *5*, 2111–2119.

(62) Elliott, E. T. Aggregate Structure and Carbon, Nitrogen, and Phosphorus in Native and Cultivated Soils. *Soil Science Society of America Journal* **1986**, *50*, 627–633.

(63) David B. Williams and C. Barry Carter. Transmission Electron Microscopy. *Plenum* **1996**, *5*, 726–743.

(64) Fraundorf, P.; Qin, W.; Moeck, P.; Mandell, E. Making Sense of Nanocrystal Lattice Fringes. *J Appl Phys* **2005**, *98*, 114308–114309.

(65) Buseck, P. R. Chapter 1. PRINCIPLES OF TRANSMISSION ELECTRON MICROSCOPY. In *Minerals and Reactions at the Atomic Scale*; De Gruyter, **1992**, *5*, 15–32.

(66) Stepan Nebaba. Patterns Detection in SAED Images of Transmission Electron Microscopy*. *Tomsk Polytechnic University, Tomsk, Russia* **2020**, *8*, 2115–2132.

(67) David J. Morgan. X-Ray Photoelectron Spectroscopy (XPS): An Introduction. *Cardiff Catalysis Institute, School of Chemistry, Cardiff University, Cardiff. CF10 3AT* **2010**, *55*, 1567–1580.

(68) Baer, D. R.; Artyushkova, K.; Richard Brundle, C.; Castle, J. E.; Engelhard, M. H.; Gaskell, K. J.; Grant, J. T.; Haasch, R. T.; Linford, M. R.; Powell, C. J.; Shard, A. G.; Sherwood, P. M. A.; Smentkowski, V. S. Practical Guides for X-Ray Photoelectron Spectroscopy: First Steps in Planning, Conducting, and

Reporting XPS Measurements. *Journal of Vacuum Science & Technology A* **2019**, *37*, 031401–031420.

(69) Greczynski, G.; Hultman, L. X-Ray Photoelectron Spectroscopy: Towards Reliable Binding Energy Referencing. *Prog Mater Sci* **2020**, *107*, 100591–100599.

(70) Grosvenor, A. P.; Kobe, B. A.; Biesinger, M. C.; McIntyre, N. S. Investigation of Multiplet Splitting of Fe 2p XPS Spectra and Bonding in Iron Compounds. *Surface and Interface Analysis* **2004**, *36*, 1564–1574.

(71) Roger Smart, S. M. M. R. X-Ray Photoelectron Spectroscopy. *Department of Physics and Materials Science Department of Physics and Materials Science City University of Hong Kong City University of Hong Kong Surface Science Western, UWO* **2001,** *3*, 4–55.

(72) Shirley, D. A. High-Resolution X-Ray Photoemission Spectrum of the Valence Bands of Gold. *Phys Rev B* **1972**, *5*, 4709–4714.

(73) Hashimoto, S.; Tanaka, A. Alteration of Ti 2p XPS Spectrum for Titanium Oxide by Low-Energy Ar Ion Bombardment. *Surface and Interface Analysis* **2002**, *34*, 262–265.

(74) Greczynski, G.; Hultman, L. X-Ray Photoelectron Spectroscopy: Towards Reliable Binding Energy Referencing. *Prog Mater Sci* **2020**, *107*, 10059–10060.

(75) Satheeshkumar, E.; Makaryan, T.; Melikyan, A.; Minassian, H.; Gogotsi, Y.; Yoshimura, M. One-Step Solution Processing of Ag, Au and Pd@MXene Hybrids for SERS. *Sci Rep* **2016**, *6*, 32049–32051.

(76) Moeini, B.; Linford, M. R.; Fairley, N.; Barlow, A.; Cumpson, P.; Morgan, D.; Fernandez, V.; Baltrusaitis, J. Definition of a New (Doniach-Sunjic-Shirley) Peak Shape for Fitting Asymmetric Signals Applied to Reduced Graphene Oxide/Graphene Oxide XPS Spectra. *Surface and Interface Analysis* **2022**, *54*, 67–77.

(77) M.I. Boden, J. G. T. Relative Sensitivity Factor Determination for X-Ray Photoelectron Spectroscopy Analysis of Silver and Selenium Using Thin-Film Standards. *J Electron Spectros Relat Phenomena* **2010**, *178*, 95–102.

(78) J.S.J. Hsu, T. K. H. C. H. C. C. H. Lin. Determination of Relative Sensitivity Factors for the Quantitative Analysis of Selenium and Silver in Thin Films Using X-Ray Photoelectron Spectroscopy. *J Anal At Spectrom* **2005**, *20*, 470–475.

(79) Tampieri, A.; Szabó, M.; Medina, F.; Gulyás, H. A Brief Introduction to the Basics of NMR Spectroscopy and Selected Examples of Its Applications to Materials Characterization. *Physical Sciences Reviews* **2021**, *6*, 2019-0086.

(80) Marion, D. An Introduction to Biological NMR Spectroscopy. *Molecular & Cellular Proteomics* **2013**, *12*, 3006–3025.

(81) Purcell, E. M.; Torrey, H. C.; Pound, R. v. Resonance Absorption by Nuclear Magnetic Moments in a Solid. *Physical Review* **1946**, *69*, 37–38.

(82) Vernet, R. du; Boekelheide, V. Nuclear Magnetic Resonance Spectroscopy. Ring-Current Effects on Carbon-13 Chemical Shifts. *Proceedings of the National Academy of Sciences* **1974**, *71*, 2961–2964.

(83) Gerothanassis, I. P.; Troganis, A.; Exarchou, V.; Barbarroussoub, K. NMR Spectroscopy: Basic Principle and phenomena, and their Application to chemistry, biology and medicine. *Chem. Educ. Res. Pract.* **2002**, *3* (2), 229–252.

(84) Babij, N. R.; McCusker, E. O.; Whiteker, G. T.; Canturk, B.; Choy, N.; Creemer, L. C.; Amicis, C. V. de; Hewlett, N. M.; Johnson, P. L.; Knobelsdorf, J. A.; Li, F.; Lorsbach, B. A.; Nugent, B. M.; Ryan, S. J.; Smith, M. R.; Yang, Q. NMR Chemical Shifts of Trace Impurities: Industrially Preferred Solvents Used in Process and Green Chemistry. *Org Process Res Dev* **2016**, *20*, 661–667.

(85) Nerli, S.; McShan, A. C.; Sgourakis, N. G. Chemical Shift-Based Methods in NMR Structure Determination. *Prog Nucl Magn Reson Spectrosc* **2018**, *106–107*, 1–25.

(86) Chatell, M.; Darcel, F.; de Certaines, J.; Benoist, L.; Bernard, A. T1 and T2 Proton Nuclear Magnetic Resonance (N.M.R.) Relaxation Times in Vitro and Human Intracranial Tumours. *J Neurooncol* **1986**, *3*, 315–321.

(87) Solomon, I. Relaxation Processes in a System of Two Spins. *Physical Review* **1955**, *99*, 559–565.

(88) Bloembergen, N.; Morgan, L. O. Proton Relaxation Times in Paramagnetic Solutions. Effects of Electron Spin Relaxation. *J Chem Phys* **1961**, *34*, 842–850.

(89) Guo, K.; Berezin, M. Y.; Zheng, J.; Akers, W.; Lin, F.; Teng, B.; Vasalatiy, O.; Gandjbakhche, A.; Griffiths, G. L.; Achilefu, S. Near Infrared-Fluorescent and Magnetic Resonance Imaging Molecular Probe with High T1 Relaxivity for in Vivo Multimodal Imaging. *Chemical Communications* **2010**, *46*, 3705–3715.

(90) Gutiérrez-Mejía, F.; Ruiz-Suárez, J. C. AC Magnetic Susceptibility at Medium Frequencies Suggests a Paramagnetic Behavior of Pure Water. *J Magn Magn Mater* **2012**, *324*, 1129–1132.

(91) Evans, D. F. The Determination of the Paramagnetic Susceptibility of Substances in Solution by Nuclear Magnetic Resonance. *J. Chem. Soc.* **1959**, *24*, 2003–2005.

(92) Malerich, C.; Ruff, P. K. Demonstrating and Measuring Relative Molar Magnetic Susceptibility Using a Neodymium Magnet. *J Chem Educ* **2004**, *81*, 1155–1160.

(93) Sitharaman, B.; Jacobson, B. D.; Wadghiri, Y. Z.; Bryant, H.; Frank, J. The Magnetic, Relaxometric, and Optical Properties of Gadolinium-Catalyzed Single Walled Carbon Nanotubes. *J Appl Phys* **2013**, *113*, 134308–134310.

(94) Si, P. Z.; Škorvánek, I.; Kováč, J.; Geng, D. Y.; Zhao, X. G.; Zhang, Z. D. Structure and Magnetic Properties of Gd Nanoparticles and Carbon Coated Gd/GdC2 Nanocapsules. *J Appl Phys* **2003**, *94*, 6779–6784.

(95) Ricard, D.; Ghanassi, M.; Schanne-Klein, M. C. Dielectric Confinement and the Linear and Nonlinear Optical Properties of Semiconductor-Doped Glasses. *Opt Commun* **1994**, *108*, 160–167.

(96) Li, W.; Grgac, K.; Huang, A.; Yadav, N.; Qin, Q.; van Zijl, P. C. M. Quantitative Theory for the Longitudinal Relaxation Time of Blood Water. *Magn Reson Med* **2016**, *76*, 270–281.

# *Annexure C: List of Figures, Schemes, Tables*

## *C1. List of Figures*

| **Figure 1.1** | The Structure and Properties of QDs (a) A Core-Shell QD Cartoon Illustration and the Lattice Structure of CdSe and ZnS and (b) Photograph and Photoluminescence of QDs Samples with Different Diameters under Ultraviolet Illumination Demonstrating Size-Tunable Emission. | **Page No.**<br>5 |
|---|---|---|
| **Figure 1.2** | Nucleation and growth of semiconductor nanocrystals; (a) Schematic diagram of a colloidal semiconductor nanocrystal; (b) Classical nucleation theory has shown using a plot of Gibbs free energy against the radius of the nucleus; (d) Plot of concentration against time showing the La Mer model for burst nucleation; and (e) Schematic diagram showing the process of Ostwald ripening. | 6 |
| **Figure 1.3** | Schematic representation Bio-functionalisation of QDs. | 32 |
| **Figure 2.1** | Representative structures of substituted thiourea (a) thiocarbamate (b) dithiocarbamate (c) selenourea (d). Here R is the substituent group outlined in Figure 2.2. | 58 |
| **Figure 2.2** | Synthesis of a wide range of thiourea, thiocarbamate, dithiocarbamate and selenourea derivatives. | 59 |
| **Figure 2.3** | (a) General reaction for the synthesis of $Ag_2S/Se$ NCs. (b) The mechanism for the formation of $Ag_2S/Se$ NCs *via* a nucleophilic attack on $Ag^+$ by the precursor through the C=S bond. | 60 |
| **Figure 2.4** | (a) PL spectra of as-prepared $Ag_2S$ NCs produced from thiourea precursors (3a-g) and (b) $Ag_2S/Se$ NCs synthesized from thiocarbamate (5a-c), dithiocarbamate (7a-c), and selenourea derivatives with tunable emission wavelength (9a-b). | 62 |
| **Figure 2.5** | TGA micrographs of precursors (a) 3c and (a) 3e showing weight % vs temperature profile (black line) and its derivative (red line). Decomposition temperature of 3c is 145 °C, while that of 3e is 150 °C. | 63 |

| | | |
|---|---|---|
| **Figure 2.6** | (a) The reaction of precursor, 3b with Ag(I) at 120 °C (black) and 150 °C (red). (b) $Ag_2S$ NCs synthesized from precursor, 3a at 150 °C exhibiting a temporal evolution of the PL emission peak. The peak saturates after 90 minutes (dotted dark blue). | 64 |
| **Figure 2.7** | Reactivity of the substituents (R= O, Me, H, and $NO_2$) at the *para* position of the precursor. | 65 |
| **Figure 2.8** | (a) PL spectra of $Ag_2S$ QDs synthesized from thiourea precursors (3a–e) consisting of different substituents at the para position of the phenyl ring (H, *p*–Me, *p*–OMe, *p*–I, and *p*–$NO_2$) b) A linear correlation between the PL emission wavelength ($\lambda_{max}$) and corresponding Hammett constants (σ) for *para* substituents. | 66 |
| **Figure 2.9** | (a) TEM micrograph of 2.2 ± 0.52 nm QD1 (b) the corresponding SAED pattern (c) the size distribution curve and (d) HRTEM image showing lattice fringes. | 75 |
| **Figure 2.10** | (a) TEM micrograph of 4.2 ± 1.1 nm QD2 (b) the corresponding SAED pattern (c) the size distribution curve and (d) HRTEM image showing lattice fringes. | 76 |
| **Figure 2.11** | XRD spectra of monoclinic a) QD1 and b) QD2. The bars indicate the positions of standard monoclinic $Ag_2S$. | 77 |
| **Figure 2.12** | FTIR Spectra $Ag_2S$ NCs. | 78 |
| **Figure 2.13** | XPS spectra of $Ag_2S$ NCs are presented in the figure, showing: (a) the survey scan; (b) the C 1s spectrum which was calibrated at 284.8 eV; (c) the Ag 3d core level spectrum; and (d) the S 2p binding energy spectrum. | 79 |
| **Figure 2.14** | The S 2p core-level XPS spectrum of deconvoluted $Ag_2S$ NCs shows two distinct chemical environments. The first corresponds to S-Ag, which represents the $Ag_2S$ NCs, and the second corresponds to S-H, which represents the ligand. | 80 |
| **Figure 2.15** | XPS spectra of $Ag_2Se$ NCs: (a) the survey analysis; (b) 3d Ag; (c) S 2p and (d) Se 3d spectra. | 81 |
| **Figure 3.1** | Various forms of *L*-cysteine at different pH values. | 105 |

| | | |
|---|---|---|
| **Figure 3.2** | Phase transfer of DDT-capped $Ag_2S$ QDs from organic phase (chloroform) to aqueous phase using L-cysteine at pH ~9. | 105 |
| **Figure 3.3** | FTIR spectra of phase transferred QDs from organic to aqueous phase (QD1 and QD2). | 105 |
| **Figure 3.4** | PL and QY results of $Ag_2S$ QDs before and after phase transfer from organic to the aqueous phase. | 106 |
| **Figure 3.5** | XRD of $Ag_2S$ NCS before and after the phase transfer from organic to the aqueous phase. | 107 |
| **Figure 3.6** | (a) UV-absorption spectrum of aqueous $Ag_2S$ QDs at different pH solutions (b) PL spectra of aqueous $Ag_2S$ QDs in different pH solutions. | 109 |
| **Figure 3.7** | (a) UV-absorption spectra of aqueous $Ag_2S$ NCs ($\lambda_{em}$ ~1065 nm, $\lambda_{abs}$ ~ 921 nm) measured on days 1, 15, and 28. (b) PL emission of the same aqueous $Ag_2S$ NCs measured on days 1, 15, and 28. (c) Photographs of colloidal solutions of $Ag_2S$ NCs taken on different days. | 110 |
| **Figure 3.8** | XRD spectra $Ag_2S$ NCs in aqueous medium monitored for 1 month. | 111 |
| **Figure 3.9** | a) UV-visible absorption spectra of $Ag_2S$ QDs for 2 hrs. Samples QD1 and QD2 are described in section 2.1, $QD_{1065}$ and $QD_{1133}$ denote $Ag_2S$ NCs emitting at 1065 and 1133 nm respectively. (b) Corresponding PL emission spectra of the $Ag_2S$ QDs. (c) These $Ag_2S$ NCs (QD1, QD2, $QD_{1065,}$ and $QD_{1133}$) were photo-irradiated under blue LED and PL emission was monitored at a different time for 2h. | 112 |
| **Figure 3.10** | (a) FTIR spectra of DDT (black) and DDT-capped $Ag_2S/ZnS$ core/shell NCs (red) showing a distinct shift of C-H stretching frequency confirming the surface passivation of $Ag_2S$ NCs by DDT. (b) A shift in C-H stretching frequency of $Ag_2S$ NCs (red) and $Ag_2S/ZnS$ core/shell NCs (black). | 114-115 |
| **Figure 3.11** | (a) PL emission spectra of $Ag_2S$ and $Ag_2S/ZnS$ core/shell NCs showing a 2-fold increase in QY. (b) UV-vis absorption spectra | 116 |

| | | |
|---|---|---|
| | $Ag_2S$ and $Ag_2S/ZnS$ core/shell NCs showing first excitonic peak. | |
| **Figure 3.12** | (a) TEM micrograph of 2.5 ± 0.8 nm of $Ag_2S/ZnS$ core-shell NCs (b) HRTEM image showing lattice fringes (c) the size distribution curve. | 116 |
| **Figure 3.13** | b) XRD patterns of the $Ag_2S$ QDs (black line) and $Ag_2S/ZnS$ core/shell QDs (royal blue line). | 117 |
| **Figure 3.14** | (a) FTIR spectra of $Ag_2S/ZnS$ core/shell QDs before and after phase transfer. (b) PL spectra showing QY of $Ag_2S/ZnS$ core/shell QDs before and after phase transfer. | 119 |
| **Figure 3.15** | (a) PL emission peak for aqueous $Ag_2S/ZnS$ NCs consistent over (b) PL emission 48 days. (b) Turbidity measurement for 48 days of same aqueous $Ag_2S/ZnS$ NCs (c) Pictorial representation of colloidal solutions for 1 month (at day 50, the colloidal solution is disturbed due to agglomeration) | 120 |
| **Figure 3.16** | (a) UV-absorption spectrum of aqueous $Ag_2S/ZnS$ NCs at different pH solutions (b) PL spectra of aqueous $Ag_2S/ZnS$ NCs in different pH solutions. | 121 |
| **Figure 3.17** | Comparison between PL intensities for the photostability test performed on the water-soluble $Ag_2S$ NCs and aqueous $Ag_2S/ZnS$ core/shell NCs. | 121 |
| **Figure 4.1** | Alignment of magnetic moments, $\mu_z$, in a magnetic field, $B_o$. | 145 |
| **Figure 4.2** | Schematic representation of a $Gd^{3+}$ chelate with inner and outer sphere water molecule, surrounded by bulk water. | 147 |
| **Figure 4.3** | Structural representation of Gd-L | 148 |
| **Figure 4.4** | Relaxivity plot of Gd-L at four different concentrations. | 150 |
| **Figure 4.5** | Plot of $1/T_1$ versus different concentrations of Gd-L | 150 |
| **Figure 4.6** | (a) Schematic representation of $Gd^{3+}$ complex-capped $Ag_2S$ QDs (Gd-QD) obtained by functionalization of L-cysteine capped $Ag_2S$ QDs with $Gd^{3+}$ complex (Gd-L); (b)FTIR spectra of L-cysteine-capped $Ag_2S$ QDs (blue), Gd-L (red) and Gd-QD (black). | 152 |

| | | |
|---|---|---|
| **Figure 4.7** | (a) $^1$HNMR spectrum (400 MHz) of Gd-L; (b) $^1$HNMR spectrum (400 MHz) of Gd-QD2 and (c) $^1$HNMR spectrum (400 MHz) of Gd-QD1 demonstrating the exchange of water protons between bound and bulk water of surrounding respectively. | 154 |
| **Figure 4.8** | Optical constants of monoclinic $Ag_2S$ (X and Z directions) | 164 |

## *C2. List of Tables*

| | | Page No |
|---|---|---|
| **Table 2.1** | List of reactivity of para substituents with their Hammett substituent parameters. | 65 |
| **Table 2.2** | PL emission peak and its line-width (FWHM) for the $Ag_2X$ (X=S, Se) NCs synthesized using substituted thiourea, selenourea, thiocarbamate, and dithiocarbamate. | 74 |
| **Table 2.3** | Summary of the synthetic conditions and properties of QD1 and QD2 | 83 |
| **Table 3.1** | A detailed investigation of phase transferred $Ag_2S$ QDs. The QY was calculated by comparison of the integrated fluorescence intensity of QDs in organic solvent (TCE) and water against standard dye IR-140 ($\Phi_f = 0.167$, ethanol). | 108 |
| **Table 3.2** | Summary of the results. | 123 |
| **Table 4.1** | The common nuclei and their nuclear spin. | 144 |
| **Table 4.2** | Longitudinal relaxivity values of Gd-QD1/Gd-QD1 and other nanoprobes. | 155 |
| **Table 4.3** | Optical constants of monoclinic $Ag_2S$ (X and Z directions); Note, I = imaginary and R = real parts of dielectric constants ($\varepsilon_1$ and $\varepsilon_2$) and refractive indexes (n and k). | 164-167 |

## *C3. List of Schemes*

| | | |
|---|---|---|
| **Scheme 2.1** | Experimental set up for synthesis of $Ag_2X$ NCs. | Page No 61 |
| **Scheme 2.2** | (a) Resonance (-R) effect of the nitro group leading to a decrease in the electron density on the nitrogen atom. (b) Hyperconjugation effect of nitro group (+I effect) leading to increase in the electron density on the nitrogen atom. | 67 |
| **Scheme 3.1** | Schematic representation of the synthesis of $Ag_2S$/ZnS core/shell NCs. | 114 |
| **Scheme 3.2** | Phase transfer of $Ag_2S$/ZnS core/shell NCs from organic (chloroform) to the aqueous phase (water) using *L*-cysteine. | 118 |
| **Scheme 4.1** | Synthesis of the ligand for biofunctionalization. | 149 |
| **Scheme 4.2** | Biofunctionalization of $Ag_2S$ QDS with Gd-L to form a dual-modal MRI/NIR-II Imaging agent. | 151 |

# *Annexure D: List of Abbreviations*

## *List of Abbreviations*

| | |
|---|---|
| $Ag_2S$ | Silver Sulphide |
| $Ag_2Se$ | Silver Selenide |
| $Ag_2Te$ | Silver Telluride |
| $Ag_2S/ZnS$ | Silver Sulfide/Zinc Sulfide |
| $AgInS_2$-ZnS | Silver Indium Sulfide-Zinc Sulfide |
| Ag (DDTC) | Silver (Diethyldithiocarbamate) |
| AgAc | Silver Acetate |
| $Ag^+$ | Silver ion |
| ASF | Absorption Spectrum Fitting |
| $CDCl_3$ | Carbon Tetrachloride |
| $COO^-$ | Carboxylate Group |
| CQDs | Colloidal Quantum Dots |
| CdSe | Cadmium Selenide |
| CdTe | Cadmium Telluride |
| CdS | Cadmium Sulphide |
| DMF | Dimethylformamide |
| DCM | Dichloromethane |
| DMSO | Dimethyl sulfoxide |
| DCE | Dichloroethane |
| DMA | Dimethyl acetamide |
| DFT | Density Functional Theory |
| 2D | 2 Dimensional |

| | |
|---|---|
| DHLA-PEG | Dihydroxy Lipoic Acid-Polyethylene Glycol |
| DNA | Deoxy Ribonucleic Acid |
| DCC | N, N- Dicyclohexylcarbodiimide |
| DDT | Dodecane Thiol |
| DME | Dimethoxy Ethane |
| DMAP | Dimethyl Amino Pyridine |
| $D_2O$ | Deuterium Oxide |
| DMSO-$d_6$ | Dimethyl- $d_6$-Sulfoxide |
| EMA | Effective Mass Approximation |
| eV | Electron Volt |
| EDG | Electron Donating Group |
| EWG | Electron Withdrawing Group |
| EtOH | Ethanol |
| FTIR | Fourier Transform Infrared Spectroscopy |
| FWHM | Full-Width Half Maximum |
| Ge | Germanium |
| GSH | Glutathione |
| Gd | Gadolinium |
| HSAB | Hard Soft Acid Base |
| HOMO | Highest Occupied Molecular Orbital |
| HRTEM | High-Resolution Transmission Electron Microscopy |
| IC | Internal Conversion |
| ISC | Inter System Crossing |

| | |
|---|---|
| InP/ZnS | Indium Phosphide/ Zinc Sulfide |
| LUMO | Lowest Unoccupied Molecular Orbital |
| LED | Light emitting diode |
| MRI | Magnetic Resonance Imaging |
| 3-MPA | 3-Mercaptopropanoic Acid |
| MSOT | Multispectral Optical Tomography |
| NCs | Nanocrystals |
| NIR-II | Second Near-Infrared Region |
| NIR-I | First Near-Infrared Region |
| $Na_2S$ | Sodium Sulfide |
| NMR | Nuclear Magnetic Resonance |
| NTU | Nephelometric Turbidity Unit |
| 1-OA | 1-octylamine |
| ODE | 1-Octadecene |
| OA | Oleic Acid |
| OAm | Oleyl Amine |
| ZnO | Zinc Oxide |
| PbS | Lead Sulfide |
| PbSe | Lead Selenide |
| *p*–OMe | *para*-Methoxy |
| *p*–Me | *para*-Methyl |
| *p*–I | *para*-Iodo |
| *p*–$NO_2$ | *para*-Nitro |

| | |
|---|---|
| PL | Photoluminescence |
| PEG | Polyethylene Glycol |
| PTT/PDT | Photothermal Therapy and Photodynamic Therapy |
| Pb $(CH_3COO)_2$ | Lead Acetate |
| PLQY | Photoluminescence Quantum Yield |
| QDs | Quantum Dots |
| QY | Quantum Yield |
| RSC | Royal Society of Chemistry |
| RB | Round bottom flask |
| RSF | Relative Sensitivity Factor |
| Si | Silicon |
| SSP | Single Source Precursor |
| -SH | Thiol or Thiolate |
| SAED | Selected Area Electron Diffraction |
| SAMs | Self Assembled Monolayers |
| SBM | Solomon, Bloembergen, and Morgan equation |
| $(TMS)_2$ | Tetramethyl Silane |
| TCE | Tetra Chloroethylene |
| TGA | Thermogravimetric Analysis |
| TEM | Transmission Electron Microscopy |
| TMAH | Tetramethylammonium Hydroxide |
| TFA | Trifluoroacetic Acid |
| TLC | Thin Layer Chromatography |

| | |
|---|---|
| THF | Tetrahydrofuran |
| UV | Ultra Violet |
| XRD | X-Ray Diffraction |
| XPS | X-Ray Photoelectron Spectroscopy |
| ZnS | Zinc Sulphide |

# *Annexure E: List of Publications and Conferences*

## *E2. Details of publications*

**(a)** **Bhardwaj, K.**; Pradhan, S.; Basel, S.; Clarke, M.; Brito, B.; Thapa, S.; Roy, P.; Borthakur, S.; Saikia, L.; Shankar, A.; Stasiuk, G. J.; Pariyar, A.; Tamang, S.; Tunable NIR-II Emitting Silver Chalcogenide Quantum Dots Using Thio/Selenourea Precursors: Preparation of an MRI/NIR-II Multimodal Imaging Agent. *Dalton Transactions* **2020**, *49*, 15425–15432.

**(b)** Basel, S.; **Bhardwaj, K.**; Pradhan, S.; Pariyar, A.; and Tamang, S.; DBU-catalyzed One-pot Synthesis of Nearly Any Metal Salt of Fatty Acid (M-FA): A Library of Metal Precursors to Semiconductor Nanocrystal Synthesis. *ACS Omega*, **2020,** *5*, 6666–6675.

**(c)** Thapa, S.; **Bhardwaj, K.**; Basel, S.; Pradhan, S.; Eling, C.; Adawi, A.; G. Bouillard, J.; Stasiuk, G.; Reiss, P.; Pariyar, A.; and Tamang, S.; Long Term Ambient Stable Cubic $CsPbX_3$ (X=Br, I) Nanocrystals with tunable emission using Molecular Halogen. *Nanoscale Advances* **2019**, *1*, 3388–3391.

**(d)** A Simple Process for the Production of High Purity Metal Long-Chain Carboxylates. Indian Patent Application (Application no. **202031006346**).

Check for updates

View Article Online
View Journal

Dalton Transactions
An international journal of inorganic chemistry

Accepted Manuscript

This article can be cited before page numbers have been issued, to do this please use: K. Bhardwaj, S. Pradhan, S. Basel, M. Clarke, B. Brito, S. Thapa, P. Roy, S. Borthakur, L. Saikia, A. Shankar, G. J. Stasiuk, A. Pariyar and S. Tamang, *Dalton Trans.*, 2020, DOI: 10.1039/D0DT02974B.

Dalton Transactions

This is an Accepted Manuscript, which has been through the Royal Society of Chemistry peer review process and has been accepted for publication.

Accepted Manuscripts are published online shortly after acceptance, before technical editing, formatting and proof reading. Using this free service, authors can make their results available to the community, in citable form, before we publish the edited article. We will replace this Accepted Manuscript with the edited and formatted Advance Article as soon as it is available.

You can find more information about Accepted Manuscripts in the Information for Authors.

Please note that technical editing may introduce minor changes to the text and/or graphics, which may alter content. The journal's standard Terms & Conditions and the Ethical guidelines still apply. In no event shall the Royal Society of Chemistry be held responsible for any errors or omissions in this Accepted Manuscript or any consequences arising from the use of any information it contains.

ROYAL SOCIETY OF CHEMISTRY

rsc.li/dalton

View Article Online
DOI: 10.1039/D0DT02974B

ARTICLE

Published on 24 September 2020. Downloaded by University of New England on 9/24/2020 2:42:57 PM.

Dalton Transactions Accepted Manuscript

# Tunable NIR-II Emitting Silver Chalcogenide Quantum Dots using Thio/Selenourea Precursors: Preparation of MRI/NIR-II Multimodal Imaging Agent

Received 00th January 20xx,
Accepted 00th January 20xx

DOI: 10.1039/x0xx00000x

Karishma Bhardwaj,[a, ‡] Sajan Pradhan,[a, ‡] Siddhant Basel,[a] Mitchell Clarke,[b] Beatriz Brito,[b,c] Surakcha Thapa,[a] Pankaj Roy,[a] Sukanya Borthakur,[d] Lakshi Saikia,[d] Amit Shankar,[e] Graeme J. Stasiuk,[b,c,*] Anand Pariyar,[a] and Sudarsan Tamang[a,*]

Aqueous-stable, Cd- and Pb- free colloidal quantum dots with fluorescence properties in the second near-infrared region (NIR-II, 1000-1400) are highly desirable for non-invasive deep-tissue optical imaging and biosensing. The low band-gap semiconductor, silver chalcogenide offers a non-toxic and stable alternative to existing Pd, As, Hg and Cd-based NIR-II colloidal quantum dots (QDs). We report facile access to NIR-II emission windows with $Ag_2X$ (X=S, Se) QDs using easy-to-prepare thio/selenourea precursors and their analogues. Aqueous phase transfer of these QDs with a high conservation of fluorescence quantum yield (retention up to ~90%) and colloidal stability is demonstrated. Bimodal NIR-II/MRI contrast agent with tunable fluorescence and high $T_1$ relaxivity 408 $mM^{-1}\ s^{-1}$ per QD (size ~2.2 nm) and 990 $mM^{-1}\ s^{-1}$ per QD (size ~ 4.2 nm) have been prepared by grafting 50 and 120 monoaqua Gd (III) complexes respectively to two different sized $Ag_2S$ QDs. The size of the nanocrystals is crucial for tuning Gd payload and the relaxivity.

## Introduction

In biological imaging, the second near-infrared (NIR-II, 1000-1400 nm) emitting fluorophores afford, in principle, a higher signal-to-noise ratio compared to their visible (400-750 nm) and the NIR-I (750-900 nm region) counterparts.[1–8] A combination of factors such as low absorbance of water and other biomolecules and low scattering/autofluorescence by tissue make the NIR-II window ideal for deep-tissue optical imaging and sensing with a high spatial and molecular resolution.[5–9] Compared to organic dyes, colloidal quantum dots (QDs) based NIR-II fluorophores have superior quantum yield, size-tunable fluorescence, broad absorption window and high molar extinction coefficient.[10–12] In addition, the surface of the QDs can be grafted with a high payload of functional molecules such as drugs, antibody, peptides, nucleic acids, cell-penetrating peptides, MRI contrast agent etc.[13–17] Specially, functionalizing QDs with another imaging agent such as a MRI contrast agent leads to the formation of a multimodal contrast agent which facilitates better visualization compared to a single imaging technique.[17–19] For example, MRI/NIR-II fluorescent imaging probes enable both excellent molecular level sensitivity (fluorescence) and anatomic resolution (MRI) due to the combination of fluorescence and MRI techniques. In recent years, the multimodal imaging agents have gained immense significance in the domain of biomedical imaging.[18–22]

The majority of the existing line of QDs -based NIR-II fluorophores contain highly toxic $Cd^{2+}$, $As^{3-}$, $Pb^{2+}$ and $Hg^{2+}$ ions[23,24] posing a real concern and practical barrier for their application in bio-imaging. In this respect, silver chalcogenides have tremendous potential in the field of *in vivo* bioimaging and sensing.[2–4,25–27] $Ag_2S$ is non-toxic and has extremely low solubility product ($K_{sp} = 6.3 \times 10^{-50}$) with minimum risk of releasing $Ag^+$ ions into the biological environment.[3,28,29] Furthermore, its low band-gap (bulk: 1.1 eV) and possible quantum confinement effect at size regime below 4 nm (exciton Bohr radius: 2.2 nm) are ideal for tuning of their emission in the ~700-1400 nm range.[13] Similarly, the bulk band-gap $Ag_2Se$ is 0.15 eV[30,31] and their calculated exciton Bohr radius using bulk parameters is 2.9 nm. Strong absorption and emission tunability at sizes well below 4-5 nm are important for achieving low hydrodynamic diameter and renal-clearance from the body.[32] Studies have shown that $Ag_2S$ exhibit negligible cytotoxic or genotoxic effects at lower to moderate doses, making it an ideal candidate for practical use in *in-vivo* imaging.[3,28,29,33,34] Despite tremendous potential in biology, the colloidal synthesis of $Ag_2X$ (X=S, Se) is still less explored compared to II-IV, III-V and II-VI semiconductor NCs. Typically, the control of the size of $Ag_2X$ QDs has been accomplished mainly either by changing of

---

[a] *Department of Chemistry, School of Physical Sciences, Sikkim University, Sikkim 737102, India. E-mail: stamang@cus.ac.in*
[b] *Department of Biomedical Sciences, University of Hull, Hull, HU6 7RX, UK.*
[c] *Department of Imaging Chemistry and Biology, School of Biomedical Engineering and Imaging, King's College London, St Thomas' Hospital, London, SE1 7EH, United Kingdom. E-mail: graeme.stasiuk@kcl.ac.uk*
[d] *Department of Material Science, North East Institute of Science and Technology (NEIST), Assam 785006, India.*
[e] *Department of Physics, Kurseong College, West Bengal, India 734203.*

‡ These authors contributed equally to this work.

Electronic Supplementary Information (ESI) available: NMR spectra, FTIR spectra, and TGA spectra of precursors. Additional optical characterization, photographs and XPS spectra of colloidal quantum dots solution. Optical constants of $Ag_2S$ and DFT calculation. NMR, Mass and FTIR characterization of Gd complex and relaxivity studies data. See DOI: 10.1039/x0xx00000x

View Article Online
DOI: 10.1039/D0DT02974B

Published on 24 September 2020. Downloaded by University of New England on 9/24/2020 2:42:57 PM.

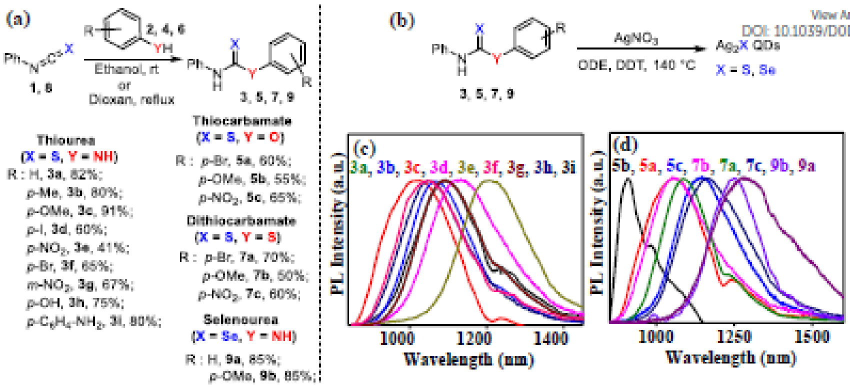

**Figure 1**. (a) Synthesis of a wide range of thiourea, thiocarbamate, dithiocarbamates and selenourea derivatives. (b) General scheme for the synthesis of $Ag_2S$/Se colloidal quantum dots (QDs). (c) PL spectra with tunable emission wavelength of as-prepared $Ag_2S$ QDs synthesized from thiourea precursors (**3a-g**) and (d) $Ag_2S$/Se QDs synthesized from thiocarbamate (**5a-c**), dithiocarbamates (**7a-c**) and selenourea derivatives (**9a-b**).

temperature[35,36] and reaction time[31,37] or both the parameters.[38,39] Both changing time and temperature can lead to the tunability of average final size, however, the methods undermine the competitive effects such as Ostwald ripening and uncontrolled depletion of molecular precursor, both leading to diminished control over final size-distribution. Size-tunability of quantum dots is crucial in many important areas of bio-imaging including-but not limited to- (a) application in multiplexed identification of several bio-molecules as spectrally distinct barcodes,[40,41] (b) controlling hydrodynamic diameter for efficient clearance of the intravenously injected quantum dots from the body[32] and (c) controlling functional molecule pay-load in quantum dots-based multimodal contrast agents.[16,17,42]

A recent study by Vela *et al.* on II-VI semiconductor NCs[43,44] and Owen[45,46] *et al.* on the synthesis of II-VI and IV-VI semiconductor NCs have introduced a more rational approach to control the photophysical properties of nanocrystals (NCs) *via* the reactivity of precursor. Vela *et al.* demonstrated the impact of phosphine-chalcogenide precursor reactivity on the composition and morphology of CdS/CdSe NCs.[43,44] Similarly, the size-dependent optical properties of PbS/PbSe was later reported by Owen *et al.* by modulating the reactivity of thio/selenourea derivatives.[45,46] However, the strategies have so far not been extended to $Ag_2X$ (X=S, Se) NCs. Herein, we report a facile synthesis of $Ag_2X$ (X=S, Se) NCs with environmentally benign and biologically conducive attributes tunable in the crucial NIR region (900-1400 nm) by controlling the reactivity of substituted thio/selenourea and their analogues *via* modification of substituent groups. These NCs have been successfully phase transferred to the aqueous medium and functionalized with a $T_1$-weighed MRI contrast agent to prepare an MRI/NIR-II imaging agent. The details of the finding are in the following.

## Result and discussion

We prepared a range of sulfur (substituted thiourea, thiocarbamate and dithiocarbamates) and selenium precursors with the direct reaction between isothiocyanate/isoselenocyanate with commercially available phenols, thiophenols or aryl amines (Figure1a). The reaction was carried out using off-the-shelf reagents in a suitable solvent such as chloroform, ethanol, dioxane or toluene at room temperature (*cf.* ESI; Experimental section), depending upon the solubility of the reactants. The reaction proceeds effortlessly yielding a good to excellent product yield (~up to 91 %) within a short time (~5-30 min, Figure 1a). In some cases, for example, in the reaction of nitro aniline with isothiocyanate in acetonitrile, heating to reflux temperature and longer reaction time is required. Inspired by the work of Owen and co-workers[45] on the synthesis of PbS, ZnS, SnS and CdS QDs using thiourea precursors, our initial attempt to synthesize the $Ag_2S$ QDs by reacting Ag-oleate with thiourea in 1-octadecene (a non-coordinating solvent) at precursor decomposition temperature (~150 °C) was unsuccessful. No photoluminescence (PL) emission was detected and the colloidal dispersion was poor (Figure S2). The colloidal stability and optical properties could not be improved even when an amine (oleyl amine) was added during the reaction as a co-capping ligand (Figure S3). However, when 1-dodecanethiol (DDT) was used as a capping ligand, stable $Ag_2S$ QDs was formed with excellent optical properties. DDT as capping ligand was found to be crucial for the successful synthesis of $Ag_2S$ QDs as the soft acid Ag (I)ion prefers soft bases like thiol (-SH) or thiolate more than amines or carboxylates. We propose that the

Dalton Transactions Accepted Manuscript

This journal is © The Royal Society of Chemistry 20xx

View Article Online
DOI: 10.1039/D0DT02974B

Published on 24 September 2020. Downloaded by University of New England on 9/24/2020 2:42:57 PM.

Dalton Transactions Accepted Manuscript

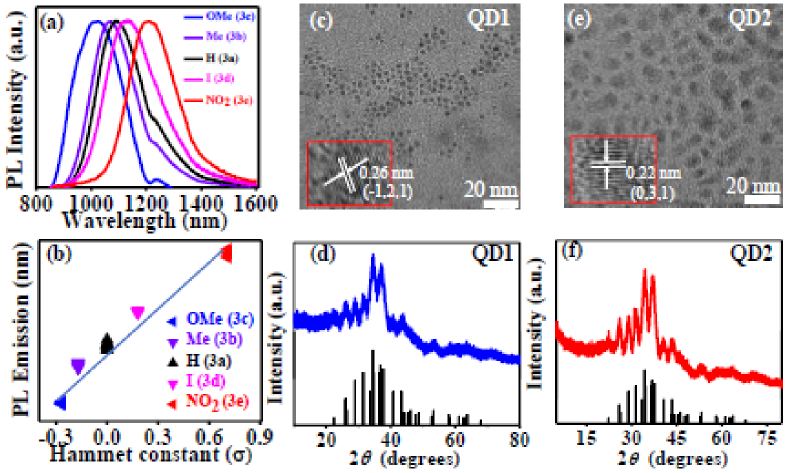

**Figure 2**. (a) PL spectra of $Ag_2S$ QDs synthesized from thiourea precursors (**3a-e**) bearing various substituents at the para position of phenyl ring (H, *p*-Me, *p*-OMe, *p*-I and *p*-$NO_2$); (b) A linear correlation of PL emission wavelength ($\lambda_{max}$) obtained from (**3a-e**) with corresponding Hammett constants ($\sigma$) for *para* substituents. (c) TEM micrograph (size~2.2 ± 0.52 nm) and (d) XRD pattern of purified **QD1** obtained from **3c.** (e) TEM micrograph (size~4.2 ± 1.1 nm) of and (f) XRD pattern of purified **QD2** obtained from **3e.** Insets in figure c and e show the lattice fringes corresponding to the monoclinic phase. In figure d and f, the XRD reflections of monoclinic $Ag_2S$ (JCPDS 14-0072) are shown as bars for comparison.

termination of surface of QDs with thiol-containing capping agents improve the colloidal stability and leads to monodisperse QDs with characteristic optical properties.[47–49] Furthermore, the standard redox potential of thiol-bound $Ag^{1+}$ ion is lower than free $Ag^{1+}$ ion which implies that the thiol-bound Ag (I) is not easily reduced to the undesired species.[31,47,48] In a typical synthesis of $Ag_2S$ QDs, as prepared substituted thiourea (**3a-g**) dissolved in DME, was quickly injected to the hot solution of the silver precursor containing a mixture of $AgNO_3$ and DDT in ODE at elevated temperature (120-150 °C) (Figure 1b). A distinct color change from red to black after 15 min indicated the formation of $Ag_2S$ QDs and the reaction was quenched by immediate cooling in an ice bath. To further understand the role of DDT we attempted to synthesize $Ag_2S$ QDs using only DDT at the reaction temperatures (120-150 °C). No formation of $Ag_2S$ QDs was noted in all the cases (Figure S4) possibly due to the high decomposition temperature (>170 °C) of DDT.[50] At elevated temperature (~200 °C) DDT formed $Ag_2S$ QDs without the use of additional S precursor, as detected by XRD and optical studies (Figure S5). However, size distribution and optical properties (emission) were poor. On the contrary, the lower decomposition temperatures of as-prepared thiourea precursor (<150 °C) compared to DDT is conducive for controlled release of sulphur at the optimized reaction temperature (120-150 °C, Figure S6) leading to improved size distribution and optical properties. Fourier transform infrared spectroscopy (FTIR) experiment performed on purified $Ag_2S$ QDs confirmed the presence of surface-bound DDT. The distinct shifting of the FTIR bands to 2916 $cm^{-1}$ and 2847 $cm^{-1}$ from 2922 $cm^{-1}$ and 2851 $cm^{-1}$ respectively attributed to the asymmetric and symmetric C-H stretching of DDT was observed (Figure S7).[51] These results show that DDT solely acts as the capping ligand for QDs in our synthetic scheme. Similarly, the other precursors such as thiocarbamates (**5a-c**) and dithiocarbamates (**7a-c**) as well as selenourea derivatives (**9a-b**) were also effective as a precursor under the optimized reaction condition to yield highly fluorescent $Ag_2S/Se$ QDs. Figure 1c demonstrates the photoluminescence (PL) emission spectra of $Ag_2S$ QDs in the NIR region (1020-1210 nm) prepared using (**3a-i**). Similarly, the NIR emission was also tunable in the range ~900 nm to 1300 nm by simply changing the substituent groups in thiocarbamates (**5a-c**), dithiocarbamates (**7a-c**) and selenourea precursors (**9a-b**) under optimized hot injection reaction condition (Figure 1d). In literature reports, the size of $Ag_2X$ (X=S, Se) QDs has been controlled mainly by changing the reaction temperature[35,36] or the reaction time[31,37] or both the parameters.[38,39] Our results offer the opportunity to control the optical properties of $Ag_2X$ (X=S, Se) QDs by controlling the precursor reactivity and conversion rates. In addition to this, the change of reaction temperature (Figure S8) and the reaction time (Figure S9) also affected the tunability of emission properties as

View Article Online
DOI: 10.1039/D0DT02974B

Published on 24 September 2020. Downloaded by University of New England on 9/24/2020 2:42:57 PM.

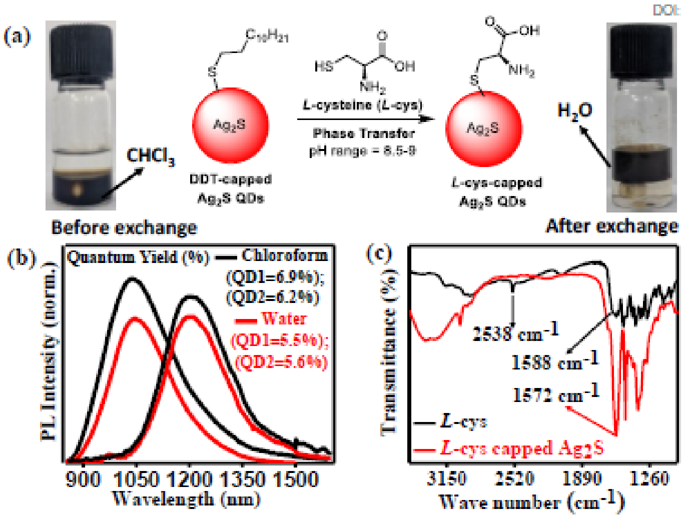

**Figure 3**. (a) Phase transfer of DDT-capped $Ag_2S$ QDs from organic phase (chloroform) to aqueous phase using *L*-cysteine at pH ~9. (b) PL emission spectra of $Ag_2S$ QDs (**QD1** and **QD2**) before (dispersed in $CHCl_3$, black) and after ligand exchange process with *L*-cysteine (dispersed in water, red). The spectra have been recorded at same absorbance (concentration) in both the phases. (c) FTIR spectra of free *L*-cysteine (black) and *L*-cysteine-capped $Ag_2S$ QDs (red).

reported in the literature.

To understand the effect of thiourea conversion reactivity on the final size, $Ag_2S$ QDs were synthesized using thiourea precursors (**3a-e**) with different substituent group under the same reaction condition (15 min, 150 °C). The final products were monitored using photoluminescence (PL) emission spectroscopy, X-ray diffraction (XRD) and transmission electron microscope (TEM) (Figure 2). The thiourea with no substituent group in the phenyl ring (**3a**) yielded $Ag_2S$ QDs with a PL emission peak at 1094 nm (Figure 2a). On increasing the electron-donating ability by introducing methyl group as a *para* substituent in phenyl ring (*p*-Me, **3b**), the PL emission exhibited a distinct blue shift to 1071 nm. Further increasing the electron-donating ability by using *p*-OMe substituent in phenyl ring (**3c**) resulted in a blue shift in the PL emission ($\lambda_{max}$~1024 nm). In contrast, the presence of *p*-I substituent (**3d**) having moderate electron-withdrawing ability resulted in a red-shift of PL peak ($\lambda_{max}$~1133 nm). A significant red-shift ($\lambda_{max}$~1209 nm) was observed in the presence of **3e** bearing *p*-$NO_2$ group indicating the formation of larger sized $Ag_2S$ QDs. Interestingly, the PL emission maxima linearly correlated with corresponding Hammett constant ($\sigma$) of the individual substituents (**3a-e**; H, *p*-Me, *p*-OMe, *p*-I and *p*-$NO_2$) of thiourea precursor corroborating a strong and predictable influence of electronic effects (Figure 2b).[52] Consistent with the PL spectra, the TEM images (Figure 2c, 2e) and XRD spectra (Figure 2d, 2f) confirm the difference in sizes of QDs formed using **3c** (**QD1**) and **3e** (**QD2**). $Ag_2S$ QDs were fairly monodisperse with **QD1** and **QD2** of average sizes 2.2 ± 0.52 nm and 4.2 ± 1.1 nm respectively (Figure 2c and 2e). The XRD pattern for **QD1** was broader compared to that of **QD2** (Figure 2d and 2f) respectively due to the finite size effect and the diffraction patterns are consistent with monoclinic $\alpha$-$Ag_2S$ phase (JCPDS 14-0072).[53,54] The strong electron-withdrawing capacity of *p*-$NO_2$ group decreased the reactivity of the thiourea, leading to the formation of larger sized QDs compared. On the other hand, the presence of electron-donating group such as *p*-OMe led to enhanced reaction rate and smaller QDs. It is interesting to note that, this trend of size/emission tunability of $Ag_2S$ QDs with respect to the reactivity of the substituted thiourea precursor is contrary to that observed in the case of PbS, ZnS or CdS QDs (Figure S10) in literature report[46] indicating that the underlining reaction pathway in our case is possibly different. A detailed investigation is required to map out the exact reaction mechanism, however, the above results can be explained by assuming rate-limiting nucleophilic attack on $Ag^+$ by the precursor through C=S bond. Furthermore, the electronics of other analogues of thiourea namely thiocarbamate (**5a-c**) and dithiocarbamates (**7a-c**) revealed a similar effect on the shift of PL of $Ag_2S$ QDs. The thiocarbamate (**5b**) formed smaller $Ag_2S$ QDs ($\lambda_{max}$~900 nm) due to its higher reactivity compared to thiourea and dithiocarbamates (Figure 1d). In the case of $Ag_2Se$ QDs

Dalton Transactions Accepted Manuscript

This journal is © The Royal Society of Chemistry 20xx

View Article Online
DOI: 10.1039/D0DT02974B

Published on 24 September 2020. Downloaded by University of New England on 9/24/2020 2:42:57 PM.

Dalton Transactions Accepted Manuscript

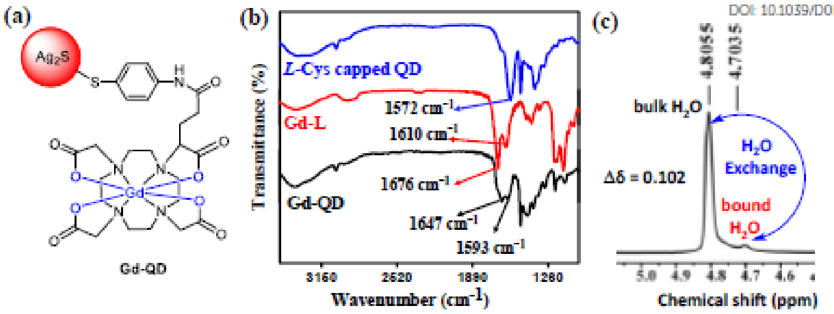

**Figure 4**. (a) Schematic representation of $Gd^{3+}$ complex-capped $Ag_2S$ QDs (**Gd-QD**) obtained by functionalization of *L*-cysteine-capped $Ag_2S$ QDs with $Gd^{3+}$ complex (**Gd-L**); (b) FTIR spectra of *L*-cysteine-capped $Ag_2S$ QDs (blue), **Gd-L** (red) and **Gd-QD** (black); (c) $^1$HNMR spectrum (400 MHz) of **Gd-QD1** demonstrating the exchange of water protons between bound and bulk water of surrounding.

synthesis, a similar trend in the shift of PL emission as a function of the para substituent (**9a** and **9b**) in selenourea derivative (Figure 1c and 1d) was observed. In some cases, such as **3i**, **5a** and **5b** (Figure 1c and 1d), small additional peak is observed in addition to the main PL emission, similar to that reported for silver chalcogenides and are attributed to the presence of surface defects.[30] $Ag_2S$ and $Ag_2Se$ NCs formed were further confirmed using X-ray photoelectron spectroscopy (XPS) (Figure S11 and S13). The C 1s signal was calibrated at 284.8 eV, prior to the assigning of other observed peaks (Figure S9a and S9b). Consistent with the literature report,[55,56] the presence of two prominent peaks at 368.9 eV and 374.9 eV in the Ag 3d core-level spectra of $Ag_2S$ QDs (Figure S9c) are ascribed to Ag $3d_{5/2}$ and$3d_{3/2}$ respectively. The spectrum of S 2p (Figure S11d) could be deconvoluted to three individual components corresponding to S-H (162.9 and 164.1 eV), S-C (161.9 and 163.1 eV) and S-Ag (161.3 and 162.5 eV) as shown in the figure S12.[57] The individual peaks S2p1/2 and S2p3/2 corresponding to each component are separated by a spin–orbit splitting of ~1.2 eV[58] and have FWHM 1-1.2. The presence of S-C and S-H binding energies, in addition to S-Ag peak explain the observed atomic ratio (S/Ag) of 1.6: 1, which is on the higher side. This is attributed to the presence of the DDT on the surface of $Ag_2S$ QDs which is also confirmed by FTIR results (Figure S7). Similar observation is also reported in the literature.[55]

The XPS spectra for $Ag_2Se$ QDs are shown in Figure S13. These QDs have excellent colloidal stability in non-polar solvents such as hexane and toluene. However, the practical application of QDs for biomedical applications relies mostly on their colloidal stability in the aqueous system with the conservation of the optical properties.[59–62] In the following, we demonstrate the phase transfer and surface functionalization of the as-prepared QDs. We substituted hydrophobic surface ligands (DDT) with a hydrophilic ligand, *L*-cysteine in basic pH (Figure 3a). We chose *L*-cysteine due to its small size and zwitterionic nature, which are considered crucial for achieving compact size and low non-specific binding in the biological set-up.[61,62] The DDT-capped $Ag_2S$ QDs of two different sizes **QD1** (size~2.2 nm) and **QD2** (size~4.2 nm) dispersed in chloroform showed a quantum yield (QY) of about 6.9 % and 6.2 % respectively (measured with respect to IR-140, the NIR-II standard dye as a reference, Figure 3b). The purified DDT-capped $Ag_2S$ QDs dispersed in chloroform was subjected to ligand exchange process in the presence of *L*-cysteine dissolved in water at a pH~9 (*cf*. ESI; Experimental section).[62] The slightly elevated pH ensures deprotonation of thiol to thiolate. The pH of the phase transfer reaction is important because the metal-thiolate binding energy is higher than the metal-thiols.[62] The phase transfer was successful within 2 h yielding the *L*-cysteine-capped $Ag_2S$ QDs in excellent yields (yield~93% and 90.0 % for **QD1** and **QD2** respectively) with a high conservation of the colloidal stability and the quantum yield (QY~5.5% and 5.6% for **QD1** and **QD2** respectively, Figure 3b). The FTIR spectrum of *L*-cysteine-capped $Ag_2S$ QDs is depicted in Figure 3c. The FTIR spectrum of pure *L*-cysteine shows a characteristic S-H stretching vibration signal at 2538 cm⁻¹ (Figure 3c). The absence of this peak in aqueous $Ag_2S$ QDs (Figure 3c) confirmed the absence of unbound *L*-cysteine in solution. A prominent peak at 1572 cm⁻¹ is ascribed to the asymmetric stretching vibration of carboxylate (COO⁻) group of surface-bound *L*-cysteine. For free L-cysteine, this peak is observed at a slightly higher frequency (~1588 cm⁻¹).

$Ag_2S$ QDs offer NIR-II emission with improved signal-to-noise ratio and functionalizing it with a $T_1$-weighed MRI contrast agent further improves its imaging efficiency and accuracy. We synthesized the $Gd^{3+}$ based complex (**Gd-L**, Figure S14a) based on our earlier report[16] (*cf*. ESI; Experimental section) and subjected to the functionalization of the surface of *L*-

Published on 24 September 2020. Downloaded by University of New England on 9/24/2020 2:42:57 PM.

cysteine capped $Ag_2S$ QDs to obtain an MRI/NIR-II fluorescence contrast agent, **Gd-QD** (figure 4a). We functionalized the surface of $Ag_2S$ QDs of two different sizes **QD1** (Size~2.2 nm) and **QD2** (Size~4.2 nm) with **Gd-L** to obtain **Gd-QD1** and **Gd-QD2** respectively (*cf.* ESI; Experimental section). The $Gd^{3+}$ based complex is known for its ability to lower the longitudinal relaxation ($T_1$) of bound water protons for improving localized signal intensity,[63] resulting in the enhancement of the image contrast.[64–73]

The FTIR spectrum of **Gd-L** complex (Figure 4b) showed peaks at 1676 cm$^{-1}$ and 1610 cm$^{-1}$ owing to the asymmetric stretching vibration of $COO^-$ group and bending vibration of N-H group respectively. The successful grafting of Gd-L on to the $Ag_2S$ QDs surface, thereby forming **Gd-QD** is confirmed by observation of asymmetric stretching vibration of $COO^-$ group at a lower frequency (~1593 cm$^{-1}$). The broad absorption peaks at the range of 3000-3500 cm$^{-1}$ are due to O-H and N-H stretching vibrations.[74] The formation of **Gd-QD** conjugate is further confirmed from nuclear magnetic resonance (NMR, 400 MHz) spectroscopy by monitoring the change in chemical shift of water due to the presence of the paramagnetic center. The difference in the chemical shifts of bulk and bound water ($\Delta\delta$) for pure ligand, **Gd-L** is 0.3917 ppm (Figure S14b). After functionalization with **QD1** and **QD2**, the distinct change in $\Delta\delta$ was observed for both **Gd-QD1** ($\Delta\delta$ = 0.102, Figure 4c) and **Gd-QD2** ($\Delta\delta$ = 0.0301, Figure S14c) respectively. This result, taken together with FTIR result where no free **Gd-L** was detected, unanimously supports the successful grafting of $Ag_2S$ with **Gd-L**. Notably, the smaller sized **Gd-QD1** exhibited a smaller longitudinal relaxivity ($r_1$) of 7.78 mM$^{-1}$s$^{-1}$ per **Gd-L** and *vice versa* was shown by larger sized **Gd-QD2** ($r_1$=8.27 mM$^{-1}$s$^{-1}$ per **Gd-L**). This is an increase from **Gd-L** which on its own exhibits an $r_1$ = 5.36 mM$^{-1}$s (Figure S15 and S16). The higher relaxivity of **Gd-QD** compared to **Gd-L** is due to the presence of quantum dots which restricts free rotation in solution, therefore increasing $r_1$.[16] The concentration of $Ag_2S$ QDs were determined at high photon energy (~450 nm), where molar extinction coefficient is independent of the size of QDs [75,76]. We used molar extinction coefficient of 1.73 × 10$^5$ M$^{-1}$ cm$^{-1}$ calculated using Ricard equation[77] at 450 nm (The optical constants used for calculation of molar extinction coefficient were determined using DFT, *cf.* ESI; Determination of Optical constants). At 400 MHz, the relaxivity per-QD for **Gd-QD1** and **Gd-QD2** was found to be 407.8 mM$^{-1}$s$^{-1}$ and 990.3 mM$^{-1}$s$^{-1}$ respectively (*cf.* ESI; Relaxivity measurements). Thus, the observed increase in relaxivity in **Gd-QD2** compared to **Gd-QD1** can be attributed to both the increase in the size of the nanocrystals which results in more restricted rotation in solution and increase in Gd payload due to larger surface area. In our study, we have demonstrated functionalization of the size-tunable $Ag_2S$ QDs exhibiting fluorescence in biologically important NIR-II diagnostic window. The obtained values for relaxivity are much higher than the smaller complexes and the commercially available MRI contrast agents.[66] The comparison of longitudinal relaxivity values of **Gd-QD1/Gd-QD2** with other MRI contrast agents are listed in Table 1. The high longitudinal relaxivity values for both **Gd-QD1** and **Gd-QD2** in comparison to other nanoprobes suggest that **Gd-QD1** and **Gd-QD2** have a promising potential as a bright MRI contrast agent in bioimaging applications.

**Table 1. Longitudinal relaxivity values of Gd-QD1/Gd-QD1 and other nanoprobes**

| nanoprobe | longitudinal relaxivity ($r$) |
|---|---|
| **Gd-QD1** | $r_1$ = 7.75 mM$^{-1}$s$^{-1}$ |
| **Gd-QD2** | $r_1$ = 8.27 mM$^{-1}$s$^{-1}$ |
| **Gd-L** | $r_1$ = 5.36 mM$^{-1}$s$^{-1}$ |
| Gadovist[66] | $r_1$ = 4.34 mM$^{-1}$s$^{-1}$ |
| Gd-doped QDs[67,74,78] | $r_1$ = 5.5–6.4 mM$^{-1}$s$^{-1}$ |
| $Gd_2O_3$ nanoparticles[79] | $r_1$ = 6.9 mM$^{-1}$s$^{-1}$ |

## Conclusions

A new method for the synthesis of bio-compatible silver chalcogenide QDs using easy-to-prepare substituted thiourea, thiocarbamate, dithiocarbamates and selenourea as S or Se precursors and DDT as capping agent is developed. The emission wavelength can be tuned in the NIR-II region by tuning reactivity of the precursor. The electronic effect of substituents groups and atoms on the size is evident from the blue or red shift in PL emission of the QDs consistent with electron-withdrawing or donating abilities of the substituent group. In the case of substituted phenyl containing precursors, the final size of QDs fits linearly with Hammett equation. The phase transfer of $Ag_2S$ QDs from chloroform to aqueous phase was achieved by surface ligand exchange of DDT with *L*-cysteine and the aqueous QDs were subsequently functionalized with $Gd^{3+}$ complex to form a dual-modal contrast agent with high NIR-II quantum yield (~5-6 %) and MRI $T_1$ water relaxivity (408-990 mM$^{-1}$ s$^{-1}$ per QD) depending upon the size of the QDs.

## Conflicts of interest

The authors declare no competing financial interest.

## Acknowledgements

ST, SP and KB acknowledge SERB-DST, Government of India for research funding (EEQ/2016/000751 and EMR/2016/002505). SB would like to thank Department of Science and Technology, Government of India (DST/INSPIRE/03/2016/001207) [IF160689] for financial support under DST-INSPIRE Scheme. AP acknowledges SERB-DST (EEQ/2016/000685) and DST-Inspire (DST/INSPIRE/04/2015/002674), for financial assistance. ST and GJS thank the Royal Society (Grant IE160227) for finacial assistance. GJS would like to thank the Medical Reseasrch Council for funding (MR/T002573/1). AS acknowledges DST-

Dalton Transactions Accepted Manuscript

This journal is © The Royal Society of Chemistry 20xx

This is an open access article published under an ACS AuthorChoice License, which permits copying and redistribution of the article or any adaptations for non-commercial purposes.

ACS OMEGA

http://pubs.acs.org/journal/acsodf

Article

# DBU-Catalyzed One-Pot Synthesis of Nearly Any Metal Salt of Fatty Acid (M-FA): A Library of Metal Precursors to Semiconductor Nanocrystal Synthesis

Siddhant Basel, Karishma Bhardwaj, Sajan Pradhan, Anand Pariyar, and Sudarsan Tamang*

Cite This: https://dx.doi.org/10.1021/acsomega.9b04448

Read Online

ACCESS | Metrics & More | Article Recommendations | Supporting Information

**ABSTRACT:** The metal salts of fatty acid (M-FA) are the most widely used metal precursors to colloidal semiconductor nanocrystals (NCs). They play a key role in controlling the composition, shape, and size of semiconductor NCs, and their purity is essential for attaining impeccable batch-to-batch reproducibility in the optical and electrical properties of the NCs. Herein, we report a novel, one-pot synthesis of a library of highly pure M-FAs at near-quantitative yields (up to 91%) using 1,8-diazabicyclo[5.4.0]undec-7-ene or the related nonionic/noncoordinating base as an inexpensive and ecofriendly catalyst in a green solvent medium. The method is highly general and scalable with vast academic and industrial potential. As a practical application, we also demonstrate the use of these high-quality M-FAs in the synthesis of the spectrum of colloidal semiconductor NCs (III−V, II−VI, IV−VI, I−VI, I−III−VI, and perovskite) having absorption/emission in visible to the near-infrared region.

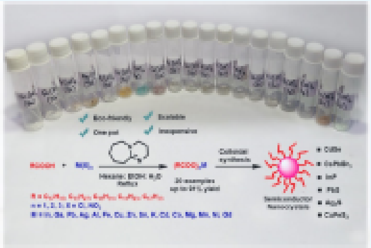

See https://pubs.acs.org/sharingguidelines for options on how to legitimately share published articles.

## 1. INTRODUCTION

Because a seminal paper by Brus et al. was published in 1983,[1] colloidal synthesis has emerged as a powerful and effective method to prepare high-quality inorganic nanocrystals (NCs).[2,3] The metal salts of fatty acids (M-FAs) are the most common form of metal precursors in nearly all semiconductor NC syntheses based on the hot injection method in the noncoordinating solvent.[4−11] In the colloidal synthesis of NCs, M-FA plays a crucial role in solubilizing the metal ions, controlling the precursor reaction, nucleation and growth processes, and passivating the surface and stabilizing the colloidal dispersion.[12−16] Therefore, the role of M-FAs is decisive for the evolution of crystal phase,[11] size,[5] and shape[17] and even the higher dimensional assembly of the NCs[17,18] with unique physical and chemical properties. In addition to this, it is well-known that M-FAs are the key ingredients in a plethora of industrial and domestic products including cosmetics,[19] lubricants,[20−22] paints,[23] biofuels,[24,25] and rubber.[26] Some of the common methods employed for the synthesis of M-FA precursors are the (1) vacuum method; (2) saponification method; (3) precipitation (double decomposition) method; and (4) direct reaction of fatty acids with metals. Conventionally, in the colloidal synthesis of semiconductor NCs, M-FAs are synthesized by the "vacuum method" where metal acetate and the desired fatty acid are vacuumed together at high temperature in high boiling solvents.[4,5,8,11,13] For example, for the synthesis of InP NCs, the indium salt of fatty acid is prepared in situ by the vacuum method prior to the reaction. Typically, a mixture of In-acetate and fatty acid (myristic acid, palmitic acid, stearic acid, oleic acid or lauric acid) is mixed in a noncoordinating solvent [1-octadecene (1-ODE)][5] and are vacuumed at 110−130 °C for 1−2 h to obtain a "clear solution" of indium carboxylate.[5,13] Unfortunately, there is no consensus about time, pressure, and temperature of this method with respect to purity and composition of the M-FA formed in situ, and this shortcoming may lead to batch-to-batch inconsistencies in the properties of the NCs. Except for a few special cases,[6,27,28] where M-FAs have been fully characterized, the purity of the M-FA precursor in most cases were not confirmed prior to the colloidal synthesis and characterization. Therefore, given the sensitivity of these colloidal reactions and in view of the uncertainty involved with the purity of M-FAs prepared by the "vacuum method", many of the kinetic studies and the conclusions reported therein may not be fully accurate, especially in quantitative studies. Recent reports have preferred pure M-FAs prepared ex situ for the synthesis and kinetic studies of NCs, emphasizing on the growing importance of the compositional purity of the precursor.[6,29] For example, Owen and coworkers[6] synthesized

Received: December 26, 2019
Accepted: March 6, 2020

© XXXX American Chemical Society

Check for updates

View Article Online
View Journal

Nanoscale
Advances

Accepted Manuscript

This article can be cited before page numbers have been issued, to do this please use: S. Thapa, K. Bhardwaj, S. Basel, S. Pradhan, C. Eling, A. Adawi, J. Bouillard, G. J. Stasiuk, P. Reiss, D. A. Pariyar and S. Tamang, *Nanoscale Adv.*, 2019, DOI: 10.1039/C9NA00486F.

This is an Accepted Manuscript, which has been through the Royal Society of Chemistry peer review process and has been accepted for publication.

Accepted Manuscripts are published online shortly after acceptance, before technical editing, formatting and proof reading. Using this free service, authors can make their results available to the community, in citable form, before we publish the edited article. We will replace this Accepted Manuscript with the edited and formatted Advance Article as soon as it is available.

You can find more information about Accepted Manuscripts in the Information for Authors.

Please note that technical editing may introduce minor changes to the text and/or graphics, which may alter content. The journal's standard Terms & Conditions and the Ethical guidelines still apply. In no event shall the Royal Society of Chemistry be held responsible for any errors or omissions in this Accepted Manuscript or any consequences arising from the use of any information it contains.

ROYAL SOCIETY
OF CHEMISTRY

rsc.li/nanoscale-advances

View Article Online
DOI: 10.1039/C9NA00486F

COMMUNICATION

This article is licensed under a Creative Commons Attribution-NonCommercial 3.0 Unported Licence.

Nanoscale Advances Accepted Manuscript

Received 00th January 20xx,
Accepted 00th January 20xx

DOI: 10.1039/x0xx00000x

# Long-Term Ambient Air-Stable Cubic $CsPbBr_3$ Perovskite Quantum Dots using Molecular Bromine

Surakcha Thapa,[a,§] Karishma Bhardwaj,[a,§] Siddhant Basel,[a,§] Sajan Pradhan[a], Charlotte J. Eling [b] Ali M. Adawi,[c] Jean-Sebastien G. Bouillard,[c] Graeme J. Stasiuk,[b] Peter Reiss,[d] Anand Pariyar[a] and Sudarsan Tamang[a,*]

**We report unprecedented phase stability of cubic $CsPbBr_3$ quantum dots in ambient air obtained by using $Br_2$ as halide precursor. Mechanistic investigation reveals the decisive role of temperature-controlled *in-situ* generated, oleylammonium halide species from molecular halogen and amine for the long term stability and emission tunability of $CsPbX_3$ (X=Br, I) nanocrystals.**

High photoluminescence quantum yield (PL QY), narrow emission linewidth, tunable band gap, large diffusion lengths and low exciton binding energies are some of the key attributes of all-inorganic caesium lead halide perovskite nanocrystals (LHP NCs) i.e., $CsPbX_3$, X=I, Br, Cl.[1,2,3,4,5,6] This novel class of NCs has been shown to be highly "defect tolerant", i.e. defect states are either shallow or localized in the valence or the conduction band.[1,2] Unlike conventional semiconductor NCs, the rigorous passivation of their surface *via* formation of core/shell structures or other methods is not required to achieve high QY. These LHP NCs are promising building blocks for light emitting diode,[3,4] solar cell,[5,6] laser,[7] photocatalysis[8] and detector[9]. Despite the recent surge of studies on $CsPbX_3$ perovskite NCs, a persisting drawback is their poor phase stability in ambient air. For example, cubic ($\alpha$) "black" phase $CsPbI_3$ ($E_g$=1.73 eV) perovskite NCs undergo rapid phase transformation to non-luminescent orthorhombic ($\delta$) "yellow" phase in ambient condition (Figure S1) leading to undesired changes of the band gap, optical and electrical properties.[6,10-11] Similarly, cubic ($\alpha$) $CsPbBr_3$ ($E_g$=2.25 eV) is very unstable at ambient condition.[12] For successful integration of these materials into devices, the issue of long-term phase stability must thus be addressed.[6,13] Most of the reported strategies involve the use of additives such as halide salt[12], phosphinic acid[14], ammonium halide[11], 2,2′-iminodibenzoic acid[15] sulphides and metal ions[16] and polymers[5] or *via* special post-synthetic purification step.[6,10] Herein, we report the first synthesis of highly stable, cubic $\alpha$-$CsPbBr_3$ perovskite NCs using $Br_2$ as an independent halide precursor. In a typical synthesis, lead nitrate is dissolved in 1-octadecene in the presence of oleyl amine (OAm) and oleic acid (OA). To this solution, $Br_2$ (**Warning:** handle the liquid $Br_2$ in fume hood, $Br_2$ vapors are toxic**)** and caesium oleate solutions (both dissolved in ODE) are sequentially added. Phase stability and emission colour tunability are achieved by controlling the reaction temperature (75-200 °C) and amount of $Br_2$ (0.6-1.2 mmol) under air-free synthetic condition (*cf. Supp. Inf.; Experimental Section)*. The "three-precursor" nature[17,16,18] of our synthetic scheme allows for independent tuning of the amount of the individual elements *viz*., $Cs^+$, $Pb^{2+}$ and $X^-$ ions and in turn, allows for the precise control over the surface chemistry.[17] Highly crystalline, monodisperse 7.62 ± 1.0 nm sized cubic $\alpha$-$CsPbBr_3$ NCs (Figure 1a) were

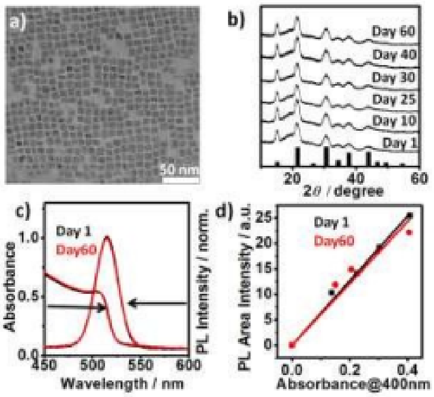

**Figure 1:** (a) TEM image of cubic $CsPbBr_3$ perovskite NCs (size: 7.62±1.0 nm) (b) XRD patterns showing film stability of $CsPbBr_3$ NCs over a period of 60 days in the air under ambient condition (Relative humidity ~50-60%). The pattern of $\alpha$-$CsPbBr_3$ (JCPDS 00-054-0752) is indicated as black bars for comparison. (c) UV-Vis absorption and normalised PL spectra of as-prepared (Day 1) $\alpha$-$CsPbBr_3$ NCs and the same sample stored in ambient air for 60 days as the colloidal solution (hexane). (d) Integrated photoluminescence vs absorbance plot[19] for day 1 (black) and day 60 samples (red). Absorbance is measured at the excitation wavelength (400 nm).

---

[a] *Department of Chemistry, School of Physical Sciences, Sikkim University, India 737102; *Email:stamang@cus.ac.in*

[b] *Department of Biomedical Sciences, University of Hull, Hull, HU6 7RX, UK.*

[c] *Department of Physics, University of Hull, Hull, HU6 7RX, UK.*

[d] *Univ. Grenoble Alpes, CEA, CNRS, IRIG/SyMMES/STEP, 38000 Grenoble, France.*

[e] *†Electronic Supplementary Information (ESI) available: [Full description of the experimental details and additional experimental data are available in supporting information]. See DOI: 10.1039/x0xx00000x*

*§These authors contributed equally to this work.*

## *D3. Conferences*

a) Presented a paper at an International e-Conference of Recent Advances in Physics & Material Sciences **2020** organized by Kurseong College & St. Joseph's College, Darjeeling, West Bengal.

b) Presented a paper (Short Invited Talk) at the International Online Conference on Materials Science and Technology (ICMT 2021) 12th - 14th November **2021** Kottayam, Kerala, India.

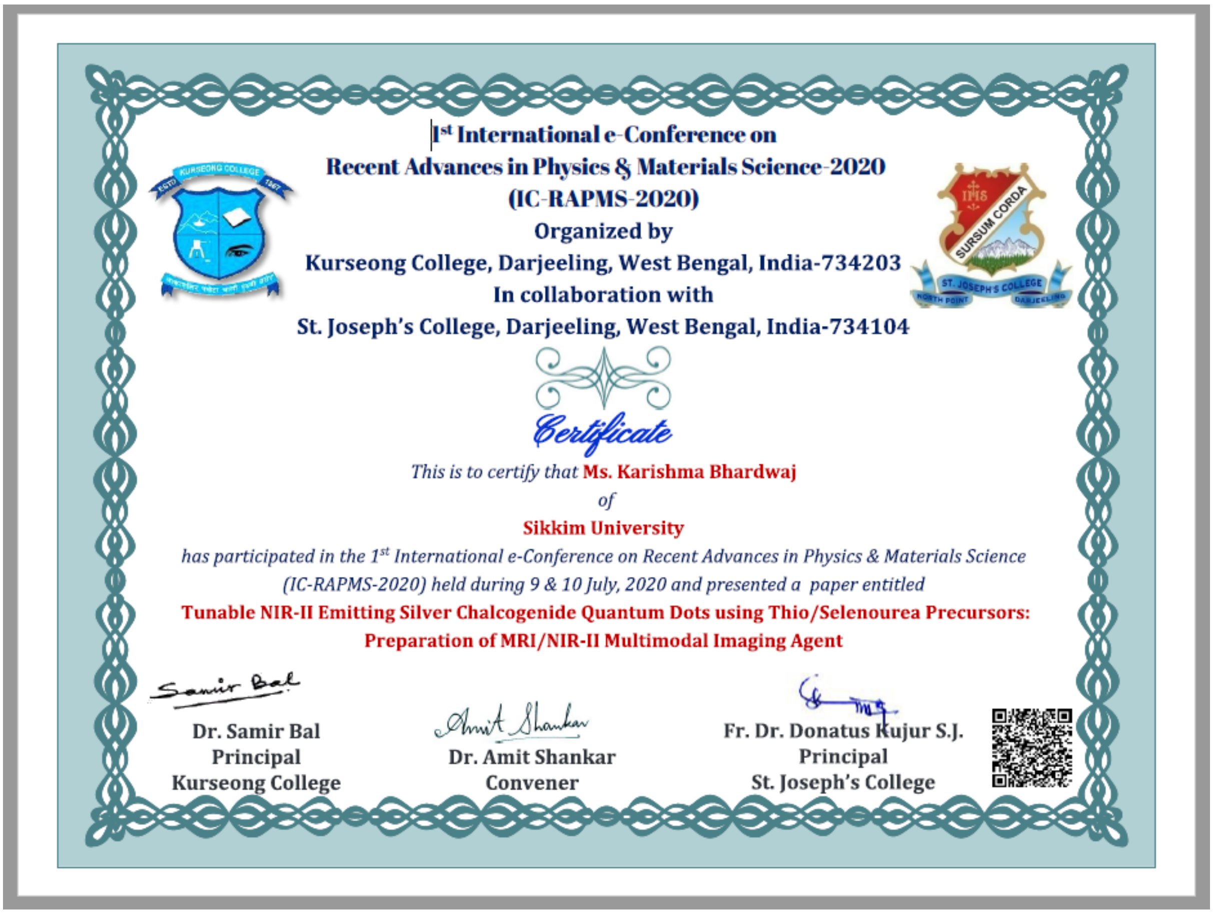

**1st International e-Conference on**
**Recent Advances in Physics & Materials Science-2020**
**(IC-RAPMS-2020)**
**Organized by**
**Kurseong College, Darjeeling, West Bengal, India-734203**
**In collaboration with**
**St. Joseph's College, Darjeeling, West Bengal, India-734104**

*Certificate*

*This is to certify that* **Ms. Karishma Bhardwaj**
*of*
**Sikkim University**
*has participated in the 1st International e-Conference on Recent Advances in Physics & Materials Science (IC-RAPMS-2020) held during 9 & 10 July, 2020 and presented a paper entitled*
**Tunable NIR-II Emitting Silver Chalcogenide Quantum Dots using Thio/Selenourea Precursors: Preparation of MRI/NIR-II Multimodal Imaging Agent**

Samir Bal
**Dr. Samir Bal**
**Principal**
**Kurseong College**

Amit Shankar
**Dr. Amit Shankar**
**Convener**

**Fr. Dr. Donatus Kujur S.J.**
**Principal**
**St. Joseph's College**

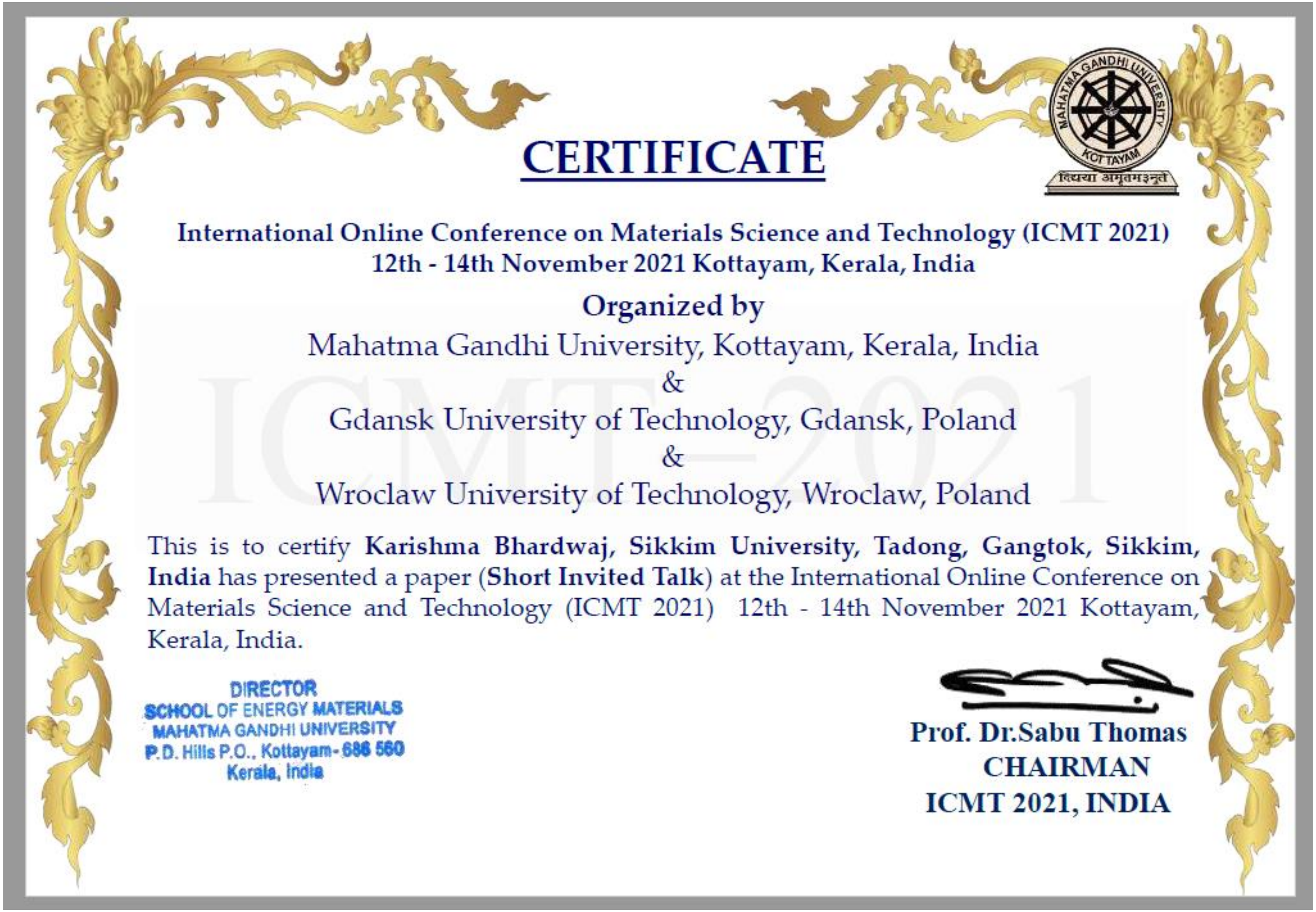

# CERTIFICATE

**International Online Conference on Materials Science and Technology (ICMT 2021)**
**12th - 14th November 2021 Kottayam, Kerala, India**

**Organized by**

Mahatma Gandhi University, Kottayam, Kerala, India
&
Gdansk University of Technology, Gdansk, Poland
&
Wroclaw University of Technology, Wroclaw, Poland

ICMT-2021

This is to certify **Karishma Bhardwaj, Sikkim University, Tadong, Gangtok, Sikkim, India** has presented a paper (**Short Invited Talk**) at the International Online Conference on Materials Science and Technology (ICMT 2021) 12th - 14th November 2021 Kottayam, Kerala, India.

DIRECTOR
SCHOOL OF ENERGY MATERIALS
MAHATMA GANDHI UNIVERSITY
P.D. Hills P.O., Kottayam- 686 560
Kerala, India

**Prof. Dr.Sabu Thomas**
**CHAIRMAN**
**ICMT 2021, INDIA**